Mechanical testing and modelling of porous construction materials

A thesis presented to the
Budapest University of Technology and Economics
in fulfilment of the
thesis requirement for the degree of
Doctor of Philosophy
in
Civil Engineering

by

Zoltán Gyurkó

Civil Engineer, MSc

Mechanical Engineer, MSc

Supervisor

Rita Nemes, PhD.

Associate Professor

Budapest, 2020

DECLARATION OF AUTHENTICITY

I declare that the contents and the work described in this thesis were performed at the Budapest University of Technology and Economics, Faculty of Civil Engineering. I certify that all material presented in this dissertation is either my own work or acknowledged wherever adapted from other sources.

ACKNOWLEDGEMENT

I would like to express my sincere gratitude to my supervisor, Associate Professor Dr. Rita Nemes, who always encouraged and supported me while preparing this PhD thesis. I would also thank for Associate Professor Dr. Adorján Borosnyói, who was my supervisor during the first two years of my PhD studies, that he set me on this journey with his bright ideas.

Many thanks to the Budapest University of Technology and Economics (BME), Faculty of Civil Engineering, Department of Construction Materials and Technologies, with the head of department Dr. György Mihály Stocker and former head of department Prof. György L. Balázs.

I would like to extend my appreciation to my colleagues at the department and at the faculty: Prof. Katalin Bagi, Dr. Katalin Szilágyi, Dr. Olivér Fenyvesi, Dr. Tamás Károly Simon, Dr. Salem Nehme, Dr. Éva Lublóy, Dr. Tibor Kausay, Dr. Zsuzsanna Józsa, Dr. Miklós Gálos, Dr. Attila Erdélyi whom I got a lot of recommendations, advices and assistance along the way.

Thanks for the years spent together to my fellow PhD students Dr. Viktor Hlavička, Dr. Olivér Czoboly, Anna Szijártó, Péter Schaul, Dr. Abdul Kader El Mir, András Jakab, Dr. Balázs Nagy, Bence Jankus and especially to my roommate Sándor Sólyom.

Many thanks for their tireless work to my colleagues at the Laboratory: Erika Csányi, Viktória Rónaky, Krisztián Takács.

Finally thanks a lot for Department of Polymer Engineering for letting me use their equipment; for the OTKA K 109233 research project for the funding provided for this PhD thesis and for the Itasca CG for providing the DEM software used for the numerical investigations.

DEDICATION

To my parents and my wife, Réka, who supported me all along…

TABLE OF CONTENTS

MAJOR NOMINATIONS

General

d_{max}	maximum aggregate size [mm]	A	surface area [mm^2]
v/c	water-to-cement ratio [-]	V	volume of a sample [mm^3 or m^3]
$\sigma_{c,lab}$	compressive strength measured in laboratory [N/mm^2]	E_c	Young' modulus [GPa or N/mm^2]
ρ_T	Body density [kg/m^3]		

Hardness testing

W_t	the total indentation work during DSI test	h_m	maximum indentation depth [mm]
F_1	loading force in the loading phase of DSI test [N]	W_e	the elastic indentation work of DSI test
h_r	residual indentation depth [mm]	F_2	loading force in the unloading phase of DSI test [N]
F	loading force [N or kN]	k and n	empirical constants of Meyer's law
d	diameter of the imprint [mm]	D	diameter of the indenter [mm]
HB	Brinell hardess [HB]	h	indentation depth [mm]
F_m	maximum of the loading force [N]	d_r	residual indentation diameter [mm]
d_m	maximum indentation diameter [mm]	W_d	dissipated (plastic) indentation work during DSI test

Size effect

d	characteristic dimension [mm]	$\sigma_N(d)$	size-dependent nominal strength [N/mm^2]
f_t'	direct tensile strength [N/mm^2]	d_a	maximum aggregate size [mm]
B, λ_o, and α	empirical constants of SEL [-]	h	height of cylinder specimen [mm]
f_c'	compressive strength measured on standard size specimen [N/mm^2]	a and b	empirical constants
$f_{c,cyl}$'	compressive strength measured on standard size cylinder specimen [N/mm^2]	$f_{c,cube}$'	compressive strength measured on standard size cube specimen [N/mm^2]

Discrete element method

k_n	Normal stiffness of the parallel bonds [N/mm^2]	k_s	Shear stiffness of the parallel bonds [N/mm^2]
$\sigma_{c,DEM}$	compressive strength from the simulation [N/mm^2]	ε	Error between the compression strength measured in the lab and in DEM [-]
R	radius of an element in DEM [mm]	$\sigma_{pb}(d)$	size dependent parallel bond strength [N/mm^2]
f'_{pb}	Normal strength of parallel bond in case of standard size specimen [N/mm^2]	m_R, m_c, m_L, m_N, m_{Dens}	Multiplier factors used to consider different aggregate types
c_L, c_N, c_{Dens}	Constants used to consider different aggregate types		

LIST OF ABBREVIATIONS

DEM	Discrete Element Method	**DE**	Discrete Element
FE	Finite Element	**FEM**	Finite Element Method
PFC	Particle Flow Code	**SCM**	Supplementary Cementitious Material
NSC	Normal Strength Concrete	**HSC**	High Strength Concrete
MK	Metakaolin	**OPC**	Ordinary Portland Cement
DSI	Depth Sensing Indentation	**SEM**	Scanning Electron Microscopy
TG	Thermogravimetry	**DTG**	Derivative of TG
DTA	Differential Thermal Analysis	**CCP**	Cellular Concrete Powder
AC	Aerated Concrete	**AAC**	Autoclaved Aerated Concrete
ACP	Aerated Concrete Powder	**CSH**	Calcium Silicate Hydrate
FPZ	Fracture Process Zone	**SEL**	Size Effect Law
MSEL	Modified Size Effect Law	**NDT**	Non-destructive Test
AR	Aspect Ratio	**CFD**	Computational Fluid Dynamics

CHAPTER 1: INTRODUCTION

This chapter outlines the research program by discussing the background of the subject area, aim and objectives of the study (through its specified scope and limitations).

1.1 Research significance and challenges

Present PhD research provides laboratory tests and numerical analyses in which the mechanical testing of porous construction materials was carried out by various test methods to fill the gap in the literature in this topic. The expected results of the research program will contribute to a more accurate understanding of the investigation and behaviour of porous construction materials and to the development of material models.

Non-destructive test methods (especially hardness testing) has a widespread and well-detailed literature in case of homogeneous materials, however in case of porous materials the literature is lacking of consistent results and conclusions. Besides that, the majority of the researches in the topic are out of date, since then new approaches and devices were developed that could provide more insight to the behaviour of the material. Numerical models could be one of those approaches that are able to describe the inner micro or macro structure of a porous material. Using non-destructive test methods and numerical models it could be achieved that from a single piece of material a large number of data would be available leading to the decrease of the required (in some cases costly or not even possible) destructive laboratory tests.

One of the aspects of material testing that was well-studied but till now no conclusive proof was derived and no comprehensive model was described is the size effect on the compressive strength of concrete. According to Bažant the topic should be further studied using numerical methods, especially using Discrete Element Method (DEM), to understand the processes inside the material during its failure (*Bažant, 1999*). The most widely used engineering modelling approach, the Finite Element Method, is not well suited for discrete problems like this. However, the DEM is nowadays on a research level phase and not easily usable for the engineering practice mostly due to the long-lasting calibration process of a model. Thus it would be practically useful to create methods that can decrease this calibration phase to make DE models faster to use for engineers. It gives a significance to this PhD thesis that numerical models are supported by laboratory tests, analytical and microstructural analyses of the materials are included.

Besides that, our world moves to a direction where apart from the strength and durability of a structure, its sustainability becomes more and more important. Therefore, such advanced type

of concretes shall be developed that possess high strength, good durability and are sustainable. The most obvious way to develop this new green version of concrete is replacing a specific amount of its ingredients by recycled materials, such as construction wastes that cannot be reused other ways, but available in large amount. Large amount of construction waste is produced in a powder form by the construction industry. Some of these materials can be advantageous for the properties of concrete thus it is worth to investigate them in more depth: by doing so not only some waste material is eliminated but the properties of concrete can be improved too.

1.2 Scope and limitations

In the present research the mechanical testing and the modelling of porous construction materials is studied (see *Fig. 1*). The PhD thesis has two major sections:

1. In the first section a wide range of structural construction materials are investigated through laboratory tests (compressive strength test, different versions of hardness tests, Young's modulus test, density) and numerical modelling methods (Discrete Element Method). The tested materials were the following:
    - Metals: aluminium, mild steel, structural steel (S235).
    - Concretes: normal strength concrete, high-strength concrete, polymer concrete.
    - Other CSH based materials: cellular concrete block (Ytong), sand-lime brick.
    - Ceramics: clinker brick, facebrick, clinker tile.
    - Natural stones: porous limestone and compact limestone, rhyolite tuff.
2. In the second section the focus was on concrete, the most widespread porous construction material. The mechanical properties of different concretes were evaluated. This section has three major sub-sections focusing on properties of concrete that has significant effect on the mechanical performance.
    a) To study the effect of aggregate type, the main variables of the concrete mixes were the following:
        - the type of aggregate: natural gravel, crushed stone, lightweight aggregate; on normal strength concrete;
        - the particle size distribution of the aggregates: A and C grading curves and no-fines as well; on normal strength concrete;

        From the design mixes 150 mm edge length cubes were cast for compressive strength tests.

b) The effect of a waste material (CCP) in powder form was investigated and compared to other waste materials and to traditional SCMs, like metakaolin:
    - in cement mortar (CEM I 42.5 N cement; w/c = 0.5)
    - in case of normal strength concrete (C20/25)
        - CEM I 42.5 N cement (270 kg/m^3); w/c = 0.57; d_{max} = 16 mm
    - in case of high strength concrete (C60/75).
        - CEM I 42.5 N cement (325 kg/m^3); w/c = 0.40; d_{max} = 16 mm

    The applied CCP had the maximum particle size (d_{max}) less than 0.09 mm. The findings of this section are only valid in case of CCP with particle size less than 0.09 mm. The applied amount of cement supplementary materials (in percentage of the cement amount) were the following:
    - CCP: 0 to 17%
    - MK: 10%
    - CCP-MK mix: 3 and 7%
    - Clay brick powder: 10%

From every mix 150 mm cubes were prepared for compressive strength tests, 100 mm edge length cubes for freeze-thaw resistance tests. From the cement pastes 40×40×160 mm prisms were prepared for flexural-tensile strength test and compressive strength test.

c) In case of the investigation of size effect, the focus was on normal strength concrete, which is in this thesis corresponds to the concretes with strength classes between C20/25 and C50/60. This is the range of strength classes within the most of the structural concretes are that is used by the construction industry. The findings of this section are limited to that range of compressive strength. The main variable parameters were the cement content, aggregate particle size distribution and water-to-cement ratio, while the other parameters were kept constant. Finally, five mixes of different strength classes were produced that were cast into different sized cube and cylinder moulds producing around 150 samples that were subjected to compressive strength test.

The findings in correspondence with the numerical simulations are only valid in case of applying Distinct Element Method, where the particles are modelled as rigid spheres (or as their bulks), and the material model is described in the contacts between the elements.

In general, in the applied concrete mixtures the amount of components were within their normal range, and the used components variants were the most generally applied in the construction

industry (except where it is specified otherwise) considering that they would not have special effect on the investigated property (e.g. that is why CEM I cement was applied):

- particle size distribution within A and C grading curves
- CEM I 42.5 type OPC
- aggregate was natural gravel (except in the study where the effect of aggregate type was investigated)
- water-to-cement ratio was between 0.35 and 0.67
- where it was needed SIKA Viscocreate 5 Neu type of plasticizer was applied in the minimum possible amount

In sum approximately 800 samples were prepared and investigated. More than 300 studies in research papers, theses, books and standards were reviewed, and excerpts from them were used in the preparation of this thesis, which may serve as a valuable document for researchers working in this field.

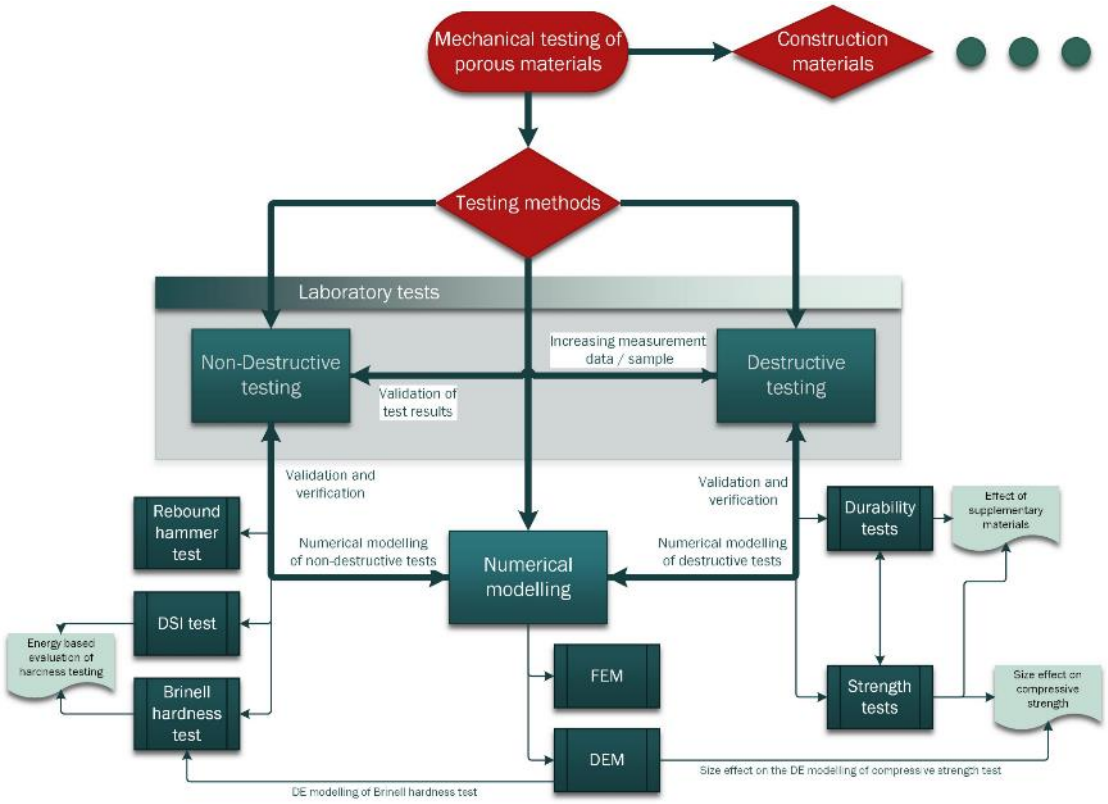

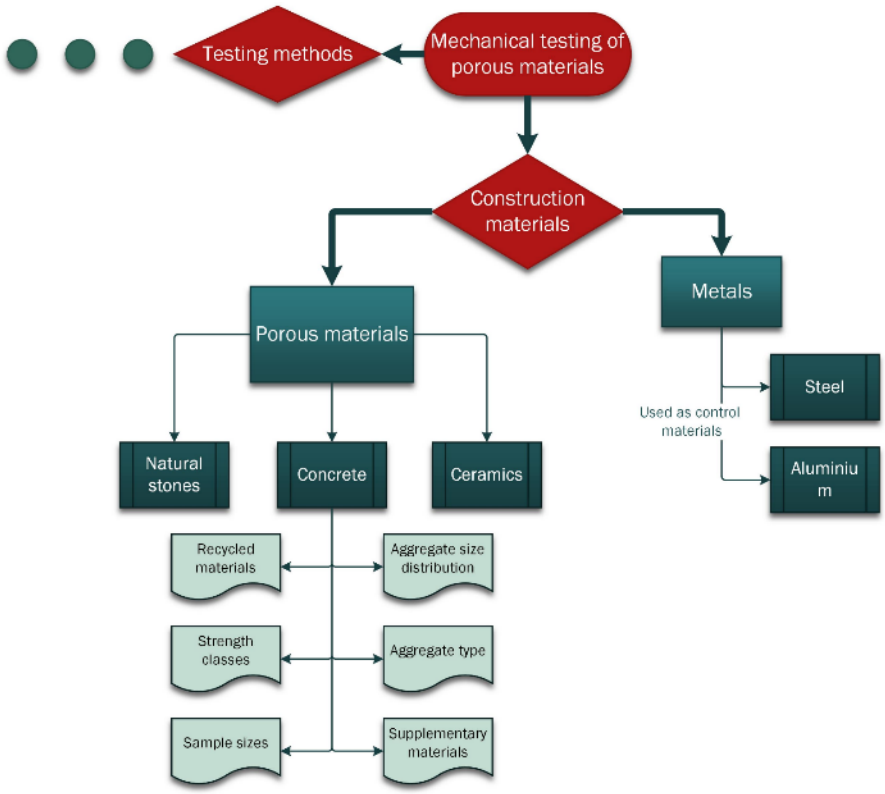

Fig. 1 *Overall research program*

1.3 Aim and objectives

An aim of this research was to investigate testing methods (either laboratory tests or modelling approaches) that reduce the number of required destructive material tests. It is beneficial in case of the inspection of already existing buildings and structures, where only a limited number of test samples can be acquired. Renovation of building is an environmentally favourable approach (instead of demolishing and rebuilding), however the extension of lifespan of a load bearing structure is only allowable if it was proven that it has sufficient load bearing capacity. The most widespread test method for the non-destructive testing of structural materials is hardness test. In case of porous construction materials hardness test was only applied in a form of dynamic hardness tests, which accuracy falls below the accuracy of destructive laboratory tests. Static hardness test are more advantageous in this aspect, however they were rarely applied for porous materials in the past. This PhD thesis is aiming to reach a better understanding on the processes in the material during a hardness test. Further aim of this thesis is to provide a deeper analysis about the open topics of mechanical testing and modelling of porous materials in focus to the most widely used porous construction material, concrete.

To reach these aims the following objectives were set for this PhD thesis:

- Find a hardness testing method that is able to provide appropriate amount of information on the behaviour of porous construction materials.
- Define a modelling approach that is suitable for the modelling of concrete and investigate the possibilities of the modelling of material testing in numerical environment:
  - the model shall be able to follow the different particle size distributions,
  - the model shall be able to follow the response of the material similarly (with an acceptable accuracy) to different type of loading schemes after proper calibration.
- Investigate the effect of the major influencing factors (like size of the specimens, aggregate type and distribution, effect of recycled materials) on the laboratory test and the numerical modelling of concrete.
  - Find a recycled material which potentially can be used in a concrete mix.
    - Investigate its effect on the mechanical and durability properties of concrete.
    - Analyse the inner structure of the material.
  - Define an approach how the different type of aggregates (crushed stone, lightweight aggregate) can be considered in a numerical model.
  - Investigate how specimen size affects the compressive strength of concrete and how it influences the numerical model parameters.

CHAPTER 2: LITERATURE REVIEW

This chapter gives a short overview of porous materials and their most important properties and introduces the background to the techniques how these properties could be tested, and the material can be described. The highlights of the current research activities in the topic are reviewed, pointing out the open questions and major problems.

2.1 Porous construction materials

Porous materials widely exist around us and play a major role in many aspects of our daily lives; among the fields they can be applied as vibration suppression, heat insulation, sound absorption, fluid filtration and structural material. Highly porous solids have high structural rigidity, and relatively low density of mass, so porous solids often serve as structural bodies in nature. Porous materials do not only exist in the nature but can be created artificially as well, like concrete, the artificial material used in the largest volume on Earth. The mechanical behaviour of porous materials can be diverse depending on the inner structures of the material. As an example, concrete can be considered as a composite material, which response to a given loading scenario is highly dependent on the properties of its components and their interaction with each other. Accurate mechanical description of such material is even more challenging than in case of a homogeneous material, and it has to be supported by laboratory tests to define the values of the key properties of the material.

2.2 Key properties of porous construction materials

2.2.1 Mechanical properties

In structural application, porous materials are mainly used in a way that they are subjected to compression, thus the characteristic that mainly determines their applicability is compressive strength. Besides that, their Young's modulus describes whether they are suitable as a construction material or not. Compressive strength is measured using high capacity presses. In the past, due to the absence of such presses, the strength of a material was associated with its surface hardness, which was much easier to measure.

2.2.1.1 Compressive strength

Compressive strength is the capacity of the material to withstand loads tending to reduce its size. For designers this is the most important property of a porous material in most cases; in industrial practice this is the property based on which a porous material is classified. The compressive strength of the material depends on several factors: the shape of the sample, the size of the sample, the condition of the loading plates and the pore water saturation of the

sample, etc. From a structural point of view, the most interesting among these is the size effect. Based on the work of many researchers, it became a well-known fact that there is an effect of size differences on the strength of specimens made of concrete (*Bažant et al. 1989, 1991, 1994, 1997; Kim et al. 2000, 2002, 2004; Tokyay and Özdemir, 1997*) [10].

2.2.1.1.1 Size effect of specimen size on the compressive strength

For standardization purposes, the concrete compressive strength measured on a standard cylinder (Ø150 mm × 300 mm - 1:2 width-to-height ratio) or cube (150 mm × 150 mm × 150 mm - 1:1 width-to-height ratio) is accepted as a unique material property (*ASTM, 2001*; *EN 206:2013*; *Kim and Yi, 2002*; *Yi et al, 2006*; *Szalai, 1982*). However, the compressive strength of concrete is not unique; it depends on the sizes and shapes of specimens due to their fracture characteristics (among other factors) (*Dombi, 1979*). In general, the measurements are performed on specimens with a straight axis and constant cross-section. Higher width-to-height ratio is not recommended if it is not aimed to deal with the effect of buckling (*Dombi, 1979*). It was proven that in case of a ratio higher than 1:3, buckling has an effect on the compressive strength of the sample. While for compressive strength tests these specimens are used for the determination of other material properties different size samples may be applied (e.g.: 100 mm × 100 mm × 100 mm cube for freeze-thaw resistance).

The so-called size effect law (SEL) was first derived by *Bažant (1984)*. After him Kim *et al.* (*Kim et al, 2000*; *Kim and Yi, 2004*) added the size-independent strength to SEL (*Eq. (1)*), with which it can approximate the nominal strength of concrete members that have similar or dissimilar crack patterns (*Kim et al, 1989*). This version of SEL is called modified size effect law (MSEL) and was also proposed by Bažant based on a different approach (*Bažant, 1987; 1993; Bažant and Xiang, 1997*).

$$\sigma_N(d) = Bf_t'/\sqrt{1 + d/\lambda_0 d_a} + \alpha f_t', \quad (1)$$

where $\sigma_N(d)$ is the size-dependent nominal strength; f_t' the direct tensile strength; d the characteristic dimension; d_a the maximum aggregate size; and B, λ_o, and α are empirical constants. Many research investigated the effect of maximum aggregate size on the fracture process zone (FPZ) and the concept of characteristic length (*Kim and Eo, 1990*). From a practical aspect, the most important is to get the compressive strength of a concrete specimen. Kim et al. (*Kim et al, 2000; Kim and Yi, 2004*) proposed *Eq. (2)* to obtain the compressive strength of a cylindrical shape specimen with various sizes and height-to-diameter ratios (*Kim et al, 1999*).

$$\sigma_N(h, d) = 0.4f_c'/\sqrt{1 + (h - d)/5} + 0.8f_c', \quad (2)$$

where the height of cylinder specimen h and diameter of cylinder specimen d are in cm. In this equation, f_c' is the maximum stress, which is usually considered as the compressive strength of concrete and determined in accordance with *ASTM C 39 (2001)*. The study suggests that this equation is usable on cylinders with maximum 4:1 h/d ratio. In this study, Kim et al. (*Kim et al, 2000; Kim and Yi, 2004*) also reached the conclusion that *Eq. (2)* is independent of d_a (if d_a is below 25 mm) and therefore it can be used for any maximum aggregate size below that. All the above-mentioned models describe that a larger specimen (made from the same concrete mix) has lower nominal strength. This strength difference is a direct consequence of energy release into a finite-size FPZ, and it cannot be explained by only Weibull-type statistics of random micro-defects (*Bažant et al, 1991*; *Bažant and Xi, 1991*; *Bažant and Chen, 1997*; *Kumar and Barai, 2012*). However presently, only a few, not too widespread design codes for concrete structures take into account the effect of size. In case of the compressive loading of concrete, the failure is caused by the distributed splitting cracks in the direction of the vertical axis as the lateral deformation increases during the failure progression. Though the mechanism of compressive failure has been well investigated, the failure mechanism and its size effect have been insufficiently studied (*Kim and Yi, 2004*).

2.2.1.2 Young's modulus

Young's modulus, or modulus of elasticity, is one of the most important mechanical properties. It defines the relationship between stress and strain in a material in the linear elasticity regime of a uniaxial deformation. The concept of a modulus describing the relationship of stresses and strains is originated from Leonhard Euler, but it is named after Thomas Young. Its determination would be the simplest from a uniaxial tensile test; however, this is from practical reasons, in case of porous materials not possible; thus Young's modulus is measured on prisms under bending load. In case of concrete, the modulus of elasticity is a function of the modulus of elasticity of the aggregates and the cement matrix and their relative proportions. The modulus of elasticity of concrete can be considered as constant at low stress levels, but it starts decreasing at higher stress levels as the number of microcracks starts to increase. The elastic modulus of the hardened paste may be in the range of 10-30 GPa and aggregates about 45 to 85 GPa. In case of normal strength concrete, it is in the range of 30 to 50 GPa. Its linear formula according to Hooke's law is: $E_c = \Delta\sigma_c / \Delta\varepsilon_c$

2.2.1.3 Surface hardness

Hardness testing was the first material testing practice in engineering, starting with the scratching hardness testing methods in the 17th century (*Barba, 1640*; *Réaumur, 1722*; *Mohs, 1812*). These methods appeared much earlier than the beginning of the systematic material testing that is considered to be started in 1857 when David Kirkaldy, Scottish engineer set up the first material testing laboratory in London, Southwark (*Timoshenko, 1953*). The research of the theoretical background of hardness was initialized by the pioneering work of Heinrich Hertz in the 19th century (*Hertz, 1881*). Hertz's proposal also formed the basis of the indentation hardness testing methods by Brinell (1900), Rockwell, (1920), Vickers (1924) and Knoop (1934) (*Fischer-Cripps, 2000*). All these methods are measuring the size of a residual plastic deformation in the tested specimen as a function of the indenter load. All methods are using a different indenter geometry (pyramid, spherical etc.), from these the spherical indenters can be used for testing both ductile materials (e.g. metals) and brittle materials (e.g. ceramics). The response of materials to the indentation test includes elastic (reversible) and plastic (irreversible) deformations as well as forming of cone cracks in brittle materials; therefore, the definition of the term 'hardness' is not evident (*Szilágyi et al, 2011*). Lately, a computer-aided version of hardness testing was developed and successfully applied on porous materials as well (*Glinicki and Zielinski, 2004*). The method is called Depth Sensing Indentation (DSI) test, and it is mostly applied to evaluate mechanical properties, like compressive strength or Young's modulus (*Tezcan and Hsiao, 2008*; *Ye et al, 2016*; *Chen et al, 2015*; *Gubicza et al, 1996*).

Hardness has a variety of meanings. To the metals industry, it may be the resistance to permanent deformation, to the metallurgist, it means resistance of penetration, to the design engineer, it is a measure of flow stress. Hardness may also be referred to as mean contact pressure. All of these characteristics are related to the plastic flow of materials. The best formulation to determine hardness is described as the following: hardness is the resistance, which exhibit the solid materials against the test tool, which is interacts with them or penetrating into them (*Chandler, 1999*). Hardness is closely related to several physical characteristics, including Young's modulus, the strength and the toughness. There are several ways to measure the hardness of a material:

- Static indentation tests (Brinell, Rockwell, Vickers)
- Rebound tests (Scleroscope and Leeb tests)
- Scratch file tests (Mohs)
- Plowing tests (Bierbaum)

- Damping tests (Herbert Pendulum test)
- etc.

From these methods the most accurate results can be given by the static indentation tests. Researchers in the 19th century developed numerous solutions for measuring hardness. The most important methods are the following: Hertz, Brinell, Shore monotron, Ludvig, Rockwell, Vickers, Drozd, Káldor-Bárczy, Brunner-Schimmer. The working principle, correlation and calculation methods for these are available in *Appendix II*. The great advantage of hardness tests is that these are so called non-destructive test (NDT) methods, so it does not result major damage during the test on the sample.

2.3 Numerical modelling of porous materials

2.3.1 Discrete Element Method

The Discrete Element Method (DEM) is a family of numerical methods for computing the motion and effect of a large number of small particles. In engineering tasks often one has to model structures, which are composed of granular materials or bricks, and whose elements are not connected in a material level. DEM is used to model grains, soil, masonry structures, domes and arches. In the last two decades the DEM has been successfully applied in various areas, like mining, powder metallurgy, civil engineering and in the oil industry (see *Fig. 2*).

A numerical technique is said to be a discrete element model if

- it consists of separate, finite-sized bodies ("discrete elements") and each of those elements are able to displace independently of each other,
- the displacements of the elements can be large,
- the elements can automatically come into and loose contact (*Bagi, 2012*).

The distinct element method is a version of DEM proposed by Peter A. Cundall in 1971 (*Cundall, 1971*). In this method, any particle that exists is regarded as a rigid element and the behaviour of this element is expressed by the equations of motion of extended bodies. A spring is provided between rigid elements which make contact with each other so as to express the interaction of force between them. Then, the equations of motion of each rigid element is solved by numerical integration along the time axis, whereby the behaviour of the element is analysed. The time integration method works with an explicit solver (central difference method).

With advances in computing power and numerical algorithms for nearest neighbour searching, it has become possible to numerically simulate millions of particles on a single processor (*Zhu, 2007*). Today DEM is becoming widely accepted as an effective method of engineering problems in granular and discontinuous materials, especially in granular flows,

powder mechanics, and rock mechanics. Recently, the method was expanded to incorporate computational fluid dynamics (CFD) and finite element method (FEM) and take thermodynamic effects into account under the name Extended Discrete Element Method. DEMs are relatively computationally intensive, which limits either the length of a simulation or the number of particles. Due to that reason this method only became practical for engineers in the 1990s, when the computer technology reached the appropriate level, where engineers were able to model realistic problems.

Advantages:

- DEM can be used to examine a wide variety of granular flow and rock mechanics problems. Several research groups have independently developed simulation software (Yade, 3DEC, PFC-3D, LS-DYNA) that agrees well with experimental findings in a wide range of engineering applications, including adhesive powders, granular flow, and jointed rock masses.
- DEM allows a more detailed study of the micro-dynamics of powder flows than is often possible using physical experiments. For example, the force networks formed in a granular media can be visualized using DEM. Such measurements are nearly impossible in experiments with many small particles.

Disadvantages:

- The maximum number of particles, and duration of a virtual simulation is limited by computational power. Typical flows contain billions of particles, but contemporary DEM simulations on large cluster computing resources have only recently been able to approach this scale for sufficiently long time (simulated time, not actual program execution time).

Any type of DE model is made up of two basic components: the elements and the contacts between them. The elements may either directly correspond to the physical units of the analysed system (e.g. stone voussoirs, sand grains, bricks), or the collection of elements as a whole represents a collection of a much larger number of real particles. The element can have different shapes, even a concave shape, but from a computational aspect circular (2D) or spherical (3D) elements are the easiest to handle, thus they are the most widely used in the current software packages (*Bagi, 2012*). Most DEM codes allow the user to define the behaviour of the element in a mechanical sense. They can be either perfectly rigid or deformable, depending on the application. When one uses a deformable element, the stress-strain relations are specified by the constitutive relations over the domain of the element. In

case of granular material models, this option is mostly neglected, because in most cases the stiffness of the particles are orders of magnitude higher than the stiffness of the simulated structure. The contacts are formed when two (or more) elements get in touch. If the distance among the points of two elements becomes zero then the elements are in contact. This distance can be even less than zero, then the elements are intersecting each other.

2.3.2 Numerical modelling of material tests and porous materials

Realistic and accurate numerical modelling of the failure of engineering materials is a challenging task, especially in case of non-homogeneous materials such as concrete. DEM, after proper calibration, could be a suitable alternative for such purposes. The accuracy of a numerical computation is influenced by many factors; therefore model validation is an unavoidable step of modelling (*Lanaro et al, 1997*). However, in the future numerical modelling will substitute laboratory tests to a greater extent (*Deotti et al, 2017*). It can be only achieved, if the process of accurate numerical modelling will not only be cost effective but agile and productive as well. Thus, it may be possible to decrease the number of necessary laboratory tests and substitute them with numerical simulations.

Only a limited number of books and articles can be found on the DE modelling of concrete. In this chapter I would like to present an overview of the publications associated with my work. It was planned to deal with different types of laboratory tests, e. g. with Brinell-hardness testing modelled with DEM too, but there was no available article found in the exact topic of Brinell-hardness testing with DEM.

Most of the researches are using ball-type models, because this describes the behaviour of concrete in the best way. This type of model is used in *PFC3D*, the software I applied in my research. In this case the aggregate particles are modelled as infinitely rigid elements, the cement among the particles are modelled by the contacts among the elements. We can take this assumption because the deformation capability of the cement is much higher than the aggregate's in case of normal strength concrete. The size effect of the elements was already investigated in the study of Liu (*Liu, 2012*). In their research they modelled asphalt concrete. Through this study, two important discoveries were made: element sizes could directly impact the simulated aggregate shapes, volumetric percentages of aggregate, time-step and computational time. As well as creep stiffness and element size effects on creep stiffness was not significant, but very significant on computational time. Of course, if more complex results are expected, smaller elements were recommended for better representing asphalt concrete micro-structural features.

The most important part of the modelling is the generation of a dense package. In the past several algorithms were investigated to solve this problem, as explained in *Appendix VII*. During the use of these algorithms, if one has a densely packed model, the next step is the verification of the model. In most cases the verification of contact parameters is obtained by using static uniaxial compression simulations. In my study this method was chosen also to adjust the parameters. With the use of the simulation of uniaxial compression tests and the comparison between the experimental and the numerical results, the calibration of the model on the behaviour of concrete at low pressure conditions is refined. The physical parameters involved are the local elastic stiffnesses (k_n k_s) (*Camborde et al, 2000*).

Numerical simulation of concrete failure process under compression was investigated also in the past on 2D cases. In the model of Wang the aggregates in concrete were considered as rigid bodies (*Wang, 2008*). Plastic behaviour after the elastic limit for a spring was considered to set up the constitutive model of the spring, and Mohr-Coulomb criterion was adopted to judge the failure of a spring.

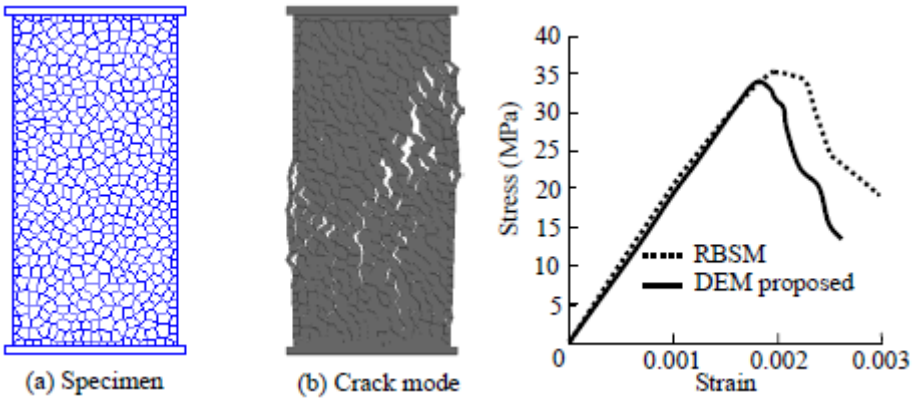

Fig. 2 *The specimen, the crack mode and the stress strain diagram of the investigation (Wang, 2008)*

The results of this investigation show that the method can simulate the propagation of damage and crack of cement-based materials both for small deformation problems and for larger deformation problems. The compressive strengths of mortar and concrete can be well predicted and the stress-strain relationships determined from the simulation are fairly accurate, as it can be seen in *Fig. 2*. During this investigation the researchers also examined the effect of boundary conditions using damped-damped and a free-free boundary conditions at the top and bottom end of the model. The results have shown small strength decrease and a steeper stress-strain curve in case of free-free boundaries. When the verification is complete process and the results were satisfactory a variety of different investigations and experiments can be done with the help of a DEM software.

As an example, DE model of concrete under high triaxial loading was investigated recently (*Tran, 2011*). The authors here built a model of concrete parallelepipeds containing about 10,000 discrete elements. In case of high pressure (up to 650 MPa) irreversible compaction of the material occurs and needs to be considered. In this investigation a local constitutive law has been developed to reproduce the discontinuous nature. Local parameters to be used in this constitutive law was set up by simulating reference uniaxial and triaxial tests in compression. Once these parameters have been obtained, the model is used to predict the response of concrete sample for triaxial compressive tests at different levels of confinement. The model made by the authors is able to predict the concrete sample's response in an accurate way, as it is shown in *Fig. 3*.

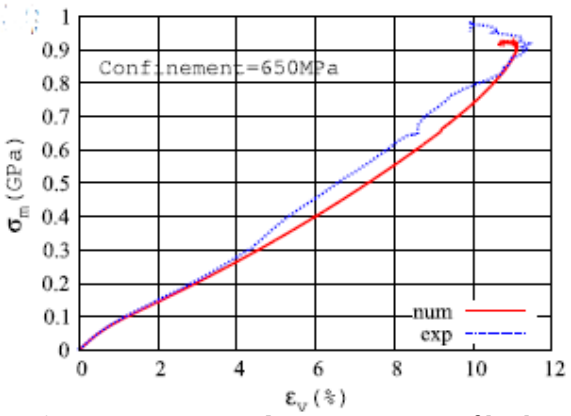

Fig. 3 *Stress-strain diagram in case of high stress (Tran, 2011)*

In my work an experiment was modelled to compare the results with real values. In the past various types of experiments were modelled by DEM, as Split Hopkins Pressure Bar test (SHPB), in which two long aligned metallic bars and a short concrete specimen between them are modelled (*Hentz, 2004*). The model of Lee and Kwon was used to simulate the breakage behaviour of a concrete block in repeated free fall tests (*Lee and Kwon, 2008*). The results of simulation were used to analyse the breakage characteristics of bonds between particles according to the number of free fall impacts. The results showed similar tendencies between the simulation and the experimental results. It was confirmed that the DEM with proper model parameters is able to simulate actual concrete characteristics.

The effect of SCMs was also modelled using DEM (*Le and Stroeven, 2013*; *2015*; *Moradi et al, 2018*; *Chandler et al, 2013*). Mostly it was found that it is not possible (or computationally effective) to model the cement and SCM particles together with the much larger aggregates. This caused numerical instabilities and resulted in extremely high computational time.

In this research I am dealing with the hardness testing of materials. In this topic *Ma et al (2014)* published a study about the DEM analysis of the scratch test, which can be also used to determine the hardness of a material. In this work, the scratch test is modelled numerically using the three-dimensional distinct element method. The effect of the cutting velocity and the

effect of the rock heterogeneity was investigated in this study with a sufficient result. In case of indentation hardness test a sphere penetrates into a surface with a given force. Different types of penetrations were already modelled in DEM, the main difference between these models and mine is that the penetration in my case is not "impact-like", but of low strain rate. To mention an example, penetration of missiles modelled with DEM was investigated in the last decade supported by the French Atomic Energy Agency (*Shiu et al, 2008*). The researchers made a three-dimensional DE model to investigate the behaviour of a non-deformable missile penetrating into a concrete slab. They wanted to know the evolution of penetration depth in terms of nose shape. In this model to connect the elements parallel bonds were used and the model was made by PFC, the same software which was used in my investigation. As a conclusion they found it that the results were coherent with the experimental values.

In general, it can be said, that all of the articles refer to the fact that they have chosen to use DEM, because in case of concrete, methods such as the FEM only give a good estimate of the weakening zones, but fail to characterize the behaviour of the fractures. Most of them uses circular (spherical) DE-s and the model is built in 2D, because of the lower computational effort. Using a 2D approach may be less time-consuming than the 3D, but the results will not be precise. The fracture process of granular materials is 3D like and the evolution of energy happens not along a line, but a surface, which has a typical shape regarding the given material, thus this process cannot be modelled in 2D satisfactorily. Based on that observation, I have chosen to use 3D modelling. As a conclusion it can be stated that DEM can be a good choice to model the penetration of a ball into a concrete surface.

2.4 Effect of recycled materials on the material properties of concrete

To use the huge amount of demolition waste, new recycling options should be developed, supported by laboratory tests and their results. The application of recycled materials in new concrete structures is inviting (*Mohammadhosseini et al, 2017*). It is not only economically beneficial (lower cost related to waste management), but a greener and more sustainable building industrial processes could be developed. The development of such material is the first step to develop a new product that can be applied in the construction industry. Thus, nowadays it became unavoidable to consider recycled materials as a component of concrete and deal with their effect on the mechanical properties of concrete.

Most of these materials (like metakaolin) are extensively studied, but there are some new materials, which has great possibilities but not yet reviewed in detail in the literature (*Borosnyói, 2016*). One of those demolitions wastes, which volume is highly increasing is

autoclaved aerated concrete (AAC). It is a world-wide well-known construction material; however, it is very young compared to the ancient ones e.g. timber, natural stone or even traditional concrete (*Kausay, 2002*). The blocks of AAC are made from lightweight aerated concrete, which besides its structural role provides heat insulation as well (*Hoff, 1972; Song et al, 2015*). The wide application of AAC in construction industry has been started between 1940-50 in Europe (see *Fig. 4*). The first buildings, made of its earlier version (aerated concrete, AC) are about to reach their design lifetime. In the EU many industrial and residential buildings were constructed from AAC blocks mostly designed for 50 years of lifetime. Therefore, large amount of AC and AAC waste can be expected to appear in building industry in the next decade(s). At the demolition of these buildings the potential in recycling the waste material arises. In the literature only a few studies can be found dealing with the recycling of AAC and those studies only dealt with the application of AAC as coarse aggregate (*Topcu et al, 2007; Sinica et al, 2009*), however, those studies showed that it is possible to apply AAC waste as aggregate in concrete. Those studies only dealt with the application of AAC as coarse aggregate (*Topcu et al, 2007; Sinica et al, 2009*), but there are other possibilities as well.

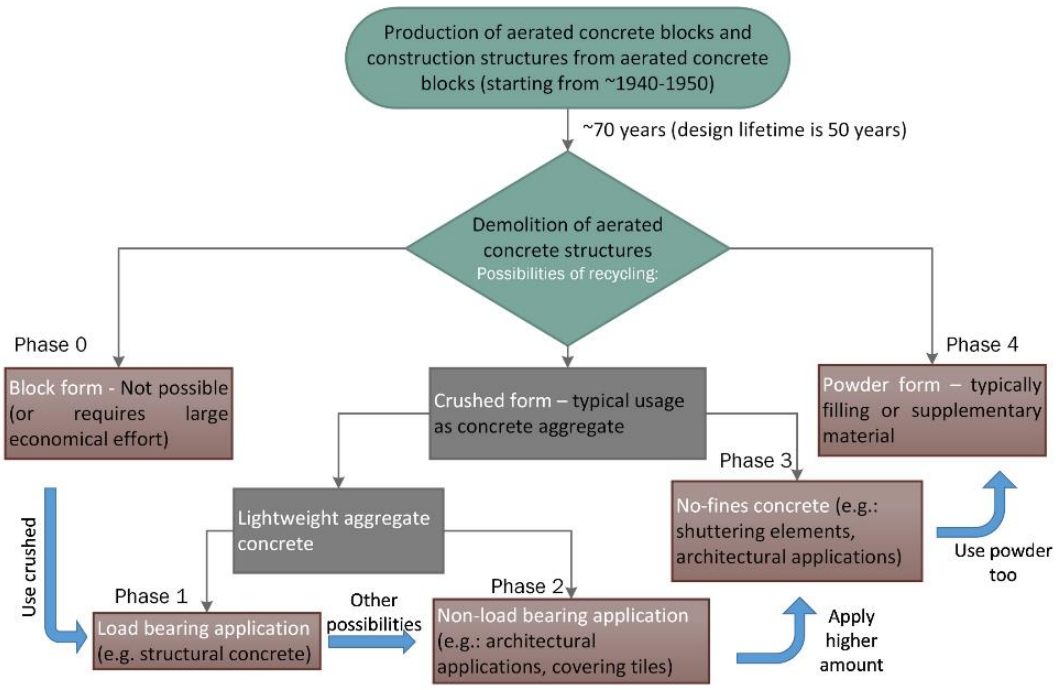

Fig. 4 *Possibilities in recycling of AAC as construction material*

There are three major forms in which AAC can be recycled: in block, crushed or powder form. In crushed form AAC can be recycled in lightweight aggregate concrete (crushed AAC waste is a lightweight aggregate; $\rho_T < 2000$ kg/m^3) or in no-fines concrete (here only applied as coarse aggregate).

In the following list the different possibilities of the reuse of AAC are given (*Fig. 4*):

- In block form: to reuse AAC in block form requires its demolition to be performed in a very professional and careful manner. This process (if it is even possible) requires extraordinary economical effort and time, making it not feasible for practical applications.
- Load bearing lightweight aggregate: *Fenyvesi and Jankus (2015)* designed concrete mixes were to produce load bearing lightweight aggregate concrete. Based on literature recommendations paste saturated mixtures were designed with high cement dosage. Here AAC was applied as fine and coarse aggregate. (*Fenyvesi and Jankus, 2015*; *Fenyvesi, 2014*). They found that for structural purposes it is not suitable.
- Non-load bearing lightweight aggregate: applications were introduced to use AAC as fine and coarse aggregate in non-load bearing applications by *Fenyvesi and Jankus (2015)*.
- No-fines concrete aggregate: AAC waste can be applied in no-fines concrete as aggregate. Here the aim is to decrease the amount of cement and thus create a cost-effective solution for the recycle of AAC.
- Powder form: During the cutting process and production of AAC blocks or rather the demolition of AAC buildings large amount of AAC powder waste arises. This powder could be applied in concrete as filling material or as supplementary material. The recycling of the powder fraction of normal concrete waste is problem as well, which has no satisfactory solution.

2.4.1 Application of AAC in powdered form

The cutting, chiselling and crushing process of cellular concrete blocks produces a significant amount of fine powder, which cannot be utilized in the later part of the construction. Besides that, during the production of AAC blocks large amount of industrial waste is generated in the form of powder. This powder (called as cellular concrete powder (CCP)) cannot be fully utilized in the previously described recycling solutions. Powder wastes typically applied in concrete as filler material, which in most cases decreases the strength of concrete. Until the magnitude of this decrease is not significant this is a feasible utilization of waste powder. If the grain size of powder is sufficiently small and its other properties are suitable as well, then it is possible that it will work as a supplementary material. It was shown by *Fenyvesi (2014)* that cellular concrete in crushed form is unfavourable as outdoor structural concrete aggregate. However, in the literature several researches can be found, who are proving that

concrete produced from waste materials can be advantageous (*Özalp et al, 2016*; *Fenyvesi 2014*). More significant performance improvement (in strength and durability) can be reached, if the waste material is added to the concrete mix in powdered form (*Gonzalez et al, 2016*; *Aprianti, 2017*). Besides that, applying waste materials in powdered form in the concrete mix can have the following positive effects:

- waste material is recycled. In this case it is advantageous if as much added to the mix as possible.
- It reduces the cost of the concrete mix (e.g. cement is partly substituted by waste material).
- It can increase the performance of concrete (used as additive or as supplementary cementitious material - SCM).

Many researches on concrete are aiming to create more advantageous concrete from strength and durability standpoint with the application of innovative admixtures and SCMs (*Siddique and Khan, 2011*). SCMs are highly advantageous, because besides their positive effects on strength and durability, they have environmental benefits, like the reduction of carbon dioxide emission and decreasing the porosity of normal strength concrete (*Gruber et al, 2001*; *Siddique and Klaus, 2009*; *Kubissa et al, 2017*; *Wilinska and Pacewska, 2018*). The strict European air-pollution regulations have produced many industrial by-products that can be used as supplementary cementitious materials, like metakaolin (MK) or silica fume. SCMs are applied to increase strength or enhance durability or to simply decrease cement content (as the most expensive component of concrete). However, nowadays the cost of typical SCMs (metakaolin, silica fume) is increasing due to the high demand. Thus, researchers are looking for other types of low-cost materials, which can have similar positive effects as SCMs.

Various waste materials can be used as SCMs as it was showed (*Özalp et al, 2016*; *Aprianti, 2017*). Mechanical behaviour of different waste materials was investigated by several researchers (*Topcu and Güncan, 1995*; *Topcu and Sengel, 2004*; *Sani et al, 2005*; *Li et al, 2005*). Ceramic waste was used as SCM in the study of Bignozzi and Saccani and it was proven to be a valid alternative to cement (*Bignozzi and Saccani, 2012*). In the research of Puertas ceramic wastes (fired red or white wall tiles) were applied in cement clinker production (*Puertas et al, 2008*). The research showed that the particle size of the applied waste material was lower than 90 μm, which resulted in a higher reactivity of this type of cement. The effect of particle size (surface area) of waste materials used as SCMs were investigated and it was found that the higher surface area (so smaller particle size) resulted higher compressive strength

and strength activity index (*Mirzahosseini and Riding, 2015*). The relationship of specific area and compressive strength was shown to be linear. By the usage of thermogravimetric analysis and calorimetry the hardening process and the mechanism of hydration in cementitious systems can be investigated (*Wu et al, 2009*; *Gruyaert et al, 2010*; *Talero and Rahhal, 2009*; *Scheinherrová et al, 2018*). Based on that, it can be investigated whether a material is suitable for potential SCM or not.

In this PhD thesis the waste of production and installation of cellular (aerated) concrete blocks are investigated. During the production and the cutting of the blocks, significant amount of waste material in form of powder is produced. The cellular concrete powder (CCP) could be easily collected and later used as concrete component. An advantage of CCP is that it is in the form of fine powder, as the result of the cutting process, thus no further preparation is needed before it is mixed to the other components of concrete. The main reaction product in cellular concrete is belongs to the tobermorite group of calcium silicate hydrates (C-S-H) (*Narayanan and Ramamurthy, 2000*). These products have very high specific surface area and are stable, which indicates that they may be used as SCM. Therefore, in my research it was intended to add the cellular (aerated) concrete powder (CCP) to concrete mixes and investigate its performance. Normal structural concrete is mostly subjected to compressive stresses, thus compressive strength test was performed on the produced specimens. Besides that, the effect of freezing (which is the most common durability issue with outdoor concrete structures) was tested. Another question regarding the replacement of cement with CCP is its optimal replacement amount. In the literature optimal dosage of cellular concrete powder was not discussed in detail.

CHAPTER 3: MATERIALS AND METHODS

Present chapter discusses the methods, approaches used for achieving the aims of this Ph.D. work. It is introduced how they have been applied in this research. After that the used materials and concrete mixes are introduced briefly, giving some insight regarding their inner structure and properties

3.1 Mechanical testing of porous construction materials

The mechanical properties that were tested included compressive strength, modulus of elasticity and surface hardness. Compressive strength was tested in accordance with the *EN 12390-3 (2009)*, while Young's modulus according to *EN 14580 (2005)*.

3.1.1 Uniaxial compressive strength test

Uniaxial compressive strength test was conducted on the specimens at 28 days of age or in some cases later (90-360 days). The specimens were wet cured before testing. This test was carried out in laboratory with the help of an accredited testing tool. To determine the strength the following equipment was used: Alpha 3-3000 S hydraulic press; calliper, with 0.1 mm accuracy; digital scale, with 0.01 kg accuracy.

Before the tests, the specimens were dried in laboratory conditions. For the investigations specimens were prepared. After that, these specimens were loaded up to failure with the same loading rate and the maximum force was recorded. The loading rate was static, and it was calculated as the function of the loaded surface.

3.1.2 Hardness tests

Hardness test methods used in material science can be divided into two main groups:

- Static hardness test methods (Brinell, Vickers, etc.),
  - By definition, in case of static hardness test methods, a hard indenter is pushed (with a given force) into the surface of the tested material, and the size of the resulting imprint is measured.
  - Their accuracy is higher in comparison to the dynamic methods; however, they cannot be performed in-situ.
  - In this research, the most widely applicable version, Brinell test, and its newer version, DSI, were applied.
- Dynamic hardness test methods (Rebound hammer, Leeb, etc.).
  - In dynamic hardness testing procedures, the indenter hits the specimen surface with impact. The specimen material can thereby be deformed. Deformation that arises is

due to the kinetic energy of the indenter. The hardness value is derived from the energy loss of a defined impact body after impacting on a sample.

3.1.2.1 Brinell hardness test

Brinell hardness test is a well-known static hardness testing method studied by many researchers mostly focusing on metals. In this chapter only its most relevant details are introduced, while a more detailed description can be found in *Appendix III*. The static hardness testing of porous stone-like materials was hardly ever dealt in 20th century since the process exists; there are only a few studies in the literature (*Crepps, 1923*; *Sestini, 1934*; *Steinwede, 1937*). In the 2000s the test is used as an alternative of the compression test to determine the strength of a material. The aim of Brinell hardness test is to acquire an indentation diameter. The relation between load and size of indentation may be expressed by a number of empirical relations. The first of these, known as Meyer's law, states that if F is the load applied and d the diameter of the impression left when the indenter is removed:

$$F = kd^n \tag{3}$$

where, k and n are empirical constants for the material when the diameter of the ball is fixed (*Tabor, 1947*). The value of n is generally around 2, however, it was not fixed to that value. In case of Brinell-hardness test, mostly another expression is used to express the relation between the force and the size of indentation. This expression is very sensitive to the conditions of the testing process.

The hardness is defined as the ratio of the load and the resulting spherical imprint:

$$HB = \frac{F}{D\pi h} \tag{4}$$

The indentation depth (h) is difficult to measure, but from the sphere diameters (D) and the indentation diameters (d) can be calculated (see *Fig. A-1 of Appendix III*):

$$h = \frac{D-\sqrt{D^2-d^2}}{2}. \tag{5}$$

After some transformation:

$$HB = \frac{2F}{D\pi\left(D-\sqrt{D^2-d^2}\right)}, \tag{6}$$

where: F is the loading force, D is the sphere diameter, d is the indentation diameter, h is the indentation depth.

The description of the applied configuration for the Brinell test, the used equipment and the measurement conditions are also detailed in *Appendix III*.

3.1.2.2 Depth Sensing Indentation test

The depth sensing indentation (DSI) test (aka. instrumented indentation test, IIT) is a widely used indentation test to determine the mechanical properties of materials (mostly metals and some kind of composites). The most frequently used DSI method was developed by Oliver and Pharr by which the hardness number can be determined without optical observation. In this method, the mean contact pressure at the maximum depth is used to characterize the properties of the material. The DSI test has two phases, the loading phase and the unloading phase. During the loading period, the indenter body penetrates into the surface of the sample at a constant rate until reaching the maximum value of the load (F_m). In this phase, the indentation diameter (or indentation depth; both terms can be used) is continuously increasing along with the loading force, while the material below the head deforms elastically and plastically too. During the unloading period, the indenter body moves away from the sample with the same rate. Elastic deformation of the material occurs during unloading and displacements are formed in the opposite direction than formed during loading, while elastic stress ceases (in case of a perfectly elastic material the total stress). In the end, only d_0 residual indentation diameter remains; from that value, we can conclude to the plastic behaviour of the material. It is theoretically possible to find the elastic properties, including Young's modulus, of materials from the unloading curve of the indentation characteristics. In the literature, only a few suggestions can be found for the calculation of Young's modulus based on indentation hardness, and most of them apply the Boussinesq problem expressed by Sneddon (*Sneddon, 1972*). Sneddon defined the load vs indentation depth functions for a linear elastic half-space for various types of indenter bodies. *Fig. 5 (left)* shows the relationship between the residual (h_r, d_r) and maximum (h_m, d_m) values of the indentation depth and diameter versus the loading force in a theoretical figure.

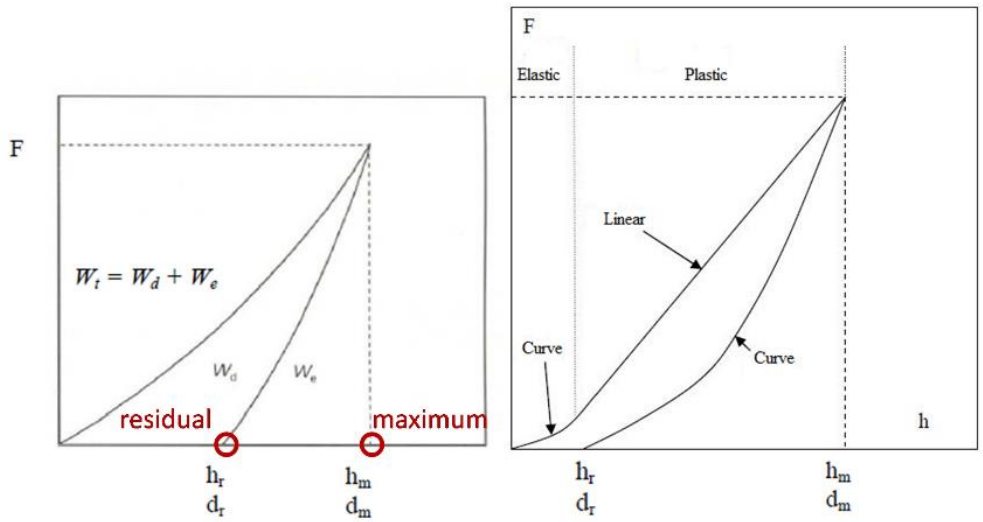

Fig. 5 Relationship of force, indentation diameter and indentation work (left); The loading-unloading characteristics of the porous materials (Tabor, 1947) (right)

Experimental results also indicated that the elastic, elastic-plastic and plastic porous solid building materials can be distinguished easily by the indentation loading-unloading characteristics. One can clearly realize the differences between the total and elastic indentation works represented as areas under the specific loading-unloading curves. In the case of the elastic-plastic materials (like concrete) one can generally observe that the dissipating (plastic) indentation energy and the elastic indentation energy have similar magnitudes; however, the ratios are very sensitive to the actual stiffness and strength of the material. As a more precise description of *Fig. 5 (left)* we can use the figure of *Tabor (1947)*, which shows that the loading phase can be build up from two parts. In the first part, the shape of the figure is a curve, and this part refers to the elastic behaviour of the material. Then the material turns into the domain of total plasticity, here the shape of the figure will be linear. The unloading phase is related to the elastic properties of the material, and the shape of the figure will be a curve. (*Fig. 5 (right)* shows the relation with the loading force (F) and indentation depth (h), but it has similar behaviour with the indentation diameter (d).) The relationship between the value of d_r (residual indentation diameter) and h_r (residual indentation depth) can be written similarly as in was in case of Brinell hardness test (see *Eq. (5)*).

In *Fig. 5 (left)* the area under the loading curve is equal to the work that is invested until reaching the maximum penetration depth that deforming the material elastically and plastically, agglomerate and set up cracks in it. This work is called the total indentation work:

$$W_t = \int_0^{h_m} F_1 \cdot dh \tag{7}$$

where: W_t is the total work, h_m is the maximum indentation depth, F_1 is the value of the loading force in the loading phase. The area under the unloading curve is called the elastic indentation work. This is the amount of work that is recovered during the unloading:

$$W_e = \int_{h_r}^{h_m} F_2 \cdot dh \tag{8}$$

where: W_e is the elastic work, h_m is the maximum indentation depth, h_r is the residual indentation depth, F_2 is the value of the loading force in the unloading phase. The difference between the two works gives the dissipated energy during the indentation:

$$W_d = W_t - W_e\,. \tag{9}$$

After rearrangement, the following expression can be written:

$$\frac{W_d}{W_t} + \frac{W_e}{W_t} = 1\,. \tag{10}$$

Thus the DSI test may be suitable for addition to the introduction of hardness metrics, the energy based examination of the entire load-unload process. The relationship of the Brinell hardness and the indentation work can be described by taking *Eq. (6)* and write it in the following form:

$$HB = \frac{2F}{D\pi\left(D-\sqrt{D^2-d^2}\right)} = \frac{2F}{D^2\pi\left(1-\sqrt{1-\left(\frac{d}{D}\right)^2}\right)} \tag{11}$$

In practical cases, the loading force (F) and indenter diameter (D) of Brinell hardness test are chosen to satisfy the following criteria: $0.25 \leq d/D \leq 0.6$. In case of $d/D \leq 0.7$ it can be assumed that $1-\sqrt{1-\left(\frac{d}{D}\right)^2} \cong \frac{1}{2}\left(\frac{d}{D}\right)^2$. If we substitute this back to *Eq. (11)*:

$$HB = \frac{2F}{D^2\pi\frac{1}{2}\left(\frac{d}{D}\right)^2} = \frac{4F}{\pi d^2}. \tag{12}$$

As it was already mentioned, the indentation work can be written as in *Eq. (7)*. If we assume linear loading curve and express h from *Eq. (4)* and later d^2 from *Eq. (12)*, then it can be interpreted as:

$$W = \frac{1}{2}F \cdot h = \frac{Fd^2}{8D} = \frac{1}{2}\frac{F^2}{D\pi \cdot HB} = \frac{C}{HB}. \tag{13}$$

It means that the indentation energy is inversely proportional to the Brinell hardness. If we express from *Eq. (4)* the loading force (F) instead of h then it leads to the following expression:

$$W = \frac{1}{32}HB \cdot D^3\pi\left(\frac{d}{D}\right)^4. \tag{14}$$

This shows that there is a theoretical relationship between the indentation work and the Brinell hardness; thus, it could be beneficial to investigate it based on that.

The specification, equipment and measurement conditions of the own DSI tests is described in *Appendix V*.

3.1.3 Young's modulus test

The Young's modulus (modulus of elasticity) was determined on 120×120×360 mm size prism specimens, according to *EN 14580 (2005)*. During the test, the prisms were subjected to cyclic continuously increasing load (max. 30% of the compressive strength of the given material), and the deformations were measured. The measurement was recorded on a computer with a measuring amplifier for later evaluation. The basis for determining the loading forces was the average of the mean values of the compressive strength test ($f_{cm,cube,test}$). Using this value, I calculated the loading forces, taking into account the conversion of the compressive strength measured on a 150 mm edge-length cube-shaped specimen to a 120 × 120 × 360 mm prism-shaped specimen: $\sigma_{c,max} = 0.85 \cdot f_{c,cube} \cdot 0.3$. The calculation of the Young's modulus was done as follows: $E_c = \Delta\sigma_c / \Delta\varepsilon_c$.

3.2 Analysis of physical and microstructure properties

Microstructure of concrete and the supplementary materials have also been investigated by scanning electron microscopy (SEM), which visually presented the porosities, microcracks and the possible interactions between the aggregates and the mortar (*Bonifazi et al, 2015*).

The other most widely applied method in material science for studying the internal processes that occur in cement-based systems is thermogravimetric analysis (TGA). TGA was applied to provide information about the processes (phase transitions, thermal decomposition, etc.) in the investigated materials. In my measurements, the following data were recorded and plotted over time:

- the temperature (T) of the investigated material [°C],
- the thermogravimetric (TG) curve [mg],
- and the first derivative of the TG curve (DTG) [mg/sec],

The measurements were performed using a MOM Q-1500 D type derivatograph with a Derill converter, applying 10 K/min heating rate. The tested materials were taken from the middle of the samples.

3.3 Numerical modelling of porous construction materials

3.3.1 Discrete Element Method

The detailed description of DEM and the Particle Flow Code (PFC) of Itasca can be found in *Appendix VI*. In this chapter I am focusing on the specialities and settings of my own models.

3.3.2 Specification of the models

In this chapter, the practical steps of the model generation of a concrete specimen in DEM are presented.

3.3.2.1 Particle size distribution of the model

Concretes are modelled in DEM as a large number of particles (discrete elements), as it can be seen in *Fig 6*. The size of the elements in the model of the concrete block was based on the aggregate sizes found in the real material. In the models, it is intended to approximate the actual particle size distribution found in concrete. The particle size distribution is compiled from the applicable grading limit curves for concrete, taking into account the minimum demand of pulp (void volume).

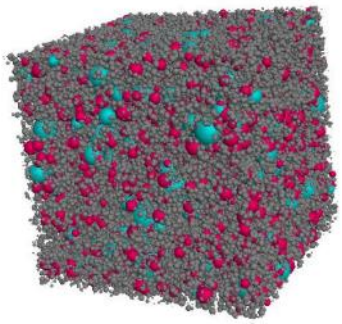

Fig. 6 *Discrete element model of a concrete cube*

The minimum size of the particles is 0.1 mm. I have conducted a sensitivity analysis on a concrete sample to see the effect on the simulated compressive strength of the minimum particle size. It was found the below 0.1 smaller particles had a negligible effect on the final compressive strength. The maximum size of the particles is the d_{max} of the given concrete (in most cases 4, 8 or 16 mm).

During the modelling, this distribution was followed by setting up the parameters in *PFC3D*. To do this, three distribution classes (0-4 mm class, 4-8 mm class and 8-16 mm class) were created, and the volume fractions were set regarding the classes based on the data of the original material. In this phase, one has to specify five parameters:

1. The minimum radius of the material in the given distribution class.
2. The radius ratio: this is the ratio of the maximum to the minimum radius in the distribution class.
3. The volume fraction: the percentage distribution of the class.
4. The group location: With this parameter, the location of the class can be specified. In the present case, the classes are uniformly distributed.
5. The name of the group: to identify them.

Because of numerical reasons, if there is more than one order of magnitude between the maximum and the minimum size of the particles, the computational time significantly increases. To further improve the speed of the computation, the built-in functions offered by the software were used. These built-in functions use constructive algorithms, which are more effective in cases, where the size difference among the balls is large.

If one would like to model a solid material correctly, an extensive set of supporting algorithms are required. These algorithms are:

- to create the synthetic solid,
- to determine the required macro properties of the material, by subjecting it to simulated laboratory testing,
- to either apply stress boundary conditions or install a specified stress field within the solid,
- to monitor and visualize damage formation within the solid.

The *PFC Fishtank* (the storage of the PFC built-in functions) provides a set of algorithms, which help the user to complete the above tasks, for example the "material genesis". The *Fishtank* can serve as a starting point for users to apply the PFC codes to solid-based applications. It contains functions to control "material genesis" (i.e., creation of solids composed of PFC particles or clumps) and also functions to support testing of the solids to measure their material properties (*Itasca CG, 2008*). In this thesis, I have used the built-in algorithms as a starting point and modified them to fit for my purposes. Some further discussion about *Fishtank* can be found in *Appendix XIII*.

There are several possibilities to define the geometry in PFC. I have defined material vessels, in which the sample can be created. The type of the vessel (cylinder, cuboid, etc.) can be used after the corresponding parameters are given. I have used both cylinder and cuboid vessels with the parameters of diameter (D_p) and height (H_p), and width (W_x), thickness (W_z) and height (H_p), respectively.

3.3.2.2 The Material-Genesis Procedure

The Material-Genesis Procedure produces a material consisting of grains and cement. (If one wants to model a granular material, then one does not need to add a cement during the procedure). The material is produced in a material vessel such that it forms an isotropic and well-connected system at a specified confining pressure. The grain size of the material is controlled by the so-called refinement level. If one increases the refinement level, then the grain size will decrease. The material can be divided into refinement regions by named ranges.

Each of these regions has a set of short-term micro-properties. Some of these properties are assigned to the particles, while the rest are to the bonds.

The steps of the Material-Genesis Procedure (for detailed description see *Appendix VIII*):

- **Compact initial assembly (**Fill the material vessel with particles (or clumps).)
- **Install specified isotropic stress** (e.g.: less than 0.01% of the compressive strength).
- **Reduce the number of "floating" particles.**
- **Finalize specimen** and remove material vessel.

This procedure runs until the mean stresses in the parallel bonds become almost zero, and the model reaches static equilibrium.

My aim was to model concrete, which is a material that has particles with a very wide selection of size. The largest particles (aggregates) can be larger than 20 mm, while the smallest cement particles can be smaller than 0.1 mm. From a modelling point of view, it is impossible to model all of the particles within such material. Because of that, only the aggregates were modelled with discrete element particles (which still have a quite large variance in size), the cement was represented by the bonds among the particles. Due to the reason that those small cement particles are not modelled and that the size of the particles has a large variance, it might happen that after the material-genesis procedure some elements have no contact with any other element (meaning, that they were generated into a void among large particles and during the calculation cycles of their movement, they did not reach any other elements or walls). If that happens during the material genesis procedure, then there is a problem because the grain-scaling procedure can only be started when a tight pack has developed. This problem is caused by the size difference between the largest and smallest particles being too big. To solve this problem, the following procedure is followed:

1. First, a material with the three different distribution classes was modelled and some calculation cycles were run to ensure the particles reach their final position.
2. Then with the help of a software routine, the positions and the radii of the particles belonging to the two larger distribution classes is saved out to an array in a separate file. (It is very helpful that the particles belong to the different distribution classes, and that the distribution class of the particles is stored in the properties of the class.)
3. After that another project is created, which is identical to the previous one, but with only the smallest distribution class. (Meaning, in this case that it contains 100% of the particles from the smallest distribution class). Here the calculation cycles were run until the model reached a static equilibrium.

4. Then using the previously saved file, which contains the positions and radiuses of the particles belonging to the two larger distributions classes, some of the particles were connected together completely to form a cluster. This is done in such a way so that the position of the particles from the larger distribution classes were put into the sample and all of the particles which were inside the radius of a given particle form a cluster, as it can be seen in *Fig. 7*. A huge advantage of this procedure is that one does not changes the stiffness of the material, thus the results will be equivalent with the original sample.

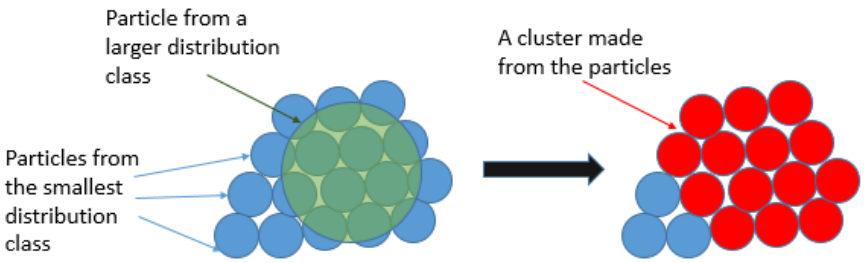

Fig. 7 *Cluster forming from particles*

3.3.2.3 Parameter setting and calibration of a DE model

The previously mentioned built-in functions can make the processing faster, but to achieve a good result, we have to understand the correct parameters. To set up the parameters correctly a uniaxial compression test in *PFC3D* was completed and compared to the experimental results. After the particle size distribution, the most important inputs are the parameters of the particles and the bonds. In the literature, the calibrations are mainly performed using a trial and error method (*O'Sullivan, 2011*). Systematic methods to vary the model parameters were developed by most of the researchers in the field of DEM (*Wang and Tonon, 2010*). Some of them built up sophisticated calibration strategies. In (*Kulatilake et al, 2001*) the model calibration against the laboratory test data was carried out by assuming that the normal stiffness of the contacts (k_n) is proportional to the Young's modulus (E) of the investigated stone. Based on the assumption of $E = k_n \cdot 4 \cdot R$ (R is the radius of the particle), they performed a parametric study to find the optimal parameters of the contacts based on predefined calibration curves. In (*Cheung, 2010*) an identical approach was shown for sandstones. Design of experiment method (which is an approach developed to determine the relationship between parameters that have an effect on the outcome of a process) was used to support model calibration of unbonded particles (*Yoon, 2007*; *Favier et al, 2001*).

Other researches showed the significance of particle size distribution in the mass response of rocks (*Schöpfer et al, 2007*; *Cho et al, 2007*; *Camusso and Barla, 2009*). In (*Potyondy and Cundall, 2004*), the three major influencing factors were determined, which have a significant effect on the material response of the system in case of a bonded particle model. These factors are the type of the contact model (linear contact, parallel bond contact, etc.), the particle size distribution and the packing of particles (which method, how dense the packing, etc.).

All these factors were considered in my model as well:

1. sufficiently dense packing was applied during the material generation process,
2. the particle size distribution was applied as an input of the model,
3. and the parameters of the contact were calibrated against laboratory measurements.

The most challenging task in the model calibration is to estimate the initial value of the parameters. In *Chapter 5* and *6* a method is proposed to estimate the normal strength of parallel bonds in case of different type of concretes.

The initial parameters of the model

Information about the parameters is obtained from the literature on the modelling of concrete and based on the material parameters of concrete. The initial model parameters are listed in *Appendix IX*.

The final parameters of the model

To find the final parameters of the model, which represent the real life behaviour of the material, an iteration method (calibration) was applied. This is the usual solution in case of DE models during the verification phase. The verification was made with the help of a uniaxial compression test (described in *Chapter 3.3.2.5*). The iteration process has the following steps (see *Fig. 8)*:

1. Set the parameters (in this case it was the mean strength and standard deviation of the strength of the parallel bonds) of the model to a given value. These two parameters have the most pronounced effect on the normal stiffness of the model, therefore these were modified during the iteration. Based on literature and a conducted sensitivity analysis, other parameters had only minor effects, so those parameters are modified after the iteration phase during the fine-tuning of the model.
2. Generate the model with a dense packing.
3. Run a uniaxial compression test.

4. Compare the result of the simulation with the result of the laboratory tests. If the value of the normal strength was higher in the model, then the mean strength of the parallel bonds was reduced, if the value of the normal strength was lower in the model, then the mean strength of the parallel bonds was increased until the difference of the numerical and laboratory test results was below a given threshold ([3], [6]).

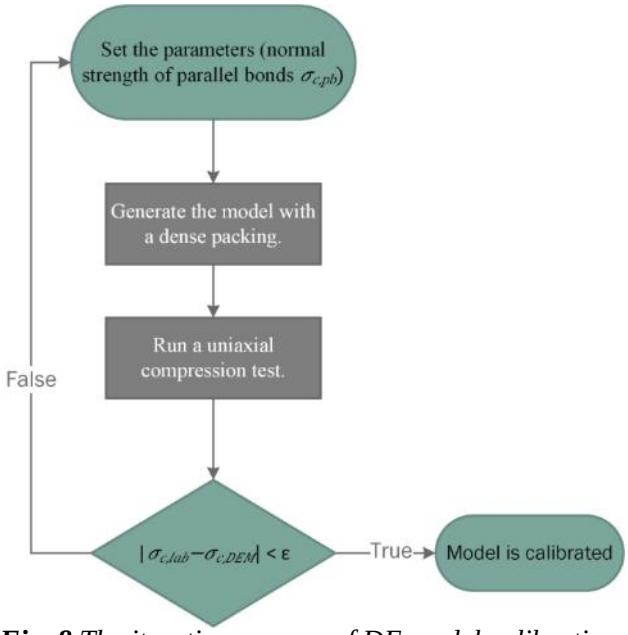

Fig. 8 *The iterative process of DE model calibration*

The above steps were repeated until the simulated compressive strength was close enough to the measured compressive strength. The applied maximum error value was chosen for 0.05 (based on the accuracy of the laboratory compression strength test), which was calculated in the following way:

$$\varepsilon = \frac{\sigma_{c,lab}-\sigma_{c,DEM}}{\sigma_{c,lab}} \leq 0.05 \qquad (15)$$

where, $\sigma_{c,lab}$ is the compressive strength from the laboratory measurement, $\sigma_{c,DEM}$ is the compressive strength from the simulation.

After the appropriate properties of the model is selected, in every case 4 additional models with the same average properties but differing from each other because of the random nature of the particle-level geometry are generated, and ran all of the analyses on these models too (see *Fig. 9*). The aim of this was to have a statistical nature of the analysis, hence to avoid accidental extreme results.

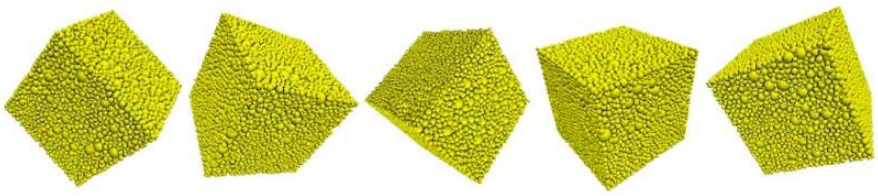

Fig. 9 *The five generated models with the same parameters but different particle arrangement*

3.3.2.4 Sensitivity analysis on the standard deviation of the normal strength of the parallel bonds [8]

The standard deviation of the normal strength of parallel bonds was chosen to be 10% of the mean value of the normal strength based on the sensitivity analysis I have conducted. Based on these investigations it is recommended to use a given value of standard deviation for the modelling of concrete, however it should be chosen under 10%. For details of this study see *Appendix X*.

3.3.2.5 Model of the uniaxial compression test

To simulate the compressive strength test, the built-in functions of the *PFC3D* software was modified and reparametrized. The process has the following steps. First the sidewalls of the sample are deactivated. It can be given, which walls are the sidewalls of the sample and the test can be done along all three axes. The friction of the remaining walls is set to a high value, because in case of the real life test, the friction between the loading plate and the sample is high too. Then, the bottom wall remains fixed while the upper wall pushes the sample with a given force or velocity until it destroys the sample (until the sample is not able to bear more stress). During the investigation the software tracks the bond break events which represent cracks. The cracks are defined with the Crack-Initiation Stress, which is controlled by the ratio of standard deviation to mean material strength (*Itasca CG, 2008*). If this ratio increases, it lowers the stress at which the first crack initiates. The crack-initiation stress is defined as the axial stress at which there exists a specified fraction of the total number of cracks in the model at the point when the peak strength has been obtained. When the test is ready, the software saves the results (the maximum stress) into a text file, so one can see them without running the program. The results are given in three different ways, because the software is able to measure stresses in different ways. There are three types: wall-based results; by using gauge particles; and/or by using measurement spheres. All three ways are for measuring stresses and Young's modulus too. The result of the compression test can be considered as a successful result, if Young's modulus has (almost exactly) the same value as it was given in the parameter settings. If Young's modulus is different, then the model is not stable and the parameters are not well defined.

The result of the compression test can be used to calibrate the model as well, in a way that this result is compared with the laboratory test results. In my models not only the final results but the characteristics of the compression tests were very similar to the laboratory test results. The curve from the model behaves quite similarly to the typical concrete stress-strain curves. As a difference it can be seen, that at the initial stage of the curve a kind of "waves" can be observed,

as it is shown in *Fig. 10*. Contrary in case of the real test, this stage is linear. This phenomenon can be originated from the structure of the DE model, which is built up from elements and bonds. In this initial part of the test a minor particle rearrangement can be observed, which cause this type of behaviour of the models.

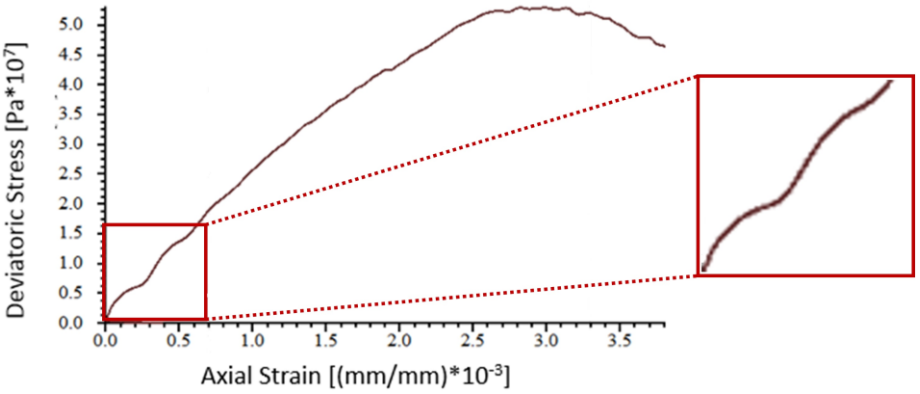

Fig. 10 *Stress-strain curve of a compressive strength test in DEM*

3.3.2.6 Model of the hardness testing procedure

For modelling hardness test methods an additional element has to be implemented, which represents the indenter that is pushed into the surface of the material. The loading sphere of the Brinell-device was produced as a particle with 10 mm diameter. The sphere is made of steel, therefore the value of the stiffness of the sphere is based on Young's modulus of the steel (~200 000 N/mm^2). Starting with this value the real value of the stiffness of the particle was calculated from the relationship in PFC Manual (in case of a 3D model):

$$k_n = 4RE_c \tag{16}$$

where R is the radius of the ball and E_c is Young's modulus of the steel. Based on this the value of $k_n = 4\times10^{12}$ N/m^2. The density of the ball was the standard density of steel: 7850 kg/m^3. The friction coefficient of the steel ball is assumed to be 0.4, because in case of a dry and clean surface the friction coefficient of the steel is between 0.5-0.8. In the present case the surface of the material cannot be assumed to be perfectly dry and clean (especially after hundreds of tests, not even with the utmost care), therefore the friction coefficient was slightly decreased.

To model the test procedure, first one has to enlarge the size of the working domain (because the steel ball would be out of the range of the domain), to be able to generate the steel sphere above the model of the concrete cube. The PFC code allows only to generate particles inside the working domain and the original size of this domain is generated based on the given size of the model (the default value of the expansion factor is 1.25). In my case the expansion

factor was modified to 4, to be able to model the process, as it is shown in *Fig. 11*. Based on tests, it did not have noticeable effect on the computational time.

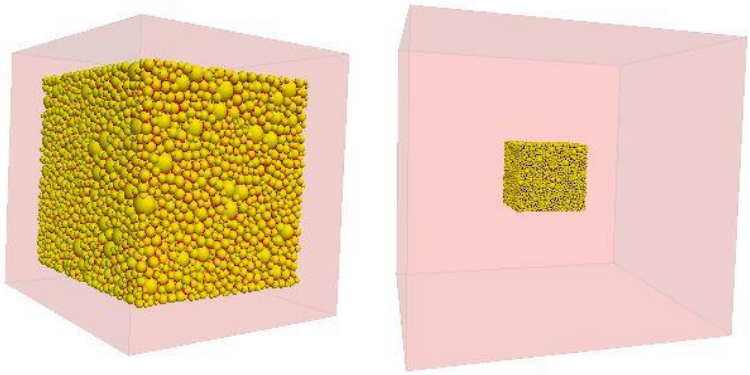

Fig. 11 *The model in the original domain (left, purple) and in the enlarged domain (right, purple)*

After the required domain size is available, the steel ball can be generated (*Fig. 12*). To identify the ball later it is useful to give it a specific ID. Later one can use it as a reference and one have to only call the ID to modify something on the ball. In this model the *ID 999999* was chosen for the steel ball, because that number of particles will not be generated. As a next step one has to fix the ball in every direction and against rotation too, because in the Brinell-test the ball is fixed. Because the steel ball is generated above the concrete block, to avoid initial contacts with the other particles (and also to demonstrate precisely the Brinell-method), one has to move the ball towards the surface of the cube. There are several ways to accomplish this, one way is to give an initial velocity to the ball in a given direction and run some calculation cycles until the ball almost touches the surface. It is important that the ball is free in the *z* direction.

Once the ball is sufficiently close to the surface of the cube, we can apply the testing force. In case of Brinell-testing we are able to apply force in different magnitudes. The force is applied to the steel ball which pushes it perpendicularly into the surface. The Brinell-test can be carried out with different forces from 1.5 kN to 30 kN, by changing the testing weight. During the test the following forces were applied: 2.5 kN, 5 kN, 7.5 kN, 10 kN, 10.625 kN, 12.5 kN, 15 kN, 17.5 kN. During the modelling the model was run on every loading level.

To apply the force we have to run a given number of calculation cycles again, during which the steel sphere is penetrating into the concrete. During this process one can plot and save different attributes, like the position or the contact forces of the steel ball. These attributes are saved into the history and the software is able to create diagrams from these data or they can be exported as a CSV file. When the loading phase of the test is finished, one has to apply a force, perpendicularly to the surface again, but now in the opposite direction, to model the

unloading phase. Thus, the steel ball is removed from the model. Here one has to apply some calculation cycles again not only for removing the ball, but to leave some time for the particles to finish ordering. Based on that reason it can be useful here to give some more cycles, than it is necessary to the sphere removing.

As one can see, during the test one has to apply the calculation cycles three times, first to move the ball close to the surface, then to push it into the surface and lastly to remove it. In this case it requires about 6000 cycles, which can be considered a small number in DE modelling terms, where much bigger numbers are usual. That shows if one has the model sample, to model the test itself does not requires large computational effort and the test can be carried out quite fast. Since the model has to be modelled only once, a huge amount of testing can be done within a short time period, even faster than the real laboratory tests. Since the steel ball is removed and the other particles are in a steady state, the test is finished.

Steps of hardness testing procedure

The following figures illustrate the step of the modelled hardness testing procedure.

1. The steel ball is generated above the model. Here the blue spheres represents the aggregate particles and the steel ball above them. First the steel ball is generated above the sample and moved with a given velocity until it reaches the surface of the sample.

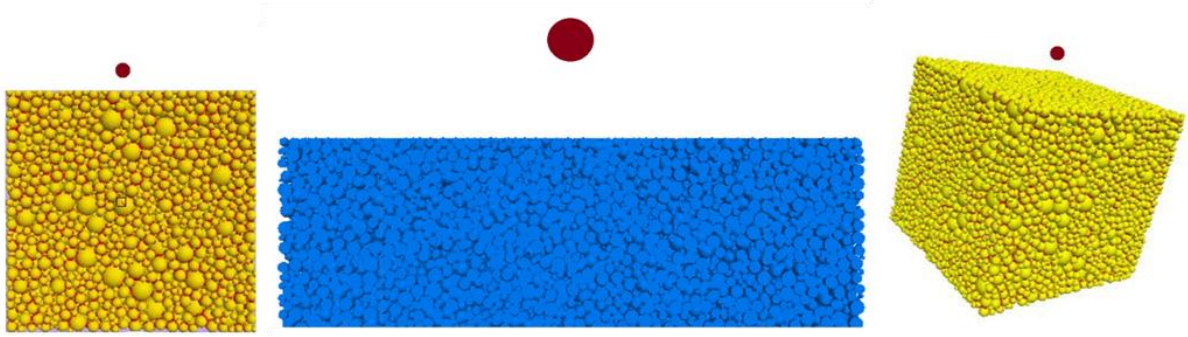

Fig. 12 *The model with the steel sphere in the initial phase in front and perspective view (the sample is cut in half in the middle picture)*

   In *Fig. 12* the sample is cut in half in the middle (where the steel ball is generated) to have a more spectacular view.

2. In the next step the ball reaches the surface of the sample, a given force is applied and the ball penetrates into the surface of the material. During this procedure the particles of the sample come into contact with the steel ball and push against each other as it can be seen in *Fig. 13*. When this happens, force arises in the parallel bonds among the elements. The forces in the parallel bonds are represented with colours from blue (smallest value) to red (largest).

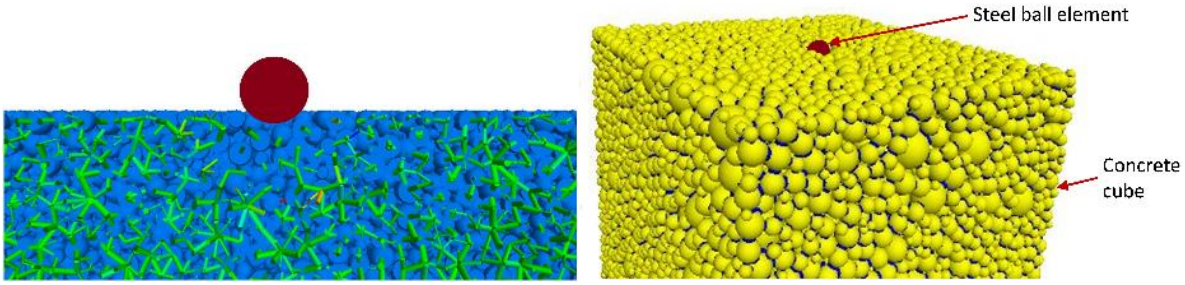

Fig. 13 *The model with the steel sphere in front view (the sample is cut in half in the middle) and in 3D view*

During the test procedure by using the different plotting settings available in the software, it can be determined which elements were affected by the penetrating steel ball. *Figure 14* shows the parallel bonds, in which any force arose during the test procedure. This illustrates that the hardness testing has only a local effect in the material and it does not extend to the whole sample.

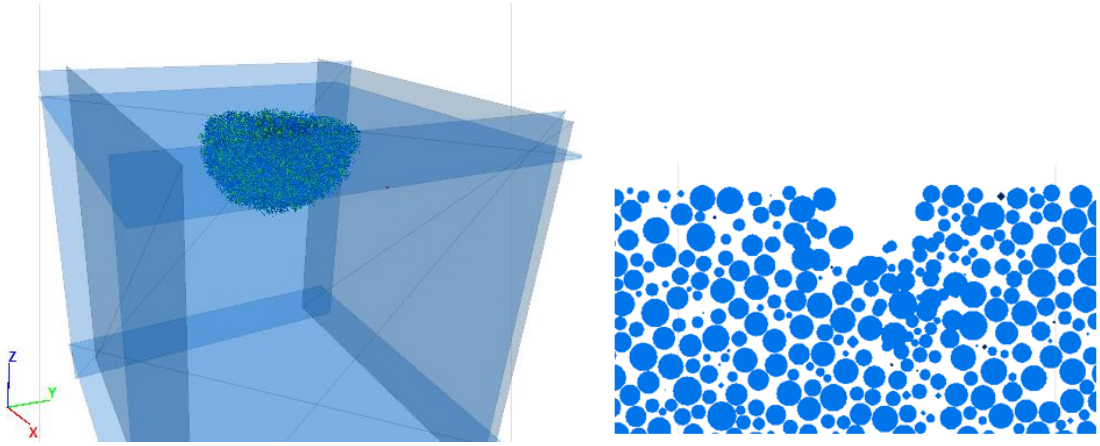

Fig. 14 *The parallel bonds, which are affected by the hardness testing (left) and the remaining imprint in a cut plane view (right)*

3. In the third step, the ball comes away from the sample (unloading phase), and a hole remains in the material as it is shown in *Fig. 14*.

3.3.2.7 Model of the DSI testing procedure

The DSI testing procedure has a similar aim, as the Brinell-hardness test and its implementation is fairly similar as well. To model this procedure, the script of the hardness testing was modified. For details see *Appendix XI*.

3.3.3 Comparison of DEM and FEM

I have conducted a study, where the DEM and FEM methods were compared. [15] First, the two methods' theoretical background was reviewed, then I have modelled in a simple approach the compressive strength testing and the Brinell hardness testing of concrete using both methods. The results were reviewed and the main advantages/disadvantages of both

methods are highlighted. It was concluded that for my purpose (the modelling of laboratory tests on porous construction materials) DEM is a more suitable approach. For further details see *Appendix XII*.

3.4 Multiparameter optimization methodology

There are several cases in materials engineering when a new model or algorithm for describing a given problem is introduced, and it contains some empirical constants or parameters that should be optimized against real-world data, leading to a multi-parameter optimization problem. There are several approaches introduced in the literature for the solution of multi-parameter optimization problems (*Tauzowski et al, 2018*; *Pollard and Radchenko, 2006*; *Saad et al, 2016*). The most practical applications use one of the following four methods:

- Simplex search,
- Linear or Nonlinear least squares,
- Gradient descent,
- Pattern search.

The above-mentioned methods minimize a cost function (aka. objective function), which is practically the error between the measured and simulated response. Such objective functions are the sum of absolute errors (SAE) or the sum of squared errors (SSE). The optimization is an iterative process, in which the model parameters are tuned in all steps according to the minimalized error. Thus, the simulated response tracks the measurement. Before the optimization, it is essential to define the initial state, the constraints, and the limits of the system. The number of necessary iteration steps to reach an optimal solution can be highly decreased by the appropriate choice of these values. If the values of the parameters change less than a predefined tolerance in successive iteration steps or the number of iteration steps reached its maximum, then the optimization is considered to be terminated. In all cases in this thesis, when optimization methods were applied, first, the different optimization methods were compared to each other on a subset of the data. The four approaches (simplex search, nonlinear least squares, gradient descent, pattern search) combined with the two mentioned objective functions (SAE, SSE) were analysed. The best (most precise and fast) performance was reached by the nonlinear adaptation (Levenberg-Marquardt) of least squares method with an SSE objective function. Similarly, accurate results were shown by the gradient descent method as well; however, the convergence was slower in that case.

3.5 Materials

3.5.1 Porous construction materials

In this chapter, the porous construction materials are introduced that were used for the general evaluation of porous materials. 15 different construction materials were tested (see *Fig. 15*), which were the following:

- **Metals** (as reference): aluminium, mild steel, reinforcing bar steel (S235).
- **Concretes**: normal strength concrete, high-strength concrete, polymer concrete.
- **Other CSH based materials**: cellular concrete block (Ytong), sand-lime brick (Silka).
- **Ceramics**: clinker brick, facebrick, clinker tile.
- **Stones**: porous limestone (2 types: A and B) and compact limestone, rhyolite tuff.

Table 1 *Particle size distribution of the concrete sample*

Particle size	Proportion
0-4 mm	40 %
4-8 mm	22 %
8-16 mm	38 %

The normal strength concrete belonged to the C40/50 strength class and had the following particle size distribution as it can be seen in *Table 1*. The high strength concrete was a C100/115 strength class concrete.

Fig. 15 *The investigated materials (bottom row: three metals, Ytong block, three ceramics, sand-lime brick, polymer concrete (150×150×150 mm); top row: two concrete and four stone specimens)*

3.5.2 Concrete mixes

In this chapter, the concrete mixes and their components are introduced that were used in studies included in *Chapter 4*, *5* and *6*. First, there are some general comments about the components that were similar in all mixes. Then each mix is described, including the properties of their components as well.

Ordinary Portland cement (OPC) CEM I 42.5 N was used in all mixes to eliminate the effect of mineral admixtures and to investigate purely the effect of studied feature (type of aggregate, supplementary materials, etc.) on the properties of the concrete. CEM I 42.5 N is the most widely used and purest type of cement that can be applied to produce various types of concrete.

It is a hydraulic cement, which is produced by pulverizing clinker consisting of calcium silicates, and usually containing calcium sulphate as an interground addition (*ASTM C150, 2004*). The cement, which was applied in all mixes, was produced by the company Lafarge, in accordance with *EN 197-1 (2011)*. The mixing water used for the reference was tap water that complies with the requirements of *EN 1008 (2003)*. Plasticiser was only used in cases when it was absolutely necessary. Then, Sika ViscoCrete-5 Neu was used, which is a modified polycarboxylates aqueous solution, to increase the workability of the fresh concrete.

The reference aggregate was natural river quartz for all fraction (0/4; 4/8 and 8/16). The maximum aggregate size used was always 16 mm, except the lightweight aggregate mixes, where it was 8 mm, due to the type of the aggregate. Before usage, the aggregates were tested to meet the requirements of *EN 12620:2002+A1 (2008)*.

3.5.2.1 Mix design applied for the aggregate type studies

The concrete mixes presented in this chapter correspond to the study in *Chapter 6.1*. It was aimed to design concrete mixes that differ from each other in the type and in the particle size distribution of the aggregate. These two properties can significantly affect the strength properties of the end product. Three different types of aggregates were applied, which are common in the construction industry: quartz gravel (G), crushed stone (S) and expanded clay (lightweight aggregate (L)) (*Gagg, 2014*). These three types of aggregates have significantly different shape, as can be seen in *Fig. 16*. While the applied lightweight aggregate (Liapor HD 5n) is a nearly sphere-shaped aggregate, the crushed stone is longish with sharp edges. The quartz gravel is somewhere between the two mentioned previously. Three different particle size distributions were applied in case of the crushed stone and the quartz gravel aggregates. Two distributions were defined according to the standard grading curves "*A"* (modulus of fineness: 6.6) and "*C"* (modulus of fineness: 4.8), which are described in *EN 12620* standard. The grading curves "*A*" and "*C*" can be described as the limits of particle size distributions. Only between these limits is it possible to produce normal strength concrete. Curve "*A"* (in case of self-compacting concrete curve "*B*") is the ideal distribution in case of quartz gravel aggregate in a strength point of view however it is not surely the case for other aggregate types. Besides these two distributions, a third, containing only coarse aggregate, was applied as well, to produce no-fines concrete. No-fines concrete is advantageous in an economical and environmental aspect because it requires only a limited amount of cement. Liapor (the applied lightweight aggregate) is a one fraction material; thus, it is not possible to reach "*A*" or "*C*" grading curves using it. Thus in total, seven concrete mixes were produced, as can be seen in

Table 2. Four nominal grading fractions (two fine and two coarse aggregate fractions) were used, according to *EN 12620* standard: fine sand 0/0.5, sand 0.5/4 mm, small gravel 4/8 mm and medium gravel 8/16 mm. As it can be seen in *Table 2* the d_{max} (maximum aggregate size) was 16 mm for quartz gravel and crushed stone, while it was 8 mm for the lightweight aggregate.

Table 2 *Particle size distributions [%] applied in the mixes. Notation: quartz gravel (G), crushed stone (S) and lightweight aggregate (L); Grading curve C (C), Grading curve A (A) and No-fines (N)*

Notation	Aggregate size [mm]			
	0/0.5	0.5/4	4/8	8/16
GC	40	30	15	15
GA	15	25	30	30
GN	0	0	50	50
SC	40	30	15	15
SA	15	25	30	30
SN	0	0	50	50
LN	0	0	100	0

The applied water-to-cement ratio (v/c = 0.67) was identical as well.

Standard size cube samples (150 mm × 150 mm ×150 mm) were produced from all the mixes. The samples were wet cured for 28 days and then uniaxial compressive strength test was carried out on them according to *EN 12390-3*. During the tests, quasi-static load rate of 11.25 kN/s was applied. Besides the compressive strength, the Young's modulus was measured. The results showed almost identical values for all the mixes; thus, it was not considered later in the optimization process; rather it was handled as a constant.

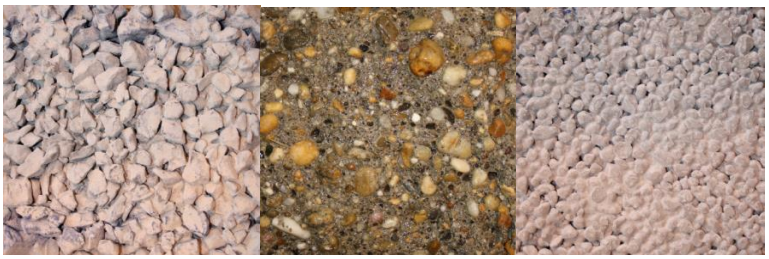

Fig. 16 *Hardened concrete samples containing the three different applied aggregates (from left to right): a) crushed stone, b) quartz gravel, c) expanded clay*

All variables and constraints in the mix design are listed in *Table 3*.

Table 3 *Variable and constraint parameters for all mixtures used for the aggregate type studies*

	Variables
1.	*Aggregate type: quartz gravel; crushed stone; lightweight (Liapor)*
2.	*Aggregate particle size distribution (%)*
	2.1 0/0.5 0 – to - 40
	a. 0.5/4: 0 – to - 30
	2.3 4/8: 15 – to - 100
	2.4 8/16: 0 – to - 50
	Constraints
3.	*d_{max} (mm): 16*
4.	*Cement type: OPC - CEM I 42.5 N*
5.	*w/c ration (by mass): 0.67*
6.	*Cement content (kg/m^3): 264*

3.5.2.2 Characteristics of cellular concrete powder

Fig. 17 *Different particle sizes (0/0.25 mm; 0.25/1.0 mm; 1/2 mm; 2/4 mm; 4/8 mm; 8/16) of crushed recycled aggregate from the same AAC waste material*

During the production of *autoclaved aerated concrete* (AAC) blocks as well as during the construction and demolition of AAC buildings, waste material is generated in various sizes. Cellular concrete powder (CCP) is the finest of these waste materials. In *Fig. 17* AAC waste is sieved into six fractions. In the present research, one type of AAC with the body density of 440 kg/m^3 was applied to produce the aggregate (in all form). The investigated type of AAC was chosen based on business sales statistics that were received from the manufacturer company. It was taken into consideration to test the other available types, but this parameter was kept constant during the present research.

The application of AAC waste as an aggregate was studied in previous researches (*Fenyvesi, 2014*; *Fenyvesi and Jankus, 2015*), however, in my study, only its finest powder form (CCP) is used. CCP was collected from a factory for cutting cellular concrete masonry in Hungary. The material was tested by chemical analytical methods; its oxidising composition has been determined, as it is shown in *Fig. 18*. The chemical compositions and physical properties of

the CCP and the applied cement can be seen in *Fig. 18*, which were tested in accordance with *EN 196-2* and *EN 525-12)*. Where *Fig. 18* shows the sieve curves for the cement and CCP and depicts that CCP had larger grain distributions than cement. The other properties (mean compressive strength, thermal conductivity, water vapour permeability, particle body density, bulk density, water absorption capacity and total porosity of the different grain sizes) of AAC in grain or block form that are relevant for the correct mix design are presented in *Appendix XV*.

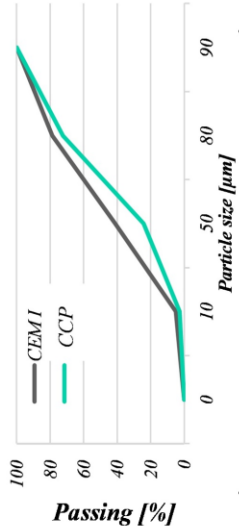

Measured property	CEM I	CCP
Density [g/cm³]	3.02	1.96
Specific surface area [cm²/g]	3326	2513
Loss on ignition	3.0	9.25
SiO_2	19.33	54.28
CaO	63.43	22.81
MgO	1.45	1.15
Fe_2O_3	3.42	2.16
Al_2O_3	4.67	5.09
SO_3	2.6	4.90
Chloride content	0.04	0.02
Free CaO	0.71	-
K_2O	0.78	-
Na_2O	0.33	-
TiO_2	-	-
Insoluble part in dilute hydrochloric acid and sodium carbonate	0.26	33.02

Fig. 18 *Grading curves and chemical compositions and physical properties of cement and CCP*

3.5.2.3 Mix design applied for the CCP studies

The concrete mixes presented in this chapter correspond to the study in *Chapter 6.2*.

3.5.2.3.1 Mix used to compare CCP against other recycled powders

The mixes contained 270 kg/m^3, CEM I 42.5 N cement, while the applied water to cement ratio was 0.57. The maximum aggregate size was 16 mm; the particle size distribution of the reference mix was the following:

Table 4 *Aggregate particle size distribution of the reference mix*

Aggregate size [mm]	Distribution [-]	Mass [kg/m^3]
0/4	0.47	936
4/8	0.25	498
8/16	0.28	557

Table 4 contains the aggregate size distribution of the reference mix, which is the same reference mix that was used later and denoted as normal strength concrete reference mix. To the mix detailed in *Table 4*. 10% (proportionally to the cement – 27 kg/m^3) waste material powder was added. It is important to highlight that waste material powder was added to the mix and it is not substituting cement (as it was done later on). The aggregate size of the powdered clay brick belonged to the 0/0.125 fraction, while the cellular concrete powder to the 0/0.09. In the fourth case, Sika Aer air-entraining agent was added (1.4 kg/m^3) to the mix to

reach 5% of air content. The aeration was controlled in the concrete, and the air content was 5% at the given temperature, consistency. At least three samples were produced from every mix for every type of test, thus in total 80 pieces of 100×100×100 mm samples were cast. The aim was to design a mix which has strength that is frequently used in the construction industry (C25/30) but has low resistance against frost. It was also aimed to use a limited amount of cement to reduce the cost and the environmental effect of the concrete.

3.5.2.3.2 Mixes used in the detailed study

Cement mortars

Three different cement mortars were used for the experiments in the first step of this research that are described in *Table 5*.

***Table 5** CCP and MK proportions in the different mortar samples*

Notation	Description	Performed laboratory tests on the samples
Reference	reference mix, 100% cement	Compressive strength test and thermogravimetric analysis at different ages of the samples
Y10	10% of cement was substituted by CCP	
MK10	10% of cement was substituted by MK	

All samples contained CEM I 42.5 N type cement and only the necessary amount of water (v/c = 0.5) was added. 40 mm × 40 mm × 160 mm prisms were cast from the above-described mortar, and their density, flexural- and compressive strength were determined.

It is important to mention that the applied aggregate size of the CCP belongs to the 0/0.09 fraction (particle size lower than 0.09 mm), while the MK does to the 0/0.018 fraction. The particle sizes were determined using Laser Diffraction Analysis. The specific surface area of CCP is lower with an order of magnitude compared to MK, as it is shown in *Table 6*.

***Table 6** Specific surface area of MK and CCP determined by Laser Diffraction Analysis*

Material	Metakaolin	Cellular concrete powder
Specific surface area [cm^2/cm^3]	28695	2513

The density and porosity of CCP and MK were also determined based on the standard *EN 12390-7*. The amount of CCP did not affect the workability of the mixes. The body density of CCP is increasing with its fineness, as it can be seen in *Fig. 19*. While, in brick form, it is only 700 kg/m^3, then in powder form it is already 2000 kg/m^3, which is still less, than concrete's density. Based on this figure, the porosity of CCP decreased with grinding and pulverizing. There are still pores in the powder, and it

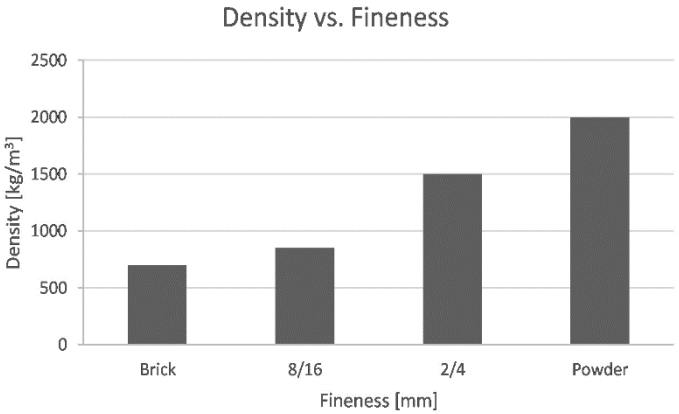

***Fig. 19** Density [kg/m^3] vs. Fineness [mm] of CCP*

could be further pulverized; however, these small pores could be advantageous for frost resistance. In the present research, the powder was not further pulverized; it was applied as it arrived to the laboratory. The bulk density of the MK in the applied powder form was 550 kg/m^3.

The main oxide components (in percentage) of the MK was the following (for the cement and CCP see *Fig. 18*): **MK**: SiO_2 ➔ 53.0%; Al_2O_3 ➔ 41.7%; Fe_2O_3 ➔ 0.52%.

Concrete mixes

Two basic concrete mixes were used during our experiments, which are described with more details in (*Borosnyói, 2016*) and (*Mlinárik et al, 2016*). The first concrete mix was designed to have relatively low resistance against freezing (it is the same that was used to compare CCP against other waste powders). The aimed strength class was C20/25 in case of the reference mix, which is a widely used concrete strength class in the industry. Concrete from the C20/25 strength class is usually appropriate for regular civil engineering structures, the reason why stronger concretes are used is the durability issues of these structures. However, if a concrete could be designed, which belongs to the C20/25 strength class and has better durability performance, then it could be applied by the industry.

Three nominal grading fractions according to European Standard *EN 12620:2002+A1:2008* were used: sand 0/4 mm, small gravel 4/8 mm and medium gravel 8/16 mm. The aggregate used in the reference mix was normal quartz gravel with d_{max} = 16 mm and distribution as follows:

Table 7 *Aggregate particle size distribution of the C20/25 class reference concrete*

Aggregate diameter [mm]	Distribution [%]	Actual mass [kg/m^3]
0/4	47	936
4/8	25	498
8/16	28	557

The reference mix's design is described in *Table 8*.

Table 8 *Mix design of the reference mix*

Component		Distribution [-]	Mass [kg/m^3]
Cement	CEM I 42.5 N	-	270
Water	w/c = 0.57	-	154
Aggregate	0/4 [mm]	0.47	936
	4/8 [mm]	0.25	498
	8/16 [mm]	0.28	557
Sum		**1**	**2415**

270 kg/m^3 cement was used, water to cement ratio was 0.57 in case of the reference mix and superplasticizers were not used. The above-detailed mixture was used as the reference mix, in which a given amount of cement was substituted by CCP (or MK) or to which a given amount of CCP (or MK) was added. Finally, there were six different mixes, shown in *Table 9*.

Table 9 *CCP and MK proportions in the different mixes of the normal strength concrete samples*

Notation	Description	Cement [kg/m^3]	CCP [kg/m^3]	MK [kg/m^3]	Performed laboratory tests on the samples
Reference	reference mix, as described above	270.0	00.	0.0	Compressive strength test, frost resistance test, freeze-thaw resistance test and thermogravimetric analysis
Y3	3% of cement substituted by CCP	261.9	8.1	0.0	
Y10	10% of cement substituted by CCP	243.0	27.0	0.0	
Y17	17% of cement substituted by CCP	224.1	45.9	0.0	
MK10	10% of cement substituted by MK	243.0	0.0	27.0	
MK/Y 7/3	10% of cement substituted 7 % by MK and 3% by CCP.	243.0	8.1	18.9	

The other reference mix was designed to be a high strength concrete with the strength class around C60/75 (for a more detailed description of the mix, see (*Borosnyói, 2016*)). This mix was used to see that the relations observed in case of the first mix (normal strength concrete) are also true in case of high strength, high frost resistance concrete. The aggregate particle size distribution of the high strength concrete mix can be seen in *Table 10*.

Table 10 *Aggregate particle size distribution of the C60/75 class reference concrete*

Aggregate diameter [mm]	Distribution [%]	Actual mass [kg/m^3]
0/4	40	774
4/8	25	484
8/16	35	677

The maximum aggregate diameter was 16 mm, and CEM I 42.5 N type cement (325 kg/m^3 together with the SCM) was used with 0.40 water to cement ratio. The dosages (in percentage) of CCP and MK were the same as in case of the normal strength concrete (*Table 11*).

Table 11 *CCP and MK proportions in the different mixes of the high strength concrete samples*

Notation	Description	Cement [kg/m^3]	CCP [kg/m^3]	MK [kg/m^3]	Performed laboratory tests on the samples
Reference	reference mix, as described above	325	0	0	Compressive strength test, frost resistance test, freeze-thaw resistance test and thermogravimetric analysis
Y3	3% of cement was substituted by CCP	315.25	9.75	0	
Y10	10% of cement was substituted by CCP	292.5	32.5	0	
Y17	17% of cement was substituted by CCP	269.75	55.25	0	
MK10	10% of cement was substituted by MK	292.5	0	32.5	
MK/Y 7/3	10% of cement was substituted 7 % by MK and 3% by CCP.	292.5	9.75	22.75	

From the above-described mixes, 100 mm and 150 mm edge length cubes were cast and used during the laboratory experiments.

3.5.2.4 Mix design applied for the size effect studies

The concrete mixes presented in this chapter correspond to the study in *Chapter 5*. To investigate the size effect on the compressive strength of concrete, concrete mixes were designed with normal compressive strength (from C20/25 to C50/60), which are frequently applied in the industry. To cover the whole range of normal strength concretes, five different mixes were designed: C20/25; C30/37; C35/45; C45/55 and C50/60. In *Chapter 5* the C20/25 concrete will be referred as Mix 1, the C30/37 as Mix 2, the C35/45 as Mix 3, the C45/55 as Mix 4, while the C50/60 as Mix 5 for easier identification. The class of the concrete was

determined based on the recommendation of *EN 206:2013* standard. The applied aggregate was normal quartz aggregate with 16 mm of maximum aggregate size (d_{max}). The chemical composition of cement was the same as in the previous cases. It was determined by using X-ray Diffraction (XRD); its specific surface area was determined by Blaine method, while its density was measured using pycnometer. The results of the measurements can be seen in *Fig. 18*. The maximum aggregate size and cement type were constant in this research. The water to cement ratio was 0.67 in case of Mix 1, 0.5 in case of Mix 2 and 3, and 0.35 in case of Mix 4 and 5. Besides the aggregates, cement, and water, no special additives were added to the mixes. The only difference between Mix 2 and 3, as well as between Mix 4 and 5 is their aggregate size distribution; the other parameters were kept constant. The final design of the mixes and the applied quantities can be seen in *Table 12*.

Table 12 *Concrete mix design*

		Mix 1 C20/25	Mix 2 C30/37	Mix 3 C35/45	Mix 4 C45/55	Mix 5 C50/60
	Cement [kg/m³]	264	380	360	500	500
	Water [kg/m³]	176.09	190	180	175	175
Aggregate [kg/m³]	0/4	910.44	984.32	641.70	594.5	789.0
	4/8	542.39	357.93	458.40	424.7	469.5
	8/16	484.28	447.42	733.40	679.4	469.5
Fresh concrete density [kg/m³]		2377.2	2361.9	2375.7	2376.6	2403

As an example, the particle size distribution of Mix 2 and 3 can be seen in *Fig. 20*.

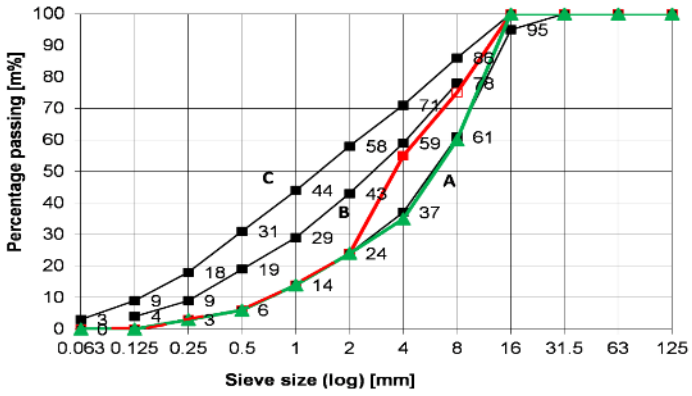

Fig. 20 *Aggregate size distribution of Mix 2 (red) and Mix 3 (green)*

The grading limit curves ("A", "B" and "C") of *Fig. 20* show that the grain aggregate applied is suitable for making concrete. The applied treatment was the same for all samples. Variables and constraints of the mix design are listed in *Table 13*.

Table 13 *Variable and constraint parameters for all mixtures used for the size effect studies*

	Variables
1.	*Cement content (kg/m³): 264 – to – 500*
2.	*w/c ratio (by mass): 0.35 – to - 0.67*
3.	*Aggregate particle size distribution (kg/m³)*
	3.1 0/4: 594 – to - 910
	3.2 4/8: 357 – to - 542
	3.3 8/16: 447 – to - 733
	Constraints
4.	*d_{max} (mm): 16*
5.	*Cement type: OPC - CEM I 42.5 N*
6.	*Aggregate type: quartz gravel*

Description of the laboratory tests

The compressive strength of concrete was measured in this research on specimens of different sizes and shapes. The shape of the sample was either cube or cylinder because these are the two standardized shapes for concrete compressive strength testing. The edge length of the cube samples was 50, 100, 150 or 200 mm, while in case of the cylinder specimens the following samples were cast (diameter × height): 60×120, 100×200 and 150×300 mm.

50 mm edge length was chosen as the minimum size based on the detailing rules of Eurocode (*EN 1992-1-1*), where the minimum size of the sample is defined as $4\times d_{max}$, which is in our case 64 mm. These sample sizes were chosen because they are applied in the standards for different test methods (e.g.: 100 mm cube for freeze-thaw test in Eurocode). At least three specimens were produced from every size and shape, which means 105 samples in sum. The geometric data of the different samples (and the specimens itself) can be seen in *Fig. 21* and in *Table 14*.

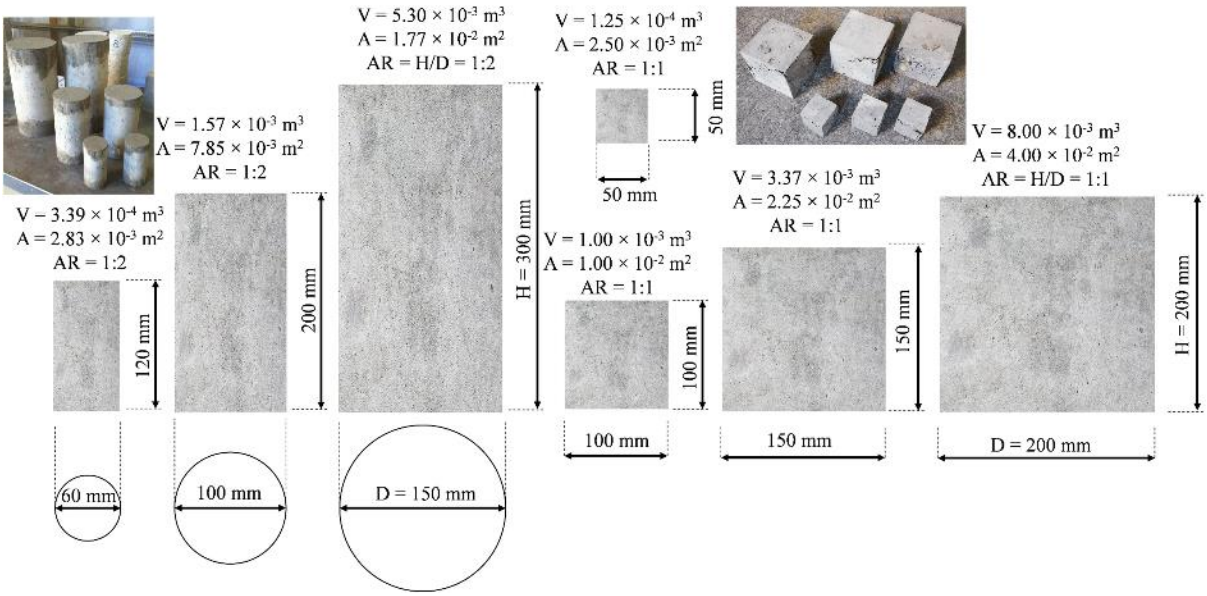

Fig. 21 *The investigated samples and their geometric data; AR = aspect ratio*

Table 14 *Dimensions of the applied specimens (standard sizes are marked with bold characters)*

Cube [edge length in mm]	Cylinder [diameter × height in mm]
50 × 50 × 50	-
-	60 × 120
100 × 100 × 100	100 × 200
150 × 150 × 150	**150 × 300**
200 × 200 × 200	-

As it was previously mentioned, the treatment of the specimens was the same. The specimens were tested for uniaxial compressive strength in the Material Testing Laboratory of the Budapest University of Technology and Economics. Besides the compressive strength, the body density of the samples was determined as well.

3.5.3 General comments on the specimens

All concrete specimens were stored under lime-saturated water for seven days and then moved to ambient laboratory conditions (20 ± 2 °C) until the time of the test. The tests were conducted at different ages (28 days or more). Around 800 samples were prepared.

1. **For compressive strength** 150×150×150 mm cubes have been tested (except in case of the size effect study) by a universal closed-loop hydraulic testing machine at a constant loading rate of 11.25 kN/s.
2. **For modulus of elasticity**, 120×120×360 mm prisms have been tested by an Instron device.
3. **For freeze-thaw and frost resistance,** 100×100×100 mm cubes have been tested.

Finally, all concrete mixes applied are summarized in *Table A-6 (in Appendix XVI)* and the ratios of the Y10 mix are also shown.

CHAPTER 4: MECHANICAL TESTING AND MODELLING

This chapter presents the results of the experimental program, during which the mechanical properties of porous materials were subjected to compressive strength test, Young's modulus test and two types of hardness test. The hardness test results were analysed using Meyer's law, and the relation of the Brinell hardness and the loading force was analysed. The tests were reproduced using DEM.

First, the mechanical properties of the construction materials listed in *Chapter 3.5.1* were determined using laboratory test. The measured properties were the compressive strength, Young's modulus, density (measured with pycnometer), body density, porosity and the velocity of sound propagation in the material; the results are shown in *Table A-7 (in Appendix XVII)*. Besides these, the hardness of all materials was measured using Brinell and DSI methods.

To prove the correctness of the measurements I have plotted to *Fig. 22* the major properties in function of the porosity. Based on literature recommendation (*Neville, 1995*; *Mehta et al, 2005*), the compressive strength of a porous material is decreasing as the porosity increases. This relation can be written in the form of power function or as an exponential function. My measurements follow the same trend, which shows that the measurements as usable for further investigation.

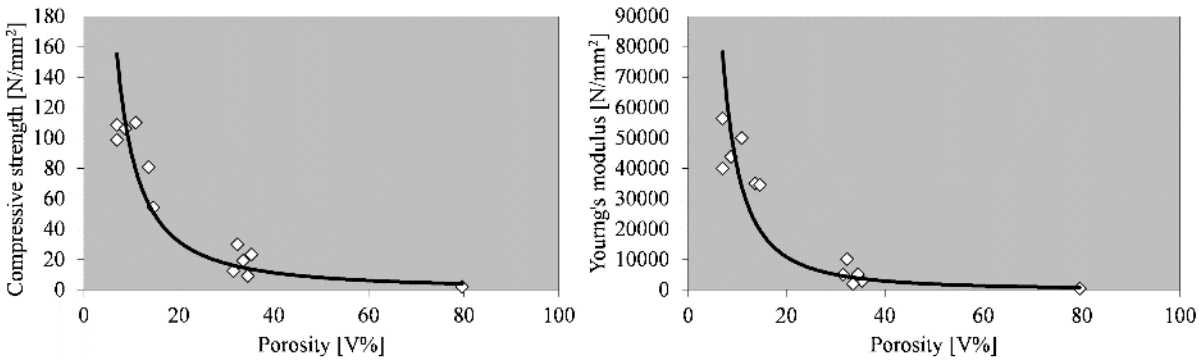

Fig. 22 *Compressive strength and Young's modulus in function of Porosity for all investigated material*

The results of the hardness tests can be seen in *Appendix XXIV*. The correctness of the results is checked using the ratios of the elastic, plastic and total indentation work, as it is shown in *Eq. (10)*. The following ratios in *Fig. 23* should give a linear relationship, and as it can be seen, the measurements follow those trends quite accurately, thus the measurements can be used for further investigation.

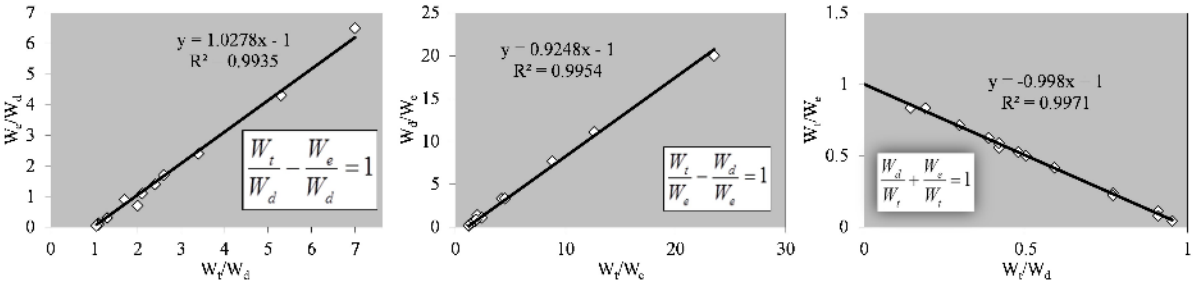

Fig. 23 *Compressive strength and Young's modulus in function of Porosity for all materials*

4.1 Evaluation of hardness results based on Meyer's power function

To investigate the effect of different load levels on the Brinell hardness, I have used Meyer's law, which gives the relation between loading force and indentation diameter in the form of a power function. In Meyer's law, there are two empirical constants *a* and *n*. If we assume that *n* is equal to 2 that leads to the following expression for the hardness:

$$HB = \frac{2F}{D \cdot \pi \cdot \left(D - \sqrt{D^2 - \frac{F}{a}} \right)} \tag{17}$$

Equation (17) shows that the Brinell hardness is dependent on the loading force. This can lead to significant differences in the value of hardness, especially in case of relatively small loading forces. In this research, I have investigated the DSI and Brinell test results in this regard to find a relation between the indentation diameter and the loading force. As it was earlier shown in *Eq. (5)* and *(6)* the indentation diameter can be calculated from the indentation depth, from which the hardness of the material can be expressed. Thus instead of the usual form (*F-d*), I have plotted (*Fig. 24*) the loading force in function of the indentation depth, which was not done previously in the literature.

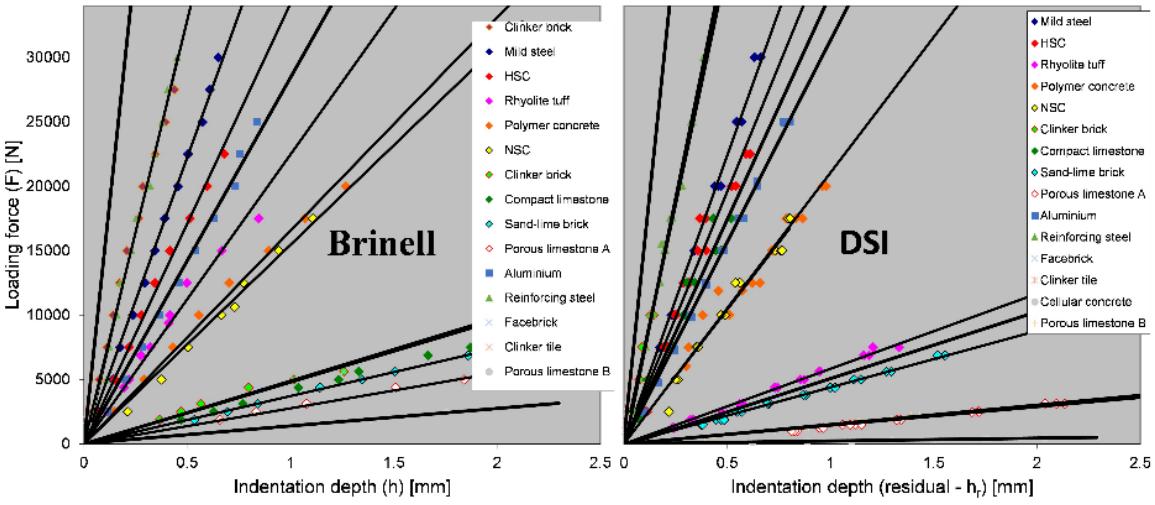

Fig. 24 *The loading force in function of indentation depth (in case of DSI the residual indentation depth) in case of Brinell test (left) and DSI test (right) for all materials*

In *Fig. 24* it can be seen that for all materials, the relation of the indentation depth and loading force is linear.

$$F = k_1 \cdot h \tag{18}$$

To see how accurate the linear regression is, the correlation coefficients (r^2) and the k_1 multipliers are shown in *Table A-8* of *Appendix XVIII*. Based on *Fig. 24* it can be concluded that the value of the multiplier k_1, which expresses the relationship between the loading force and the indentation depth, is a constant for each material; thus it can be applied as a material parameter. The lowest correlation coefficient was 0.937, which was found in case of the facebrick for Brinell testing, while the other values were even higher than that. Based on that, the linear correlation can be approved. The linear relation was true not only for the porous materials but for the investigated metals as well.

As it was already defined in *Eq. (5)* that there is a quadratic relationship between h and d. I have plotted d^2 in function of F as it can be seen in *Fig. 25*.

$$d = \sqrt{D^2 - (D - 2h)^2} \quad \rightarrow \quad d^2 \propto h \tag{19}$$

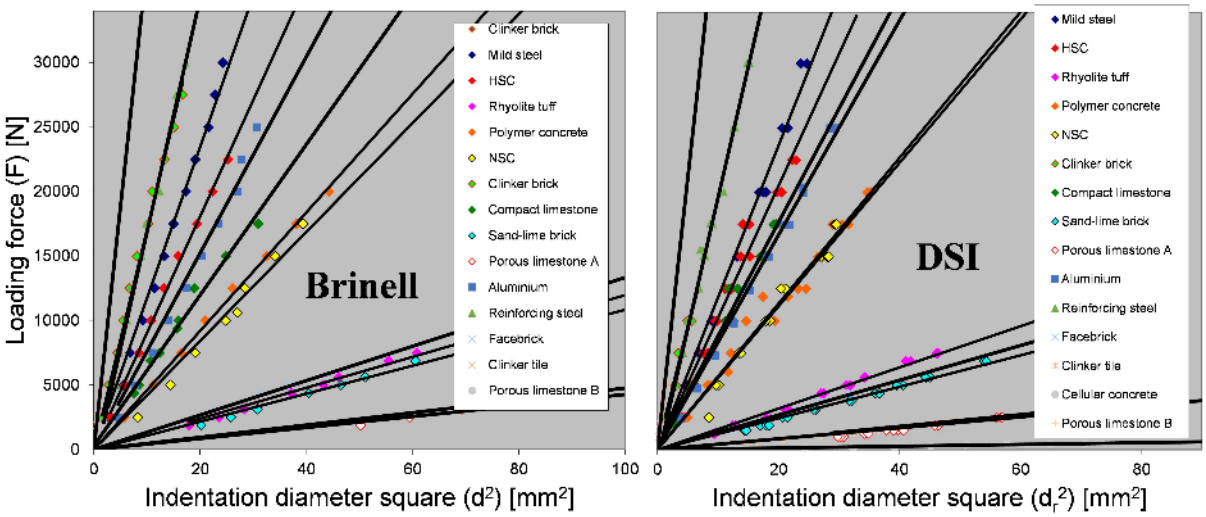

Fig. 25 *The loading force in function of indentation diameter square (in case of DSI the residual indentation diameter square) in case of Brinell test (left) and DSI test (right) for all materials*

In *Fig. 25* it can be seen (as it was expected based on *Eq. (19)*) the relationship of the indentation diameter square and the loading force is linear.

$$F = k_2 \cdot d^2 \tag{20}$$

To verify the correctness of my results and conclusions, I enclose the data of k_2 constants and r^2 correlation coefficients shown in *Table A-9* of *Appendix XVIII*. In this case, even the weakest correlation factor value remains above 0.932, which confirms the correctness of the assumption.

Based on these, the following conclusions can be drawn:

- The value of the exponent *n* in Meyer's power law is not around 2, but exactly 2. It can also be assumed that the results published by *Meyer (1908)* also showed this correlation, but due to the accuracy of the equipment, the measurements were not appropriate to lead to that conclusion.
- The multiplication factor *a* in Meyer's power law is a material-dependent value that can be specified individually for each material.

4.2 Brinell hardness in function of the loading force

In the literature, it was shown that in case of concrete there is a maximum value of Brinell hardness in function of the loading force (or using the previously described equations in function of the indentation depth) (*Szilágyi et al., 2011*). In this part of the research, I have extended this work to other porous materials as well. First, I have tested that the observation of Szilágyi is true for my concrete samples as well. Based on *Fig. 26* it can be concluded that the observation is correct; thus, I have extended it to the other materials as well.

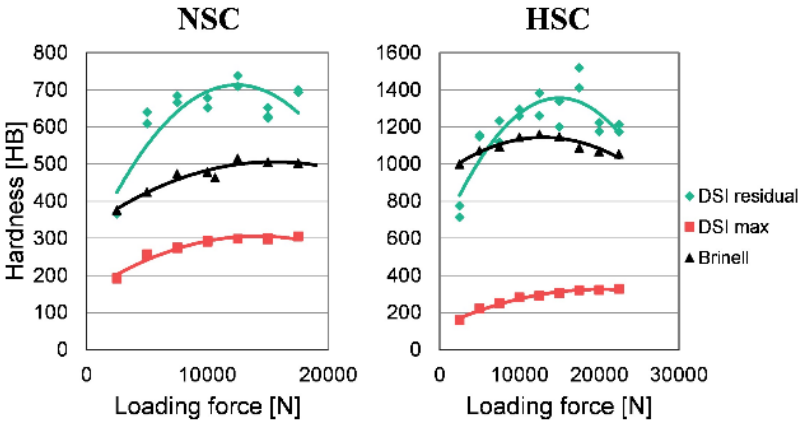

Fig. 26 *Brinell hardness in function of the loading force for concretes*

The figures for all materials can be seen in *Appendix XXIV*, but some as a representation can be seen in *Fig. 27* as well. It can be seen on the figures that to some extent, this behaviour was observable for all porous materials.

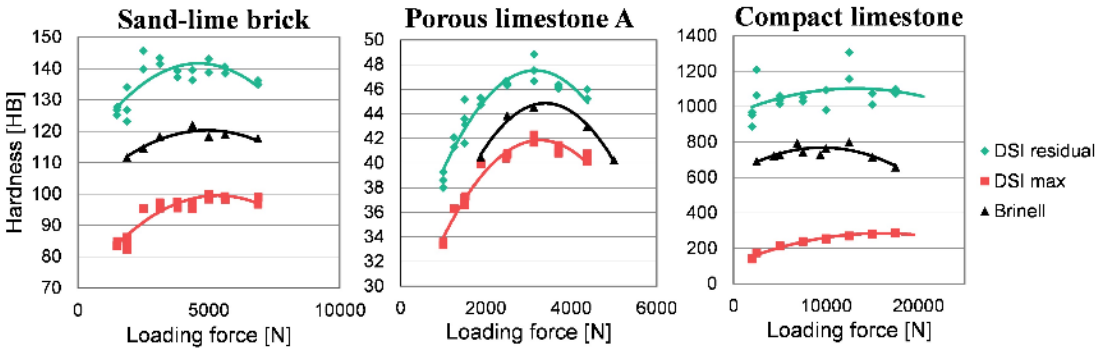

Fig. 27 *Brinell hardness in function of the loading force for other porous materials*

It can be seen on these figures that in case of all materials, the curves of the Brinell test are between the curves of the DSI test, as it was expectable. The reason behind it is the difference between the two methods. In case of the Brinell hardness test, the sample is kept under loading for a given amount of time (in my case 30 s), which gives time to the material to make plastic deformations; in case of DSI, there is no such time period. Due to that, the residual indentation diameters of the DSI test is always somewhat smaller than in case of the Brinell test.
Based on the observations of this chapter it can be concluded that a maximum value of Brinell hardness in function of the loading force exists for all porous materials, meaning that this behaviour is connected to the porous properties of the investigated materials.

4.3 Energy based evaluation of hardness testing

In this chapter, based on the DSI test results, the elastic, plastic and total indentation energy are investigated and their relationship to mechanical properties, like compressive strength and Young's modulus of the materials. As it was mentioned in *Chapter 2.2.1.3*, the response of materials to the indentation test includes elastic (reversible) and plastic (irreversible) deformations as well as forming of cone cracks in brittle materials (*Szilágyi et al, 2011*). DSI method allows researchers to study the penetration process on an energy basis. First, the resulting figures of the DSI tests were plotted. In contrast to the traditional Brinell test, the DSI test provides not only the residual indentation depth/diameter but also the maximum. Based on that and the loading-unloading curves, the mechanical behaviour of the materials can be investigated. Based on the ratio and the shape of the loading-unloading curve, I have arranged all tested materials into three groups, describing their mechanical response to hardness testing: elastic, elasto-plastic and plastic. A material was considered to be elastic if its h_r/h_m ratio was lower than 20% and its loading curve has no significant and visible linear part (based on the proposal of *Tabor (1947)*, as it is shown in *Fig. 5*). Elasto-plastic materials have a significant linear part, besides the significant curved part in their loading curve and their h_r/h_m ratio is between 20% and 80%; while the plastic materials loading curve is fully linear and their h_r/h_m ratio is higher than 80%. As an example, one material from every group is plotted in *Fig. 28*, while the arrangement of the materials is shown in *Table 15*. All figures for all materials can be seen in *Appendix XXIV*.

Table 15 *Indentation diameter/depth ratios and the mechanical behaviour of all materials*

Material	d_r/d_m	h_r/h_m	*Mechanical behaviour*
Aluminium	0.65	0.39	Elasto-Plastic
Mild steel	0.59	0.32	Elasto-Plastic
Reinforcing steel bar	0.49	0.22	Elasto-Plastic
Normal strength concrete	0.69	0.45	Elasto-Plastic
High strength concrete	0.51	0.23	Elasto-Plastic
Polymer concrete	0.65	0.37	Elasto-Plastic
Cellular concrete block	0.96	0.91	Plastic
Sand-lime brick	0.85	0.69	Elasto-Plastic
Clinker brick	0.35	0.12	Elastic
Facebrick	0.82	0.65	Elasto-Plastic
Clinker tile	0.19	0.03	Elastic
Porous limestone A	0.95	0.87	Plastic
Porous limestone B	0.92	0.83	Plastic
Compact limestone	0.48	0.21	Elasto-Plastic
Rhyolite tuff	0.81	0.62	Elasto-Plastic

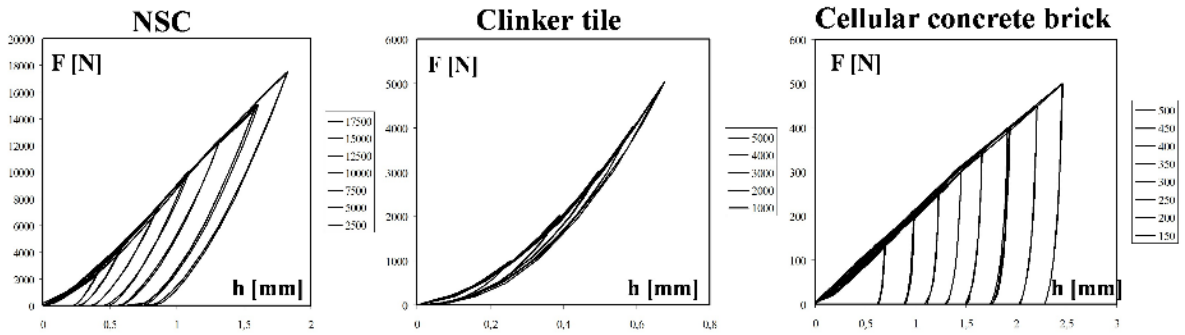

Fig. 28 *DSI test results of an elasto-plastic (NSC), elastic (Clinker tile) and plastic (Cellular concrete brick)*

A typical example of elasto-plastic materials is metals. This is well known based on a wide range of literature data, and the method of static hardness testing was developed for such materials. The elastic and dissipated (plastic) energy both contributes significantly in the total indentation energy in case of metals (e.g. in case of S235 steel W_t = 25124 Nmm, W_e = 17762 Nmm, W_d = 7361 Nmm). Based on the results, it can be observed that other materials, mostly concretes show similar behaviour, as it can be seen in *Fig. 28*. Even polymer concrete, which is an unconventional type of concrete, fits into the group of elasto-plastic materials.

After that, the elastic, plastic and total indentation energy's relation was investigated with other mechanical properties. Based on the results, it could be observed that the relationship between both elastic and dissipated energy can be described by the same type of power function in case

of both strength characteristics (comp. strength; Young's modulus). Taking into account the correlation coefficients, it can be stated that only the relationship between the elastic energy and the compressive strength (presented in *Fig. 29*, *left*) can be given with sufficient accuracy, the other values. Based on this energy-based approach, it can be observed that the Brinell hardness of materials appears to be more related to its elastic properties. The relationship with plastic characteristics can only be assumed. The connection of the energies and the Brinell hardness was also investigated. After some transformations, it was discovered that there is a relationship between the elastic energy and the peak Brinell-hardness of the materials. The peak Brinell hardness (HB) is written in function of the ratio of the total (W_t) and the elastic (W_e) indentation energy (*Eq. (21)*).

$$HB = k \cdot \frac{1}{\left({W_t}/{W_e}\right)^2} \tag{21}$$

The results indicate that there is a strong correlation between the peak Brinell hardness and the elastic indentation energy of the porous materials. *Equation (21)* was applicable for all investigated materials, except the clinker tile, which behaved fully elastically within the applied load range. Thus it could be stated that an expression was derived between the peak Brinell hardness and elastic indentation energy of plastic and elasto-plastic materials. Based on the experiment, the value of parameter '*k*' in the expression was found to be 3894.2 N/mm^2 as it can be seen in *Fig. 29*, *right*.

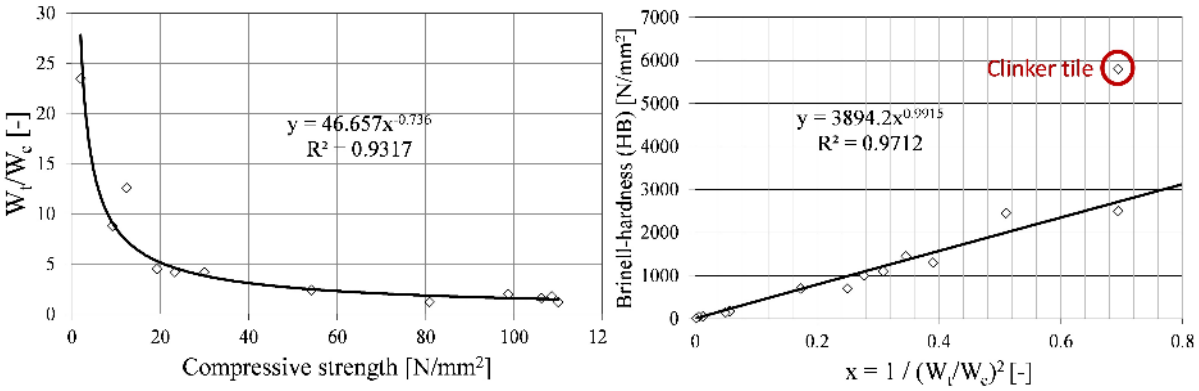

Fig. 29 *Relationship of the compressive strength and the ratio of the total and elastic energy (left); Relationship of the peak Brinell-hardness and the ratio of the total and elastic energy (right)*

It can be concluded that based on the results, materials can be arranged into groups, according their mechanical behaviour: elastic, elasto-plastic and plastic. The energy-based analysis of the DSI results indicated that there is a linear relationship between the Brinell hardness and the elastic indentation energy of elasto-plastic and plastic construction materials. The measurement results indicate that based on the found expression, a material property can be defined, which is valid for all elasto-plastic and plastic materials.

4.4 DE modelling of mechanical tests

To further investigate the previously described topics, DE models of compressive and hardness tests were created, according to the description given in *Chapter 3.3.2.5* and *3.3.2.6*. The numerical material tests were performed on one chosen material, normal strength concrete. First, using the compressive strength routine, the model parameters were calibrated according to *Chapter 3.3.2.3*. The calibration led to a mean parallel bond strength of 42.51 N/mm^2. As it was also mentioned in *Chapter 3.3.2.3*, four additional models were generated. In compression test, the generated models behaved very similarly to each other and gave almost exactly the same result to the uniaxial compression test as the original model did, as it is shown in *Table 16*. All the results of the models were in a 0.5 % range compared to the results generated in the first model.

Table 16 *Compressive strength measured using the calibrated parameter set on 5 models*

# of the model	1	2	3	4	5
Compressive strength (N/mm^2)	54.24	54.19	54.26	54.03	54.20

From these values, Young's modulus of the concrete can be recalculated by using the following expression:

$$E_c = 10{,}000 \times f_c^{\frac{1}{3}} \qquad (22)$$

where f_c is the normal strength of the concrete. By using an averaged value of the model data, the value of the recalculated Young's modulus is 37840 N/mm^2 that is close to the measured value (8.6% higher). After that, the hardness testing procedure was performed. With the help of the measuring tool provided by the software, the distance between the edges of the residual ball print in two diagonals, which are perpendicular to each other (the diagonals along axis X and Y) are measured. The diameter of the ball print was measured between the elements on the upper edge of the print. The closest point of these elements to each other was chosen for the measurements because these points approximate best the edges of the print in reality. In reality, the aggregates are not always on the surface of the print, and they are covered with cement. However, the particles in the model represent the aggregates surrounded with cement; thus, the inner distance of these elements are the realistic value. The results are shown in *Fig. 30* and listed in *Table A-10* in *Appendix XIX*.

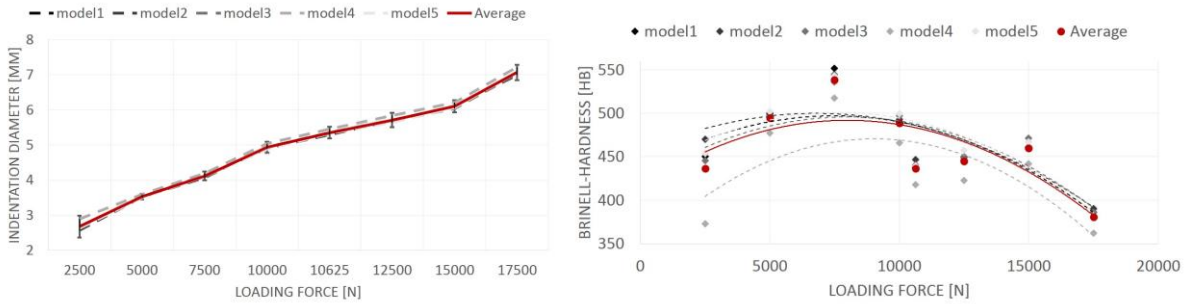

Fig. 30 *Indentation diameter and Brinell hardness of the 5 models and their average*

After the model averaging the highest Brinell-hardness value appears in case of the 7500 N loading, and the smallest in case of the largest loading. It can also be seen, that in the diameter values between first and the second as well as between the last two values a quite large difference appears. Those differences are much higher than the other differences between the other two values and cause a bigger jump in the Brinell-hardness values too. This means that between those two load levels, the particles in the model have larger movements, than in other cases. The reason for that could be that on those two load levels more parallel bond connections break, which allows the particles more movement. The DSI test was also modelled according to *Chapter 3.3.2.7*. It can be observed in *Fig. 31*, where were the load steps changed because there is a break observable in the figure, and the steepness of the model is changing. Except for the first section of the figure, the steepness of the figure looks linear; there are only small changes in the steepness of the different loading levels. The different behaviour of the first section can be explained with the initial position of the loading sphere. The sphere was generated in the position directly above the surface of the material, but to avoid the undesirable intersections, which can happen during the particle generation, the sphere does not touch the surface of the sample, and a short movement is needed to reach the surface of the material and create contacts.

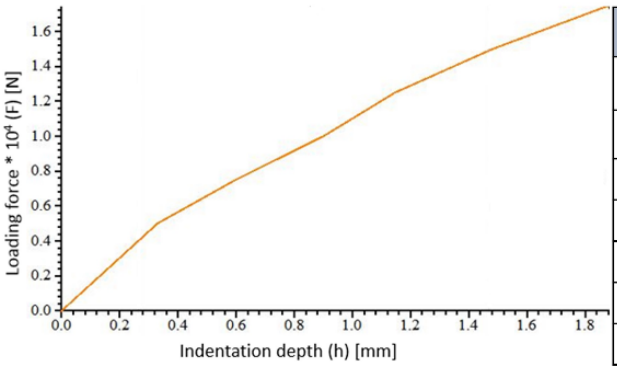

Loading force [N]	d_{max} [mm]	HB_{max} [HB]	d_{res} [mm]	HB_{res} [HB]
2500	3.0	348	2.6	463
5000	3.6	478	3.4	534
7500	4.8	397	4.1	543
10000	5.8	349	4.8	519
12500	6.4	339	5.6	464
15000	7.2	316	6.0	477
17500	7.9	292	6.9	403

Fig. 31 *Loading curve of the DSI DE mode test and the measured values*

If we compare the model results to the laboratory measurement results, it can be seen that there are significant differences in percentage between the model and the laboratory measurements,

especially in case of very low and high loading forces, as it is shown in *Table A-11* of *Appendix XIX*. In case of medium loading forces, the measured values are fairly close to the model results. However, in value, the differences are fairly small, and the model follows the trend of the laboratory experiments as it is shown in *Fig. 32*.

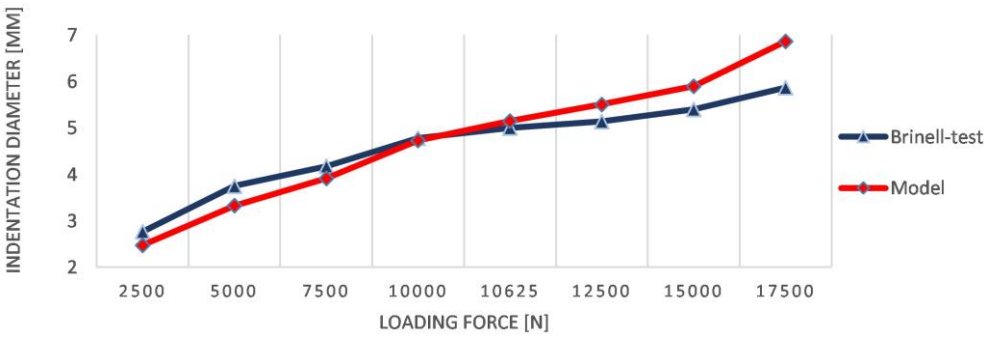

Fig. 32 *Indentation diameter vs. loading force in case of the Brinell test (laboratory and DE model)*

Similar comparison can be made in case of the DSI test and its model. Here, especially in case of the maximum diameter, even higher differences can be spotted. However, in some cases, the model was quite accurate here as well, as it can be seen in *Table 17*.

Table 17 *DSI test results from the laboratory test and the model; the differences between them*

Loading force [N]	DSI DE model				DSI lab test				Differences [%]			
	d_{max} [mm]	Hb_{max} [HB]	d_{res} [mm]	Hb_{res} [HB]	d_{max} [mm]	Hb_{max} [HB]	d_{res} [mm]	Hb_{res} [HB]	d_{max}	HB_{max}	d_{res}	HB_{res}
2500	3.0	348	2.6	463	3.99	192	2.92	366	25	-80	10	-26
5000	3.6	478	3.4	534	4.83	256	3.16	624	25	-86	-7	14
7500	4.8	397	4.1	543	5.64	274	3.70	675	15	-44	-10	19
10000	5.8	349	4.8	519	6.23	292	4.27	664	7	-19	-12	22
12500	6.4	339	5.6	464	6.79	299	4.56	723	5	-13	-22	35
15000	7.2	316	6.0	477	7.33	299	5.28	635	2	-5	-13	24
17500	7.9	292	6.9	403	7.73	305	5.43	696	-1	4	-27	42

To check that the model behaviour is similar to the real laboratory experiments, I have analysed the results on the model based on Meyer's law and checked that the observed phenomena of maximum HB value could be observed on the model as well or not. In *Fig. 33* the square of the indentation diameter is plotted in function of the loading force for all models and for the corresponding laboratory test results as well. Based on the figure, the same observation can be done as previously, meaning the quadratic behaviour of Meyer's law can be proven using the models as well (min correlation coefficient is 0.9513). In the figure, it can be seen as well that the model results are fairly close to their corresponding laboratory test results.

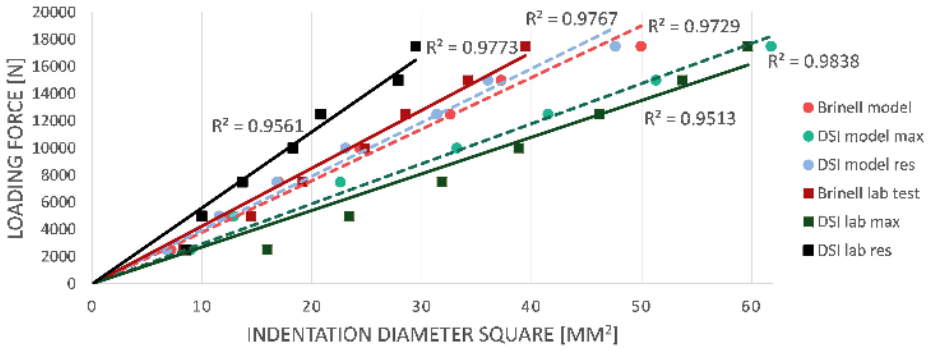

Fig. 33 *Indentation diameter square vs loading force in case of all DE model and lab test results*

The Brinell hardness was plotted in function of the loading force as well. Similar observation can be done, as it was done in *Chapter 4.2*, based on *Fig. 34*, which shows that the models have similar behaviour to the real-world results. It can be seen that there is a maximum value for Brinell hardness in function of the loading force in case of the models as well; however, its value is different. While in case of the laboratory measurements the peak value of Brinell hardness was observed around 12-15,000 N, in case of the models this value is shifted below 10,000 N. This observation indicates that the model is able to follow the expected behaviour of the material qualitatively, but not quantitatively. This can be attributed to the fact that aggregates composing a real sample are irregular in shape, whereas, the effect of irregularity is lost once aggregates are simplified to a spherical representation for simulations (which is the case for the 0/4 aggregate fraction in my case). Regardless, both figures have the extreme hardness values belonging to a smaller load level than the maximum load level. It can be concluded that the assumption that the Brinell-hardness has a maximum value in function of the loading force can be observed in the model data too.

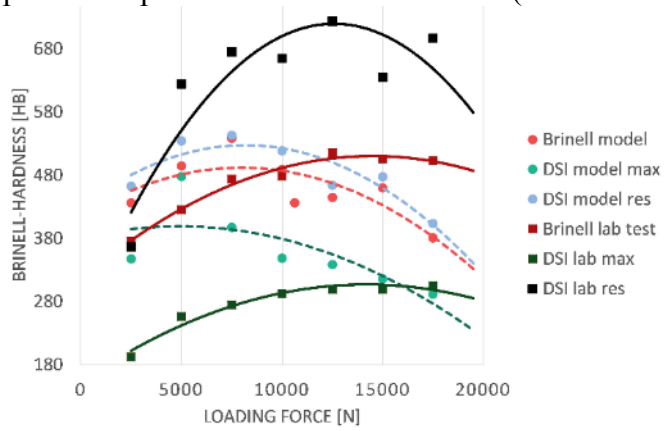

Fig. 34 *Brinell hardness in function of the loading force for the models and their corresponding lab test*

CHAPTER 5: SIZE EFFECT

In this chapter, the effect of size on compressive strength of normal strength concrete is investigated. Modified version of size effect law is introduced with an algorithm to create a size effect model. The results of the laboratory tests are compared to the results of the model and with literature. The algorithm with an additional step is applied for estimation of the strength parameters of a DE model.

5.1 Size effect law

Equation (2) gives a good estimate for cylinder specimens with higher than unique *h/d* ratio. This equation can be generalized to contain only one size-dependent variable (*d*), which may be applicable for both cubes and cylinders. It could be written in the following form:

$$\sigma_N(d) = Bf_c'/\sqrt{1 + d/S} + \alpha f_c', \tag{23}$$

where B [-], S [mm or mm^2 or mm^3], and α [-] are empirical values. Using this model by knowing the size and the standard compressive strength of the sample, the nominal strength of the given sized sample can be determined. There are different possibilities to choose which size measure of a sample to use:

- diameter (in case of cylinder samples) and edge length (in case of cube samples) (d),
- compressed surface area (A), or
- volume of the specimen (V).

Equation (23) is proposed as using the standard compressive strength measured on cylinders. However, in Europe, it would be more relatable to use the standard compressive strength measured on a standard size cube specimen. Therefore, in this chapter, the possibilities of using all these variables in the estimation of nominal compressive strength are investigated. For cube strength estimation, a method was proposed by del Viso, which was tested on high strength concrete samples (*del Viso et al, 2008*). The proposed law gives the standard cube compressive strength based on compression strength measured on arbitrary size cube, the size of the specimen and an empirical constant.

5.2 Laboratory test results

It is important to point out that size effect is dependent on the failure mode. The failure mode of a specimen was categorized by visual inspection on the crack pattern during the test and on the shape of the remaining material. All cube specimens (described in *Chapter 3.5.2.4*) had the same crack pattern, and we have found that the lateral sides got spalled during the test leading to the typical hour-glass failure mode of concrete cubes. In case of the cylinder specimens, a

main inclined fracture surface was observed. The visual inspection evidences that the extent of cracking throughout the specimen is less dense in cylinder specimens that in cubes.

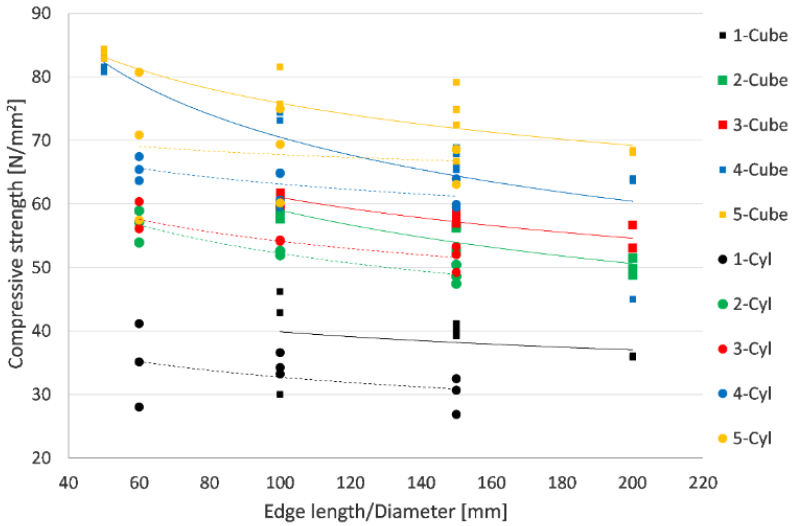

Fig. 35 *Summary of compressive strength test results*

The results (*Fig. 35*) show that the compressive strength of the samples is decreasing with the increase of the size (edge length/diameter or volume), regardless of the shape or the strength class of the concrete sample. This is the expected behaviour already observed by many researchers previously (*Bažant et al, 1991*; *Kim et al, 2000*; *Balázs et al, 1999*; *Kim and Yi, 2002*; *Yi et al, 2006*). The shape and strength class influence the rate of decrease. If the measured compressive strengths of all samples are compared to the standard strength, then it gives the strength ratio plotted in *Fig. 36*. An interesting observation can be made based on the figure: among different mixes, with the decrease of the compressive strength the specimen size has an increasing effect. It can be seen that the differences in strength ratios are much higher in case of Mix 1 than in case of Mix 5. This means that in case of concretes with lower compressive strength, the specimen size has an even more important role. It can be explained by the more extent heterogeneity of the material. As we go towards the higher strength concretes the material becomes more and more homogeneous and thus the number of potential internal structural errors decreases.

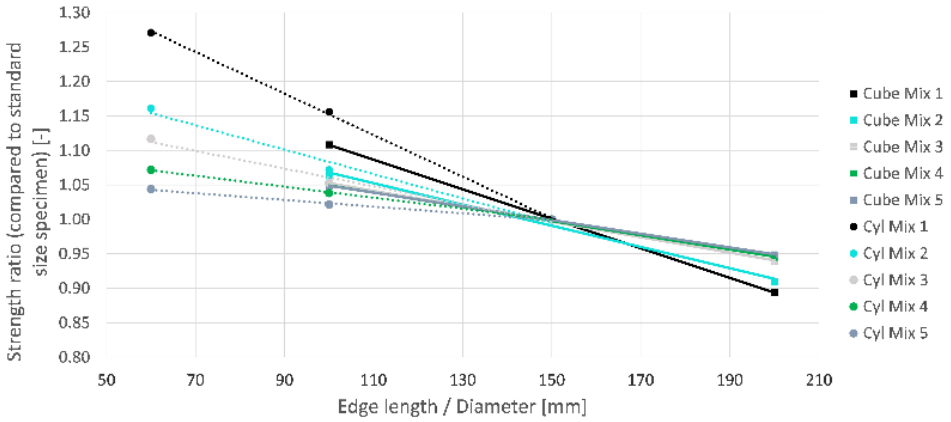

Fig. 36 *Strength ratio (compared to standard size specimens) vs Edge length / Diameter for all mixes (cube and cylinder results separately)*

5.3 Algorithm to estimate compressive strength of different sized specimens

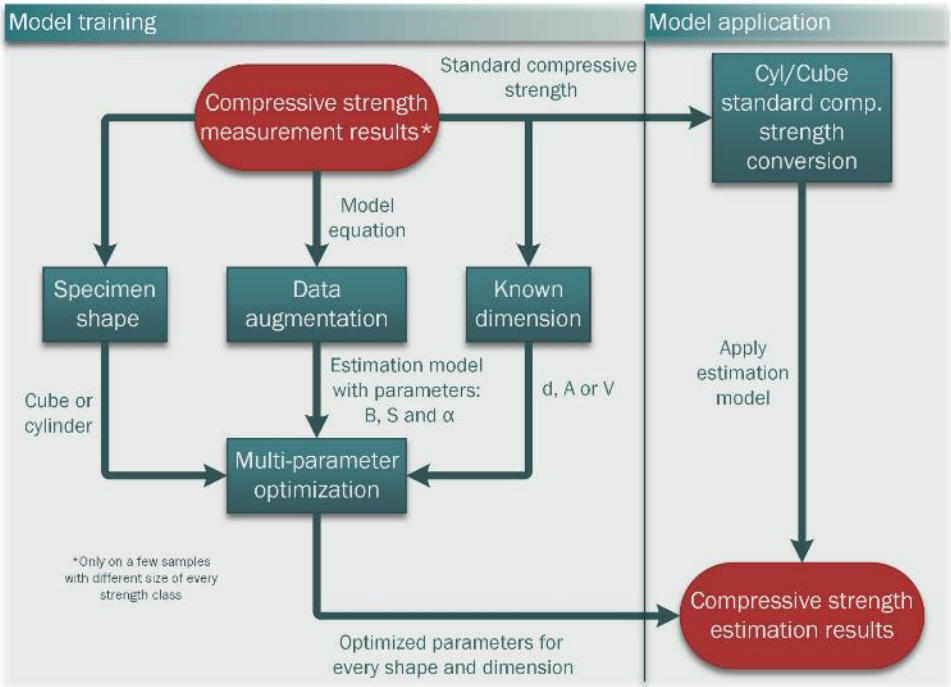

Fig. 37 *Main steps of the developed algorithm*

Using the acquired data model equations were defined for every shape and mix to estimate the compressive strength based on the volume of the sample, as it is shown in *Fig. 37*. The model equations were defined in the form of the power formula:

$$f_c'(V) = a \cdot V^{-b}, \tag{24}$$

where V is the volume of the sample in m^3, while a and b are constants (e.g. in case of Mix 5 for cubes, a = 55.36; b = 0.015).

The model equations were used for interpolation to calculate the possible compressive strengths for given volumes. The corresponding edge lengths (for cubes) and diameters (for 1:2 cylinders) with their surface were calculated as well. The range in the volume of the

investigations was divided uniformly into 8 points, where the compressive strength was determined. See *Fig. 38* as an example; the table of the other mixes can be found in *Table A-14* of *Appendix XXI*. Thus, the number of measurement results was increased, which could be used for the validation and verification of the proposed model, leading to a presumably more precise estimation.

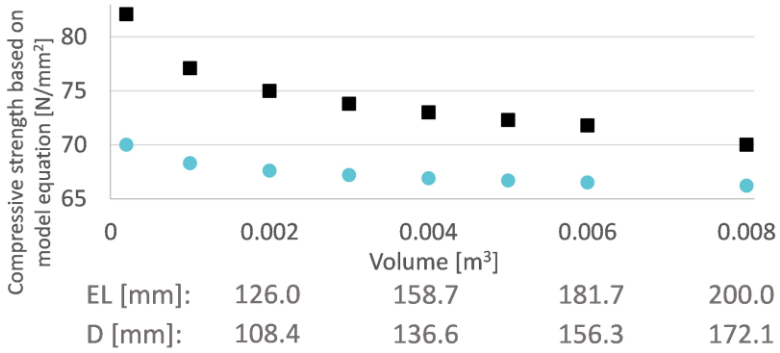

Fig. 38 *Compressive strength for different volumes based on the model equation in case of Mix 5 (EL = edge length of the cube samples; D = diameter of the cylinder samples)*

Using the acquired data as measured output for the optimization scheme, the parameters of *Eq. (23)* could be tuned. It was aimed in our research to use *Eq. (23)* with different parameter sets to estimate the compressive strength of different size concrete samples. It is also aimed to find parameter sets that can be used to estimate the compressive strength of different size cube samples based on the standard compressive strength measured on a cylinder and vice versa. The notation in the following sections are the following: e.g.: Cyl-to-Cube – Cube strength estimated based on the standard strength of cylinder. In case of Cyl-to-Cube and Cube-to-Cyl estimations an additional step was included, during which the standard size cube compressive strength ($f'_{c,cube}$) was calculated from the standard size cylinder strength ($f'_{c,cyl}$) or vice versa (f_c' of *Eq. (23)*). This step was required because the size effect law is valid only for one specimen shape when all the sizes are scaled up in equal proportion. This step was done based on linear regression. In the literature, there are many recommendations for that relationship. Most of them estimate the standard cube compressive strength as the 113-126 % of standard cylinder compressive strength (*Palotás, 1947*). Based on our measurements, the relationship can be written in the linear form defined in *Eq. (25)* for normal strength concretes (with strength class between C20/25 to C50/60).

$$f'_{c,cube} = 0.907 \cdot f'_{c,cyl} + 12 \qquad (25)$$

In *Eq. (23)* there are different possibilities to choose which size measure to use. It was also aimed to find the optimal parameters for *d* as diameter, surface area or volume as well. In sum, it means 4 × 3 (Shapes × Dimensions) evaluations of the data, as it is shown in *Fig. 39*.

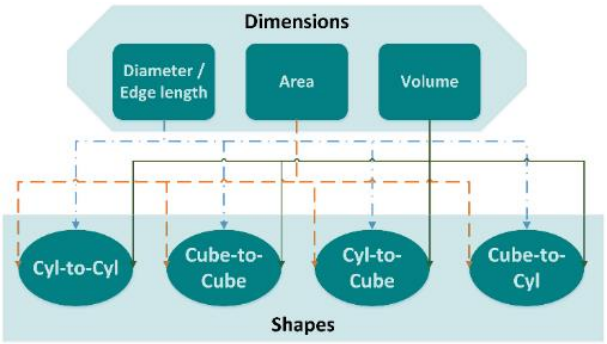

Fig. 39 *Overview of the different optimization / evaluation versions*

The results were compared to the most widely used approaches that can be found in the literature (original MSEL, MSEL modified by Yi et al (cylinder and cube), del Viso) (*Kim and Yi, 2002*; *Yi et al, 2006*; *del Viso, 2008*). The initial conditions for the parameter tuning were the same (the values defined by Kim and Eo (*Kim et al, 1989*) in all cases, except the value of S, which is strongly connected to the size measure used. The applied initial parameters can be seen in *Table 18*.

Table 18 *Initial parameter setup*

d	B	α	S
Edge length / diameter [mm]	0.4	0.8	50
Surface area [mm^2]			500
Volume [mm^3]			50000

5.3.1 Edge length / diameter (d) applied as size-related variable

The parameters of *Eq. (23)* were obtained from the method described in *Chapter 3.4* (least-squares method; SSE objective function). The optimized parameters for the different specimen shapes can be seen in *Table 19*.

Table 19 *Optimized parameters based on specimen diameter/edge length*

Shape	B	α	S
Cyl-to-Cyl	0.55	0.72	52.32
Cube-to-Cube	0.99	0.41	76.66

5.3.2 Surface area (A) applied as size-related variable

From *Eq. (23)* using the geometry of the given specimen *Eq. (26)* can be derived. The parameters of *Eq. (26)* were obtained from the method described in *Chapter 3.4* (least-squares method; SSE objective function).

$$\sigma_N(A) = Bf_c'/\sqrt{1 + A/S} + \alpha f_c' \qquad (26)$$

The optimized parameters for the different specimen shapes can be seen in *Table 20*.

Table 20 *Optimized parameters based on specimen surface area*

Shape	B	α	S
Cyl-to-Cyl	0.32	0.82	8018
Cube-to-Cube	0.55	0.67	12001

5.3.3 Volume (V) applied as size-related variable

From *Eq. (23)* using the geometry of the given specimen *Eq. (27)* can be derived. The parameters of *Eq. (27)* were obtained from the method described in *Chapter 3.4* (least-squares method; SSE objective function).

$$\sigma_N(V) = Bf_c'/\sqrt{1+V/S} + \alpha f_c' \qquad (27)$$

The optimized parameters for the different specimen shapes can be seen in *Table 21*.

Table 21 *Optimized parameters based on specimen volume*

Shape	B	α	S
Cyl-to-Cyl	0.23	0.97	162310
Cube-to-Cube	0.36	0.82	1039100

5.4 Evaluation of the estimation model results

The estimation results were evaluated on the basis of $\sigma_n(d)/f_c'$ as the function of the volume.

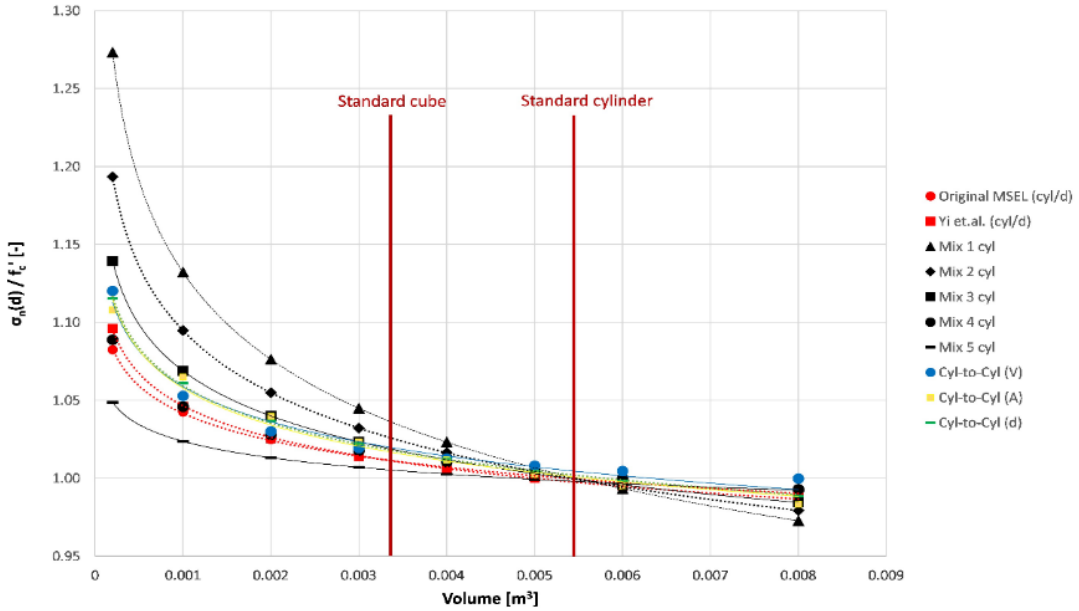

Fig. 40 *Results for estimating cylinder strength (red – literature; black -measurements; other – own estimation models)*

In *Fig. 40*, the results for estimating cylinder strength are shown from the measurements (Mix 1-5), from the literature (MSEL, Yi et al (*Yi et al, 2006*) and from the own estimation models. The results show that with the increase of the specimen size, the strength ratio approaches a limit. Based on *Fig. 40*, it can be seen that the functions for the same estimation model (e.g. Cyl-to-Cyl) with different size measure (d/A/V) are strongly correlate to each other; in a practical point of view they can be considered as equal). It is relatable as *A* and *V* are the functions of *d* (e.g.: A = d^2 and V = d^3 for cubes). However, we would like to emphasize that in case of structures or specimens with different h/d ratio, this is not obviously true.

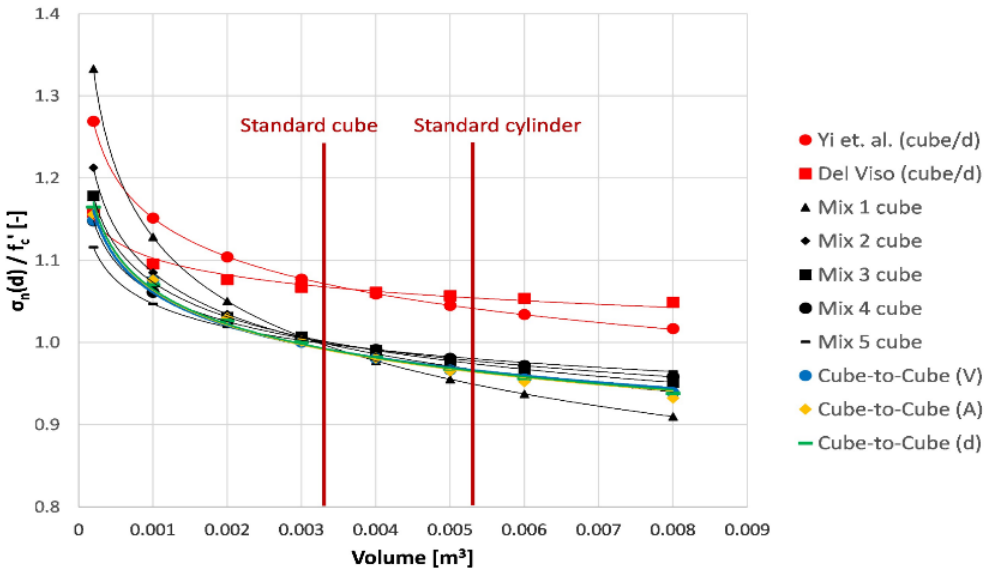

Fig. 41 *Results for estimating cube strength (red – literature; black – measurements; other – own estimation models)*

It can be seen that the estimation models from the literature and the Cyl-to-Cyl estimation models (diameter, area, and volume-based as well) quite accurately approximate the measurement results, especially in case of larger sizes. In this evaluation methodology, the Cube-to-Cyl estimation models coincide with the Cyl-to-Cyl models (same parameter set is used only f_c' is different).

For cubes (*Fig. 41*), fewer estimation models can be found in the literature (as SEL and MSEL were defined for cylinders). Based on the results of our measurements, these estimation models of literature overestimate the strength of the specimen, especially in case of higher volumes. The Cube-to-Cube estimations show good correlation with the measurement data, regardless of the used size measure (d/A/V). Similarly to cylinders, in this evaluation methodology, the Cyl-to-Cube estimation models coincide with the Cube-to-Cube models (same parameter set is used only f_c' is different).

5.4.1 Error analysis

To see how accurate the different estimation models are, an error analysis was conducted. For that, the compressive strength was estimated and compared to the measurement data by using the optimized parameter sets. The error in N/mm^2 and in % (based on the standard cyl/cube strength) was calculated for every mix, for every size, for every estimation model. The results are summarized in *Fig. 43*. The average and maximum errors are also plotted. While the first reflects the accuracy of a given model, the second shows its robustness (how accurate it is for very different concrete mixes).

The lowest average error (0.87) was achieved by the Cube-to-Cube (diameter/edge length) estimation model; however, similarly, low values can be found for all Cube-to-Cube and Cyl-to-Cyl models as well as for some models of the literature (MSEL, Yi et al (cyl) (*Yi et al, 2006*)). The lowest maximum error belongs to the Cyl-to-Cyl (volume) model. Similar values can be found for other Cyl-to-Cyl models, for some Cube-to-Cube models and even for some Cube-to-Cyl models. Cyl-to-Cube models performed somewhat worse in this aspect. It has to be noted that the accuracy of Cyl-to-Cube and Cube-to-Cyl models are also dependent on the accuracy of *Eq. (25)*. With a perfectly estimating *Eq. (25)* the same accuracy can be reached as it was reached by the Cube-to-Cube or Cyl-to-Cyl models. It is interesting to point out that in average error, there was a negligible difference between the most accurate model and the literature; however, in case of maximum error, the difference is more significant. This analysis reflects that the estimation of cube strength is always showing higher maximum error than the estimation of cylinder strength using these models.

$$e_{max,Cyl-to-Cyl} \leq e_{max,Cube-to-Cube} \;\&\; e_{max,Cube-to-Cyl} \leq e_{max,Cyl-to-Cube} \tag{28}$$

When the two metrics are looked together combined, the most accurate performance was done by the Cyl-to-Cyl models and Yi et al (cyl) (*Yi et al, 2006*). To estimate the cube strength from standard cube strength, the Cube-to-Cube (d) model is found to be the most accurate. For the estimation of cylinder strength based on standard cube strength, the Cube-to-Cyl (d) and (A) models are recommended. These models have higher average error, but similar maximum error to the previous models. For the estimation of cube strength from standard cylinder strength, the Cyl-to-Cube (d) model makes the smallest error, but it has somewhat higher maximum error. However, this conversion is the least important in a practical point of view, as it is rarely used (strength classes are based on cylinder strength; it is easier to work with cubes).

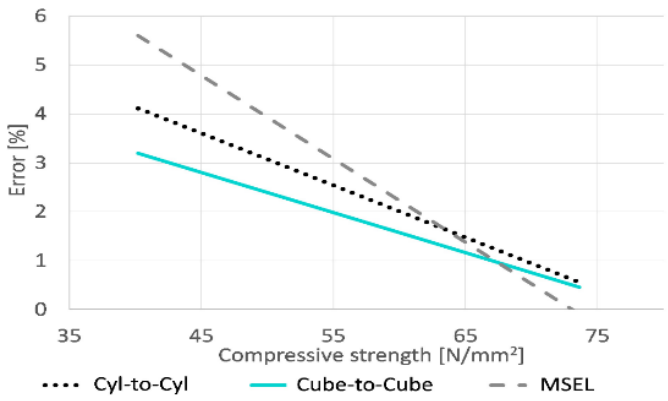

Fig. 42 *Error [%] of the estimation models in function of the standard compressive strength [N/mm²] of the mixes*

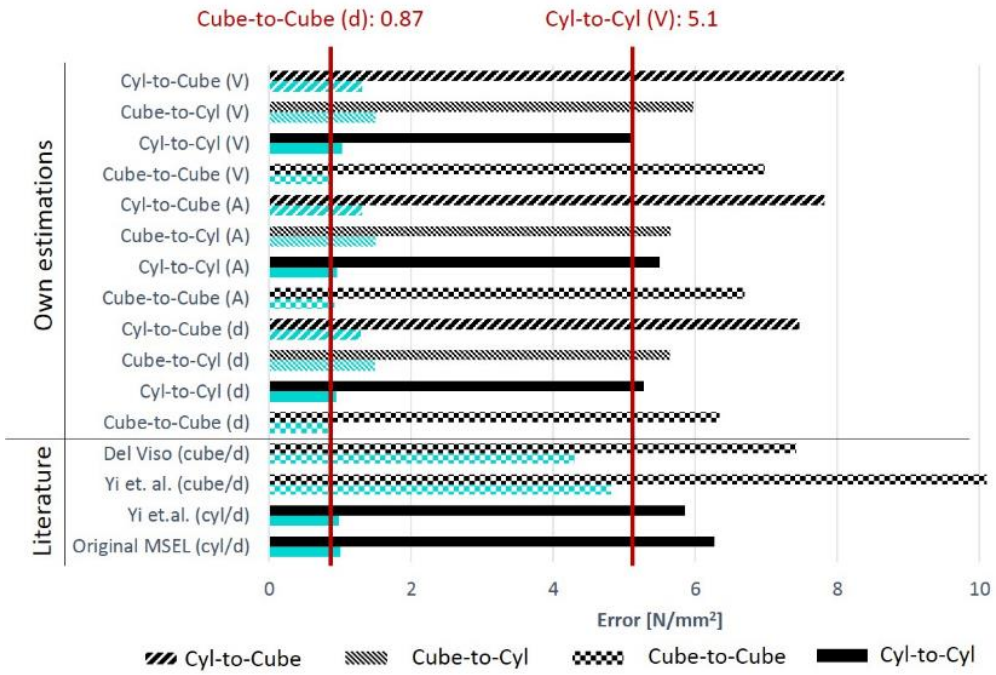

Fig. 43 *Average (cyan) and maximum (black) error of the different estimation models*

In the error analysis, it was also found that with the increase of compressive strength, the average error decreases (see *Fig. 42*). It can be explained by the inhomogeneity of the concretes with lower compressive strength. As we are moving forward to the higher strength classes, the material becomes more and more homogeneous that explains the lower errors found.

5.4.2 Remarks to industrial application

As it was mentioned in *Chapter 5.4*, based on *Fig. 40* and *Fig. 41*, with the increase of specimen size, the strength ratio decreases and approaches a certain limit. This limit corresponds to a certain size for cubes and cylinders as well. This phenomenon was analysed by taking the difference between two strength ratio values that follow each other with 0.001 m^3. As an example, one of the mixes is shown here with numerical values as well in *Table 22*. The values corresponding to the other mixes can be seen in *Appendix XXI*.

Table 22 *Strength ratios and the differences between them*

Volume [m^3]	Mix 3			
	$\sigma_c(d)/f_c'$ [-]		Difference [-]	
	Cube	Cylinder	Cube	Cylinder
0.0002	1.15	1.14	0.095	0.070
0.001	1.06	1.07	0.039	0.029
0.002	1.02	1.04	0.022	0.017
0.003	1.00	1.02	0.015	0.012
0.004	0.98	1.01	0.012	**0.009**
0.005	0.97	1.00	**0.009**	0.007
0.006	0.96	1.00	0.007	0.006
0.008	0.94	0.98	-	-

The difference values are always continuously decreasing, which shows (from an engineering point of view) that the functions are approaching a limit (asymptotic). To prove that there is a limit for this function, we have performed a simple limit value analysis on *Eq. (23)*. The function was first divided by f_c' (same as in *Figs. 40* and *41*) then the size variable (d) was substituted with 0 and infinite. Both resulted in two constants ($B + \alpha$ and α respectively) as limit value, which shows that there is a real limit value for the function. We have decided to choose this limit value as the first volume, where the difference is smaller than a given threshold value, which, in our case, was chosen to be 0.01 (1 %). Thus, for all the recipes, the limit volume was derived, which is shown in *Table 23*. In average for cubes is about 0.006 m^3 (~182 mm edge length cube), above which, regardless of the increase of the size, the compressive strength of the specimen will not decrease. 182 mm edge length is higher than the standard size (150 mm) but smaller than the maximum sample size used in this study (200 mm). For cylinders, this value is lower, around 0.004 m^3 (137 mm diameter 2:1 ratio cylinder). This value is smaller than the standard cylinder size, thus the standard size is appropriate for material testing. These values (182 mm for cubes and 137 mm for cylinders) are the minimum recommended sizes for compressive strength testing to cancel out size effect.

Table 23 *Strength ratio differences for every mix*

	Strength ratio difference [-]	
	Cube	Cylinder
Mix 1	0.008	0.006
Mix 2	0.006	0.005
Mix 3	0.005	0.004
Mix 4	0.006	0.003
Mix 5	0.005	0.002
Average	**0.006**	**0.004**

By looking at the curves and values in *Fig. 40* and *Fig. 41*, it can be observed that the size effect is more significant in case of lower strength classes. The maximum and minimum values in case of Mix 1 (which has the lowest strength class: C20/25) are 1.32/1.29 and 0.90/0.99 for cubes/cylinders respectively, while in case of Mix 5 (which has the highest strength class: C50/60) these values are 1.13/1.05 and 0.95/0.99. The deviation of the values in case of the higher strength class specimen is significantly lower, as it is shown in *Fig. 44*. This means that the size effect is dependent on the strength of the concrete specimen. It could be caused by the level of inhomogenety of the different mixes. In case of a lower strength concrete, the difference in compressive strength and Young's modulus between the cement matrix and the aggregate is significant, while in case of higher strength, the difference is decreasing. It is also worth mentioning that a lower strength concrete can be produced by many different mixes

(different v/c, h/c, compacting, etc.), while in case of a high strength concrete, there are not that many variations.

Another observation can be made based on the acquired data, which is connected to the first part of this section: size effect is more significant in case of cubes than in case of cylinders. As it was described previously, cylinders above 0.004 m^3 volume can be considered to be equivalent (from a compressive strength point of view), while cubes only above 0.006 m^3. The strength ratios for cubes also have higher variation than the strength ratios for cylinders. In case of a 1:2 ratio cylinder during compressive strength test, the middle 1:1 ratio zone becomes purely compressed (without tension), while in case of a cube, there is no such zone. Therefore, only a fraction of the whole volume of the cube specimen is taking part in the load-bearing; thus, all small failures have higher effect on the compressive strength.

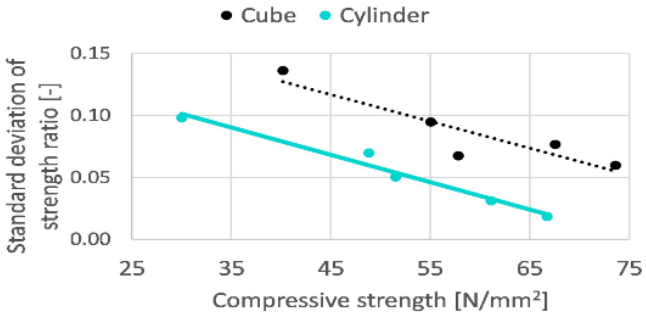

Fig. 44 *Standard deviation of strength ratio of the 5 mixes in function of their standard compressive strength*

5.5 Size effect law applied on parallel bond strength

The above-described algorithm can be applied for the parallel bonds of a DE model. By extending the model in this way, a relation can be given, which describes the relationship of compressive strength and parallel bond strength as a function of specimen size.

As it was discussed earlier in DE models, the parameter that has the highest effect on the compressive strength result is the parallel bond strength. Thus we are proposing a modified version *Eq. (2)* applicable for parallel bond strength. It could be written in the following form:

$$\sigma_{pb}(d) = Bf'_{pb}/\sqrt{1 + d/S} + \alpha f'_{pb} \qquad (29)$$

where B, S, and α are empirical values, as earlier. Based on this model (if the specimen size and the parallel bond strength of the standard size sample are known), the nominal strength of the given sized sample can be determined.

Based on the parallel bond strength results of the numerical experiments, the same type of model equations can be used as it was in case of the compressive strength. It is applicable for all mixes (for cylinders and cubes as well) to estimate the parallel bond strength based on the volume of the sample. The only differences are the values of the *a* and *b* constants (e.g. in case

of Mix 2 for cylinders, a = 19.75; b = 0.128). The model equations were applied as an interpolation to calculate the expected parallel bond strengths for given volumes. The chosen range of volume was divided uniformly into 8 points (corresponding to the same values as in the previous chapter). At those volumes, the parallel bond strength was determined, as it can be seen for Mix 2 in *Fig. 45*, while in case of the other mixes in *Table A-20* of *Appendix XXI*.

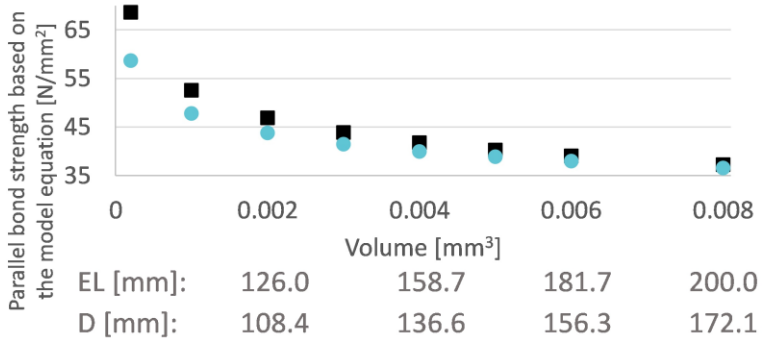

Fig. 45 *Parallel bond strength for different volumes based on the model equation in case of Mix 2 (EL = edge length of the cube samples; D = diameter of the cylinder samples)*

The parameters of *Eq. (29)* was tuned, using the so obtained data as the measured output of the optimization scheme. One of the aims of the research was to apply *Eq. (29)* with different optimized parameter sets to estimate the parallel bond strength of different size specimens. Another aim was to estimate the parallel bond strength of different size cube specimens based on the parallel bond strength measured on a cylinder and vice versa. The notation of the parameter sets will be the same as it was in the previous chapter. For the Cube-to-Cyl and Cyl-to-Cube estimations, an additional step was included in the process. From the standard size cube compressive strength, the standard size cylinder compressive strength was calculated or vice versa using *Eq. (25)*.

The initial conditions were chosen to be the same as previously (the values defined by Kim and Eo (*Kim et al, 1989*) for compressive strength) because there were no available data in the literature. B was chosen to 0.4 [-]; α to 0.8 [-] and S to 50 mm. Then based on *Chapter 3.4*, an optimization process was performed (least-squares method; SSE objective function). The optimized parameters for the different specimen shapes can be seen in *Table 24*.

Table 24 *Optimized parameters based on specimen volume*

Shape	B [-]	α[-]	S [mm]
Cyl-to-Cyl	1.967	0.09	40.698
Cube-to-Cube	1.614	0.101	66.767

In most practical cases the parallel bond strength of a standard size specimen is not known, but rather the compressive strength of the standard size cylinder/cube. So the relationship of the parallel bond strength and compressive strength of standard size specimens was investigated.

It was found that the same linear relation can be written for both cylinder and cube specimens, as it can be seen in *Eq. (30)* and *Fig. 46*. It was applicable for all normal strength concrete mixes with density between 2200 and 2400 kg/m^3.

$$f'_{pb} = 0.79 f'_c \tag{30}$$

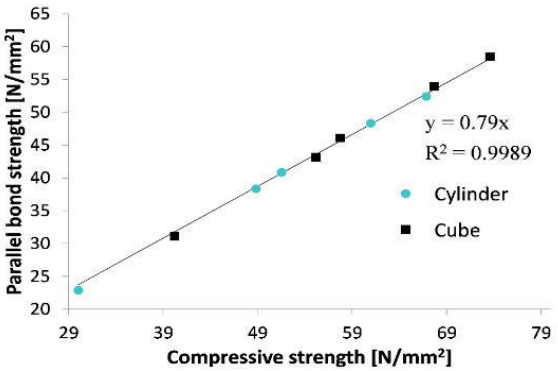

Fig. 46 *Parallel bond strength vs. Compressive strength for standard size specimens*

5.5.1 Estimation model results

The results of the estimation process were evaluated on the basis of $\sigma_{pb}(d)/f_{pb}'$ as the function of the volume. In *Fig. 47*, the results for estimating cylinder strength are shown from the measurements (Mix 1-5) and from the own estimation model. The results show that with the increase of the specimen size, the strength ratio approaches a limit, similarly to the compressive strength, which is the consequence of the linear relationship of the compressive and parallel bond strength. It can be read from *Fig. 47* that the estimation model (Cyl-to-Cyl) strongly correlates to the measurement results, especially in case of larger size specimens. In this evaluation methodology, the Cube-to-Cyl estimation models coincide with the Cyl-to-Cyl models (they apply the same parameter set; only f_{pb}' is different).

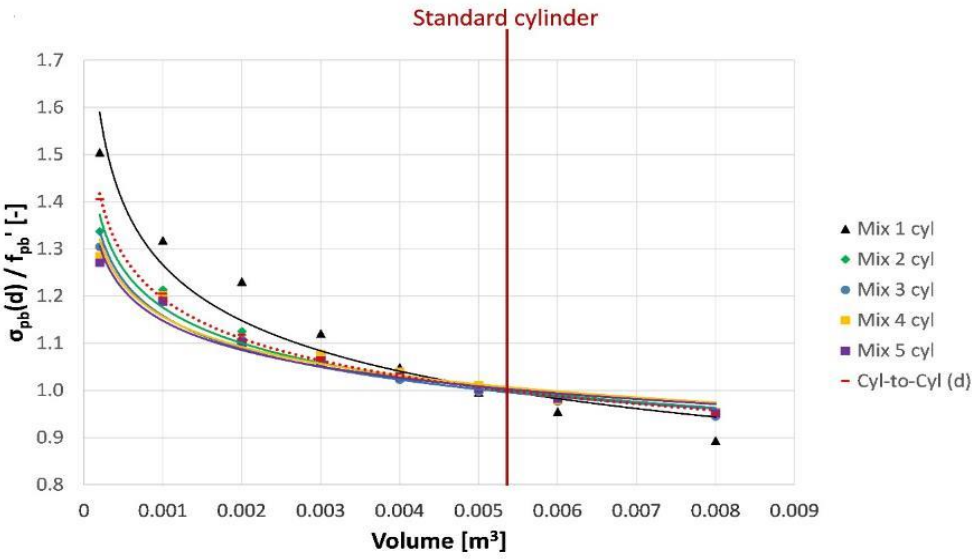

Fig. 47 *Results for estimating cylinder parallel bond strength (red – own estimation models; other – measurements)*

The Cube-to-Cube estimations also show good correlation with the measurement data, similarly to cylinders, as it can be seen in *Fig. 48*. In this evaluation methodology, the Cyl-to-Cube estimation models coincide with the Cube-to-Cube models (same parameter set is used only f_{pb}' is different). The correctness of the models is shown by both *Fig. 47* and *48*; the $\sigma_{pb}(d)/f_{pb}$' ratio is equal to 1 for all models and measurements at the volume of the standard size specimen. *Fig. 47* and *Fig. 48* shows that the size effect is more significant in case of models with lower standard parallel bond strength, analogically with compressive strength as it was mentioned earlier (*Fig. 44*). The maximum and minimum values in case of Mix 1 (which has the lowest strength class: C20/25) are 1.54/1.50 and 0.83/0.89 for cubes/cylinders respectively, while in case of Mix 5 (which has the highest strength class: C50/60) these values are 1.28/1.27 and 0.90/0.95. The deviation of the values in case of the higher strength class specimen is significantly lower, as it is shown in *Fig. 48*. The dependency on size can be traced back to the size dependence of compressive strength on concrete specimens. As it was mentioned earlier in this section, it is caused by the level of inhomogeneity of the different mixes. From the figures, it can also be read that size effect is more significant on cube samples than on cylinder samples. When we take the difference in $\sigma_{pb}(d)/f_{pb}$' for the largest (0.008 m^3) and smallest specimen (0.0002 m^3) in case of cubes (Mix 1:0.71; Mix 2:0.49; Mix 3:0.43; Mix 4:0:40; Mix 5:0.38) the values are always higher than the values in case of cylinders (Mix 1:0.61; Mix 2:0.39; Mix 3:0.36; Mix 4:0.33; Mix 5:0.32). In case of a 1:2 ratio cylinder during compressive strength test, the middle 1:1 ratio zone becomes purely compressed (without tension), while in case of a cube, there is no such zone. Therefore, only a fraction of the whole volume of the cube specimen is taking part in the load-bearing; thus, all small failures have a higher effect on the compressive strength.

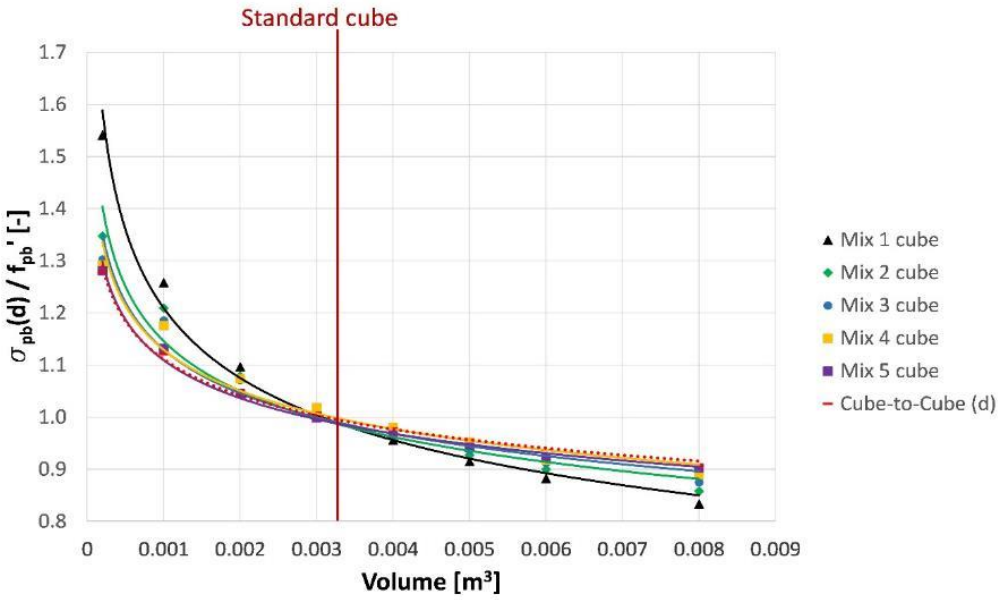

Fig. 48 *Results for estimating cube parallel bond strength (red – own estimation models; other – measurements)*

5.5.1.1 Error analysis

Error analysis was performed to see how accurate the different estimation models are. The parallel bond strength was estimated and compared to the measurement data by using the previously obtained optimized parameter sets. The error in N/mm^2 and in % (based on the standard cylinder/cube parallel bond strength) was calculated for every size, for every estimation model, and for every mix. The results in percentages are shown in *Fig. 49*. Similarly, low average error (2.8%) and maximum error (13.5%) were performed by the Cube-to-Cyl and Cyl-to-Cyl models. The Cube-to-Cube and Cyl-to-Cube models performed somewhat worse in this aspect. The average error of those models can be considered as low, but their maximum error is significant. It has to be noted again that the accuracy of Cyl-to-Cube and Cube-to-Cyl models are also dependent on the accuracy of *Eq. (25)*. It is interesting to point out that in average error, there was relatively small difference between the most accurate model and the least accurate (2.3% difference); however, in case of maximum error, the difference is more significant (16.1%). This analysis reflects that the estimation of cylinder parallel bond strength always shows lower average and maximum error, than the estimation of cube parallel bond strength using these models, as it can be seen in *Eq. (31)*.

$$e_{max,Cube-to-Cyl} \leq e_{max,Cyl-to-Cube} \tag{31}$$

The Cyl-to-Cube model makes the highest average and maximum error as well. However, this conversion is the least important in a practical point of view, as it is rarely used (strength classes are determined based on cylinder strength; it is easier to work with cubes).

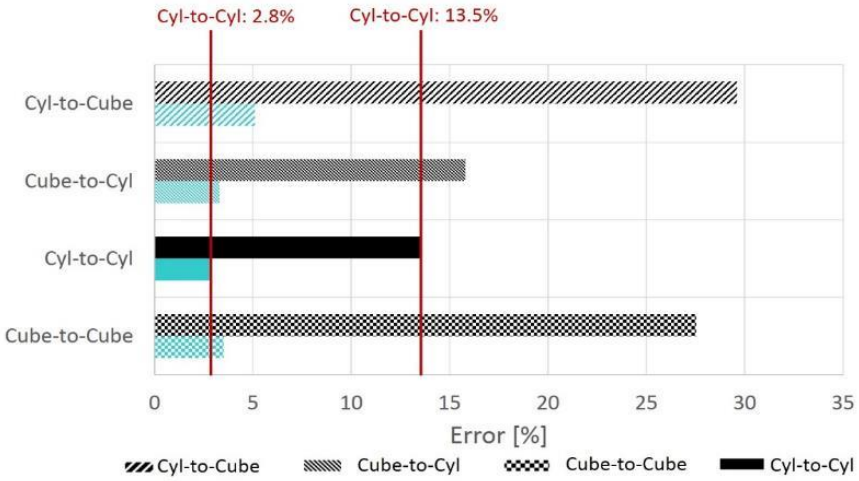

Fig. 49 *Average (cyan) and maximum (black) error of the different estimation models*

It was also investigated that till which size can the model be considered as sufficiently accurate. The aim here is to find the smallest specimen size that can be applied for parameter tuning of a DE model. As it was already mentioned, it could highly increase the productivity of DE modelling. In *Fig. 50* the average error of all models and their standard deviation is shown on the left, while on the right side, the separate models' error is shown versus the specimen size. It can be clearly seen that the best fit is somewhere in the middle of the presented range, which size belongs to a 140-160 mm edge length cube or 120-140 mm diameter cylinder. A limit value was defined based on the compressive strength classes of concrete. In our definition, the model is considered to be accurate until due to the error the investigated concrete's strength class does not change. In the range of normal strength concrete, the smallest difference (in %) between two strength classes are between the C45/55 and C50/60, which is 5%. (The range of normal strength concrete goes from C20/25 till C50/60.) According to *Fig. 50*, the error and its standard deviation become too high around 0.001 m^3 (~100 mm cube or 86 mm cylinder). Thus, it is recommended to use at least a 120 mm cube or 100 mm cylinder to the parameter tuning of a DE model. However, using a specimen with this size makes it possible to tune the parameters even for a 200 mm edge length cube or 170 mm diameter cylinder with acceptable precision. With this significant amount of computational time can be spared. As an example, one iteration of the material genesis process of a 170 mm diameter cylinder takes around 22-24 hours, while for the 100 mm diameter cylinder it is only 5-7 hours. For further details of the effect of particle number on computational time, see *Appendix XIV*.

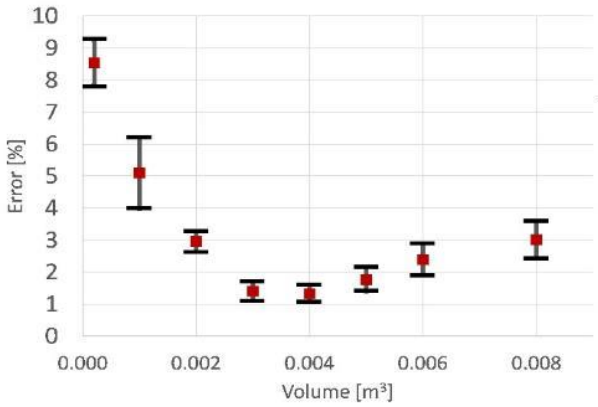

Volume [m³]	Error [%]			
	Cube-to-Cube	Cyl-to-Cyl	Cube-to-Cyl	Cyl-to-Cube
0.000	7.5	10.6	8.6	7.5
0.001	6.9	3.0	3.3	7.1
0.002	2.6	3.4	3.5	2.4
0.003	0.8	1.6	1.6	1.6
0.004	1.3	0.9	1.7	1.4
0.005	2.2	0.7	2.1	2.1
0.006	3.1	0.9	2.6	2.9
0.008	3.7	1.4	3.1	3.9

Fig. 50 *Average error of all estimation models and their standard deviation as the function of volume*

5.6 Closing remarks

In concrete research, the application of smaller size specimens has many advantages, especially for detailed material modelling where with the size of the element the computational time is increasing cubically. Thus, valuable time, cost and effort could be spared, if reliable and accurate models for different size specimens would be available. The main findings of this part of the research are the following:

- The results showed that the laboratory measurements agree to the literature results, namely that the compressive strength is decreasing with the increase of the size of the specimen.
- In case of the smallest specimens (cubes with 50 mm edge length), the deviation of the compressive strength tests was higher compared to the other specimens, but on average they fit to the pattern.
- Based on the size effect law of Bažant, an equation was derived to estimate the compressive strength and the parallel bond strength of different size and shape specimens. The parameters of the equation were optimized against the measurement data using the least-squares method with SSE objective function.
- The Cyl-to-Cyl compressive strength estimation model results showed good correlation with measurement data and with the literature estimation models as well.
- The Cube-to-Cube compressive strength estimation model results also showed good correlation with the measurements, where the currently available literature models had higher errors, sometimes not on the safe side (strength overestimation).
- The Cube-to-Cyl compressive strength estimation model showed also good correlation with the measurements, which could be useful for the industry practice.

- The Cyl-to-Cube compressive strength model was also investigated and compared to the previous ones, it showed higher maximum error.
- Size effect is more significant on concretes with lower strength class (e.g. C20/25) due to the higher level of inhomogeneity of the material. This observation can be made with a different process only considering the laboratory measurement results as well. This observation is also true in case of parallel bonds as well (due to the linear relation of the compressive and parallel bond strength). The size effect on parallel bond strength is more significant in case of lower standard parallel bond strength.
- Size effect is more significant on the cube specimens (higher deviation in strength ratio) than on the cylinder samples, which can be caused by the side ratios of the specimens and the size of the purely compressed zone.
- A limit value for the size was determined for both cube ($0.006\ m^3$) and cylinder ($0.004\ m^3$) specimens, above which the size effect on compressive strength can be neglected.
- A linear equation was defined to estimate the parallel bond strength of a standard size specimen from the compressive strength of a standard size specimen measured in laboratory, independently of its shape (either cube or cylinder).
- Both the Cyl-to-Cyl and Cube-to-Cube parallel bond strength estimation model results showed good correlation with measurement data; however, the Cube-to-Cube model has higher maximum error.
- The error analysis showed that the estimation of cylinder parallel bond strength has lower average and maximum error, than the estimation of cube parallel bond strength using the defined estimation models.
- It was also investigated that which is the smallest size for which the model can be considered as sufficiently accurate to use for parameter tuning and material generation of DE models. It was found that using a 120 mm cube or 100 mm cylinder the compressive or parallel bond strength of a 200 mm edge length cube or 170 mm diameter cylinder can be estimated with acceptable precision. This leads to a significant reduction in computational time.

CHAPTER 6: EFFECTS ON THE MECHANICAL PROPERTIES, DURABILITY AND DE MODELLING

In this chapter, the effect of different aggregate type and size distribution on the mechanical properties and numerical modelling of concrete is investigated. An estimation model is proposed to consider these effects in a DE model. This chapter also presents the results of the experimental program for producing concretes containing CCP as cement substitution material. First CCP is compared against other waste powders, then its dosage and microstructural properties are investigated. The mechanical properties and durability properties of concrete containing CCP are evaluated.

6.1 Effect of aggregate type and particle size distribution

6.1.1 Estimation model to consider aggregate types in a DE model

In the present study, an estimation model is introduced for a parameter of Discrete Element (DE) models, which can be applied as a support function during the calibration process of DE model. The estimation model proposed in *Chapter 5.5* was further developed to be applicable for concretes containing different types of aggregates (crushed stone, quartz gravel and expanded clay) and particle size distributions (from high amount of fines to no-fines concrete). It is highly beneficial in an economical and environmental aspect to apply no-fines concrete, because thus the amount of required cement, which is the most expensive component of concrete, can be decreased significantly. No-fines concrete mix can be obtained when the fine aggregate fraction of a normal concrete mix is eliminated (*Carsana et al, 2013*). The inner structure of a no-fines concrete strongly differs from the inner structure of "normal" concrete. This difference can be well grasped by the aggregate-to-cement (a/c) ratio of concrete. However, this property of concrete is only known, if the mix composition of the given sample is known, which is sometimes not possible (e.g.: if a specimen from a historical building is investigated).

The results of the mechanical response computation from DEM were validated against measurement data. DEM could be a powerful tool to simulate accurately the laboratory tests carried out on concrete samples when it is correctly calibrated. Thus, it may be possible to decrease the number of necessary laboratory tests and substitute them with numerical simulations. In this study, I have been using a nonlinear adaptation (Levenberg-Marquardt) of least squares method with an SSE objective function.

The formulation of the problem is written in the following formula:

$$f_{pb} = f(\rho, f_c) \tag{32}$$

where f_{pb} is the normal strength of the parallel bonds (DE model parameter), ρ is the density of hardened concrete and f_c is the compressive strength measured on real samples.

The proposed equation can be expressed in the following way:

$$f_{pb} = m_R \cdot m_C \cdot m_L(\rho) \cdot m_N(\rho) \cdot m_{Dens}(\rho) \cdot f_c \tag{33}$$

where:

- m_R is a multiplier factor, which describes the relationship of the compressive and the bond strength. Its initial value was derived from the average ratio of the bond strength and compressive strength.
- m_C is a multiplier that takes into account the effect of crushed aggregate.
- m_L is also a multiplying factor, taking into consideration the effect of lightweight aggregate. It is clearly proportional to the density of the material; thus, it was expressed as follows:

$$m_L = \frac{c_L}{\rho} \tag{34}$$

where c_L is a constant value.

- m_N is the no-fines multiplier, which takes into account that only coarse aggregate is present in the aggregate frame. Based on our measurements, this is square proportional to the density of the concrete:

$$m_N = \left(\frac{\rho}{c_N}\right)^2, \tag{35}$$

where c_N is a constant value.

- m_{Dens} is the density factor, which considers the effect of varying density in different mixes:

$$m_{Dens} = \frac{c_{Dens}}{\rho} \tag{36}$$

where c_{Dens} is a constant value.

All multiplying factors and constants are positive real numbers, by definition ($\{m_i,c_i\} \in \mathbb{R}$ & $\{m_i,c_i\} > 0$). There was a training set of measurement results on which the optimization was performed. It was part of the training set that for each concrete, which parameters have to be considered (activeness vector). The parameters that are not "active" for a given material were substituted by 1. For example, in case of the SN mix, the m_R, m_C, m_N and m_{Dens} parameters were active, while m_L was set to equal to 1, as it can be seen in *Fig. 51*.

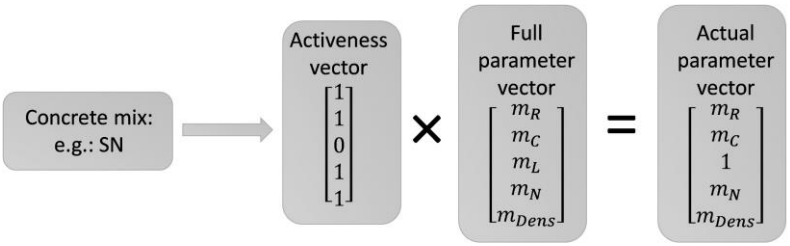

Fig. 51 *Calculation of the actual parameter vector*

By substituting the *Equations (34)*, *(35)* and *(36)* back to *Eq. (33)*, we will get a model which has five parameters that have to be optimized against measurement data. Based on the actual parameter vector of the given concrete mix, the active parameters were considered in the optimization. The importance of initial values was already highlighted in this section earlier. In *Table 25* the initial conditions of the optimization can be seen.

Table 25 *Initial conditions*

m_R [-]	m_C [-]	c_N [kg/m^3]	c_L [kg/m^3]	c_{Dens} [kg/m^3]
1	1	2000	2000	2000

Based on the model introduced in this chapter, using the training data set, the above parameters were optimized. Other factors (size effect, cement type, v/c ratio, etc.) can be found as well, which influence the outcome; however, this study only deals with two of them: particle size distributions and different aggregate types.

6.1.2 Measurement and model results

In *Table 26* the final results (mean values calculated from the individual samples) are summarized: density and compressive strength from the laboratory measurements, normal strength of the parallel bonds from the DE model and a/c ratio from the image processing and from calculations. The notation of the samples is described in *Chapter 3.5.2.1*.

Table 26 *Results of the experiments (compressive strength and density), the numerical simulation (normal strength of parallel bonds) and the image processing (a/c ratio)*

Notation	Material/model property		
	Compressive strength f_c [N/mm^2]	Density ρ [kg/m^3]	Normal strength of parallel bonds f_{pb} [N/mm^2]
GC	26.7	2257	20.8
GA	32.0	2343	24.5
GN	22.5	2095	21.2
SC	53.3	2364	42.3
SA	40.6	2430	32.4
SN	10.7	1854	8.9
LN	16.0	1200	17.5

The SC sample reached the highest compressive strength (53.3 N/mm^2) in total, while (as it was expected) among the quartz gravel samples the GA sample has the highest compressive strength (32.0 N/mm^2). In this mix, a higher amount of fine aggregate was applied that is

advantageous in case of quartz gravel as aggregate. Both for crushed stone and for quartz gravel, the no-fines mixes (GN & SN) have lower compressive strength, due to their non-ideal aggregate frame and low cement amount. However, it has to be mentioned that these mixes are quite beneficial economically. It is worth to mention that the LN mix, which has a more ideal aggregate skeleton (compared to the other no-fines samples), has reached a relatively high (e.g.: higher than SN) compressive strength. This behaviour can be explained by the more ideal structure of the spherical-shaped particles of the lightweight aggregate compared to the non-ideal structure of the other two no-fines samples.

From a density aspect, not surprisingly the no-fines samples have smaller body densities with 10-20% compared to the other quartz gravel and crushed stone samples. The other gravel and crushed stone sample's (GC, GA, SC and SA) densities are fairly close to each other. In general, the crushed stone samples have slightly higher density, and they have lower porosity as well, due to the shape of the aggregate.

12 or more iteration steps (*Fig. 8*) in the simulation were needed to reach the final values of the normal strength of parallel bonds. By using these f_{pb} values in the model, the simulated compressive strength test resulted in identical compressive strength values to the measured values. There is no obviously visible relationship between the three kinds of data. The estimation method introduced in *Chapter 6.1.1* was applied to the data, and the parameters (*Table 25*) were optimized to fit these data. The best-fitting parameters are shown in *Table 27*.

When the optimized parameters (*Table 27*) were applied to the training data, the mean error of the bond strength estimation was found to be lower than 2% (max error was 3.5%). By further optimizing the parameters, it was not possible to found a better fitting on such a wide range of concrete mixes. However, the accuracy of the uniaxial compressive strength test is about 5%; thus, this accuracy for estimation is acceptable. Another larger (test) data set was used to test the derived equation (*Eq. (33)*). The test data set contained various quartz gravel, crushed stone and lightweight aggregate concretes from earlier measurements of the authors that can be seen in *Appendix XXV*. As it was expected, the estimation error was higher than it was in case of the training data set, but only slightly (10%). It is still an acceptable level to estimate the initial value for an iteration process (the calibration of a DE model). And it was observed that the model was not accurate in cases when two different type of aggregates (like lightweight aggregate with quartz gravel) were combined in the same mix. When the initial value of the bond strength was chosen randomly (without any estimation), then at least 12 iteration steps were needed for a correct model calibration. By using the estimation model

introduced in this paper, the number of iterations needed for calibration decreased to maximum 4. Thus the computational effort needed to calibrate a DE model decreased significantly, and this leads to the direction of a more productive and efficient application of DE modelling.

Table 27 *The optimized model parameters*

m_R [-]	m_C [-]	c_N [kg/m^3]	c_L [kg/m^3]	c_{Dens} [kg/m^3]
0.845	1.04	2022.9	2438.1	2153.9

6.2 Effect of supplementary and waste materials

6.2.1 Comparison of CCP against other recycled powders

In the first part of this research, four different types of concrete mixes were applied, one with air-entraining agent, one with cellular concrete powder, one with clay brick powder and a reference mix. The objective of the research was to investigate the effect of different waste materials applied as supplementary material on the strength and durability of normal strength concrete. The performance of the mixes with waste materials was compared to a reference mix and a mix with air-entraining agent. Besides the basic properties of concrete, the compressive strength and the freeze-thaw resistance were measured. A reference concrete was designed, which has appropriate compressive strength (C25/30) and low resistance against freeze-thaw. In the literature, two methods are the most widespread to increase the durability of concrete:

- the application of air-entraining agents,
- or the increase of the density of concrete with small size powders.

In this part of the study, these methods were applied and compared to CCP.

6.2.1.1 Compressive strength test results

The uniaxial compression test results show that, compared to the reference mix, the air-entraining agent significantly decreases the compressive strength of the concrete (30%), while the cellular concrete powder increases the strength (37%), as it can be seen in *Fig. 52*. The clay brick powder has a negligible effect on the compressive strength.

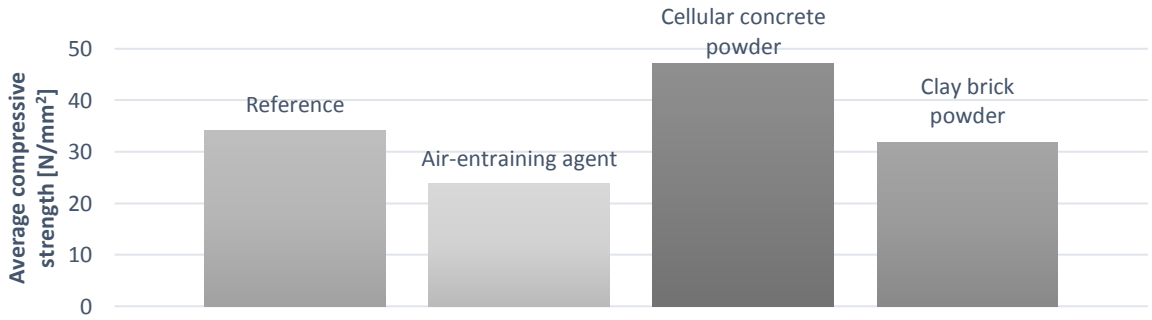

Fig. 52 *Average 28 days compressive strength of the concretes*

Besides the compressive strength, the air-entraining agent also decreases the density of concrete, while the waste materials have a negligible effect on the density.

In a durability point of view the mix containing air-entraining agent and the mix containing CCP were the most advantageous. CCP highly increased the frost and freeze-thaw resistance of the samples. The clay brick powder had no significant effect on the durability. The durability test results and their discussion can be seen in *Appendix XXVI*.

As a conclusion, it can be stated that the performance of concrete can be improved by the application of waste material additives like cellular concrete powder. However, the optimal dosage of cellular concrete powder still requires further investigation.

6.2.2 Detailed investigation of CCP in powder form

6.2.2.1 Objectives

The objective of this part of the research is to investigate the effect of CCP on normal strength concrete (NSC) and on high strength concrete (HSC), by using different concrete mixes. It is aimed to find a roughly optimal quantity of CCP in concrete and compare it to SCMs in strength and durability point of view. The dosage of SCMs or CCP could be very important because above a given amount, SCMs reduce the performance of both strength and durability parameters (*Borosnyói, 2016*). In that study, SCMs applied in concrete with different dosages were investigated at various ages. High strength concrete (HSC) mix (C60/75) was used that contained maximum 17% (compared to the mass of cement) SCM. The applied SCMs were silica fume, metakaolin and the mix of them. The major outcomes were the following:

- the optimal amount of SCM is close to 10%, which was also found in other studies (*Ženíšek et al, 2016*),
- the strength increase, caused by the SCMs, is the highest at 28 days of age. After that, in all cases, a proportionally smaller strength increase was measured.
- The mixture, when the two SCMs were mixed, performed better than the reference mixture, but not better than the SCMs applied singly.

Based on the findings of this study in my research, I also applied maximum of 17% of supplementary material, and I have compared the performance of CCP with a traditional SCM and also investigated their combined use.

6.2.2.2 Research plan

The research plan for this part of my research to achieve the stated objectives was the following:

1. Firstly, the effect of CCP was investigated on cement mortars containing different amount of CCP or MK. Here the aim was to see clearly the effect of CCP without any other possible disturbances.
2. In the next step, a given percentage of cement is substituted by CCP in normal strength concrete. The mixes with different amount of CCP are compared to a mix containing MK and another containing the mixture of CCP and MK.
3. Then a high strength concrete mix (same as in the study of *Borosnyói, 2016*) is used, and CCP is mixed to the concrete mix, by substituting a given amount of cement. It is also compared to a mix containing MK and another containing the mixture of CCP and MK.
4. The microstructure of CCP and of the concrete mixes are analysed using thermogravimetric analysis and scanning electron microscope to get an understanding of the observed phenomena.

All the samples described in step 2-4 are tested for compressive strength, frost resistance and freeze-thaw resistance, as it can be seen in *Fig. 53*. The samples of step 1 are subjected to compressive strength test. Besides these, thermogravimetric analysis was performed on all the samples.

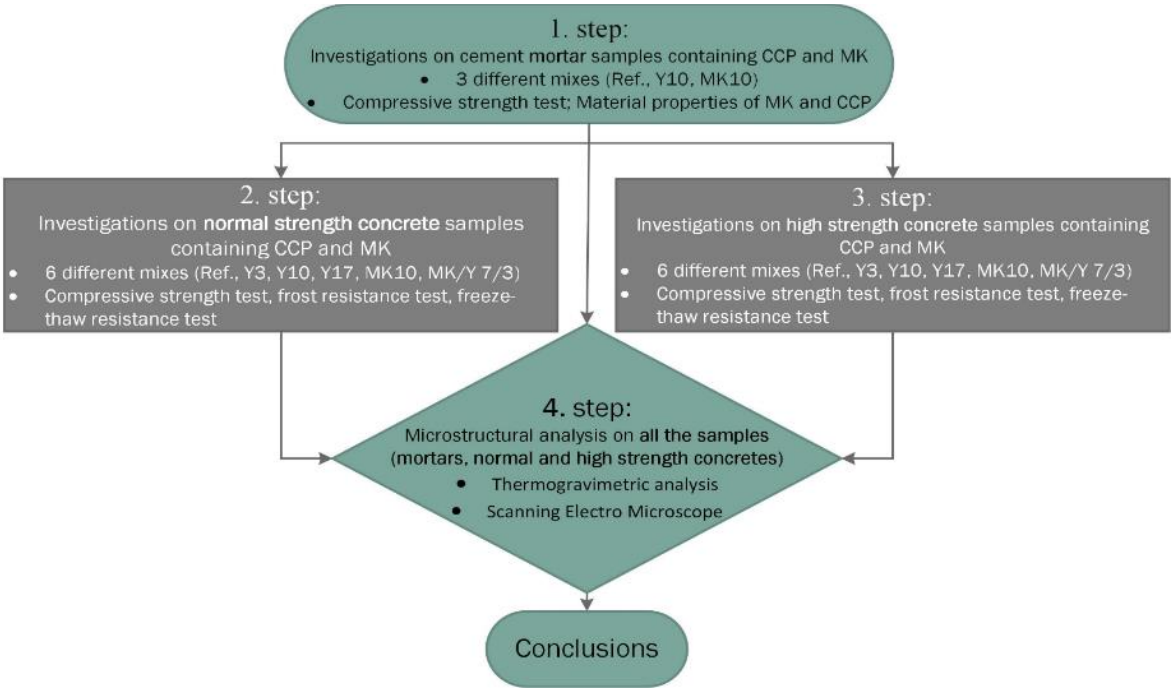

***Fig. 53** Research steps flowchart of the detailed investigation of CCP*

6.2.2.3 Results of long-time measurements on mortars

In the present chapter, the results of the laboratory tests are presented and discussed. First, the effect of CCP on cement mortars was investigated as it was mentioned in *Chapter 6.2.2.2*. The results in different ages can be seen in *Table 28*.

Table 28 *Compressive strength results of the mortar prism samples*

	Compressive strength [N/mm^2]				
	2 days	**7 days**	**28 days**	**90 days**	**180 days**
Reference	53.1	72.6	74.2	76.4	86.1
Y10	47.3	65.4	73.9	83.4	84.8
MK10	50.3	68.6	72.0	94.0	104.0

The results show (*Table 28*) that in early ages all the added materials (CCP, MK) decrease the compressive strength, however, after a given time (~90 days) their effect on strength becomes positive. The thermogravimetric analysis shows that in the curves of the derivatograms presented in *Fig. 54*, there are three characteristic, mass-changing endothermic transformations:

1. peak: the evaporation of the unbounded water content of the sample furthermore the loss of gypsum and ettringite phase in the range of 80 to 240 °C,
2. peak: the decomposition of the calcium hydroxide phase with loss of water at 430-540 °C (*Ibrahim et al, 2004*): $Ca(OH)_2 \rightarrow CaO + H_2O$,
3. peak: mainly carbon dioxide loss of calcium carbonate, which was the result of the carbonation of calcium-hydroxide, above 600 °C: $CaCO_3 \rightarrow CaO + CO_2$.

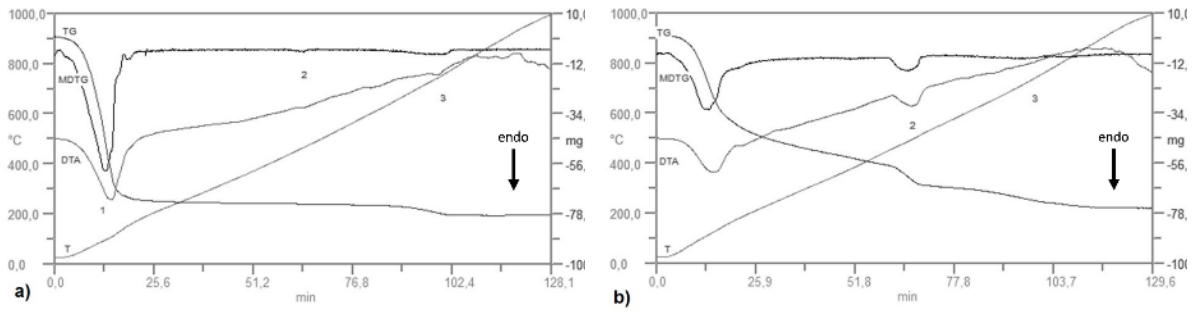

Fig. 54 *Result of the TG analysis (Time vs Temperature and Mass change) of the Reference mortar after mixing (0 days – **a)**) and at 180 days (**b)**) of age*

The decrease of the first peak's size clearly shows the decrease of unbounded water content (mixing water) in the sample and indicates the increase of $Ca(OH)_2$ content. Similar behaviour was observed on the Y10 and MK10 samples as well.

The calculated mass losses of the above mentioned three degradation processes are listed in *Table A-41* of *Appendix XXVII*. Based on the loss of water resulting from the decomposition of calcium hydroxide, the amount of portlandite present in the system at a given age was

calculated, which is also shown in *Table A-41* of *Appendix XXVII*. The table highlights the mass loss in the range of 600-800 °C that is the carbon dioxide loss of calcium carbonate, which was indicated by the 3rd peak mildly observable in *Fig. 54* as well.

In a strength point of view, until 28 days of age, the Reference has the highest compressive strength. Until 28 days of age, as the $Ca(OH)_2$ content increasing, the strength increases as well in all mixes with similar tendency. Until the age of 28 days, the strength of the three mixes increases similarly. The 28th day's compressive strength, which is used in the standards, is almost the same for all the mortars. After 28 days the compressive strength of the Y10 mortar increases with the same rate as the Reference mix and their $Ca(OH)_2$ content reaches the same level, as it can be seen in *Fig. 55*. Meanwhile, in case of the MK10, the rate of $Ca(OH)_2$ content increase is slighter compared to the other two mortars; however, its compressive strength is increasing with a higher rate than previously. In that phase, the effect of the supplementary material is more significant than the hardening of cement. Based on that it can be seen that the CCP is not working similarly to a traditional SCM (metakaolin), its behaviour is closer to a filler material. The figure shows that after 90 days of age, the $Ca(OH)_2$ content of MK10 is slightly decreasing. The reason behind it is that MK has high reactivity with $Ca(OH)_2$, but low reaction rate, thus it requires more time to form CSH crystals that integrate into the crystal structure of concrete. In case of Y10, this behaviour cannot be seen, which also indicates that CCP does not work as a traditional SCM; there is no hydration of CCP. However, CCP does not decrease the $Ca(OH)_2$ content in long term; thus the alkalinity of the mix remains unchanged, which is advantageous against corrosion when the concrete is applied together with steel reinforcing bars. It means that CCP can be used in higher amount compared to MK. Based on the previous experiences of the authors, from MK, more than 20% is not recommended, because it can highly decrease the alkalinity of the concrete.

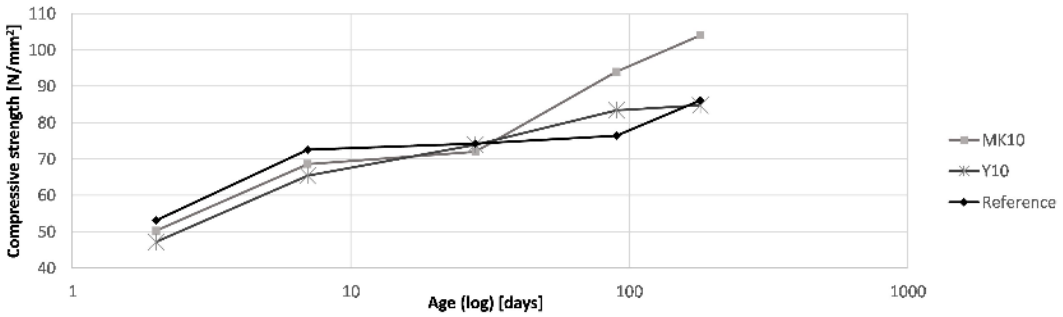

Fig. 55 *Compressive strength of the Reference, MK10 and Y10 mortars at different ages*

The density and flexural strength measurement data were recorded as well, but the results did not indicate any finding.

6.2.2.4 Compressive strength results of the concrete samples

6.2.2.4.1 Normal strength concrete with CCP and MK substituting cement

As it was mentioned in *Chapter 6.2.2.2*, it was investigated, what effect the CCP has, if it is added to the mix of a normal strength concrete. The C20/25 concrete was chosen to be used in the experiments, because on a concrete with relatively low compressive strength and low frost resistance, the effect of CCP could be significant and easily observed. CCP in different amounts was mixed to the reference mix by substituting a given amount of cement. Based on literature data (*Borosnyói, 2016*) from 3 to 17% of the cement amount was substituted. In *Fig. 56* the compression test results are presented, which show that even a small amount (3%) of CCP could increase the compressive strength of NSC. With the increase of the amount of CCP in the mix, the compressive strength is increasing as well, until a given point around 10%. 17% of CCP is already showed less advantageous performance, than the 10%, which increased the compressive strength with 34%. Based on the laboratory tests, the Y10 mix could be called as a rough optimum. Similar value for SCMs (metakaolin and silica fume) was found in (*Borosnyói, 2016*). It is important to see that the Y10 mix increased the strength, and it also decreased the amount of cement in the mix by 10%, which in large scale could be economically highly beneficial.

The final aim of this part of the research was to determine whether CCP could be used as an alternative to traditional SCMs or not. Therefore, MK (a typically used SCM) was mixed to the reference mix. 10% (substituting cement) dosage of MK was applied, based on the final conclusions of (*Borosnyói, 2016*). Besides that, the interaction of the MK and CCP was tested. *Fig. 56* shows that the MK10 was the most advantageous, it increased highly (by 61%) the compressive strength of NSC. The mix of the CCP and MK increased the strength as well, however not as much as the MK10 mix. Comparing to the Y10 mix, the MK10 mix is still superior; however, CCP is a freely available construction waste, which does not require any preparation before mixing, while nowadays metakaolin is produced in factories.

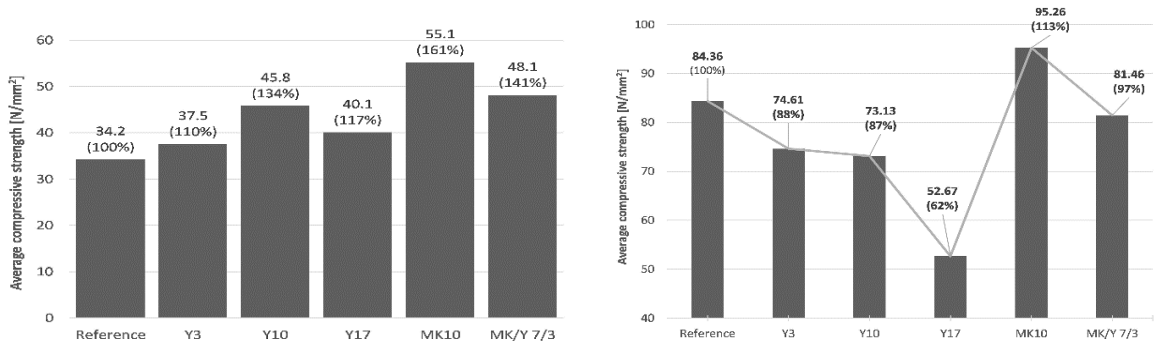

Fig. 56 *Compressive strength of the* ***normal (left) and high (right) strength*** *concretes if cement substituted by CCP or by MK in different amounts (average 28 days)*

The impressive performance of the CCP could be explained by its form, which is a fine powder (made of a cement-based material) that increases the specific area of the aggregates and works as a filling material (see *Chapter 6.2.2.3*). CCP came to the laboratory in powder form, and its density was close to the density of the applied cement. By adding this fine powder to the concrete mix, a more favourable aggregate frame is developed, which contains more fine particles. At this w/c ratio, CCP decreased the porosity of the concrete as well. This physical effect is a reason behind the advantageous performance of the mixes containing CCP. The maximum strength increase was 34% (Y10 mix), which was possible using a filler material (CCP). Most SCMs work as a filling material too, and their particle size is smaller than the particle size of cement. It is not the case for CCP, which from this standpoint could not be considered as a real SCM. Nevertheless, CCP is still increasing the compressive strength of concrete. It would be interesting to see its effect if it is pulverized to the particle size of traditional SCMs. Traditional SCMs has a chemical effect as well (their reaction with $Ca(OH)_2$), which was not observed in case of CCP and can be explained by the size of the CCP particles that are an order of magnitude higher than the MK particles. MK was able to increase the strength to a greater extent (61%) because it works as a filler material and as a hydraulic component as well. The MK/Y 7/3 mix had slightly better performance than the Y10 mix, but worse than the MK10 mix. The amount of filling material was the same here (10% was substituted), but only a lower amount (7%) was a hydraulic material. Based on literature (*Borosnyói, 2016*), it is advisory to apply at least 10% to reach beneficial results. If only 7% of cement is substituted by MK, it is not able to exert its favourable effects, or these effects are perceivable only later (not at the age of 28 days).

To get a better understanding of the processes taking place in the material, a thermogravimetric (TG/DTG/DTA) analysis was performed on CCP. In *Fig. 57* the result of the thermogravimetric measurements performed on CCP can be seen. In the figure, an exothermic

peak is visible around 110 minutes (700 °C). Cellular concrete was autoclaved above 180 °C, and there tobermorite ($C_5S_6H_5$ - a special type of CSH) was developed, which favourably affects the strength of concrete. The ideal CSH frame of tobermorite, as a filling material, increases the strength of concrete, as it was observable in the compressive strength measurements.

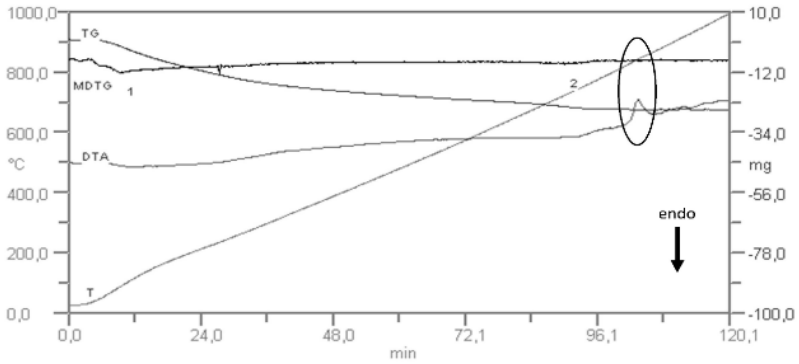

Fig. 57 *Result of the TG measurements on CCP (Time vs Temperature and Mass change)*

The surface topography was investigated by Scanning Electron Microscope (SEM) method, to have a picture about the microstructure of CCP. As it can be seen in *Fig. 58*, the size of fine particles is within the range of sizes of an ideal filling material. However, larger particles can be seen as well, which contain pores that decrease the strength, although it could be advantageous in a frost resistance point of view. These particles can absorb water into their capillary system, which later works as an internal curing during the hardening of concrete.

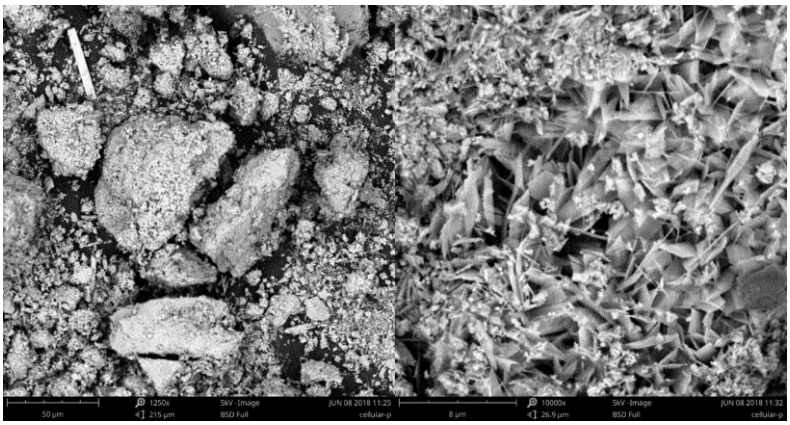

Fig. 58 *SEM of CCP at 1250x (left) and 10000x (right) magnification*

6.2.2.4.2 High strength concrete with CCP and MK substituting cement

The previous investigations were repeated on a high strength concrete (used as reference mix) as well. The same mix design for the reference mix was used as in (*Borosnyói, 2016*). This mix produced a C60/75 class concrete. In this case, by the increase of the amount of CCP, the compressive strength decreased. In *Fig. 56* it can be seen that the decrease until 10% of CCP is not so significant (almost the same in case of the Y3 and Y10 mixes). In case

of the Y17 mix, the strength drop was much higher, of 62% of the strength of the reference mix was reached by the Y17 mix. When MK was added to the mix, it was still able to increase its strength (by 13%), however not as significantly as in case of the NSC. The MK/Y mix slightly decreased the compressive strength, as it can be seen in *Fig. 56*.

In the work of Borosnyói (*Borosnyói, 2016*), the MK10 mix performed even better. There 110.42 N/mm^2 compressive strength was measured on that mix at 28 days of age. The difference in the results presented in the paper of Borosnyói (*Borosnyói, 2016*) and in the present case could be explained by the different quality of MK because the reference mix compressive strengths were very close to each other.

While in case of NSC, the CCP had a positive effect on strength, in case of HSC, this benefit cannot be observed. This can be caused by the phenomena observed in the literature (*Fenyvesi and Jankus, 2015*) that if the normal aggregate is substituted by recycled cellular concrete, the sulphate content is higher, which can lead to a sulphate swelling that leads to cracking. In the present case, part of the cement amount was substituted by cellular concrete. This relatively low amount of substitution caused sulphate swelling as well. In case of NSC, which has higher porosity, this swelling has a positive effect by decreasing the porosity. The swelling particles fill the pores, and in the vicinity of the small CCP particles, only small forces arise that cannot cause severe damage in the concrete. However, in case of HSC, where the porosity is much lower (low amount and size of pores), there is no room for swelling, and higher forces (due to restrained deformations) arise, leading to the failure of the material. As it can be seen in *Fig. 56* the more CCP is added, the higher the strength decrease was, which can be explained by the higher amount of swelling material. This explains why the MK/Y mix has significantly lower strength as well compared to the MK10 mix.

This could explain, why in case of NSC, the Y10 mix had the best performance. While in case of the Y3 mix, the amount of CCP is not enough to fill the pores and in case of the Y17 mix, the amount of CCP is too high, the Y10 mix contains just enough CCP to fill the pores, but not too much to cause high forces inside the material. Based on that, it can be concluded that the optimal CCP amount is dependent on the porosity of concrete. In the present case, this optimum is around 10% for NSC. If the porosity of the concrete is too low (HSC), the substitution of cement with CCP cannot be advantageous in a compressive strength point of view.

The results of the durability tests can be seen in *Appendix XXVI*. In short the frost resistance results showed that in case of NSC among the mixes containing CCP the Y10 is the most superior and both mixes containing MK increased the frost resistance significantly. In case of

HSC with the increase of CCP the compressive strength started to decrease. The freeze-thaw resistance results in case of NSC showed the beneficial effects of CCP. All mixes containing CCP and/or MK decreased the weight loss. The most advantageous was the Y3 mix. Its performance was closely followed by the Y10 and MK/Y 7/3 mixes. In case of HSC except the Y17 mix, all other mixes were highly advantageous. As a conclusion in a durability point of view the application of CCP can be advantageous if it is applied with correct dosage.

6.2.3 DE modelling of concretes containing potential SCMs

The concrete mixes of *Chapter 3.5.2.3.2* and their compressive strength test have been modelled using DEM. This part of the study does not provided new scientific results, thus its results can be read in *Appendix XXII*. The main findings of the study are also presented in *Chapter 6.2.5*.

6.2.4 Effect of CCP and MK on the hardness of cement mortars

The effect of CCP and MK on the hardness of cement mortars were investigated as well. This part of the study does not provided new scientific results, thus its results can be read in *Appendix XXIII*. The main findings of the study are also presented in *Chapter 6.2.5*.

6.2.5 Closing remarks

The main observations and findings are the following:

- CCP works as a filler material (physical effect), not as a traditional SCM, like MK (chemical effect).
- The amount of $Ca(OH)_2$ is the same in case of the Reference mortar and in case of the Y10 (10% substitution of cement by CCP) mix, which indicates that there is no hydration of CCP during the hardening of concrete.
- CCP was found to be able to increase the compressive strength of normal strength concrete, which can be explained by the filling effect of the optimal size particles of CCP.
- The optimal dosage (considering compressive strength and maximum possible dosage) of CCP in case of normal strength concrete is around 10% of the cement amount.
- Compared to MK, CCP was less advantageous from strength point of view; however, it has to be taken into account that CCP is a freely available construction waste and its usage comes with environmental and economic benefits.
- In case of high strength concrete CCP decreased the compressive strength, while MK was still beneficial, that can be explained by the sulphate swelling of CCP that cause microcracks in the material if its porosity is too low.

- CCP was found to be highly advantageous to increase frost and freeze-thaw resistance of normal strength concrete. The optimal dosage of CCP was for frost resistance around 10%, while for freeze-thaw resistance around 3%.
- On high strength concrete, the only real advantage of CCP was the decrease of mass loss during the freeze-thaw resistance tests (with low dosage). MK performed similarly on freeze-thaw test.
- Based on the SEM analysis, CCP introduces optimal sized air-bubbles in the concrete and fine particles to decrease the number of disadvantageous pores.
- Thus, in overall, the optimal application dosage of CCP is 10% that substitutes the maximum amount of cement, but still advantageously influences the strength and durability parameters of concrete.
- The hardness test results from both Brinell and DSI test unanimously indicated that on a higher load level (4375 N in the present case), the standard deviation of the results (indentation diameter / Brinell hardness) is lower. In case of MK10, the change in the compressive strength (compared to the reference) was followed by the hardness test results. However, in case of the Y10 mortar, the compressive strength decreased, while the measured Brinell hardness increased. This can be explained by the filler effect of aerated concrete powder, which increased the surface hardness of the samples.
- The hardness results were analyzed on an indentation energy basis, using the data available from the DSI tests. The analysis showed that all materials could be considered to be elasto-plastic material. It was found that the aerated concrete powder has no effect on the total indentation energy, while the metakaolin increases it, which correlates with its hardness values compared to the reference mix.
- The analysis also highlighted that the change in the hardness value is connected to the elastic indentation energy, while it is seemingly independent from the dissipated (plastic) indentation energy. This indicates that the change in the compressive strength caused by additives influences the elastic properties of the material.
- The DE modelling of concretes containing CCP and MK showed that the powders does not affect the relation of compressive strength and parallel bond strength and thus the model of *Chapter 3.3.2* can be applied for these materials as well.

In this chapter, it was shown that CCP in fine powder form (d_{max} < 0.09 mm) with correct dosage (+10% (m/m to the amount of cement)) can increase mechanical and durability characteristics of NSC. Based on that, the application of CCP powder as filling material is a

suitable way for recycling. CCP has many similarities to other SCMs like it has high specific surface area and contains CSH crystals. These crystals can integrate with the concrete's crystal skeleton and strengthen it. It was not proven that CCP takes an active role in the hydraulic processes during hardening of concrete, but it was seen that its positive effect depends on the particle size of CCP. If the particle size is larger than 0.09 mm, the positive effect of CCP cannot be seen. Particles under this size could only contain nano pores, which are related to CSH phases (*Schober, 2011*).

CHAPTER 7: NEW SCIENTIFIC RESULTS

7.1 New scientific results I [1, 2, 3, 5, 6, 7, 9]

New scientific results hardness of porous construction materials

7.1.1 I have confirmed through laboratory experiments on porous construction materials that the relationship between the loading force and the square of the residual indentation diameter is linear during ball indentation tests. Consequently, the exponent n in Meyer's power law is exactly 2 for porous construction materials. The multiplication factor a in Meyer's power law is material-dependent, and can be determined individually for each porous construction material [1][2]. I have confirmed that a peak value is observable in the Brinell-hardness when represented as a function of the loading force [1][2]. My observations confirm and extend the validity of a hypothesis given about this peak for concretes, to other porous construction materials.

7.1.2 I have confirmed through laboratory experiments on porous construction materials that the DSI method is applicable, and provides a robust tool to increase the precision of deformation readings (both for maximum and residual indentation diameters) and makes the indentation energy based hardness analysis possible. I have confirmed that the indentation energy has much closer connection to the mechanical parameters (Young's modulus, compressive strength) than the indentation diameter based on Brinell tests. I have defined a linear relationship between the peak Brinell-hardness and the ratio of the total and elastic indentation energy, and I confirmed its validity for plastic and elasto-plastic porous construction materials [1][2] [6][7].

7.1.3 I have confirmed through numerical experiments on concretes that Discrete Element (DE) models can be constructed to describe both the linear relationship between the square of indentation diameter and loading force during ball indentation tests and the peak value of Brinell-hardness represented as a function of the loading force [3][5][6][7][9].

7.2 New scientific results II [20]

New scientific results about size effect on compressive strength of concrete

7.2.1 I have developed a new algorithm that can provide the compressive strength of normal strength concretes (C20/25-C50/60) in the range of 2200-2400 kg/m^3 body density for standard test specimens (150 mm cube or ∅150/300 mm cylinder) with acceptable accuracy.

7.2.2 I have confirmed through laboratory experiments with normal strength concretes on a wide range of geometry of cylinder and cube specimens that the size effect (defined as the specimen compressive strength related to the strength of the standard size specimen) is

higher for concretes of lower strength and lower for concretes of higher strength. The strength ratio shows a linear relationship over the studied range of strength (C20/25-C50/60) [20] I have also confirmed experimentally that the size effect is more significant on cube specimens than on cylinder specimens in the studied range of strength (C20/25-C50/60).

7.2.3 I have confirmed through laboratory experiments that a limiting specimen volume can be found for both cube (0.006 m3) and cylinder (0.004 m3) specimens, above which the size effect on compressive strength can be neglected (i.e. less than 1% related to the standard compressive strength) [20]. I have confirmed through numerical experiments and defined the value of the smallest specimen size for which a DE model can be considered as sufficiently accurate for parameter tuning and material generation of DE models as well as to predict specimen size effect.

7.3 New scientific results III [13, 17, 20]

New scientific results about the consideration of the aggregate type and size distribution in the modelling of compressive strength test of concrete using DEM

7.3.1 I have confirmed through numerical experiments on normal strength concretes (C20/25-C50/60) in the range of 2200-2400 kg/m^3 body density that a linear relationship exists between the normal strength of parallel bonds in a DE model and the measured mean compressive strength of standard specimens (150 mm cube or ∅150/300 mm cylinder) [20].

7.3.2 I have developed a new parameter optimization based estimation algorithm for the normal strength of parallel bonds in a DE model based on the measured compressive strength of concrete. The algorithm takes into account the effect of different aggregate types and particle size distributions [13] [17].

7.4 New scientific results IV [11][12][14][18][19]

New scientific results about incorporating unprocessed waste powder materials with normal strength concrete as a cement replacing materials

7.4.1 I have confirmed through laboratory experiments that recycled cellular concrete in fine powder form can improve the mechanical and durability characteristics of normal strength concrete (C20/25-C50/60). Based on microstructural analysis I have confirmed that CCP swells during hardening in a cementitious environment. I have confirmed that the magnitude of swelling depends on the CCP particle size and can lead to the formation of microcracks in the matrix. I have confirmed that below d_{max} = 0.09 mm particle size no microcrack formation occurs. I have determined the optimal dosage of CCP (10% (m/m) related to the mass of cement) to achieve the advantages of CCP.

CHAPTER 8: FUTURE PERSPECTIVE

This thesis introduces a variety of further research possibilities that can extend it.

1. DEM
   a. Using DEM to model other regularly used material testing methods, which require advanced equipment and a lot of preparations, before they can be performed like Young's modulus test or the direct or cyclic pull-out tests. For the latter two solutions are under development by the author of this thesis. The short description of the solution is the following: If the bar can be assumed to be rigid during the test (which is a reasonable assumption), it is possible to model the bar either as a clump (rigidly connected spheres), but also (and preferably) as a wall. If a CAD definition of the bar is available, then it could be exported as an STL file (maybe some manipulation will be required to have a manifold data-structure). A fixed velocity could then be imposed on this bar-wall, and the reaction force measured with a history. The issue then will be to use a proper contact model to handle the interaction between the concrete balls and the bar (maybe a custom model shall be developed), as well as use a reasonable resolution to capture the interactions with the "grooves" of the bar.
   b. Another DEM related topic which was studied (laboratory measurement carried out) but not included in detail in this thesis is the modelling of lightweight aggregates using DEM.
2. CCP ➔ CCP has been proven to be a waste material, which has the potential to be used in structures. As a next step, structural elements (e.g. reinforced concrete girders) shall be cast from concrete (that utilizes CCP), and they shall be tested for in various loading cases.
3. Hardness testing
   a. Hardness testing of concretes containing SCMs or waste materials, using DSI test methods. This topic was also covered by the laboratory tests of the author, but the results are not included in this thesis.
   b. Hardness testing of lightweight aggregate concretes. Using different type of lightweight aggregates, it shall be tested that hardness test methods are working on lightweight aggregate concretes or not. This topic was also covered by the laboratory tests of the author, but the results are not included in this thesis.
   c. Based on the loading-unloading curves of the DSI test an expression shall be defined between the Young's modulus or the compressive strength and the total/plastic/elastic energy of the material, which is usable by practising engineers. Thus using the results of this theses from the DSI method, the compressive strength could be estimated.

LIST OF PUBLICATIONS

[1] Szilágyi, Katalin; Borosnyói, Adorján; **Gyurkó, Zoltán** (2012). Kőszerű anyagok statikus keménységvizsgálata, *Engineering Geology Rock Mechanics Conference 2011*, pp. 297-312. , 16 p. ISBN 978-615-5086-04-5

[2] Szilágyi, Katalin; Borosnyói, Adorján; **Gyurkó, Zoltán** (2013). Static hardness testing of porous mineral-based building materials, *Építőanyag – Journal of Silicate Based and Composite Materials*, 65:1, 6-10, 5 p. ISSN 00 13-970x, http://dx.doi.org/10.14382%2Fepitoanyag-jsbcm.2013.2

[3] **Gyurkó, Zoltán**; Bagi, Katalin; Borosnyói, Adorján (2014) A. Discrete Element Modelling of uniaxial compression test of hardened concrete, *Építőanyag – Journal of Silicate Based and Composite Materials*, 66:4 pp. 113-119. , 7 p. ISSN 00 13-970x, https://doi.org/10.14382%2Fepitoanyag-jsbcm.2014.21

[4] **Gyurkó, Zoltán**; Borosnyói, Adorján (2015). Normál szilárdságú beton keménységvizsgálatának diszkrét elemes modellezése, *Műszaki Tudomány az Észak-Kelet Magyarországi Régióban 2015*, pp. 276-283., 8 p.

[5] **Gyurkó, Zoltán**; Borosnyói, Adorján (2015). Keménységmérés diszkrét elemes modellezése, *XII. Magyar Mechanikai Konferencia*, pp. 340-348., 9 p.

[6] **Gyurkó, Zoltán**; Borosnyói, Adorján (2015). Static hardness testing and DEM modelling of hardened concrete, *Concrete Structures*, 16, pp. 52-56, 5 p.

[7] **Gyurkó, Zoltán**; Borosnyói, Adorján (2015). Brinell-hardness testing and discrete element modelling of hardened concrete, *Építőanyag – Journal of Silicate Based and Composite Materials*, 67:1, 8-11, 4 p. ISSN 00 13-970x, https://doi.org/10.14382%2Fepitoanyag-jsbcm.2015.2

[8] **Gyurkó, Zoltán**; Nemes, Rita (2016). Effect of Standard Deviation of Contact Normal Strength in DEM for Concrete, *Contemporary Achievements in Civil Engineering 2016: Conference Proceedings*, 373-380., 8 p.

[9] **Gyurkó, Zoltán**; Borosnyói, Adorján (2016). DEM modelling of hardness testing of normal-strength concrete, *Proceedings of 11th fib International PhD Symposium in Civil Engineering*, 477-484, 8 p.

[10] **Gyurkó, Zoltán**; Nemes, Rita (2016). Size Effect on Cylinder and Cube Strength of Concrete, *Concrete Structures*, 17, 18-22, 5 p.

[11] **Gyurkó, Zoltán**; Szijártó Anna; Nemes, Rita (2017). Increasing freeze-thaw resistance of concrete by additions of powdered cellular concrete and clay bricks, *Procedia Engineering*, 193, 11-18, 8 p. https://doi.org/10.1016%2Fj.proeng.2017.06.180

[12] **Gyurkó, Zoltán**; Szijártó Anna; Abed, Mohammed; Nemes, Rita (2017). Effect of Cellular Concrete Powder on Durability of Normal Strength Concrete, *The 12th Central European Congress on Concrete Engineering. CCC2017 Proceedings*, 179-186, 8 p.

[13] **Gyurkó, Zoltán**; Nemes, Rita (2018). Discrete Element Modelling of Compressive Strength Testing of No-Fines Concrete, *Proceedings*, 2, 555-561, 7 p., https://doi.org/10.3390%2FICEM18-05470

[14] **Gyurkó, Zoltán**; Nemes, Rita (2018). Comparison of modelling of hardness testing with DEM and FEM, *Proceedings of the 12th International PhD Symposium in Civil Engineering*, 405-412, 8 p.

[15] **Gyurkó, Zoltán**; Nemes, Rita (2018). Energy-based evaluation of hardness testing with discrete element method, *IOP Conference Series: Materials Science And Engineering*, 426, 8 p., https://doi.org/10.1088%2F1757-899X%2F426%2F1%2F012013

[16] **Gyurkó, Zoltán**; Szijártó Anna; Abed, Mohammed; Nemes, Rita (2018). Effect of Cellular Concrete Powder on Durability of Normal Strength Concrete, *Architecture Civil Engineering Environment*, 11 : 2, 59-64, 6 p. https://doi.org/10.21307/ACEE-2018-022

[17] **Gyurkó, Zoltán**; Nemes, Rita (2019). Fracture modelling of normal concrete using different types of aggregates, *Engineering Failure Analysis*, 101, 464-472, 9 p., https://doi.org/10.1016%2Fj.engfailanal.2019.04.008

[18] **Gyurkó, Zoltán**; Jankus, Bence; Fenyvesi, Olivér; Nemes, Rita (2019). Sustainable applications for utilization the construction waste of aerated concrete, *Journal Of Cleaner Production*, 230, 430-444, 15 p., https://doi.org/10.1016%2Fj.jclepro.2019.04.357

[19] **Gyurkó, Zoltán**; Szijártó Anna; Nemes, Rita (2019). Cellular concrete waste as an economical alternative to traditional supplementary cementitious materials, Journal of Thermal Analysis And Calorimetry, 15 p., https://doi.org/10.1007%2Fs10973-019-08303-8

[20] **Gyurkó, Zoltán**; Nemes, Rita (2020). Specimen Size and Shape Effect on the Compressive Strength of Normal Strength Concrete, *Periodica Polytechnica Civil Engineering*, 64:1, 276-286. , 11 p., https://doi.org/10.3311/PPci.15338

STANDARDS

ACI CT-13. 2013. "ACI Concrete Terminology", ACI Standard, American Concrete Institute.

ASTM C150. 2004. "Standard specification for portland cement", Annual Book of ASTM Standards, American Society for Testing and Materials.

ASTM C 39/C 39M 2001 "Standard Test Method for Compressive Strength of Cylindrical Concrete Specimens" (PA: The American Society for Testing Materials)

CEN/TS 12390-9:2016 "Testing hardened concrete. Freeze-thaw resistance with de-icing salts, Scaling".

EN 197-1:2011 "Cement. Composition, specifications and conformity criteria for common cements", European Standard; Brussels, Belgium; CEN.

EN 12390-3:2009 "Testing hardened concrete. Part 3: Compressive strength of test specimens", European Standard; Brussels, Belgium; CEN.

EN 12390-7:2009 "Testing hardened concrete". Part 7: Density of hardened concrete, European Standard; Brussels, Belgium; CEN.

EN 206:2013 "Concrete. Specification, performance, production, conformity", European Standard; Brussels, Belgium; CEN.

EN 196-2:2013 "Cement testing methods. Part 2: Chemical analysis of cement", European Standard; Brussels, Belgium; CEN.

EN 525-12:2014 "Chemical analysis of cement. Part 12: Determination of free lime content", European Standard; Brussels, Belgium; CEN.

EN 14580:2005 "Natural stone test methods. Determination of static elastic modulus", European Standard; Brussels, Belgium; CEN.

EN 1992-1-1:2010 "Eurocode 2: Design of concrete structures. Part 1-1: General rules and rules for buildings", European Standard; Brussels, Belgium; CEN.

EN 12620:2002+A1:2008 "Aggregates for concrete", European Standard; Brussels, Belgium.

EN 1008:2003 "Mixing water for concrete - Specification for sampling, testing and assessing the suitability of water, including water recovered from processes in the concrete industry, as mixing water for concrete", European Standard; Brussels, Belgium; CEN.

fib 2009 "Structural Concrete Textbook on behaviour, design and performance, Second edition Volume3: Design of durable concrete structures", fib Bulletin No. 53, International Federation for Structural Concrete.

MSZ 4715-3:1972 "Testing of hardened concrete. Hydro-technical properties", (Megszilárdult beton vizsgálata. Hidrotechnikai tulajdonságok), in Hungarian.

REFERENCES

Aprianti S, E., "A huge number of artificial waste material can be supplementary cementitious material (SCM) for concrete production a review part II.", Journal of Cleaner Production 142. 4178-4194, 2017. https://doi.org/10.1016/j.jclepro.2015.12.115

Bagi, K. "Fundaments of the discrete element method", Lecture notes, 2012

Balázs, G., Borján, J., Horváth, A., Schwerteczky, F. „Effect of inhomogenity on strength and deformation characteristics of concrete", Periodica Polytechnica Civil Engineering, 37(4), pp. 313-320, 1999. [online] Available at: https://pp.bme.hu/ci/article/view/3824 [Accessed: 03 February 2020]

Barba, A. A. "Arte de los metales", Reprint. Lima, 1817.

Bažant, Z. P. "Identification of strain-softening constitutive relation from uniaxial tests by series coupling model for localization ", Cement Concrete Research, 19(6), pp. 973–977, 1989. https://doi.org/10.1016/0008-8846(89)90111-7

Bažant, Z. P. "Size effect on structural strength: a review", Archive of Applied Mechanics, 69, 703–725, 1999. https://doi.org/10.1007/s004190050252

Bažant, Z. P., Chen, E.-P. "Scaling of structural failure", Applied Mechanics Reviews, ASME, 50(10), pp. 593–627, 1997. https://doi.org/10.1115/1.3101672

Bažant, Z. P., Xi, Y. "Statistical size effect in quasi-brittle structures: II. Nonlocal theory", Journal of Engineering Mechanics, American Society of Civil Engineers, 117(11), pp. 2623–2640, 1991. https://doi.org/10.1061/(ASCE)0733-9399(1991)117:11(2623)

Bažant, Z. P., Xiang, Y. "Compression failure of quasibrittle materials and size effect", AMD Symposium Series ASME Applied Mechanics Division, 185, Damage Mechanics in Composites, ASME Winter Annual Meeting, Chicago, pp. 143–148, 1994.

Bažant, Z. P., Xi, Y., Reid, S. G. "Statistical size effect in quasi-brittle structures: I. Is Weibull theory applicable?", Journal of Engineering Mechanics, American Society of Civil Engineers. 117(11), pp. 2609–2622, 1991. https://doi.org/10.1061/(ASCE)0733-9399(1991)117:11(2609)

Bažant, Z. P. "Size effect in blunt fracture; concrete, rock, metal", Journal of Engineering Mechanics, American Society of Civil Engineers, 110(4), pp. 518–535, 1984. https://doi.org/10.1061/(ASCE)0733-9399(1984)110:4(518)

Bažant, Z. P. "Fracture energy of heterogeneous material and similitude", SEM-RILEM Int. Conference on Fracture of Concrete and Rock, pp. 390–402, 1987. https://doi.org/10.1007/978-1-4612-3578-1_23

Bažant, Z. P. "Size effect in tensile and compressive quasibrittle failures I. part", JCI Int. Workshop on Size Effect in Concrete Structures, pp. 141–160, 1993.

Bažant, Z. P., Xiang, Y. "Size effect in compression fracture: Splitting crack band propagation", Journal of Engineering Mechanics, American Society of Civil Engineers, 123(2), pp. 162–172, 1997. https://doi.org/10.1061/(asce)0733-9399(1997)123:2(162)

Bignozzi, M.C., Saccani, A. "Ceramic waste as aggregate and supplementary cementing material: A combined action to contrast alkali silica reaction (ASR)", Cement and Concrete Composites, 34, 1141–1148, 2012. https://doi.org/10.1016/j.cemconcomp.2012.07.001

Bonifazi, G., Capobianco, G., Serranti, S., Eggimann, M., Wagner, E., Di Maio, F. & Lotfi, S. "The ITZ in concrete with natural and recycled aggregates: study of microstructures based on image and sem analysis", Conference: Euroseminar on Microscopy Applied to Building Materials, Vol. 1, Delft, 2015.

Borosnyói, A. "Long term durability performance and mechanical properties of high performance concretes with combined use of supplementary cementing materials" Construction and Building Materials, 112:307–324, 2016. https://doi.org/10.1016/j.conbuildmat.2016.02.224

Camborde, F., Mariotti, C., Donzé, F.V. "Numerical study of rock and concrete behaviour by discrete element modelling" Computers and Geotechnics, 27 (4), 225-247, 2000. https://doi.org/10.1016/s0266-352x(00)00013-6

Camusso, M., Barla, M. "Microparameters calibration for loose and cemented soil when using particle methods", International Journal of Geomechanics, 9, 217–229, 2009. https://doi.org/10.1061/(asce)1532-3641(2009)9:5(217)

Carsana, M., Tittarelli, F., Bertolini, L. "Use of no-fines concrete as a building material: Strength, durability properties and corrosion protection of embedded steel", Cement and Concrete Research 48 (2013) 64–73. https://doi.org/10.1016/j.cemconres.2013.02.006

Chandler, H. "Hardness testing", ASM International, 192 p., 1999.

Chandler, M. Q., Peters, J. F., Pelessone, D. "Discrete element modeling of calcium-silicate-hydrate", Modelling and Simulation in Materials Science and Engineering, 21(5), 055010, 2013. https://doi.org/10.1088/0965-0393/21/5/055010

Chen, P., Han, Q., Ma, T., Lin, D. "The mechanical properties of shale based on micro-indentation test", Petroleum Exploration and Development, 42 (5), 723-732, 2015. https://doi.org/10.1016/s1876-3804(15)30069-0

Cheung, G. "Micromechanics of Sand Production in Oil Wells", Ph.D. Thesis, Imperial College, London, UK, 2010.

Cho, N., Martin, C., Sego, D.C., "A clumped particle model for rock", International Journal of Rock Mechanics & Mining Sciences, 44, 997–1010, 2007. https://doi.org/10.1016/j.ijrmms.2007.02.002

Crepps, R. B. "Ball Test Applied to Cement Mortar and Concrete", Bulletin No.12, Engineering Experiment Station, Purdue University, LaFayette, Indiana, 32 p., 1923.

Cundall, P. A. "A computer model for simulating progressive large scale movements in blocky rock systems" Procs. Symposium of the International Society of Rock Mechanics, Nancy, France, Vol. 1., Paper II-8, 1971.

del Viso, J. R., Carmona, J. R., Ruiz, G. "Shape and size effects on the compressive strength of high-strength concrete", Cement and Concrete Research, 38(3), pp. 386-395, 2008. https://doi.org/10.1016/j.cemconres.2007.09.020

Deotti, L., Karstunen, M., Almeida, M. C. F., Almeida, M. S. S. "Modeling of Laboratory Tests on Saint-Roch-de-l'Achigan Clay with S-CLAY1S Model", International Journal of Geomechanics, 17, 2017. https://10.1061/(ASCE)GM.1943-5622.0000701

Dombi, J. "Építőanyagok szilárdsága és szilárdságvizsgálata – 1. Nyomószilárdság", (Strength and strength test of construction materials – 1. Compressive strength), SZIKKTI Tudományos közlemények (SZIKKTI Scientific publications), Budapest, p. 51, 1979. (in Hungarian)

Favier, J.F., Abbaspour-Fard, M.H., Kremmer, M. "Modeling nonspherical particles using multisphere discrete elements", ASCE Journal of Engineering Mechanics, 127, 969–1074, 2001. https://doi.org/10.1061/(asce)0733-9399(2001)127:10(971)

Fenyvesi, O. "Recycling of different industrial wastes as concrete aggregate" (in Hungarian). Meddő? Hulladék? Nem! Haszonanyag! Conference, Budapest, Hungary (2014) 111–118, 2014.

Fenyvesi, O., Jankus, B. "Opportunities in recycling AAC waste as aggregate for lightweight concrete", Építőanyag. – Journal of Silicate Based and Composite Materirals 67, 66–70, 2015. https://doi.org/10.14382/epitoanyag-jsbcm.2015.11

Fischer-Cripps, A. "Introduction to Contact Mehanics", Mechanical Engineering Series, Springer 221 p., 2000. https://doi.org/10.1007/978-0-387-68188-7

Gagg, C. R. "Cement and concrete as an engineering material: An historic appraisal and case study analysis", Engineering Failure Analysis, 40, 114–140, 2014. https://doi.org/10.1016/j.engfailanal.2014.02.004

Glinicki, M. C. A., Zielinski, M. "Depth-sensing indentation method for evaluation of efficiency of secondary cementitious materials", Cement and Concrete Research, 34, 721–724, 2004. https://doi.org/10.1016/j.cemconres.2003.10.014

Gonzalez, M., Tighe, S. L., Hui, K., Rahman, S., de Oliveira Lima, A., "Evaluation of freeze/thaw and scaling response of nanoconcrete for Portland Cement Concrete (PCC) pavements", Construction and Building Materials. 120, 465–472, 2016. https://doi.org/10.1016/j.conbuildmat.2016.05.043

Gruber, K. A., Ramlochan, T., Boddy, A., Hooton, R.D., Thomas, M.D.A. "Increasing concrete durability with high-reactivity metakaolin" Cement and Concrete Composites, 23, 479–84, 2001. https://doi.org/10.1016/s0958-9465(00)00097-4

Gruyaert, E., Robeyst, N., De Belie, N. "Study of the hydration of Portland cement blended with blast-furnace slag by calorimetry", Journal of Thermal Analysis and Calorimetry, 102(3), 941–951, 2010. https://doi.org/10.1007/s10973-010-0841-6

Gubicza, J., Juhasz, A., Arato, P., Szommer, P., Tasnadi, P., Voros, G. "Elastic modulus determination from depth sensing indentation test", Journal of Materials Science Letters, 15, 2141-2144, 1996. https://doi.org/10.1007/bf00241151

Hentz, S., Donzé, F. "Discrete element modelling of concrete submitted to dynamic loading at high strain rates", Computers and Structures, Vol. 82. 2509-2524, 2004. https://doi.org/10.1016/j.compstruc.2004.05.016

Hertz, H. "Über die Berührung fester elastischer Körper", Journal für die reine und angewandte Mathematik, 1881/5, pp. 12-23, 1881.

Hoff, G. C. "Porosity-strength considerations for cellular concrete", Cement and Concrete Research, 2:91–100, 1972. https://doi.org/10.1016/0008-8846(72)90026-9

Ibrahim, I. A., ElSersy, H. H., Abadir, M. F. "The use of thermal analysis in the approximate determination of the cement content in concrete", Journal of Thermal Analysis Calorimetry, 76:713, 2004. https://doi.org/10.1023/B:JTAN.0000032255.58397.4b

Itasca Consulting Group "Particle Flow Code in Three Dimensions", Users Guide, Minneapolis, Minnesota, USA, 2008.

Kausay, T. "Gázbeton-pórusbeton (Gasbeton-porenbeton – in Hungarian)" BETON, Vol. X, Issue: 7-8, page 25, 2002. ISSN: 1218-4837

Kim, J. K., Yi, S. T., Tang, E. I. "Size effect on flexural compressive strength of concrete specimens", ACI Structural Journal, 97(2), pp. 291–296, 2000. https://doi.org/10.14359/859

Kim, J. K., Yi, S. T. "Size effect on compressive strength of concrete", In: 11th International Conference on Fracture, ICF11, Turin, Italy, 2004, pp. 5270-5275.

Kim, J. K., Yi, S. T. "Application of size effect to compressive strength of concrete members", Sadhana, 27(4), pp. 467-484, 2002. https://doi.org/10.1007/bf02706995

Kim, J. K., Eo, S. H., Park, H. K. "Size effect in concrete structures without initial crack", Fracture mechanics: Application to concrete, pp. 179–196, 1989.

Kim, J. K., Eo, S. H. "Size effect in concrete specimens with dissimilar initial cracks", Magazine Concrete Research, 42(153), pp. 233–238, 1990. https://doi.org/10.1680/macr.1990.42.153.233

Kim, J. K., Yi, S. T., Park, H. K., Eo, S. H. "Size effect on compressive strength of plain and spirally reinforced concrete cylinders", ACI Structural Journal, 96(1), pp. 88–94, 1999. https://doi.org/10.14359/599

Kubissa, W., Simon, T., Jaskulski, R., Reiterman, P., Supera, M. "Ecological high performance concrete", Procedia Engineering, 172, 595–603, 2017. https://doi.org/10.1016/j.proeng.2017.02.186

Kulatilake, P.H.S.W., Liang, J., Gao, H. "Experimental and numerical simulations of jointed rock block strength under uniaxial loading", Journal of Engineering Mechanics, 127, 1240–1247, 2001. https://doi.org/10.1061/(asce)0733-9399(2001)127:12(1240)

Kumar, S., Barai, S.V. "Size-effect of fracture parameters for crack propagation in concrete: a comparative study", Computers and Concrete, 9 (1), 1-19, 2012. https://doi.org/10.12989/cac.2012.9.1.001

Lanaro, F., Jing, L., Stephansson, O., Barla, G. "D.E.M. modelling of laboratory tests of block toppling", International Journal of Rock Mechanics and Mining Sciences, 34, 1997. https://doi.org/10.1016/S1365-1609(97)00116-0

Le, N. L. B., Stroeven, P. "Evaluation by discrete element method (DEM) of gap-graded packing potentialities for green concrete design", The International Conference on Sustainable Built Environment for Now and the Future. Hanoi, 26 - 27 March 2013.

Le, N. L. B., Stroeven, P. "Packing issue in cement blending for sustainability developments - approach by discrete element method", International Journal of Research in Engineering and Technology, 3(25), 89-96, 2015. https://doi.org/10.15623/ijret.2014.0325015

Lee, H., Kwon, J. "Application of DEM model to breakage and liberation behavior of recycled aggregates from impact-breakage of concrete waste", Minerals Engineering, Vol. 21. 761-765, 2008. https://doi.org/10.1016/j.mineng.2008.06.007

Li, J., Zhang, C., Xiao, J. "On statistical characteristics of the compressive strength of recycled aggregate concrete", Structural Concrete, 6, 149-153, 2005. https://doi.org/10.1680/stco.2005.6.4.149

Liu, Y., You, Z., Zhao, Y. "Three-dimensional discrete element modeling of asphalt concrete: Size effects of elements". Construction and Building Materials, 37, 775–782, 2012. https://doi.org/10.1016/j.conbuildmat.2012.08.007

Ma, Y., Huang, H., Yang, R. "DEM Analysis of Using the Scratch Test to Probe Rock Heterogeneity"., Rock Mechanics and Its Applications in Civil, Mining, and Petroleum Engineering, 198-207, 2014. https://doi.org/10.1061/9780784413395.023

Mehta, P. K., Monteiro, P. J. M. „Concrete: Microstructure, Properties, and Materials", McGraw Hill, 2006, 659 p., 2005.

Meyer, E. „Untersuchungen uber Harteprufung und Harte", Zeitschrift des VereinesDeutscher Ingenieure, Vol. 52, No. 17, 645–654, 740–748, 835–844, 1908.

Mirzahosseini, M., Riding, K.A. "Influence of different particle sizes on reactivity of finely ground glass as supplementary cementitious material (SCM)", Cement and Concrete Composites, 56, 95–105, 2015. https://doi.org/10.1016/j.cemconcomp.2014.10.004

Mlinárik, L., Kopecskó, K., Borosnyói, A. "Properties of cement mortars in fresh and hardened condition infl uenced by combined application of SCMs", Építőanyag – Journal of Silicate Based and Composite Materials, 68:62–66, 2016. https://doi.org/10.14382/epitoanyag-jsbcm.2016.11

Mohammadhosseini, H., Yatim, J. M., Sam, A. R. M., Awal, A. S. M. A. "Durability performance of green concrete composites containing waste carpet fibers and palm oil fuel ash", Journal of Cleaner Production, 144, 448–458, 2017. https://doi.org/10.1016/j.jclepro.2016.12.151

Mohs, F. "Versuch einer Elementar-Methode zur Naturhistorischen Bestimmung und Erkennung von Fossilien", University of Graz, 1812.

Moradi, G., Refahi, A., Mohandesi, J. A. "Distinct Element Method Approach to Fracture Toughness of Geopolymeric Concretes to Study the Micro-Mechanical Parameters", International Journal of Civil Engineering and Concrete Structures, 3(2), 2018.

Narayanan, N., Ramamurthy, K. "Structure and properties of aerated concrete: a review" Cement and Concrete Composites, 22: 321–329, 2000. https://doi.org/10.1016/S0958-9465(00)00016-0

Neville, A. M. „Properties of concrete", John Wiley & Sons, 1996, 844 p., 1995.

O'Sullivan, C. "Particulate discrete element modeling". Spoon Press, Abingdon, 2011. https://doi.org/10.1201/9781482266498

Özalp, F., Yilmaz, H.D., Kara, M., Kaya, Ö., Sahin, A., "Effects of recycled aggregates from construction and demolition wastes on mechanical and permeability properties of paving stone, kerb and concrete pipes", Construction and Building Materials 110, 17–23, 2016. https://doi.org/10.1016/j.conbuildmat.2016.01.030

Palotás, L. "A vasbeton" (Reinforced concrete - in Hungarian), Magyar Építőmesterek Egyesülete, 1947.

Pollard, D., Radchenko, P. "Nonlinear least-squares estimation", Journal of Multivariate Analysis, 97(2), pp. 548-562, 2006. https://doi.org/10.1016/j.jmva.2005.04.002

Potyondy, D.O., Cundall, P. A. "A bonded-particle model for rock". International Journal of Rock Mechanics & Mining Sciences, 41., pp. 1329–1364, 2004. https://doi.org/10.1016/j.ijrmms.2004.09.011

Puertas, F., García-Díaz, I., Barba, A., Gazulla, M.F., Palacios, M., Gómez, M.P., Martínez-Ramírez, S. "Ceramic wastes as alternative raw materials for Portland cement clinker production", Cement and Concrete Composites, 30, 798–805, 2008. https://doi.org/10.1016/j.cemconcomp.2008.06.003

Réaumur, R. A. F. "L'art de converter le fer forgé en acier", French Academy of Sciences, Paris, 1722.

Saad, L., Aissani, A., Chateauneuf, A., Raphael, W. "Reliability-based optimization of direct and indirect LCC of RC bridge elements under coupled fatigue-corrosion deterioration processes", Engineering Failure Analysis, 59, 570-587, 2016. https://doi.org/10.1016/j.engfailanal.2015.11.006

Sani, D., Moriconi, G., Fava, G., Corinaldesi, V. "Leaching and mechanical behaviour of concrete manufactured with recycled aggregates", Waste Management, 25, 177–82, 2005. https://doi.org/10.1016/j.wasman.2004.12.006

Scheinherrová, L., Doleželová, M., Havlín, J., Trník, A. "Thermal analysis of ternary gypsum-based binders stored in different environments", Journal of Thermal Analysis and Calorimetry, 133, 177-188, 2018. https://doi.org/10.1007/s10973-018-7398-1

Schober, G. "Porosity in autoclaved aerated concrete (AAC): A review on pore structure, types of porosity, measurement methods and effects of porosity on properties", 5th International Conference on Autoclaved Aerated Concrete, 39–43, 351–359, 2011.

Schöpfer, M.P., Abe, S., Childs, C., Walsh, J.J. "The impact of porosity and crack density on the elasticity, strength and friction of cohesive granular materials: Insights from DEM modelling", International Journal of Rock Mechanics & Mining Sciences, 46, 250–261, 2007. https://doi.org/10.1016/j.ijrmms.2008.03.009

Sestini, Q. "La prova Brinell applicata al materiali cementizi come prova di resistenza", Le Strade, 1934/7, Vol. 16. 255-264, 1934.

Shiu, W., Donzé, F. V., Daudeville, L. "Penetration prediction of missiles with different nose shapes by the discrete element numerical approach". Computers and Structures, 86., 2079–2086, 2008. https://doi.org/10.1016/j.compstruc.2008.03.003

Siddique, R., Khan, M.I. "Supplementary Cementing Materials", Springer, Berlin, 2011. https://doi.org/10.1007/978-3-642-17866-5

Siddique, R., Klaus, J. "Influence of metakaolin on the properties of mortar and concrete: a review", Applied Clay Science, 43, 392–400, 2009. https://doi.org/10.1016/j.clay.2008.11.007

Sinica, M., Sezamanas, G., Mikulskis, D., Kligys, M., Cesnauskas, V., Zacharcenko, P., Kuprijenko, P., Scerbina, N., Pivenj, N., "Investigation of the Composite Material with Inclusions of Autoclaved Aerated Concrete Chips", Materials Science (Medziagotyra), 15(4), 356-362, 2009. ISSN 1392-1320.

Sneddon, I. N. "The relation between load and penetration in the axisymmetric boussinesq problem for a punch of arbitrary profile", International Journal of Engineering Science, 3/1:47–57, 1972. https://doi.org/10.1016/0020-7225(65)90019-4

Song, Y., Li, B., Yang, E., Liu, Y., Ding, T. "Feasibility study on utilization of municipal solid waste incineration bottom ash as aerating agent for the production of autoclaved aerated concrete", Cement and Concrete Composites, 56:51–58, 2015. https://doi.org/10.1016/j.cemconcomp.2014.11.006

Steinwede, K. "Über die Anwendung des Kugelhärteversuches zur Bestimmung der Festigkeit des Betons", PhD Dissertation, Hannover: Gebrüder Janecke, 1937.

Szalai, K. "A beton minőségellenőrzése" (Quality Control of Concrete – in Hungarian), Szabványkiadó, Budapest, 1982.

Szilágyi, K., Borosnyói, A., Dobó, K. "Static indentation hardness testing of concrete: A long established method revived", Építőanyag – Journal of Silicate Based and Composite Materials, Volume 63, Issue 1-2, pp. 2-8, 2011. https://doi.org/10.14382/epitoanyag-jsbcm.2011.1

Tabor, D. "A simple theory of static and dynamic hardness", Proceedings of the Royal Society of London, Series A, Mathematical and Physical Sciences, Vol. 192, Issue 1029, pp. 247-274, 1947.

Talero, R., Rahhal, V. "Calorimetric comparison of portland cements containing silica fume and metakaolin. Is silica fume, like metakaolin, characterized by pozzolanic activity that is more specific than generic", Journal of Thermal Analysis and Calorimetry, 96, 383, 2009. https://doi.org/10.1007/s10973-008-9096-x

Tauzowski, P., Lógó, J., & Pintér, E. "Parametric Study on the Element Size Effect for Optimal Topologies", Periodica Polytechnica Civil Engineering, 62(1), pp. 267-276, 2018. https://doi.org/10.3311/PPci.11551

Tezcan, J., Hsiao, K. J. "Nondestructive evaluation of material strength using depth-sensing indentation", Engineering Structures, 30, 2206–2210, 2008. https://doi.org/10.1016/j.engstruct.2007.06.011

Timoshenko, S. P. "History of strength of materials – With a brief account of the history of theory of elasticity and theory of structures", McGraw Hill, 452 p., 1953.

Tokyay, M., Özdemir, M. "Specimen shape and size effect on the compressive strength, of higher strength concrete", Cement and Concrete Research, 27, 1281-1289, 1997. https://doi.org/10.1016/s0008-8846(97)00104-x

Topcu I. B., Seridemir, M. "Prediction of properties of waste AAC aggregate concrete using artificial neural network", Computational Materials Science, 41(1), 117-125. ISSN: 0927-0256, 2007. https://doi.org/10.1016/j.commatsci.2007.03.010

Topcu, I.B., Güncan, N.F. "Using waste concrete as aggregate", Cement and Concrete Research, 25, 1385–1390, 1995. https://doi.org/10.1016/0008-8846(95)00131-u

Topcu, I.B., Sengel, S. "Properties of concretes produced with waste concrete aggregate", Cement and Concrete Research, 34, 1307–1312, 2004. https://doi.org/10.1016/j.cemconres.2003.12.019

Tran, V.T., Donzé, F.-V., Marin, P. "A discrete element model of concrete under high triaxial loading". Cement & Concrete Composites, 33, 936–948, 2011. https://doi.org/10.1016/j.cemconcomp.2011.01.003

Wang, Z., Lin, F, Gu, X. "Numerical Simulation of Failure Process of Concrete Under Compression Based on Mesoscopic Discrete Element Model", Tsinghua Science and Technology, 13, 19-25, 2008. https://doi.org/10.1016/s1007-0214(08)70121-4

Wang, Y., Tonon, F. "Calibration of a discrete element model for intact rock up to its peak strength", International Journal for Numerical and Analytical Methods in Geomechanics, 34, 447–469, 2010. https://doi.org/10.1002/nag.811

Wilinska, I., Pacewska, B. "Influence of selected activating methods on hydration processes of mixtures containing high and very high amount of fly ash". Journal of Thermal Analysis and Calorimetry, 133, 823–843, 2018. https://doi.org/10.1007/s10973-017-6915-y

Wu, Z.B., Guan, B.H., Lou, W.B., Ye, Q.Q., Fu, H.L. "Calorimetric study of calcium aluminate cement blended with flue gas desulfurization gypsum". Journal of Thermal Analysis and Calorimetry, 98(3), 737–742, 2009. https://doi.org/10.1007/s10973-009-0107-3

Ye, D., Xu, H., Feng, X., Xu, Y., Xiao, L. "Depth-sensing indentation-based studies of surface mechanical behavior and fatigue damage evolution of an austenitic stainless steel subjected to cyclic straining", Materials Science & Engineering A, 650, 38–51, 2016. https://doi.org/10.1016/j.msea.2015.10.024

Yi, S. T., Yang, E. I., Choi, J. C. "Effect of specimen sizes, specimen shapes, and placement directions on compressive strength of concrete", Nuclear Engineering and Design 236, pp. 115-127, 2006. https://doi.org/10.1016/j.nucengdes.2005.08.004

Yoon, J. "Application of experimental design and optimization to PFC model calibration in uniaxial compression simulation", International Journal of Rock Mechanics & Mining Sciences, 44, 871–889, 2007. https://doi.org/10.1016/j.ijrmms.2007.01.004

Ženíšek, M., Vlach, T., Lenka, L. "Dosage of Metakaolin in High Performance Concrete" Key Engineering Materials, 722:311-315, 2016 https://doi.org/10.4028/www.scientific.net/KEM.722.311

Zhu, H., Zhou, Z, Yang, R. "Discrete particle simulation of particulate systems: Theoretical developments", Chemical Engineering Science, 62., pp. 3378-3396, 2007. https://doi.org/10.1016/j.ces.2006.12.089

Appendix

Appendix table of contents

I. List of figures and tables

LIST OF FIGURES

LIST OF TABLES

II. Methods of hardness measuring

Table A-1 *Methods of hardness measuring*

Author, name, instrument	Working principle, correlation	Calculation method of the measured parameters
Hertz (1881)	Contact between a ball and the measured material until the permanent ductile deformation or the crack is reached.	$H_r = 6 \cdot \frac{p}{d^2} \cdot \pi$
Brinell (1900)	Penetration of a steel sphere; ∅ 1.25; 2,5; 5 or 10 *mm* 15,65-3000 *kg*;	$HB = \frac{2 \cdot F}{D \cdot \pi \cdot \left(D - \sqrt{D^2 - d^2}\right)}$
Shore monotron	Diamond ball ∅ 0,75 *mm*, or steel ball ∅ 1/16"; 2,5 *mm* and the standard depth; 0,045 *mm*	The degree of hardness is the load, that is necessary to the impression of the measuring body in a standard depth.
Ludvig (1907)	Impression of a 90° steel cone into the material.	The hardness is given in the function of the load and the projected area.
Rockwell and super Rockwell (1922)	120° diamond cone or 1/2"; 1/4"; 1/8"; 1/16"-os steel sphere impression with different loads; 150-100-60 *kg* or in case of super Rockwell 45-30-15 *kg*	The determination of the hardness based on the indentation depth taking into account the effect of preloading.
Vickers (1925)	136° diamond cone impression with 1-120 *kg* load.	$HV = 1{,}854 \frac{F}{d^2}$
Drozd (1958)	With *P* ball load measures the indentation depth and calculates the hardness.	$H = \frac{P - P \cdot s}{H \cdot \pi \cdot h}$
Káldor M.-Bárczy P. (1967)	Vickers normal hardness is determined with the help of the *n* value (material characteristic).	$HN = 1.8544 \cdot \frac{P}{d^n}$
Brunner, G.G.- Schimmer L. (1978)	It measures the indentation depth of a parabolic diamond body in the function of the load and the relationship is linear, regardless of the quality of the material.	$HW_{szil} = \frac{F_p(y)}{y}$ and $HW_{szil} = C \cdot \left(1 - \frac{y_0}{y}\right)$ y_0 max. penetration depth y residual penetration depth C machine constant

III. Brinell hardness test

According to *Hertz (1881)*, hardness is the least value of pressure beneath a spherical indenter necessary to produce a permanent set at the centre of the area of contact. As Hertz's criterion has some practical difficulties, the hardness values defined by the practical methods usually indicate different relationships between the indenter load and the tested specimen's resistance to penetration or permanent deformation. Nowadays, the most commonly used method for measuring the surface hardness is the so-called indentation hardness test; however, it is mainly used for metals, plastic and some composites (*Chandler, 1999*). The static hardness testing of porous stone-like materials was hardly ever dealt in a century since the process exists. In the USA R. B. Crepps and R. E. Mills, in Italy Q. Sestini and in Germany K. Steinwede dealt with this problem; at the beginning of the 20th century (*Crepps, 1923*; *Sestini, 1934*; *Steinwede, 1937*). Then because of the relative inefficiency and the lack of appropriate technology this type of test was pushed into the background and came only into the focus in the 80s when the computational background was available to process and evaluate the data. In the 2000s the test is used as an alternative of the compression test to determine the strength of a material.

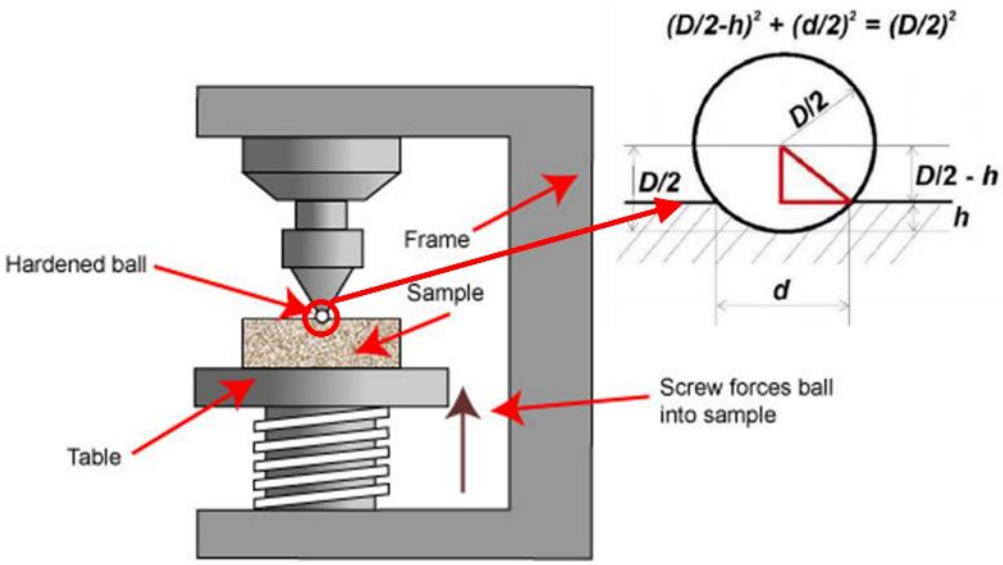

Fig. A-1 *Brinell-hardness test overview (Chandler, 1999) and the relation of sphere diameter and indentation diameter (Fischer-Cripps, 2000)*

The most well-known indentation hardness testing method is the Brinell-test. In case of Brinell method, a hardened, polished steel ball is pushed into the surface of the material with a specified load and time (see *Fig. A-1*). The test consists of applying a constant load (force), usually 500 to 3000 kg, on a 10 mm diameter (or smaller) hardened steel ball to the flat surface

of a workpiece. The load is applied for a specified time (10-15 s for hard materials (like metals) and about 30 s for soft materials (like porous materials)). This time period is required to ensure the plastic flow. There are some other influencing factors and interesting phenomena about Brinell hardness test, which are described in *Appendix IV*. The aim is the required indentation diameter, which is measured in millimetres. The relation between load and size of indentation may be expressed by a number of empirical relations. The first of these, known as Meyer's law, states that if F is the load applied and d the diameter of the impression left when the indenter is removed:

$$F = kd^n \tag{A-1}$$

where, k and n are empirical constants for the material when the diameter of the ball is fixed (*Tabor, 1947*). The value of n is generally around 2, however, it was not fixed to that value. In case of Brinell-hardness test, mostly another expression is used to express the relation between the force and the size of indentation. This expression is very sensitive to the conditions of the testing process.

For accurate results, the indentations must not be made close to the edge of the workpiece. The error in the Brinell number will be negligible if the distance from the centre of the indentation is not less than three times the diameter of the indentation from the edge of the workpiece. The indentation points also must not be too close to each other, because in this case, the material may be cold worked by the first indentation. This condition is likely to produce an abnormally small indentation. The distance between the centres of the indentations should be at least three times the diameter of the indentation (*Chandler, 1999*). The accuracy is influenced by the surface smoothness (or roughness) too. The surface of the workpiece should be filed, ground or polished. For accurate results, the surface must be representative of the material.

The hardness is defined as the ratio of the load and the resulting spherical imprint:

$$HB = \frac{F}{D\pi h} \tag{A-2}$$

The indentation depth (h) is difficult to measure, but from the sphere diameters (D) and the indentation diameters (d) can be calculated (see *Fig. A-1*):

$$h = \frac{D-\sqrt{D^2-d^2}}{2}. \tag{A-3}$$

After some transformation:

$$HB = \frac{2F}{D\pi\left(D-\sqrt{D^2-d^2}\right)}, \tag{A-4}$$

where: F is the loading force, D is the sphere diameter, d is the indentation diameter, h is the indentation depth.

Fig. A-2 *Brinell hardness tester (left); Steel ball indenter head (middle); Results of the Brinell-hardness test in practice on a concrete sample (right)*

During my investigations, a traditional Brinell hardness tester machine was used, as it can be seen in *Fig. A-2*. In my research, all materials were subjected to a wide range of load levels. Maximum loads by the Brinell tests were taken in the range of 1.5 kN to 30 kN. The Brinell test was carried out by a 10 mm diameter hard steel indenter. Every test on every material was carried out under the same conditions and using the same asset. For example, in the case of concrete specimens, the tests were performed on four surfaces of the cubes, which were located vertically in the formwork (the other two sides were not suitable for the test, because their surface was not sufficiently uniform due to the concrete-making process). The measurements were made in different load increments. At least five test repetitions were carried out in every load level complying with the rules of Brinell-testing (like minimum distance of the prints from each other or from the edge of the specimen). To receive a statistically correct result, the diameter of the ball prints on every load level was averaged. The maximum loading force operated on the surface of the material for 30 seconds. To read the size of the prints, a hand microscope was used, which has a built-in ruler with a precision of 0.1 mm. All the measurement was taken on a print in two directions (perpendicular to each other). The result came from the average of these two measurements.

IV. Influencing factors and phenomena of Brinell test

An important factor in Brinell-test, which is not mentioned in the main text, is the thickness of the sample. If one knows the thickness of the material, with the help of *Table A-2*, one can tell the recommended ball diameter.

Table A-2 *Usable ball diameters for a given sample thickness (Chandler, 1999)*

Thickness of the sample, t [mm]	Ball diameter, ∅D [mm]
v ≥ 8 mm	∅ 10 mm
8 mm ≥ v ≥ 4 mm	∅ 5 mm
4 mm ≥ v ≥ 2 mm	∅ 2,5 mm
2 mm ≥ v ≥ 0,8 mm	∅ 1 mm

Also, it is important that the load must be transmitted without vibration or shocking effect to the sample. The loading time as measurement affecting parameter is a function of the tested material. During the test, in the static phase, so long need to load the sample, that we obtain an evaluable print. In case of harder materials, the evaluable print forms in a shorter time than in case of softer materials. While conducting Brinell-tests, the phenomenon of sinking-in or piling-up can be commonly observed around the spherical shape body, as can be seen in *Fig. A-3*. During the compression of the ball, the material is trying to shirk from it, so in the plastic zone around the body significant lateral displacement can be observed. These effects must be taken into account when measuring the diameter of the indentation because as a result of this, a higher value can be measured as the real one. The piling-up is primarily the characteristic of perfectly ductile materials, but the phenomenon can be observed in other materials, such as ceramics. The sinking-in can be mostly observed on softer materials. In this case, the material around the indenting body is also sinking in together with the ball.

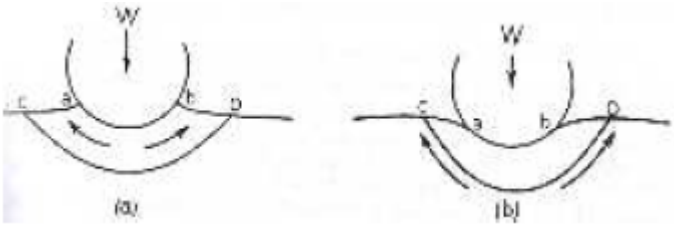

Fig. A-3 *Special phenomenon: "Piling-up" and "Sinking-in" (Tabor, 1947)*

The disadvantage of the Brinell-hardness test is that the results are significantly affected by the test conditions. The main influencing factors are the diameter of the sphere, the magnitude of the loading force, the relation of the sphere diameter and the thickness of the tested material, the distance of the prints, the rate of the indentation of the ball and the duration of loading.

V. Specification of the DSI measurements

In my research the DSI tests were conducted at the laboratory of the Department of Polymer Engineering. The testing device was a Zwick Z050 computer-controlled universal tensile testing machine (see *Fig. A-4*). During the DSI test, the computer-aided device pushes the indentation body into the surface of the sample with constant loading or indentation velocity. During the measurement, the device continuously registers the magnitude of the loading force and the depth of the indentation. Meantime the device draws on the screen of the computer the so-called indentation curve in a force [N] – displacement [mm] coordinate system based on the data, which is recognized directly in real-time. The capacity of the machine was 50 kN, the test speed can be varied between 0.0001 and 500 mm/min. My choice for the loading rate was 1.0 mm/min. To avoid the measurement errors, at least five measurements in every load level was made.

Fig. A-4 *Zwick Z050 computer-controlled universal tensile testing machine (www.zwick.fr)*

Description of the test:

- The samples were placed into the device after adequate preparation.
- The samples were loaded with the help of a computer control interface.
- The results were checked after completion of the program.
- Then the samples were placed, under the probe, a proper distance from the previous measurement and the test was repeated.

VI. The PFC (Particle Flow Code) of Itasca

In this chapter, the PFC software will be introduced, which DEM software is used to create my models. A general particle model simulates the mechanical behaviour of a system comprised of a collection of arbitrarily shaped particles, as it can be seen in *Fig. A-5*. The model is made up of distinct particles that displace independent of each other and interact only at contacts or interfaces between the particles.

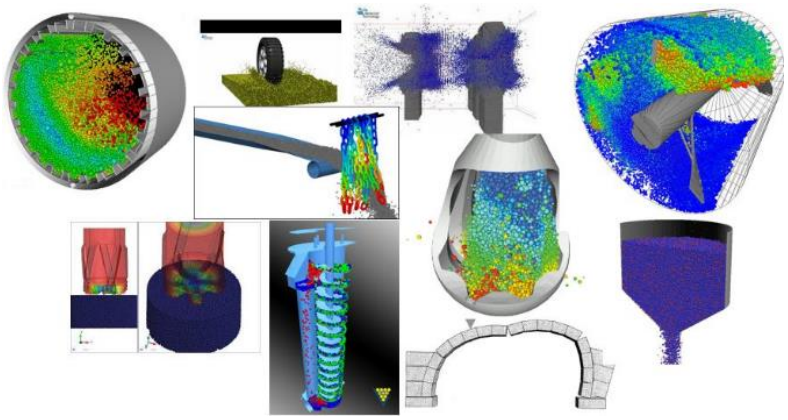

Fig. A-5 *Different applications of DEM (www.itascacg.com, demsoftware.net, Bagi, 2012)*

The relationship between the motion of the particles and the forces causing that motion can be described with Newton's second law. The force system may be in static equilibrium (in which case, there is either no motion at all, or motion happens only with constant velocities), or it may be such as to cause the particles to accelerate.

PFC3D (Particle Flow Code) contains the following assumptions:

1. The particles are treated as rigid bodies.
2. The contacts occur over a vanishingly small area (i.e., at a material point).
3. Behaviour at the contacts uses a soft-contact approach where the rigid particles are allowed to overlap one another at contact points, and the relative displacements of the two material points forming the contact are considered to reflect the contact deformations which are related to the contact forces.
4. The magnitude of the overlap is related to the compressional component of contact force via the corresponding force-displacement law, and all overlaps are small in relation to particle sizes.
5. Bonds (i.e. tension-resisting contacts) can also exist between particles.
6. All particles are spherical. However, the clump logic of PFC supports the creation of super-particles of arbitrary shape: overlapping spheres may be "glued together" to form an

irregular particle. Hence, a clump consists of a set of overlapping spherical particles and behaves as a single rigid body with a deformable boundary.

In addition to traditional particle-flow applications, *PFC3D* can also be applied to the analysis of solids. In such models, the continuum behaviour is approximated by treating the solid as a compacted assembly of many small particles. In *PFC3D* the particles are linked with contacts, which arise when the distance between two particles is vanishing. In this case, forces and moments arise between the particles, which can be (tensional or compressional) normal forces, tangential forces, or bending moments. To the analysis of solids, we can use so-called "cemented" contacts, (e.g. parallel bond contact) which can simulate the binder between the larger particles. Measures of stress and strain rate can be defined as average quantities over a representative measurement volume for such systems. This allows one to estimate interior stresses for granular materials such as soils, or solid materials such as rock, concrete or plastics.

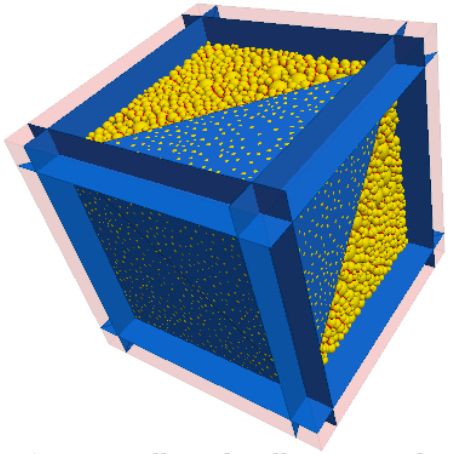

Fig. A-6 *Balls and walls generated in PFC*

The *PFC3D* particle-flow model includes two types of elements, "balls" (spherical particles, yellow in *Fig. A-6*) and "walls" (blue in *Fig. A-6*). Walls allow the user to apply velocity boundary conditions to assemblies of balls for purposes of compaction and confinement. The balls and walls interact with each other via the forces that arise at contacts. The equations of motion are satisfied for each ball. However, the equations of motion are not considered for walls (i.e., forces acting on a wall do not influence its motion). Instead, wall motions are specified by the user. In *PFC3D* the interaction of the particles is treated as a dynamic process, perhaps with states of equilibrium developing whenever the internal forces are in balance. Like in most DEM codes, in *PFC3D* the dynamic behaviour is represented numerically by a timestepping algorithm in which it is assumed that the velocities and accelerations are constant within each timestep. This assumption is based upon the idea that the timestep chosen may be so small that, during a single timestep, disturbances cannot propagate further from any particle than its immediate neighbours. Then, at all times, the forces acting on any particle are determined exclusively by its interaction with the particles with which it is in contact. The timestepping algorithm, in principle, could be explicit or implicit. In *PFC3D* an explicit method (central difference method) is applied, because the use of an explicit, as opposed to an implicit, numerical scheme makes it possible to simulate the nonlinear interaction of a large number of

particles without excessive memory requirements or the need for an iterative procedure. Due to the nature of the explicit time integration, the calculation method overestimates, compared to the exact solution, the displacement increment which arises in Δt timestep. Therefore, the limitation of the length of the timestep is necessary. Consequently, the model is very sensitive to the reduction of the timestep. If the length of timestep is close to the "infinitesimally small", then the results will not change (it is particularly important to check the effect of decreasing timestep length in the case of dynamic processes).

The calculations performed in PFC by using two types of rules:

- Newton's second law (particles) → applied to determine the motion of each particle arising from the contact and body forces (not applied to walls, since the wall motion is specified by the user).
- Force-displacement law (contacts) → used to update the contact forces arising from the relative motions at the contacts.

The PFC software is equipped by a user interface (UI); however, it is only usable for the visualization of the models. The material models and test routines shall be written in a software code. PFC has its own type of programming language: FISH, which is a C++ based higher-level programming language. For further description of FISH see *Appendix XIII*.

VI.I Overview of available approaches for constructing random particle arrangement

The first step of the DE modelling is the preparation of the geometrical model. In this step, the position and the shape of the elements are specified. The definition of the geometrical model is relatively easy if the discrete elements exactly correspond to the units of the real structure. However, in several cases (e.g. sand, corn stored in a silo, concrete) thousands of densely packed elements (representing a huge number of real grains) have to be defined randomly. In this case, we need to prepare random dense initial arrangements of contacting elements. There are several techniques to solve this problem. The most widespread are the following:

- dynamic techniques,
- constructive algorithms (e.g. Inwards Packing Method (*Bagi, 2005*)),
- collective rearrangement techniques.

For the detailed description of those methods, see *Appendix VII*.

VI.II Calculation cycle

The calculation cycle in *PFC3D* is a timestepping algorithm that requires the repeated application of the law of motion to each particle. In the calculation cycle, the force-displacement law is used to each contact, and in every cycle, the wall positions are also updated (see *Fig. A-7*). Contacts, which may exist between two balls, or between a ball and a wall, are formed and broken automatically during the course of a simulation. At the start of each timestep, the set of contacts is updated from the known particle and wall positions. The force-displacement law is then applied to each contact to update the contact forces based on the relative motion between the two entities at the contact. Next, the law of motion is applied to each particle to update its velocity and position based on the resultant force and moment arising from the contact forces and any body forces (gravity etc.) acting on the particle. Also, the wall positions are updated based on the specified wall velocities.

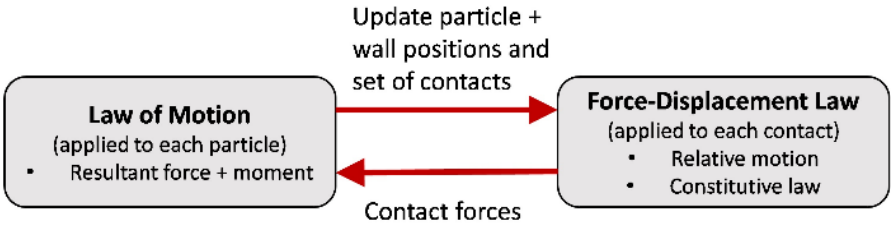

Fig. A-7 *Calculation cycle in PFC3D*

VI.III Mechanical Damping

In *PFC3D,* two types of damping are available for the kinetic energy dissipation: *Local damping* and *viscous damping* (*Itasca CG, 2008*). Local damping acts on each ball, while viscous damping acts at each contact. Local damping applies to each ball a damping force, proportionally to the unbalanced force. Viscous damping adds normal and shear dashpots at each contact. These dashpots act in parallel with the existing contact model and provide forces that are proportional to the relative velocity difference between the two contacting entities (ball-ball or ball-wall). By default, local damping is active, and viscous damping is inactive.

VI.IV Contact models

Contact models are used in *PFC3D* to the simulation of material behaviour (*Itasca CG, 2008*). The contact model shows how to derive the contact forces from the deformations (here the deformations mean the relative movements of the two material points which are in contact). *PFC3D* provides two standard contact models, which do not consist tensile resistance (linear and Hertz) and two types of tension resisting contacts and also several alternative contact models. In my models, a special type of contact model (parallel bond) is used, which was developed for the modelling of ‘cemented’ contacts.

VI.IV.I Force – Displacement Law of the contacts

In *PFC3D* the behaviour of the contacts is described by the force-displacement law (*Itasca CG, 2008*). This law gives the theoretical background of the relationship between the displacements and forces. The force-displacement law is related to the relative displacement between two entities at a contact to the forces and moments transmitted between the two elements. For both ball-ball and ball-wall contacts, these contact forces and moments arise from a contact occurring at a point (using the soft-contact approach). For ball-ball contact, a frictional contact model together with an additional force and moment arising from the deformation of the cementitious material represented by a parallel bond can also act on each particle. For ball-wall contacts, no cementation can be applied.

The force-displacement law operates at a contact and can be described in terms of a contact point, $x^{[C]}_i$, lying on a contact plane which is defined by a unit normal vector, *ni*. The contact point is within the interpenetration volume of the two entities. For ball-ball contact, the normal vector is directed along the line between ball centres; for ball-wall contact, the normal vector is directed along the line defining the shortest distance between the ball centre and the wall. The contact force is distributed into a normal component acting in the direction of the normal vector, and a shear component acting in the contact plane. The force-displacement law is described for both ball-ball and ball-wall contacts.

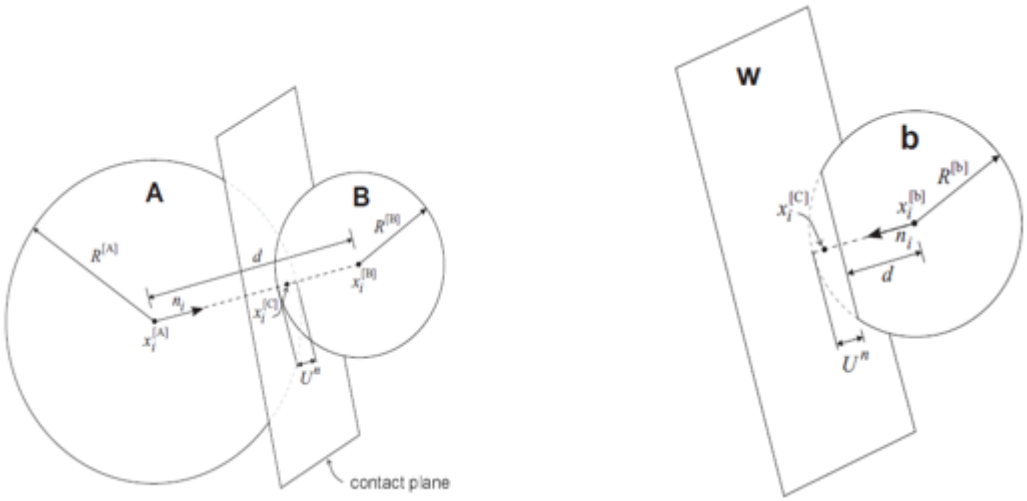

Fig. A-8 *Notation used to describe ball-ball and ball-wall contacts (Itasca CG, 2008)*

For ball-ball contact, the unit normal, n_i, that defines the contact plane is given by

$$n_i = \frac{x_i^{[B]} - x_i^{[A]}}{d} \text{ (ball-ball)} \qquad \text{(A-5)}$$

where $x_i^{[A]}$ and $x_i^{[B]}$ are the position vectors of the centres of balls A and B, and *d* is the distance between the ball centres (see *Fig. A-8*).

$$d = \left| x_i^{[B]} - x_i^{[A]} \right| \text{ (ball-ball)} \qquad \text{(A-6)}$$

For ball-wall contact, *ni* is directed along the line defining the shortest distance, *d*, between the ball centre and the wall. This direction is found by mapping the ball centre into a relevant portion of space defined by the wall.

The overlap *Un*, defined to be the relative contact displacement in the normal direction, is given by

$$U^n = \begin{cases} R^{[A]} + R^{[B]} - d\,, & (ball - ball) \\ R^{[b]} - d\,, & (ball - wall) \end{cases} \qquad \text{(A-7)}$$

where $R^{[\Phi]}$ is the radius of ball Φ.

The location of the contact point is given by

$$x_i^{[C]} = \begin{cases} x_i^{[A]} + (R^{[A]} - \frac{1}{2}U^n)n_i\,, & (ball - ball) \\ x_i^{[b]} + (R^{[b]} - \frac{1}{2}U^n)n_i\,, & (ball - wall) \end{cases} \qquad \text{(A-8)}$$

The contact force vector *Fi* (which represents the action of ball A on ball B for ball-ball contact, and the action of the ball on the wall for ball-wall contact) can be resolved into normal and shear components with respect to the contact plane as

$$F_i = F_i^n + F_i^s \qquad \text{(A-9)}$$

where F_i^n and F_i^s denote the normal and shear component vectors, respectively. The normal contact force vector is calculated by

$$F_i^n = K^n U^n n_i \qquad \text{(A-10)}$$

where K^n is the normal stiffness [force/displacement] at the contact. The value of K^n is determined by the current contact-stiffness model. The normal stiffness of the contact is given by the user, and with this, the program is able to calculate the contact force vector and from this the displacements of the balls.

The shear stiffness is calculated in incremental form

$$\Delta F_i^s = -k^s \Delta U_i^s \qquad \text{(A-11)}$$

because it relates to the increment of shear displacement.

VI.IV.II General remarks: Slip behaviour and cemented contacts

In *PFC3D*, slip behaviour provides the link between the normal and shear force, such that the two contacting entities can slip on each other (*Itasca CG, 2008*). The relation provides no normal strength in tension and allows slip to occur by limiting the shear force. Slip behaviour is always active unless there is a contact bond between the entities, in which case

the contact-bond behaviour overwrites the slip behaviour. The linear and Hertz models describe the force-displacement behaviour for particle contact occurring at a point. The parallel-bond component, on the other hand, describes the force-displacement and moment-rotation relations for cementitious material existing between the two balls. These two behaviours can occur simultaneously, in the way that we have a cementitious material (parallel-bond), but in the material, the particles come in contact with each other (linear or Hertz-model). Thus, in the absence of a contact bond, the slip behaviour is active in conjunction with the parallel-bond component.

VI.IV.III Contacts with tensile resistance

Parallel bond

PFC3D allows particles to be bonded together at contacts. Contacts arise and vanish during calculation cycles. The contact detection is defined in PFC with an efficient technique that is shortly described below. The two standard bonding behaviours are contact bonds and parallel bonds. Both bonds can be envisioned as a kind of glue joining the two particles. The contact-bond glue is of a vanishingly small size that acts only at the contact point, while the parallel-bond glue is of a finite size that acts over either a circular or rectangular cross-section lying between the particles. The contact bond can transmit only a force, while the parallel bond can transmit both a force and a moment. Once a bond is formed at a contact between two particles that contact continues to exist until the bond is broken. Particles may be bonded only to one another; a particle may not be bonded to a wall. I have investigated four types (contact bond, linear bond, Hertz bond, parallel bond) of contacts and based on their description and behaviour on a simple model, I have chosen to use parallel bond. The short description of the other contacts can be found also in this chapter.

A parallel bond provides the force-displacement behaviour of a finite-sized piece of cementitious material deposited between two balls. These bonds establish an elastic interaction between particles that acts *in parallel* with the slip or contact-bond behaviours. Thus, the existence of a parallel bond does not exclude the possibility of slip. Parallel bonds can transmit both forces and moments between particles, while contact bonds can only transmit forces acting at the contact point. Thus, parallel bonds may contribute to the resultant force and moment acting on the two bonded particles. A parallel bond can be envisioned as a set of elastic springs with constant normal and shear stiffness, uniformly distributed over a circular cross-section lying on the contact plane and centred at the contact point. These springs act in parallel with the point-contact springs that are used to model particle stiffness at a point. Relative motion at

the contact causes a force and a moment to develop within the bond material as a result of the parallel-bond stiffness. This force and moment act on the two bonded particles. The visualization of parallel bonds can be seen in *Fig. A-9*.

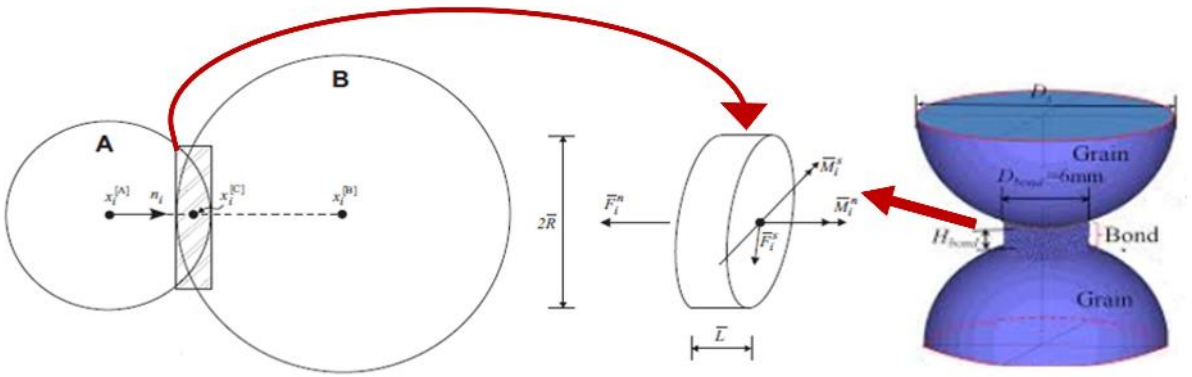

Fig. A-9 *Parallel bond depicted as a cylinder of cementitious material (based on Itasca CG, 2008)*

Contact bond

A contact bond can be envisioned as a pair of elastic springs (or a point of glue) with constant normal and shear stiffnesses acting at the contact point. (*Itasca CG, 2008*) These two springs have specified shear and tensile normal strengths. If a contact bond exists between two particles, slip is not possible.

Contact bonds also allow tensile forces to develop at a contact. These forces arise when U_n <0 (i.e., there is no overlap). In this case, the contact bond acts to bind the balls together. The magnitude of the tensile normal contact force is limited by the normal contact bond strength. If the magnitude of the tensile normal contact force equals or exceeds the normal contact bond strength, the bond breaks, and both the normal and shear contact forces are set to zero.

VI.IV.IV Contacts without tensile resistance

In this case the contact model does not contain tensile resistance. These types of contact models are used, when it does not make sense to assume tensile resistance between the particles (e.g. dry sand). *PFC3D* offers different options with different failure conditions to model such a contact. The behaviour of this type of contact is written by the force – displacement law. The description of the other

Linear model

The linear model provides a sliding behaviour, an optional contact-bond behaviour, and a constant stiffness behaviour. A parallel-bond component can be added to a contact with the linear contact model. The contact stiffness is defined by the normal and shear stiffnesses, k_n

and k_s [force/displacement], of the two contacting entities (ball-to-ball or ball-to-wall). If the parallel-bond breaks up, but the two particles are touching each other again, then a frictional contact will appear between them. Another possibility to model a linear contact is the Coulomb-frictional contact model. In this case the normal force cannot become positive. If there is no overlap between the two elements, then the contact does not exist anymore. The tangential force has a limit depending on the compression. If the tangential force reaches this limit, the relative tangential translations increase beside a constant tangential force, as long as the direction of relative translations does not change.

Hertz model

The Hertz model provides sliding behaviour and stiffness that varies as a function of the elastic constants of the two contacting entities, overlap and normal force. The Hertz model is not defined for tensile forces, and in this sense is incompatible with bonding. However, a parallel-bond component can be added to a contact with the Hertz contact model. The Hertz-Mindlin contact model is a nonlinear contact formulation based on an approximation of the theory of Mindlin and Deresiewicz and described in *Cundall (1988)*. It is strictly applicable only to the case of spheres in contact, and does not reproduce the continuous nonlinearity in shear (instead, the initial shear modulus is used, but it depends on the normal force).

VI.V Contact detection

PFC3D uses an efficient technique to identify pairs of balls (or balls and walls) that are in contact, and to represent their geometric and mechanical characteristics. It is important to have a data structure that allows relevant data to be retrieved rapidly when it is needed, particularly in view of the explicit nature of the mechanical calculations, which often contains many thousands of calculations through the main cycle. (*Cundall, 1988*) All data blocks are stored and managed internally by *PFC3D*. Each physical entity (such as a ball, a wall or a contact) is represented by a "data element." A single data element is assigned for each ball, wall, and contact. Each data element contains geometric and mechanical data, as well as a pointer, which points to the next element in the arbitrarily ordered linked list of similar elements. Contacts are being formed and broken continually during the simulation, making it imperative that an efficient technique be used to identify pairs of entities. It is not possible to check all possible pairs before each timestep, because the search time would increase quadratically with the number of entities in this case. Instead, the space containing the balls and walls is divided into rectangular three-dimensional cells. Each element is mapped into the cell or cells that its "envelope space" occupies. The envelope of an entity space is defined as the smallest three-dimensional brick-shaped box with sides parallel to the coordinate axes that can contain the

entity. Once all entities have been mapped into the cell space, it is easy to identify the neighbours to a given entity, because the cells which correspond to its envelope space contain entries for all nearby entities. The overall computer time for neighbour detection is, consequently, directly proportional to the number of entities, provided that cell volume is proportional to average entity volume.

VI.VI Mechanical Timestep Determination

The equations of motion are integrated in *PFC3D* using a centred finite-difference scheme. (*Itasca CG, 2008*) The computed solution produced by these equations will remain stable only if the timestep does not exceed a critical timestep that is related to the minimum eigen-period of the total system. However, if the examined system is not elastic, there is dissipation in the system:

- because of the contact friction/contact fracture
- and because of the damping (to reduce the numerical originated oscillations).

Due to these effects, the estimation of the critical time step in *PFC3D* is very unreliable, so the users should pay special attention to this and need checking whether the chosen time step length was correct.

VII. Overview of available approaches for constructing random particle arrangement

VII.I Dynamic techniques

Dynamic methods are the typical approach to place the required number of particles into the domain of interest (*Bagi, 2012*). In this case the preparation of the initial arrangements is made by the DEM code and the software itself generates the geometry and the location of the assemblies. In these algorithms each movement of a particle requires the solution of the relevant differential equation. This procedure slows down the calculation process. One possible way to use this technique is to place the required number of particles into the domain of interest, but with much smaller diameters than their expected final size. Then the diameter of each particle is increased until reaching the required density level. During the densification process there are multiple collisions, until the particles push each other into an evenly dense arrangement.

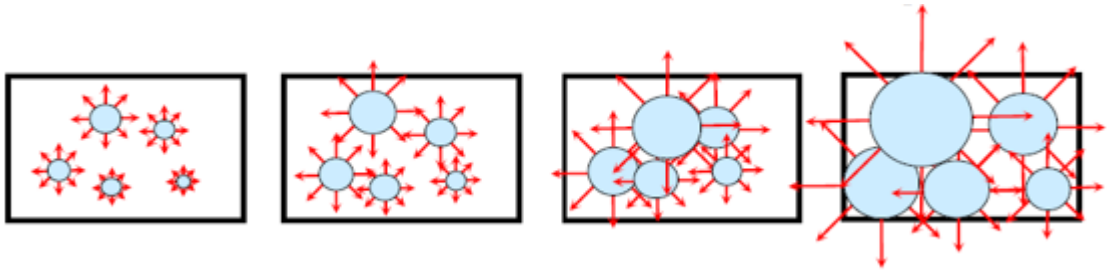

Fig. A-10 *Gradual increase of the elements (Bagi, 2012)*

As an alternative solution, having assigned the final size to the particles, they can be placed into a larger domain than the finally expected whose walls are slowly moved inwards until the required density is reached. This method also involve multiple collisions during the densification process.

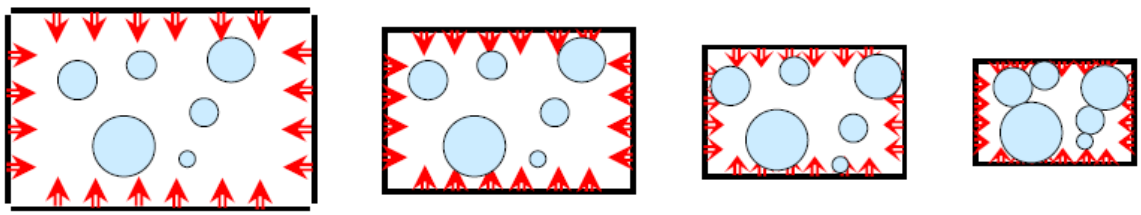

Fig. A-11 *Isotropic compression (Bagi, 2012)*

A next possibility is the simulation of a gravitational deposition. In this case the particles are fall into the domain of interest and then find their equilibrium position due to gravitational forces. Here the final size of the particles is used from the beginning of the process.

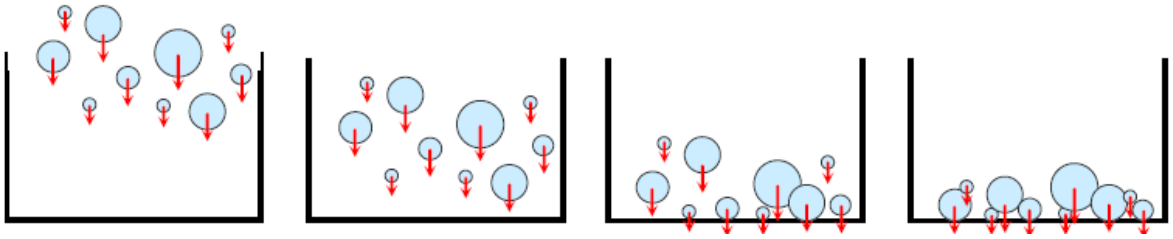

Fig. A-12 *Gravitational deposition (Bagi, 2012)*

These techniques are quite time-consuming, because the large amount of necessary calculations.

VII.II Constructive algorithms

In these algorithms the assemblies are prepared with the help of purely geometrical calculations. With this the user is able to avoid the simulation of the dynamics of particle motions. Therefore, these algorithms are more efficient by orders of magnitude, but the chosen method must be programmed, because they are commercially not available for free. Nevertheless, because the dynamic sample preparation methods are rather time-consuming the constructive methods are becoming more popular in practice.

To produce random sets of equal or non-equal spheres one can find several methods in literature (e.g.: Stienen model, lily-pond model, SSI, dropping method etc.). From these methods the ***SSI*** (Simple Sequential Inhibition) method is used in the *PFC2D* and *PFC3D* codes. In this case the spheres of given diameters are placed at random positions in the domain of interest. If a newly placed particle intersects a previous one then the new particle is rejected and the algorithm places another particle into another part of the domain. This process runs after a pre-defined high number of unsuccessful tries to place a new particle in the domain.

In the dropping method the required domain is filled up starting from the bottom, adding one particle in each step to the already existing set of grains. The new particle needs to touch exactly two previous particles (with no overlaps) or one of the walls of the domain. The new particle is placed on the previous ones, so that if the previous particles are assumed to be fixed, then with the application of a downwards force the new grain would be in stable position.

There is another new constructive method (Inwards Packing Method) introduced in an article written by Bagi for the preparation of random, isotropic assemblies of contacting circular discs with a user-defined grain size distribution (*Bagi, 2005*).

A brief description of the method:

With the help of the algorithm one can fill up a domain that is bounded by fixed straight walls with a given grain size distribution. The steps of the algorithm are the following:

1 As a first step the edges of the domain are filled, in a way that the particles are producing a closed chain, called the initial front.

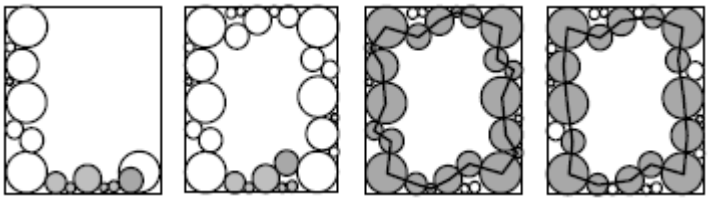

Fig. A-13 *The initial front (Bagi, 2005)*

2 The new particles inside the initial front packed along the front in a way that it connects two already existing particles. The front is then updated, and a next particle can be generated.

3 When no other new particle can be placed without overlapping then a few smaller particle are inserted into the domain until a given number of unsuccessful tries.

4 As a last step the already existing assembly can be densified by adding new particles into the voids. (*Bagi, 2005*)

Because of the complexity of the problem, several of existing methods have difficulties in handling large numbers of particles. The simulation model made by Sobolev proposes to overcome this. (*Sobolev, 2004*) The model assumes that the centers of the spheres are randomly generated at the intersections of a cubic lattice. The largest possible spheres are packed first; subsequent spheres are limited by the set of minimum diameters, which is specified by the constraints imposed by two major parameters imitating the compaction gradient: a reduction coefficient and the number of packing trials. One of the biggest aims of the model is, that it is able to follow a given particle size distribution, but it is not always generates particles which are in contact.

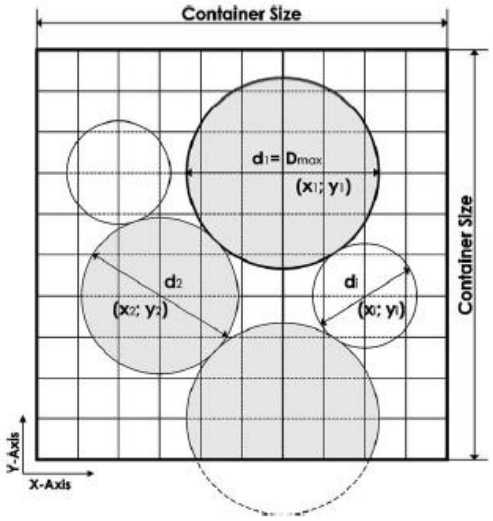

Fig. A-14 *2D representation of the packing model (Sobolev, 2004)*

VII.III Collective rearrangement techniques

In these methods the number of particles is defined by the user and this number is fixed during the sample preparation process. Initially the particles are placed randomly in the domain of interest. Overlaps are allowed and their size are reduced during the process by moving the grains. In every step the displacements of each particle are calculated from the overlaps, similarly to the dynamic techniques. These techniques, like the dynamic methods, are rather time-consuming.

VIII. The steps of the Material-Genesis Procedure

- **Compact initial assembly:** Fill the material vessel with particles (or clumps). If there are confining walls, then they are made frictionless, and their normal stiffness is much larger than the average normal stiffness. The particles are placed randomly (with a 35% porosity) with a much smaller radius than the required, and no two particles overlap. Then, the particle radii are increased gradually to their final values, and the system is allowed to reach static equilibrium under zero friction.
- **Install specified isotropic stress:** The radii of the particles are changed uniformly to achieve a specified isotropic stress (mean value of the three principal stresses). This is a typically low value relative to the material strength (e.g.: less than 0.01% of the uniaxial compressive strength).
- **Reduce the number of "floating" particles:** After the first two steps, one has achieved an assembly of nonuniform radius particles, placed randomly. These kinds of assemblies can contain a lot of floating particles (those which have fewer than three contacts). It is desirable to reduce the numbers of this type of element, in order to obtain a denser network of bonds.
- **Finalize specimen**: If all of the contact and parallel bonds are installed, then all particles are assigned the specified friction coefficient. The material vessel can be removed, and the specimen can be used for a boundary-value simulation, or it can be subjected to material testing.

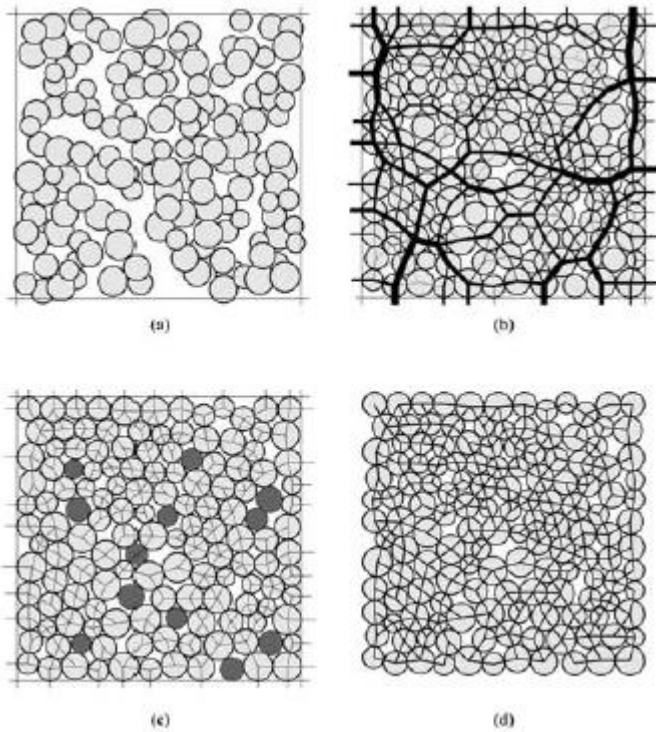

Fig. A-15 *Material genesis procedure: (a) particle assembly after initial generation but before rearrangement; (b) contact force distribution after the second step; (c) floating particles and contacts after the second step; (d) parallel-bond network (Itasca CG, 2008)*

This procedure runs until the mean stresses in the parallel bonds becomes almost zero, and the model reaches static equilibrium, as it can be seen in *Fig. A-16*.

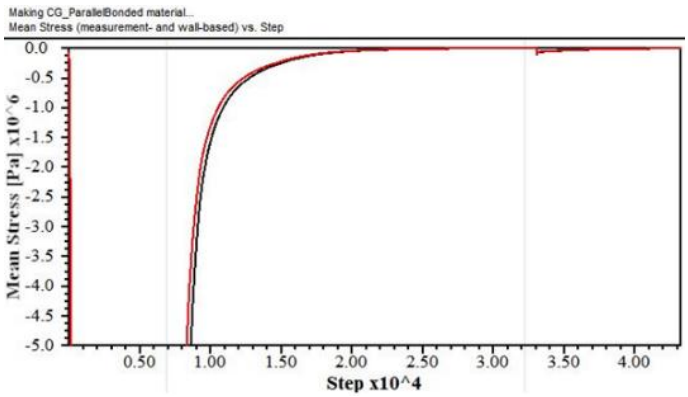

Fig. A-16 *Mean Stress in parallel bonds versus the number of steps*

IX. The initial parameters of the DE model of normal strength concrete

Information about the parameters is obtained from the literature on the modelling of concrete. The most important parameters which influences the behaviour of the model are the density of the balls, the friction coefficient, as well as the shear and normal strength of the bonds, as it is shown in *Fig. A-17*. The bulk modulus of the balls is considered as a constant (it is equal to 1), because the elements are infinitely rigid.

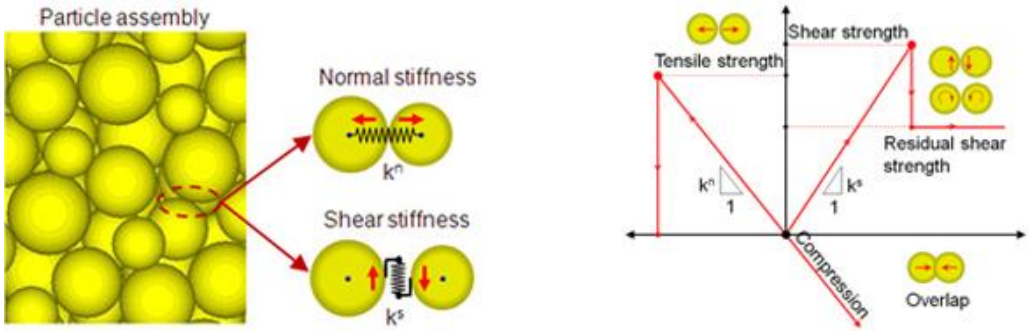

Fig. A-17 *Normal and shear stiffness of the parallel bonds (www.ngi.no)*

Parameters of the balls:

- Bulk modulus = 1 (infinitely rigid discrete elements).
- Ball or bulk density = Density of concrete in kg/m^3.
- Friction coefficient = 0.40 (*Szilágyi, 2009*).

Parameters of the parallel bonds (*Szilágyi, 2009*):

- $k_n=E_c/(R_a+R_b)$ ➔ $E_{c,pb} = 3.5\times10^{10}$ N/m^2,
- the mean value of the normal strength = 5×10^7 N/m^2,
- the standard deviation of the normal strength = 5×10^6 N/m^2,
- the mean value of the shear strength = 3×10^6 N/m^2,
- the standard deviation of the shear strength = 3×10^5 N/m^2.

During the modelling the standard deviation of the normal strength is set to a tenth of the mean value of the normal strength based on literature recommendations and *Appendix X*.

X. Sensitivity analysis on the standard deviation of the normal strength of the parallel bonds [8]

The standard deviation of the normal strength was chosen to be 10% of the mean value of the normal strength based on the sensitivity analysis I have conducted. Present chapter shows the results of the compression test models that are presented together with the results of the sensitivity analysis. For every investigated concrete type five models were created for every standard deviation values. In every case the normal strength was measured and for every standard deviations it was averaged. After that its difference from the real mean value (with 0 standard deviation) was calculated as an absolute value to be able to analyse the results statistically. In *Table A-3* the results for a C12/16 concrete sample can be seen.

Table A-3 *Results of the sensitivity analysis (C12/16)*

Standard deviation of the strength of the parallel bonds [%]	0	1	10	20	30	40	50	70	100
Average normal strength of the material [N/mm^2]	**26.5**	**26.36**	**26.16**	**25.26**	**24.42**	**24.48**	**24.3**	**26.08**	**28.44**
Difference from mean value [N/mm^2]	0	0.14	0.34	1.24	2.08	2.02	2.2	0.42	1.94
Difference from mean value [%]	0	0.53	1.28	4.68	7.85	7.62	8.3	1.58	7.32

The behaviour for the different types of concrete were very similar as it can be seen on *Fig. A-18*. It can be seen on the figure that with the increase of the standard deviation the difference of the compressive strength of the samples also increases.

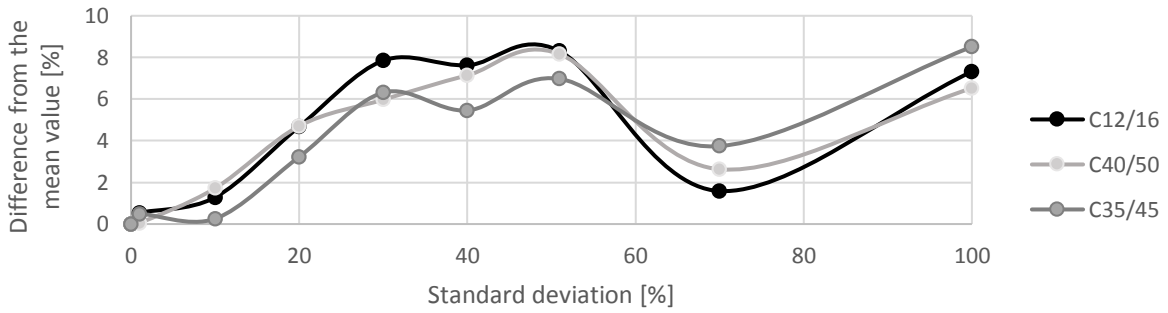

Fig. A-18 *Difference from the mean value in function of the standard deviation*

This is valid only until the standard deviation reaches a given value (around 50 %), after that a decrease was observable for all concrete samples. It is important to mention that until 50% the differences are increasing on the safe side of the mean value. In case of 100% standard deviation the difference is again higher, than it was in case of 70%. It is not clearly understood until now, why this decrease in the results appeared. It has to be mentioned that all the values in difference were under 9%, which can be considered as significant difference. However, if we keep the value of standard deviation under 10% then a very small difference can be observed, but the measurements become more realistic. In real measurements there is also a

small difference in the results. In case of the modelling if we choose the value of standard deviation to 0 then always the same result appears, which is unrealistic. Based on these investigations it is recommended to use a given value of standard deviation for the modelling of concrete, however it should be chosen under 10%.

XI. Model of the DSI testing procedure

The DSI testing procedure has a similar aim, as the Brinell-hardness test: to determine the hardness of the material. However, an important difference is that the Brinell-test is using a given constant load during the testing, while during the DSI test, the load is increasing continuously. To model this procedure, the script of the hardness testing was modified. In this code, instead of a constant loading, a loop was constructed during which after a given number of steps the loading force always increases with a predefined increment. In my case the load step was always 2500 N. Thus, the measured load steps were the following: 2.5 kN, 5 kN, 7.5 kN, 10 kN, 12.5 kN, 15 kN, 17.5 kN. In every load step, several calculation cycles were run. If one decreases the number of load steps and increases the number of loops, a more accurate result can be reached, but due to the large computational effort, this value was chosen. During this cycle, the code monitors the displacement of the loading sphere along the *z* axis as well as the actual loading force. From these two values, the required diagram can be plotted. From this plot, the maximum value of the indentation depth can be read (as it was explained in *Chapter 3.1.2.2*.

XII. Comparison of DEM and FEM

In this chapter, DEM is compared with the most widely used numerical method in engineering, the FEM. The similarities and the differences between the two approaches are highlighted, and it is shown, which is more useful in which cases. It is also worth to mention that these methods can be applied together or separately (*Chung et al, 2016*). Often an engineering problem can be modelled using only one of the aforementioned methods like a steel beam would be simulated by FEM, a small assembly of gravel particles by DEM. If one would like to model a steel beam lying on a gravel bed, one has to use both of the methods together. Or the same phenomena can be modelled by using both methods to gain more precise information (*Fig. A-19*). In an article by Rousseau about this topic the authors combined the DEM with FEM to investigate the effect of an impact into a concrete structure (*Rousseau, 2009*). The aim of the study was to combine the advantages of the DEM with the effectiveness of the FEM and reduce the computation time. The DEM was used to model the media in the vicinity of the impact, the remaining parts were modelled with FEM.

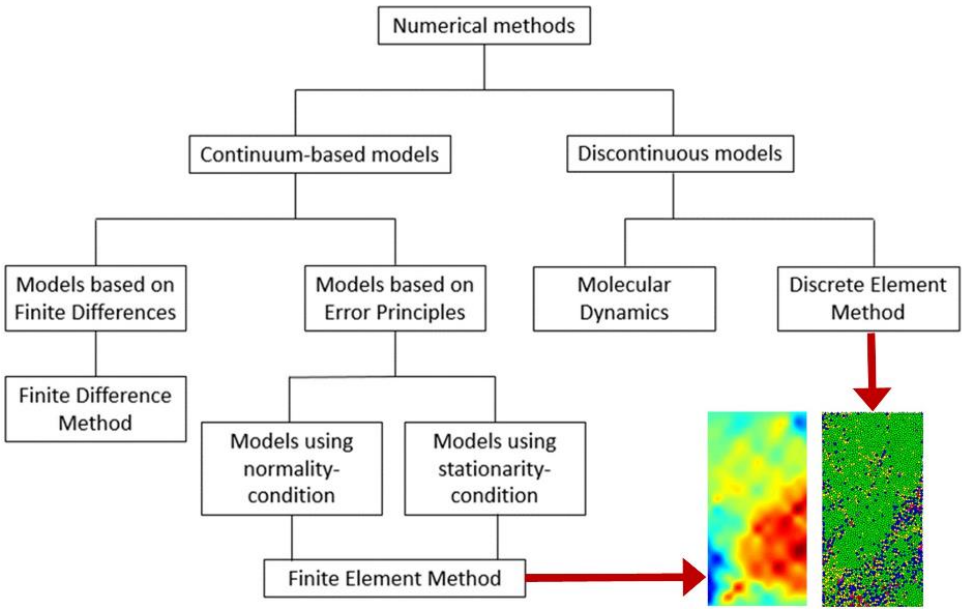

Fig. A-19 *Classification of numerical methods and the simulation results of a biaxial test modelled in DEM (left) and in FEM (right)*

Figure A-19 shows a classification of the most important numerical methods in engineering. Numerical methods can be divided into two main groups, according to the continuity of the applied mechanical model: continuum-based versus discontinuous models. DEM belongs to the group of Discontinuous Models, together with the different Molecular Dynamics methods. Molecular Dynamics uses point-like elements, while DEM uses finite sized elements, being extended in space. In case of Molecular Dynamics, the distant elements also interact with each

other, while in case of DEM, only those elements express forces on each other that are in contact. In the group of the Continuum-based Models, the most well-known method is the Finite Element Method, which belongs to the group of models based on error principles. There are two different types of error principles, the so-called Normality (or Projection) condition, where the selected error-vector assigned to the problem must be orthogonal to a sub-space, and the so-called Stationary (or Length) condition, where the bilinear form of the selected error vector must have a minimum at the solution of the problem. The main idea of FEM is that the basis functions determining the space of calculation are defined in a special way; thus, FEM can belong to both groups.

The main difference between the two methods is that FEM is rigorously derived from the continuum theory and it is being used for the description of deformable continuous bodies, while DEM describes particulate materials, usually modelled by perfectly rigid particles and their interactions determined from fictitious overlaps of these rigid particles (*Vadluga and Kacaianauskas, 2007*). Another significant difference is the different space discretization. FEM uses assemblies of finite elements, while discrete parameters are attached to the nodal points, which can be found within the continuous elements. To the solution, an algebraic model is used, which covers all elements in the domain. In case of FEM, there are two difficulties that are sometimes handled inadequately: the rapid changes in the structural geometry and the time tracking of dynamic processes. Conversely, in case of DEM, the aim is to describe the mechanical behaviour of a granular material composed of discrete elements, which are considered separately and represents a material particle in the sample. Additionally, DEM operates based on the single-point approach, meaning that all the parameters of a particle (discrete element) are associated with the centre of the particle.

The main goal of any DEM simulations is the continuous tracking of the particle behaviour. The given position of a particle in a DE model is defined by a dynamic equilibrium of forces acting on the particle, which is defined on the basis of fully deterministic equations of motion of classical mechanics. These properties allow the DEM simulations to handle shock type behaviour well (like a rapid change in the geometry). This method has several advantages compared to the FEM in the field of granular material investigation, but there is a disadvantage too; the maximum number of particles and duration of a virtual simulation is limited by computational power. Typical samples contain billions of particles, but contemporary DEM simulations on large cluster computing resources have only recently been able to approach this scale for sufficiently long time (simulated time, not actual program execution time). Meaning, that we need to narrow the scale of the simulated particles. In my case it was solved in a way,

that only the aggregate particles of concrete were modelled, while the cement particles were represented by the bonds among the particles.

DEM is based on Newton's second law ($F = m \times a$), while Finite Element Method applies $F = K \times d$, inverted to $d = K^{-1} \times F$. It can be said that the methods are respectively force- and displacement based. In *Table A-4*, the differences and similarities of the DEM and the FEM are summarized.

Table A-4 *Comparison of Discrete Element Method and Finite Element Method*

Method	**DEM**	**FEM**
Type of elements	Discrete Elements	Finite Elements
Mobility of the elements	Elements can move independently to each other	Movements of an element always depend on the neighbour elements
Model continuity	Discontinuous	Continuous
Usually modelled materials	Granular Materials	Continuous Materials
Background	Describes granulated materials	Derived from continuum theory
Constitutive equation	Newton's second law: $F = m \times a$	$d = K^{-1} \times F$
Nodes	A node point belongs to only one element	Node points very often belong to multiple elements
Advantages	Able to handle rapid change in geometry	Fast and accurate in case of continuous materials
Disadvantages	Large computational effort	Time tracking of dynamical processes, handling of rapid geometry changes

I have conducted a study where I have compared DEM and FEM on two specific examples. I have modelled in a simple approach the compressive strength testing and the Brinell hardness testing of concrete using both methods. The laboratory test results showed that the compressive strength of the real material is 54.23 N/mm^2. In case of the DE model, quantitatively the result is the same, and its σ-ε curve is very similar to the σ-ε curve of the real material. The finite element model was slightly conservative (on the safe side), the compressive strength was 44.13 N/mm^2.

The average indentation diameter measured in the laboratory was 3.95 mm. The DE model slightly underestimated the indentation diameter (3.53 mm) and thus overestimated the hardness and compressive strength of the material. The model was capable of capturing the remaining imprint on the surface of the material. The result could be improved by applying different failure criteria because, in this model, a standard failure criterion was used (*André et al, 2013*). The FE model strongly underestimated the indentation diameter (2.05 mm); however, the modelling of a hardness test was possible. The model could be improved by using a more detailed material model for concrete or with the further tuning of the contact stiffness. In conclusion, DE model is an appropriate choice for this purpose [15].

XIII. General description of the FISH programming language

FISH is a programming language embedded within the *PFC3D* software. (*Itasca CG, 2008*) By using this software the user is able to define new variables and functions, which makes the software more diversified. The user is able to plot or print the new variables, special particle generators can be implemented, servo-control may be applied to a numerical test or unusual distributions of properties may be specified. In this section I would like to give a short overview about the most frequently used *FISH* commands and highlight some interesting properties of this programming language.

FISH programs are simply embedded in a normal PFC data file: lines following the word "define" are processed as a FISH function; the function terminates when the word "end" is written into the code. Functions are allowed to contain other functions, which can also contain other functions and so on. The order in which functions are defined does not matter, so long as they are all defined before they are used (e.g., invoked by a PFC command). Since the compiled form of a FISH function is stored in PFC's memory space, the "save" command saves the function and the current values of associated variables. I have been created my files in a way that they all are called in a different file (by using CALL function). It makes the running and testing of the program easier, because if some parts of the code are not necessary in a case then they are disabled only by commenting out one line in the calling file. The PLOT and PRINT functions are used to show the relevant information for the user. The PRINT function writes the required data above the command line into the Console panel, while the PLOT function creates a new plot, where charts, walls, domains or the model itself can be plotted. SET command can be used to set the value of any user-defined FISH symbol, independent of the FISH program in which the symbol was introduced. To create charts always the command HISTORY is used, which is stores the values of the predefined variable during the process, and it can be plotted in function of the timestep or in function of any other given parameter or variable. “If” statements and looping is also possible in *FISH* which has practical use in a case, if we want to select a large number of balls in a model and for example change a property of them. The looping is opened with the function LOOP and closed by the ENDLOOP function. The “if” statement has the similar use in *FISH* as in every programming language, it used as a conditional expression to select between alternatives in runtime. There are three statements, which are allowed to make decisions in a program: IF, ELSE, ENDIF. The ELSE option can be repeated as many times as necessary (number of the different alternatives). One of the most important commands in the FISH, is the so called CYCLE command, which makes the program

running and makes calculation cycles. After the CYCLE command only one parameter is given, which determines the number of calculation cycles. There is also a not so frequently used, but in case of models with a huge amount of particles very useful command, called RESTORE. This command restores the model into a given (previously saved) state. This command was very useful in my case, because with help of it, at the start of the tests, the saved model state was always restored, thus I was able to perform a lot of test on the same sample. By using this function I spared a lot of time during my project.

If somebody do not want to learn a new programming language, but he or she has programming skills in other languages, it is also possible to use the plug-in option of the software. With this option, the user may create *FISH* scripting intrinsics and load them at runtime as plug-ins. The *FISH* intrinsic must be written in C++ and compiled as a DLL file (dynamic link library) that can be loaded whenever it is necessary to use. The *FISH* intrinsic uses a C++ interface that provides access to the internal structure of *FISH*, as well as the data of PFC. When loaded, this intrinsic behaves exactly the same as any of the predefined *FISH* intrinsics. This is not only a possibility but it has several advantages too over the traditional *FISH* functions, like they are faster to execute (it does not makes the calculation cycles faster).

The *PFC Fishtank* is provided to users because most of them do not have the time and/or expertise to construct such a set of functions themselves and are, instead, more interested in applying solids-based models to particular applications. For such users, the *PFC Fishtank* can serve as a good starting point. The algorithms, which can be found in the *PFC Fishtank* are intended for modification by those who are comfortable with computer programming and knowledgeable about the FISH language (the language developed by Itasca for their softwares). The users, who have these skills, the built-in algorithms can serve as a basis for writing their own PFC codes to solids based applications or for performing biaxial or triaxial tests upon different particle assemblies. The greatest advantage of these algorithms that by using them one can spare a huge amount of time and resource, because they are the part of the source code of PFC (and thereby they are also a part of the basic set of commands). It is important to understand, that the *PFC Fishtank* functions have been applied primarily to modeling hard, crystalline rock materials such as granite. When one applies these algorithms to systems with very different characteristics, it will be necessary to modify some of the control parameters to obtain stable model behavior. The codes are monitoring the behavior of the material and with the help of those control parameters can be determined the actual state of the model. The control parameters can be imagined as the given values of the points, where the process can go further

on different ways and based on the comparison of that parameter and the calculated value, the code chose in which to go further. Also, many of the algorithms (e.g.: those used to obtain a dense packing with low stresses in the bonds) involve simulation of highly nonlinear processes, and thus it cannot be guaranteed that the model will behave stably for every cases (different input parameters). For these reasons, the concepts underlying the particular implementations of these algorithms are described in some detail, to enable the user to extend or fine-tune specific algorithms for specialized applications. In the present case some of the parameters had to be modified too.

XIV. Relation of element number and computational time of a DE model

All the numerical simulations presented in this thesis were performed on a workstation with an Intel® Core™ i7-5820K CPU (3.30 GHz) and 64 GB DDR RAM and an ASUS® R9 390 graphic card with 4 GB inbuilt memory.

It was investigated what is the relation between the number of elements, the computational time and the size of the specimens, using the specimens and models of the size effect study. Besides that, the effect of minimum particle size was tested. It was observed that the edge length of the cube specimens and the diameter of the cylinder specimens are in a cubic relationship with the number of particles in the model (see *Fig. A-20*), as it was expected. This relationship is not influenced by the chosen minimum particle size. As it comes from the relation of the volume and the edge length (or diameter), the relationship of the volume with the number of elements is linear. As expected based on the particle size distribution of the mixes, Mix 2 contains the highest number of elements, while Mix 4 the lowest.

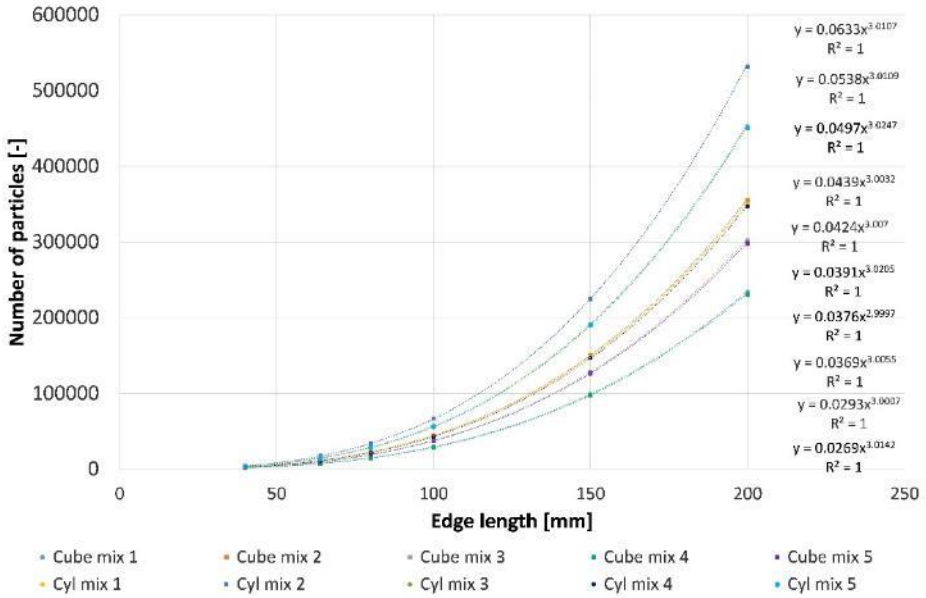

Fig. A-20 *Edge length vs. Number of particles in the DEM*

Similar relationship (cubic) was observed between the edge length and the number of contacts as well. It means that the number of contacts and particles are in a linear relation. After the material generation, the ratio of the number of contacts and particles was slightly above two, meaning that every particle had at least two contacts.

The computational time of the material generation is strongly corresponding to the number of elements (and contacts) and it shows a quadratic polynomial relation between them.

Similarly to the element number, the computational time is also increasing according to a quadratic polynomial with the volume of the specimen. As it can be seen in *Fig. A-21* in case of the larger samples the number of particles is high, which requires high computational effort (~30 hours), which is unacceptable for practical engineering application. It is aimed in this study to propose an approach which can decrease the required time necessary for material generation.

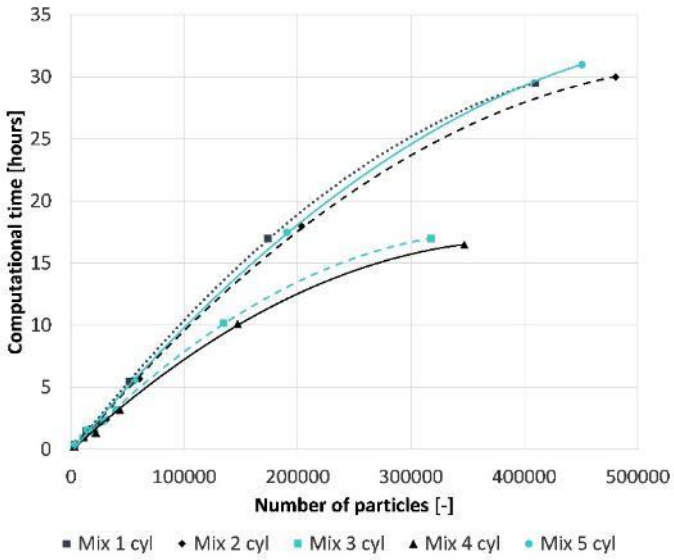

Fig. A-21 *Computational time vs. Number of particles for all three mixes measured on cylinders*

It was also investigated how the computational time is influenced by the minimum particle size. It was found that the number of elements increases with the decrease of the minimum particle size, however only to a slight extent. It had a negligible effect on the computational time in overall.

XV. Properties of AAC

The most important properties of the original AAC block (the base material of the study), based on its declaration of performance:

- mean compressive strength: 3.0 N/mm^2,
- thermal conductivity: 0.125 W/mK,
- water vapour permeability (dry/wet): 5/10.

In a mix design point of view, there are some important properties of the aggregate depending on the grain size. Therefore, many differences were found in the lightweight aggregate performance compared with earlier researches, where AAC waste was used only as coarse aggregate (*Sinica et al, 2009*; *Shui et al. 2014*). These main properties were particle body density and total porosity of the different grain sizes. It is because during the crushing process porosity is decreasing, while the particle body density, as well as the bulk density (in different rate), are increasing, as it is shown in *Fig. A-22*. These parameters are extremely important because they are input data of the concrete mix design process. This effect is not obviously true in case of the water demand of the lightweight aggregate concrete mixture, because as the inner open porosity (apparent water absorption capacity) of the aggregate is decreasing during the crushing process, the specific surface of the smaller grain sizes is increasing, which can be seen in *Table A-5*. These parameters are determinative in the aspect of consistency, especially if the concrete is going to be pumped because a lower consistency mixture can stick in the pipe. This change in the water demand of the concrete mixture should be calculated during the mix design (water dosage and super plasticiser admixtures). The open porosity causes internal curing of the cement matrix, which is advantageous for concrete parameters (e.g. strength, water tightness, early age shrinkage, durability, etc.); therefore, it is also advantageous in the point of view of cost-efficiency.

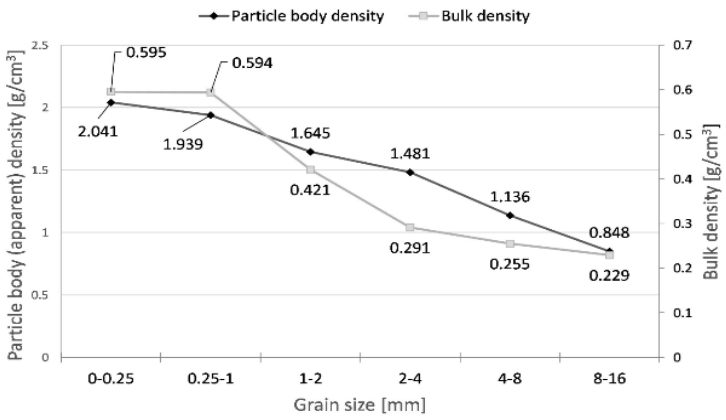

Fig. A-22 *Change of the particle body (apparent) density and bulk density due to the aggregate particle size*

Table A-5 *Aggregate material properties due to the grain size*

Grain size [mm]	Water absorption capacity [m%]	Water absorption capacity [V%]	Particle body (apparent) density [g/cm^3]
0/0.25	-	-	2.041
0.25/1	-	-	1.939
1/2	14.7%	24.2%	1.645
2/4	13.0%	19.3%	1.481
4/8	17.1%	19.4%	1.136
8/16	15.3%	13.0%	0.848

Water absorption in case of the 0/0.25 and 0.25/1 fractions cannot be measured, because the water amount on the surface of the grains is higher than the water amount inside the grains. Water absorption of the coarse aggregate was determined by using pycnometric method. The 1 hour water absorption value was used to design the water demand of the mixes in the different phases.

XVI. Summary table of all applied concrete mixes

Table A-6 *Summary of all applied concrete mixing proportioning and the composition of the Y10 mix*

Name of mixture	*CEM I 42.5 N*	*Waste material*	*Fine aggregate*	*Coarse aggregate*		*Water*
			0/4	*4/8*	*8/16*	
GC	*264*	*0*	*1356*	*291*	*291*	*176*
GA	*264*	*0*	*775*	*581*	*581*	*176*
GN	*264*	*0*	*0*	*584*	*584*	*176*
SC	*264*	*0*	*1356*	*291*	*291*	*176*
SA	*264*	*0*	*775*	*581*	*581*	*176*
SN	*264*	*0*	*0*	*584*	*584*	*176*
LN	*264*	*0*	*0*	*503*	*0*	*176*
Reference	*270*	*0*	*936*	*498*	*557*	*154*
Y3	*262*	*8.1*	*936*	*498*	*557*	*154*
Y10	*243*	*27*	*936*	*498*	*557*	*154*
Y17	*224*	*46*	*936*	*498*	*557*	*154*
MK10	*243*	*27*	*936*	*498*	*557*	*154*
MK/Y 7/3	*243*	*27*	*936*	*498*	*557*	*154*
Reference	*325*	*0*	*774*	*484*	*677*	*130*
Y3	*315*	*10*	*774*	*484*	*677*	*130*
Y10	*292*	*33*	*774*	*484*	*677*	*130*
Y17	*270*	*55*	*774*	*484*	*677*	*130*
MK10	*292*	*33*	*774*	*484*	*677*	*130*
MK/Y 7/3	*292*	*33*	*774*	*484*	*677*	*130*
Size effect						
Mix 1	*264*	*0*	*910*	*542*	*484*	*176*
Mix 2	*380*	*0*	*984*	*358*	*447*	*190*
Mix 3	*360*	*0*	*642*	*458*	*733*	*180*
Mix 4	*500*	*0*	*595*	*425*	*679*	*175*
Mix 5	*500*	*0*	*789*	*470*	*470*	*175*

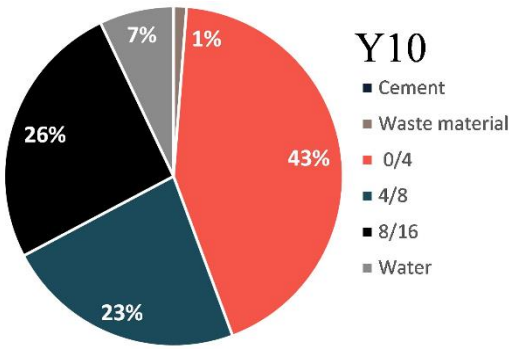

XVII. Material properties of the materials used in the hardness studies

Table A-7 *Material properties of the investigated materials*

Material	***Compressive strength [N/mm^2]***	***Young's modulus [N/mm^2]***	***Density [kg/m^3]***	***Body density [kg/m^3]***	***Porosity [V%]***	$\sqrt{\frac{E}{\rho}}$ ***[m/s]***
Aluminium	*350*	*70000*	*2700*	*2700*	*0*	*5.1*
Mild steel	*420*	*200000*	*7850*	*7850*	*0*	*5.0*
Reinforcing steel bar	*600*	*210000*	*7850*	*7850*	*0*	*5.2*
Normal strength concrete	*54.2*	*34578*	*2300*	*2258*	*14.65*	*3.9*
High strength concrete	*106.2*	*43802*	*2645*	*2414*	*8.72*	*4.3*
Polymer concrete	*98.7*	*40000*	*2254*	*2097*	*6.96*	*4.4*
Cellular concrete block	*2.02*	*500*	*2535*	*516*	*79.66*	*1.0*
Sand-lime brick	*19.3*	*2000*	*2575*	*1711*	*33.54*	*1.1*
Clinker brick	*80.9*	*35000*	*2745*	*2370*	*13.65*	*3.8*
Facebrick	*23.3*	*3000*	*2645*	*1711*	*35.3*	*1.3*
Clinker tile	*233*	*65000*	*2531*	*2254*	*10.96*	*5.4*
Porous limestone A	*12.4*	*5199*	*2640*	*1808*	*31.52*	*1.7*
Porous limestone B	*9.2*	*5127*	*2725*	*1769*	*39.61*	*1.7*
Compact limestone	*108.5*	*56402*	*2690*	*2502*	*6.99*	*4.7*
Rhyolite tuff	*30*	*10206*	*2385*	*1615*	*32.27*	*2.5*

XVIII. Correlation coefficients and multipliers of Meyer's law

Table A-8 *Correlation coefficients and k_1 multipliers of all materials for both DSI and Brinell test*

Materials	***DSI***		***Brinell***	
	k_1 [N/mm]	***r^2***	***k_1 [N/mm]***	***r^2***
Aluminium	*31325*	*0.997*	*25213*	*0.999*
Mild steel	*44816*	*0.996*	*44471*	*0.995*
Reinforcing steel bar	*75838*	*0.991*	*65454*	*0.99*
Normal strength concrete	*20842*	*0.963*	*15455*	*0.986*
High strength concrete	*39128*	*0.963*	*34192*	*0.994*
Polymer concrete	*21059*	*0.959*	*16553*	*0.99*
Cellular concrete block	*225*	*0.993*	*-*[1]	*-*
Sand-lime brick	*4391*	*0.995*	*3718*	*0.998*
Clinker brick	*74535*	*0.941*	*65817*	*0.988*
Facebrick	*5019*	*0.994*	*4909*	*0.937*
Clinker tile	*168043*	*0.969*	*149776*	*0.9932*
Porous limestone A	*1438*	*0.991*	*2764*	*0.983*
Porous limestone B	*1509*	*0.977*	*2765*	*0.984*
Compact limestone	*34909*	*0.962*	*22477*	*0.976*
Rhyolite tuff	*5832*	*0.992*	*4096*	*0.997*

[1] In case of the cellular concrete block the Brinell test was not applicable, because even on the lowest load level the sample broke rigidly.

Table A-9 *Correlation coefficients and k_2 multipliers of all materials for both DSI and Brinell test*

Materials	***DSI***		***Brinell***	
	k_2 [N/mm^2]	***r^2***	***k_2 [N/mm^2]***	***r^2***
Aluminium	*833.4*	*0.993*	*677.9*	*0.996*
Mild steel	*1180.2*	*0.992*	*1171.6*	*0.991*
Reinforcing steel bar	*1883.7*	*0.941*	*1696.4*	*0.985*
Normal strength concrete	*557.7*	*0.957*	*421.9*	*0.973*
High strength concrete	*1024.9*	*0.965*	*902.8*	*0.997*
Polymer concrete	*569.2*	*0.966*	*459.5*	*0.998*
Cellular concrete block	*6.8*	*0.988*	-	-
Sand-lime brick	*123.7*	*0.98*	*108.4*	*0.982*
Clinker brick	*1952.2*	*0.99*	*1703.5*	*0.992*
Facebrick	*134.9*	*0.987*	*136.4*	*0.969*
Clinker tile	*4211.9*	*0.969*	*3754.9*	*0.9934*
Porous limestone A	*45.9*	*0.932*	*47.7*	*0.9465*
Porous limestone B	*42.5*	*0.95*	*83.3*	*0.995*
Compact limestone	*908.79*	*0.963*	*598.9*	*0.986*
Rhyolite tuff	*161.8*	*0.982*	*119.7*	*0.986*

XIX. DE modelling of Brinell hardness test

Table A-10 *Indentation diameter and Brinell hardness of the 5 models and their average*

Force [N]	Model 1		Model 2		Model 3		Model 4		Model 5		Average	
	d_{rm} [mm]	HB [HB]	d_{rm} [mm]	HB [HB]	d_{rm} [mm]	HB [HB]	d_{rm} [mm]	HB [HB]	d_{rm} [mm]	HB [HB]	d_{rm} [mm]	HB [HB]
2500	2.63	450	2.58	470	2.65	445	2.89	372	2.62	453	2.68	436
5000	3.51	500	3.51	498	3.52	495	3.59	477	3.50	501	3.53	495
7500	4.07	551	4.09	544	4.12	536	4.19	517	4.10	543	4.12	538
10000	4.93	489	4.91	493	4.89	497	5.04	466	4.88	499	4.93	489
10625	5.34	437	5.29	446	5.32	440	5.45	417	5.33	439	5.35	436
12500	5.70	446	5.68	448	5.67	450	5.84	422	5.63	457	5.71	445
15000	6.09	460	6.10	459	6.03	471	6.21	441	6.05	467	6.10	460
17500	7.03	385	6.99	390	7.03	385	7.21	362	7.06	381	7.07	381

Table A-11 *Brinell test results from the laboratory test and the model; the differences between them*

Loading force [N]	Brinell model			Brinell lab test			Differences [%]	
	d [mm]	d^2 [mm^2]	HB [HB]	d [mm]	d^2 [mm^2]	HB [HB]	d	HB
2500	2.7	7.2	436	2.9	8.3	376	7	-16
5000	3.5	12.5	495	3.8	14.4	425	7	-16
7500	4.1	16.9	538	4.4	19.1	474	5	-13
10000	4.9	24.3	489	5.0	24.8	479	1	-2
12500	5.7	32.6	445	5.3	28.5	516	-6	13
15000	6.1	37.2	460	5.8	34.2	506	-4	9
17500	7.1	49.9	381	6.3	39.4	503	-12	24

XX. Mechanical testing of lightweight aggregate concrete

In this part of the study, 6 concrete mixes were designed containing 5 different type of lightweight aggregate. List of the applied aggregate types:

- Normal weight aggregate (NWA) - quartz gravel - concrete used as reference.
- Poraver: an expanded porous recycled glass aggregate, which has open pores.
- Geofil: an expanded porous recycled glass aggregate which has closed surface (no open pores).
- Liapor: an expanded clay aggregate with similar strength to Geofil.
- Liasand: an expanded clay aggregate. In this case the aggregate particles are crushed to get a fine powder, which is utilized as aggregate.
- Brick: recycled ceramic (brick) aggregate.

Using these aggregates concrete samples were casted with the following aggregate composition:

Table A-12 *Applied aggregate types in the different aggregate size fractions for all mixes*

	Aggregate size [mm]		
	0/4	4/8	8/16
Reference	NWA	NWA	NWA
Liapor	NWA	Liapor	Liapor
Liasand	Liasand	Liapor	Liapor
Brick	NWA	Brick	Brick
Geofil	NWA	Geofil	Geofil
Poraver	NWA	Poraver	Poraver

The applied cement was a CEM I 42.5 N type Portland cement. The amount of water was adjusted according to the water absorption of the given aggregate type. From the mixes 40 x 40 x 160 mm prisms were casted. The samples were subjected to the following mechanical tests:

- compressive strength test (at the age of 3, 7 and 28 days),
- flexular-tensile strength test (at the age of 3, 7 and 28 days),
- hardness tests:
  - Brinell test,
  - DSI test.

Besides that the carbonation of the samples were investigated as well. Before the hardness tests a sensitivity analysis were performed on the samples to find, which load level and ball diameter to use for the hardness tests. The analysis showed that most of the samples damaged above 5000 N loading, while below 2500 N the imprint size was too small for further reliable

investigation. As the results the two chosen load levels were 2500 N and 4375 N, because these load levels are possible to use on both Brinell and DSI test machines as well.

The results of the compressive strength tests, flexural strength tests, Brinell hardness tests and DSI tests can be seen in *Table A-13*.

Table A-13 *Measurement results of mechanical tests performed on lightweight aggregate concretes*

Aggregate type	Compressive strength [N/mm²]			Flexural tensile strength [N/mm²]			DSI [HB]		Brinell [HB]	
	3	7	28	3	7	28	2500 N	4375 N	2500 N	4375 N
Liapor	25.7	41.3	42.5	3.2	4.4	4.9	146	155	71	88
Liasand	21.5	29.1	29.8	3	3.5	4	139	157	15	0
Normal	29.6	47.1	51	3.5	3.8	4.1	141	136	192	110
Brick	33.8	51.7	56.6	4.7	5.4	5.6	106	121	102	123
Geofil	28.7	34.5	36.7	3.6	4.8	4.9	134	149	106	77
Poraver	10.2	14.3	16.8	2.5	3.1	3.4	72	74	36	36

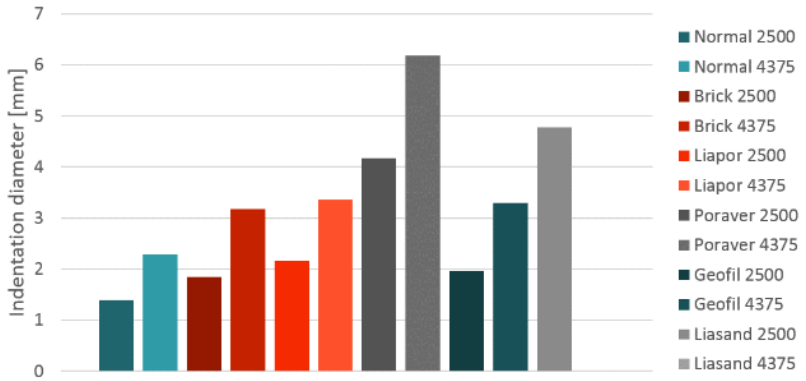

Fig. A-23 *Indentation diameter from the Brinell hardness test for all samples on two load levels (2500 N and 4375 N)*

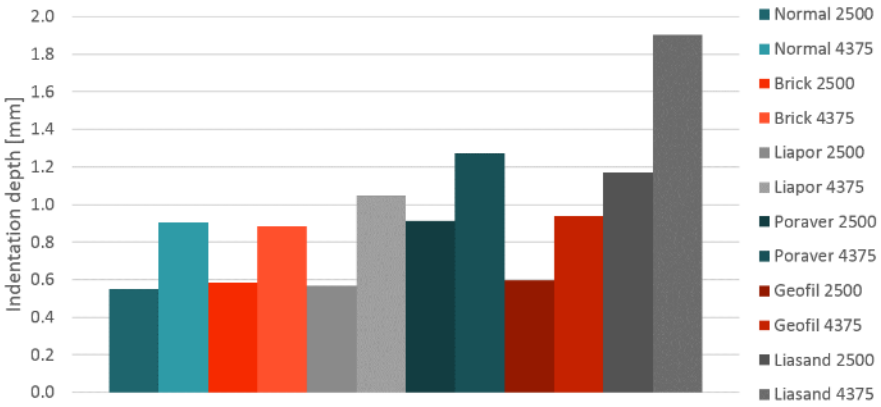

Fig. A-24 *Indentation diameter from the DSI test for all samples on two load levels (2500 N and 4375 N)*

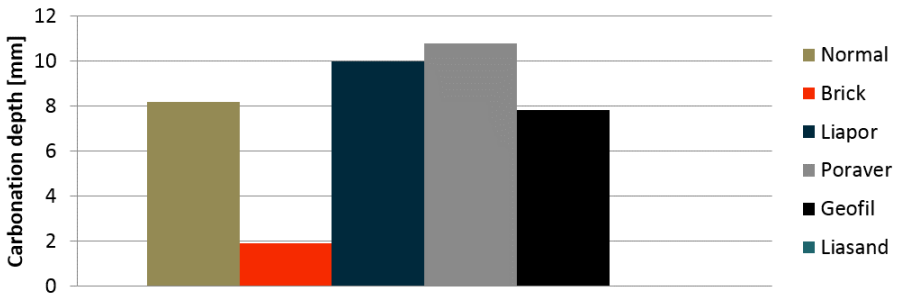

Fig. A-25 *Carbonation depth measured after 1 year on the samples*

XXI. Compressive strength for different volumes based on model equation

The following table shows the compressive strength values calculated from the measurement data using the model equation defined in *Chapter 4*.

Table A-14 *Compressive strength for different volumes based on the model equation in case of Mix 1-5*

Cube edge length [mm]	**Cylinder diameter [mm]**	**Volume [m³]**	**Compressive strength based on model equation [N/mm²]**									
			Mix 1		**Mix 2**		**Mix 3**		**Mix 4**		**Mix 5**	
			Cube	**Cyl**	**Cube**	**Cyl**	**Cube**	**Cy**	**Cube**	**Cyl**	**Cube**	**Cyl**
58.5	50.3	0.0002	53.6	38.2	66.8	58.3	68.1	58.7	77.6	66.5	82.1	70.0
100.0	86.0	0.001	45.4	34.0	59.7	53.5	62.1	55.1	71.7	63.9	77.1	68.3
126.0	108.4	0.002	42.2	32.3	56.9	51.5	59.6	53.6	69.3	62.8	75.0	67.6
144.2	124.1	0.003	40.5	31.4	55.4	50.4	58.2	52.7	67.9	62.2	73.8	67.2
158.7	136.6	0.004	39.3	30.7	54.3	49.6	57.3	52.1	67.0	61.7	73.0	66.9
171.0	147.1	0.005	38.4	30.2	53.5	49.0	56.5	51.7	66.2	61.4	72.3	66.7
181.7	156.3	0.006	37.7	29.8	52.8	48.6	55.9	51.3	65.7	61.1	71.8	66.5
200.0	172.1	0.008	36.6	29.2	51.8	47.8	55.0	50.7	64.7	60.7	70.0	66.2

Table A-15 *Strength ratios and the differences between them in case of Mix 1*

Volume [m³]	Mix 1			
	$\sigma_c(d)/f_c'$ [-]		Difference [-]	
	Cube	Cylinder	Cube	Cylinder
0.0002	1.33	1.27	0.205	0.141
0.001	1.13	1.13	0.078	0.056
0.002	1.05	1.08	0.043	0.031
0.003	1.01	1.04	0.030	0.022
0.004	0.98	1.02	0.022	0.017
0.005	0.96	1.01	0.018	0.013
0.006	0.94	0.99	**0.014**	**0.010**
0.008	0.91	0.97	-	-

Table A-16 *Strength ratios and the differences between them in case of Mix 2*

Volume [m³]	Mix 2			
	$\sigma_c(d)/f_c'$ [-]		Difference [-]	
	Cube	Cylinder	Cube	Cylinder
0.0002	1.21	1.19	0.127	0.099
0.001	1.09	1.09	0.051	0.040
0.002	1.03	1.05	0.029	0.023
0.003	1.01	1.03	0.020	0.016
0.004	0.99	1.02	0.015	0.012
0.005	0.97	1.00	0.012	**0.010**
0.006	0.96	0.99	**0.009**	0.008
0.008	0.94	0.98	-	-

Table A-17 *Strength ratios and the differences between them in case of Mix 3*

Volume [m³]	Mix 3			
	$\sigma_c(d)/f_c'$ [-]		Difference [-]	
	Cube	Cylinder	Cube	Cylinder
0.0002	1.15	1.14	0.095	0.070
0.001	1.06	1.07	0.039	0.029
0.002	1.02	1.04	0.022	0.017
0.003	1.00	1.02	0.015	0.012
0.004	0.98	1.01	0.012	**0.009**
0.005	0.97	1.00	**0.009**	0.007
0.006	0.96	1.00	0.007	0.006
0.008	0.94	0.98	-	-

Table A-18 *Strength ratios and the differences between them in case of Mix 4*

Volume [m³]	Mix 4			
	$\sigma_c(d)/f_c'$ [-]		Difference [-]	
	Cube	Cylinder	Cube	Cylinder
0.0002	1.15	1.09	0.087	0.043
0.001	1.06	1.05	0.035	0.018
0.002	1.03	1.03	0.020	**0.010**
0.003	1.01	1.02	0.014	0.007
0.004	0.99	1.01	0.011	0.006
0.005	0.98	1.00	**0.009**	0.005
0.006	0.97	1.00	0.007	0.004
0.008	0.96	0.99	-	-

Table A-19 *Strength ratios and the differences between them in case of Mix 5*

Volume [m³]	Mix 5			
	$\sigma_c(d)/f_c'$ [-]		Difference [-]	
	Cube	Cylinder	Cube	Cylinder
0.0002	1.12	1.05	0.069	0.025
0.001	1.05	1.02	0.028	0.011
0.002	1.02	1.01	0.016	**0.006**
0.003	1.00	1.01	0.011	0.004
0.004	0.99	1.00	**0.009**	0.003
0.005	0.98	1.00	0.007	0.003
0.006	0.98	1.00	0.006	0.002
0.008	0.96	0.99	-	-

Table A-20 *Compressive strength for different volumes based on the model equation in case of Mix 1,2,3,4 and 5*

Cube edge length [mm]	Cylinder diameter [mm]	Volume [m3]	Parallel bond strength based on the model equation [N/mm^2]									
			Mix 1		Mix 2		Mix 3		Mix 4		Mix 5	
			Cube	Cyl	Cube	Cyl	Cube	Cyl	Cube	Cyl	Cube	Cyl
58.5	50.3	0.0002	54.9	49.7	68.6	58.7	68.5	58.6	77.5	72.8	79.1	76.1
100.0	86.0	0.001	40.0	34.2	52.6	47.8	54.2	48.8	62.8	59.6	65.8	63.5
126.0	108.4	0.002	34.8	29.2	46.9	43.8	48.9	45.1	57.3	54.7	60.8	58.7
144.2	124.1	0.003	32.1	26.6	43.9	41.5	46.1	43.0	54.4	52.0	58.1	56.0
158.7	136.6	0.004	30.4	24.9	41.8	40.0	44.2	41.6	52.3	50.2	56.2	54.3
171.0	147.1	0.005	29.0	23.6	40.3	38.9	42.8	40.6	50.8	48.8	54.8	52.9
181.7	156.3	0.006	28.0	22.6	39.1	38.0	41.7	39.8	49.6	47.7	53.7	51.8
200.0	172.1	0.008	26.5	21.2	37.3	36.6	40.0	38.5	47.8	46.0	51.9	50.2

XXII. DE modelling of concretes containing potential SCMs

The concrete mixes of *Chapter 6* and their compressive strength test have been modelled using DEM. As CCP and MK are too fine powders to be considerable in the same model with the aggregates, the effect of CCP and MK was considered in the contact parameters of the model. The results are included in *Table A-21*. The model described in *Chapter 6.1.1* is used to estimate the parallel bond strength and to see, how these fine powders are affecting this estimation model.

Table A-21 *DE modelling results of concretes containing MK and CCP*

Type	Name	Particle size distribution			Density [kg/m^3]	Compressive strength [N/mm^2]	Parallel bond strength [N/mm^2]	Estimated bond strength [N/mm^2]	Error [-]	Error %
		0/4	4/8	8/16						
High strength	Reference	40	25	35	2383	84.36	70.30	64.43	5.87	8.35
	Y3	40	25	35	2371	74.61	61.80	57.28	4.52	7.32
	Y10	40	25	35	2355	73.13	60.50	56.50	4.00	6.61
	Y17	40	25	35	2326	52.67	41.62	41.20	0.42	1.01
	MK10	40	25	35	2405	95.26	78.70	72.07	6.63	8.43
	MK7Y3	40	25	35	2399	81.46	64.40	61.78	2.62	4.06
Normal strength	Reference	47	25	28	2323	34.21	25.75	26.80	-1.05	4.08
	Y3	47	25	28	2277	37.53	29.70	29.99	-0.29	0.99
	Y10	47	25	28	2278	45.80	36.50	36.58	-0.08	0.23
	Y17	47	25	28	2293	40.09	31.50	31.82	-0.32	1.00
	MK10	47	25	28	2332	55.15	43.50	43.04	0.46	1.06
	MK7Y3	47	25	28	2322	48.13	37.80	37.72	0.08	0.21

Based on *Table A-21* it can be concluded that fine powders (CCP and MK) does not add a non-linearity to the relation of the compressive strength and parallel bond strength. The estimation errors are similar to the model described in *Chapter 6.1.1*. It can be observed that the HSC has higher estimation error compared to the NSC (in average 5.96% vs. 1.26%).

XXIII. Effect of CCP and MK on the hardness of cement mortars

To investigate the effect of CCP and MK on the Brinell hardness the cement mortars of *Chapter 6* have been used. The mortars have been subjected to DSI and Brinell hardness tests. As a first step, sensitivity analysis for Brinell and DSI test was conducted on some of the reference samples, which can be seen in *Fig. A-26*. The aim of the analysis was to determine the optimal loading force for both Brinell and DSI tests. The loading force cannot be too small, otherwise the imprints on the surface of the material will be too small, and the results cannot be used, while in case of a too high load, the ball would penetrate fully to the material or it could break the sample. The results indicated to use 2500 – 4375 N loading force range, thus in the latter part of the study, the results of those two load (upper and lower) levels are analyzed.

Fig. A-26 *One of the samples in the Brinell tester (**left**) and one in the DSI tester (**right**)*

Based on the measurement results it was observed that the standard deviation of the Brinell hardness (or the indentation diameter) is lower in case of the higher load level (4375 N) than in case of the lower load level (2500 N), as it can be seen in *Fig. A-27*. This observation was true for both measurement methods (Brinell and DSI) and in case of DSI both for the maximum and residual values as well. The average standard deviations in indentation diameter were the following of all materials for 2500 N and 4375 N load level respectively:

- Brinell: 0.19 and 0.16 mm,
- DSI maximum: 0.40 and 0.09 mm,
- DSI residual: 0.51 and 0.29 mm.

This indicates that it is more advantageous to perform static hardness tests on the possible maximum load level to make the measurements more accurate. *Figure A-27*reflects on another phenomenon, namely that the calculated Brinell hardness is always higher in case of the higher

load level. It was studied in previous researches that the Brinell hardness has a maximum value if represented as function of the loading level (*Szilágyi et al, 2011*).

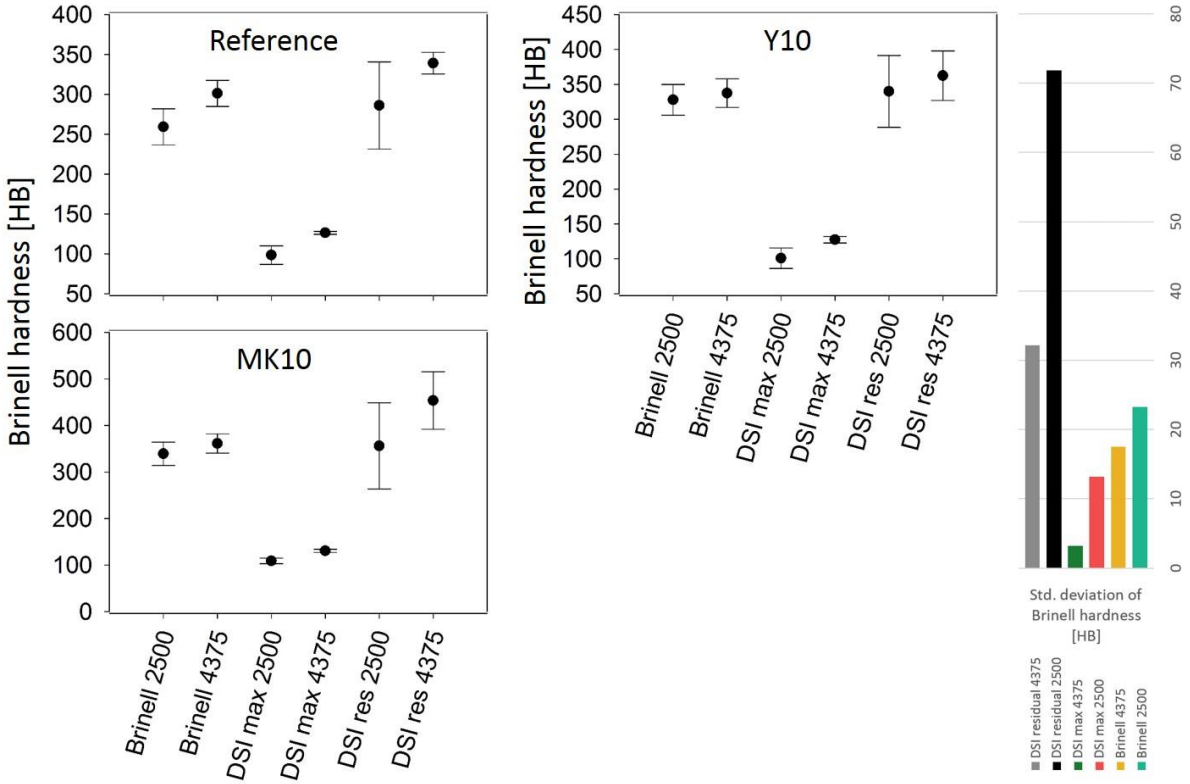

Fig. A-27 *Mean values of Brinell hardness from the different measurement methods and their standard deviation*

As it was expected, the value of indentation diameter (and consequently Brinell hardness) in case of the Brinell test falls between the maximum and residual value of the DSI test (*Fig. A-27*). The values of the Brinell test result should be very similar to the values of the DSI test results, with the difference that in case of the Brinell test, the sample is kept "under loading" for 15 seconds. During this time frame, irreversible plastic deformations develop in the material for which there is no time given in case of DSI test.

By comparing the compressive strength and hardness test results, it can be seen that, as it was expected, with the increase or decrease of the compressive strength, the hardness values are also increasing or decreasing. It is valid in case of MK; however, in case of CCP, the relation is reversed. It could be caused by the filling effect of CCP, which fills the pores of the cement paste, and thus it increases its surface hardness. The effect of carbonation was excluded because the samples were stored in a hermetically locked container.

Usually, the effect of a supplementary material on the compressive strength is analyzed through a ratio of the compressive strength, compared to the reference material. In our case, the effect of a given supplementary material on the hardness was investigated using a ratio compared to the reference material. For MK, as it was mentioned, the hardness ratio follows the change of the compressive strength ration (as it can be seen in *Table A-22*); however, quantitatively the values differ. If we assume a linear correlation between the compressive strength and the hardness, the most accurate estimation is given by the Brinell hardness test at the higher load level.

Table A-22 *Compressive and hardness test results*

				F = 2500 N			F = 4375 N		
Type of hardness test	Sample name	Compressive strength	Compressive strength ratio [-]	Indentation diameter [mm]	Brinell hardness [HB]	Hardness ratio to the reference mix [-]	Indentation diameter [mm]	Brinell hardness [HB]	Hardness ratio to the reference mix [-]
Brinell	Reference	88.1	1.00	3.45	259	1.00	4.20	301	1.00
	Y10	83.8	0.95	3.08	328	1.26	3.98	338	1.12
	MK10	104.4	1.18	3.03	339	1.31	3.85	361	1.16
DSI maximum	Reference	88.1	1.00	5.48	98	1.00	6.26	126	1.00
	Y10	83.8	0.95	5.44	101	1.02	6.25	127	1.01
	MK10	104.4	1.18	5.21	109	1.10	6.18	130	1.03
DSI residual	Reference	88.1	1.00	3.29	286	1.00	3.97	339	1.00
	Y10	83.8	0.95	3.02	340	1.19	3.84	362	1.07
	MK10	104.4	1.18	3.00	338	1.15	3.45	454	1.34

It can be read from the loading-unloading curves of the DSI test that the tested materials have elasto-plastic behavior (significant residual deformation, non-linear loading-unloading curve), as it is shown in *Fig. A-28*.

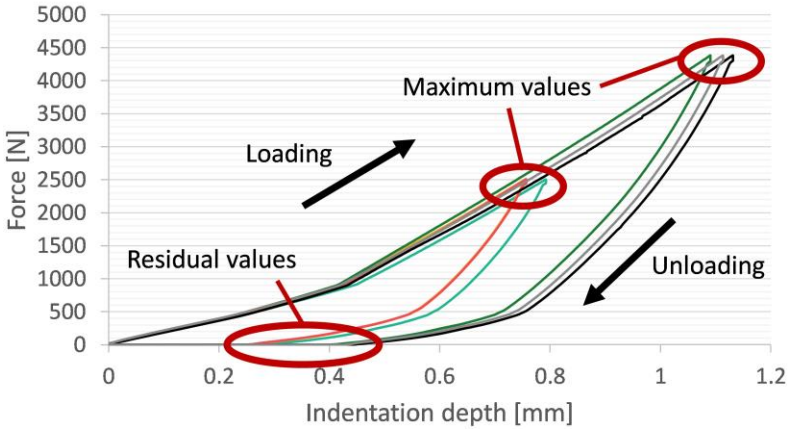

Fig. A-28 *Real loading-unloading curves for one of the reference samples*

One of the advantages of DSI test method over Brinell test that it provides information regarding the indentation work (energy) generated during the penetration of the indenter, as it is shown in *Table A-23*. Based on that, the material behavior can be analyzed. It can be seen that between the two load levels, the load increase ratio was 1.75 (4375/2500); however, the increase ratio in the total work is about 2.5. The reference material is more elastic (elastic work ratio is higher than the plastic). In case of the MK10 mix, the distribution of the work is universal between the plastic and elastic works. The CCP has no significant effect on the total work; the MK decreases the total work, which indicates that the material has higher hardness. Another interesting observation is that the dissipated energy changes much less due to the different types of additives than the elastic energy. It could be considered to be constant in case of the lower loading level (2500 N). This indicates that the compressive strength increase/decrease caused by supplementary materials influences the elastic properties of the material and so the compressive strength/hardness is related to the elastic properties of the porous materials.

Table A-23 *Generated indentation energy during the DSI test*

	2500 N					4375 N				
	Total work average [kNmm]	Dissipated (plastic) work average [kNmm]	Elastic work average [kNmm]	Plastic work ratio [-]	Elastic work ratio [-]	Total work average [kNmm]	Dissipated (plastic) work average [kNmm]	Elastic work average [kNmm]	Plastic ratio [-]	Elastic ratio [-]
Reference	0.76	0.33	0.43	44%	56%	1.94	0.77	1.17	40%	60%
Y10	0.79	0.34	0.46	43%	57%	1.88	0.87	1.01	46%	54%
MK10	0.69	0.35	0.34	50%	50%	1.74	0.88	0.86	51%	49%

XXIV. Measurement results corresponding to Chapter 4

Table A-24 *Measured material properties*

Material	***Compressive strength [N/mm²]***	***Young's modulus [N/mm²]***	***Density [kg/m³]***	***Body density [kg/m³]***	***Porosity [V%]***	$\sqrt{E/\rho}$ $[m/s$	***Brinell hardness [HB]***	W_t/W_d	We/Wd	W_t/W_e	$1/(W_t/W_e)^2$	d_r/d_m	h_r/h_m	***Mechanical behaviour***
Aluminium	*350*	*70000*	*2700*	*2700*	*0*	*5.1*	*1000*	*2.1*	*1.1*	*1.9*	*0.277*	*0.65*	*0.39*	*Elasto-Plastic*
Mild steel	*420*	*200000*	*7850*	*7850*	*0*	*5.0*	*1450*	*2.4*	*1.4*	*1.7*	*0.346*	*0.59*	*0.32*	*Elasto-Plastic*
Reinforcing steel bar	*600*	*210000*	*7850*	*7850*	*0*	*5.2*	*2450*	*3.4*	*2.4*	*1.4*	*0.510*	*0.49*	*0.22*	*Elasto-Plastic*
Normal strength concrete	*54.2*	*34578*	*2300*	*2258*	*14.65*	*3.9*	*700*	*1.7*	*0.9*	*2.4*	*0.174*	*0.69*	*0.45*	*Elasto-Plastic*
High strength concrete	*106.2*	*43802*	*2645*	*2414*	*8.72*	*4.3*	*1300*	*2.6*	*1.7*	*1.6*	*0.391*	*0.51*	*0.23*	*Elasto-Plastic*
Polymer concrete	*98.7*	*40000*	*2254*	*2097*	*6.96*	*4.4*	*700*	*2*	*0.7*	*2*	*0.250*	*0.65*	*0.37*	*Elasto-Plastic*
Cellular concrete block	*2.02*	*500*	*2535*	*516*	*79.66*	*1.0*	*7.5*	*1.05*	*0.05*	*23.5*	*0.002*	*0.96*	*0.91*	*Plastic*
Sand-lime brick	*19.3*	*2000*	*2575*	*1711*	*33.54*	*1.1*	*140*	*1.3*	*0.3*	*4.5*	*0.049*	*0.85*	*0.69*	*Elasto-Plastic*
Clinker brick	*80.9*	*35000*	*2745*	*2370*	*13.65*	*3.8*	*2500*	*5.3*	*4.3*	*1.2*	*0.694*	*0.35*	*0.12*	*Elastic*
Facebrick	*23.3*	*3000*	*2645*	*1711*	*35.3*	*1.3*	*170*	*1.3*	*0.3*	*4.2*	*0.057*	*0.82*	*0.65*	*Elasto-Plastic*
Clinker tile	*233*	*65000*	*2531*	*2254*	*10.96*	*5.4*	*5800*	*7*	*6.5*	*1.2*	*0.694*	*0.19*	*0.03*	*Elastic*
Porous limestone A	*12.4*	*5199*	*2640*	*1808*	*31.52*	*1.7*	*45*	*1.1*	*0.09*	*12.6*	*0.006*	*0.95*	*0.87*	*Plastic*
Porous limestone B	*9.2*	*5127*	*2725*	*1769*	*39.61*	*1.7*	*50*	*1.1*	*0.13*	*8.8*	*0.013*	*0.92*	*0.83*	*Plastic*
Compact limestone	*108.5*	*56402*	*2690*	*2502*	*6.99*	*4.7*	*1100*	*2.4*	*1.4*	*1.8*	*0.309*	*0.48*	*0.21*	*Elasto-Plastic*
Rhyolite tuff	*30*	*10206*	*2385*	*1615*	*32.27*	*2.5*	*190*	*1.3*	*0.3*	*4.2*	*0.057*	*0.81*	*0.62*	*Elasto-Plastic*

Table A-25 *Hardness test results of aluminium*

	DSI results															Brinell results				
	Force [N]	**h_m [mm]**	**h_r [mm]**	**h_r/h_m [-]**	**W_t [Nmm]**	**W_e [Nmm]**	**W_d [Nmm]**	**W_t / W_e [-]**	**W_t / W_d [-]**	**d_m [mm]**	**d_r [mm]**	**d_r/d_m [-]**	**DSI d_r^2**	**HB_m [HB]**	**HB_r [HB]**	**Force [N]**	**d [mm]**	**Brinell d^2 [mm^2]**	**h [mm]**	**HB [HB]**
Aluminium	2459	0.241	0.101	0.42	261	159	102	1.65	2.55	3.07	2.00	0.65	4.00	325	775	2500	2.1	4.61	0.1	682
	2486	0.241	0.096	0.40	274	167	106	1.64	2.57	3.07	1.95	0.64	3.80	328	824	5000	2.8	7.88	0.2	792
	4751	0.414	0.168	0.41	922	522	400	1.77	2.31	3.98	2.57	0.65	6.61	365	900	7500	3.3	11.06	0.3	839
	4829	0.414	0.162	0.39	940	543	397	1.73	2.37	3.98	2.52	0.63	6.38	371	949	10000	3.8	14.07	0.4	872
	7270	0.608	0.243	0.40	2096	1188	908	1.76	2.31	4.78	3.08	0.64	9.48	381	952	12500	4.2	17.50	0.5	868
	7340	0.613	0.245	0.40	2139	1212	927	1.76	2.31	4.80	3.09	0.64	9.56	381	954	15000	4.5	20.39	0.5	886
	9906	0.831	0.322	0.39	3941	2217	1724	1.78	2.29	5.52	3.53	0.64	12.4	379	979	17500	4.9	23.57	0.6	886
	9806	0.825	0.327	0.40	3883	2133	1750	1.82	2.22	5.50	3.56	0.65	12.6	378	954	20000	5.2	27.16	0.7	869
	9990	0.83	0.321	0.39	4005	2243	1761	1.79	2.27	5.52	3.53	0.64	12.4	383	991	22500	5.3	27.88	0.8	950
	12358	1.037	0.399	0.38	6142	3336	2806	1.84	2.19	6.10	3.91	0.64	15.3	379	986	25000	5.5	30.64	0.8	952
	12355	1.033	0.395	0.38	6218	3350	2868	1.86	2.17	6.09	3.90	0.64	15.1	381	996					
	12506	1.036	0.393	0.38	6265	3468	2798	1.81	2.24	6.09	3.89	0.64	15.1	384	1013					
	14999	1.244	0.474	0.38	8871	4834	4038	1.84	2.20	6.60	4.25	0.64	18.0	384	1007					
	15006	1.25	0.484	0.39	9044	4858	4185	1.86	2.16	6.61	4.29	0.65	18.4	382	987					
	17491	1.453	0.553	0.38	12008	6492	5516	1.85	2.18	7.05	4.57	0.65	20.9	383	1007					
	17487	1.471	0.58	0.39	12223	6464	5759	1.89	2.12	7.08	4.67	0.66	21.8	378	960					
	19979	1.668	0.644	0.39	15777	8299	7478	1.90	2.11	7.46	4.91	0.66	24.1	381	988					
	20390	1.679	0.644	0.38	16332	8660	7672	1.89	2.13	7.48	4.91	0.66	24.1	387	1008					
	24998	2.059	0.773	0.38	24473	12776	11698	1.92	2.09	8.09	5.34	0.66	28.5	386	1029					
	24922	2.048	0.777	0.38	24692	12614	12078	1.96	2.04	8.07	5.35	0.66	28.6	387	1021					
	25002	2.06	0.804	0.39	24215	12714	11501	1.90	2.11	8.09	5.44	0.67	29.5	386	990					
	Average			**0.39**						**Average**		**0.65**	Elasto-Plastic							

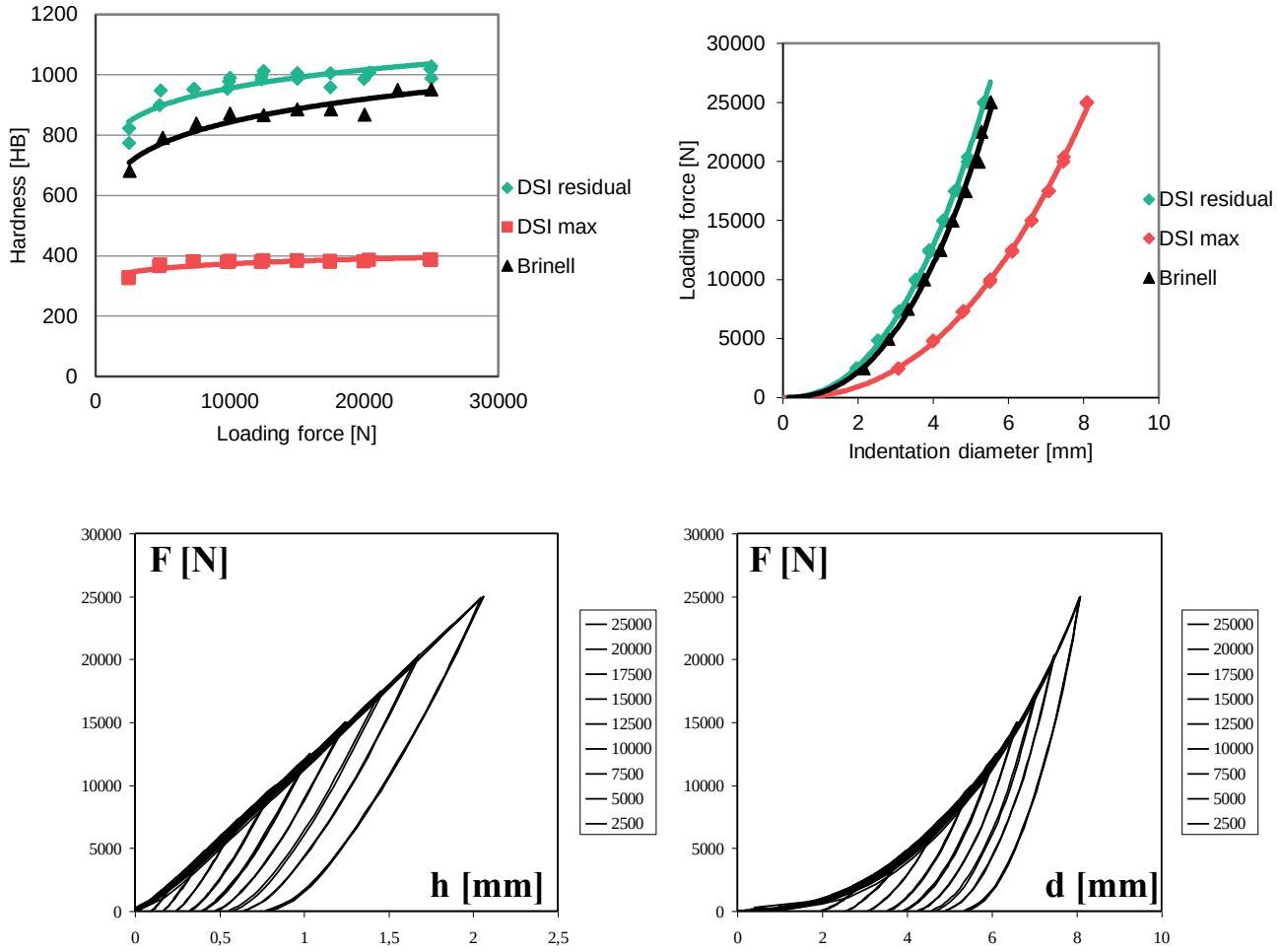

Fig. A-29 *Hardness test results of aluminium*

Table A-26 *Hardness test results of mild steel*

	DSI results															Brinell results				
	Force [N]	**h_m [mm]**	**h_r [mm]**	**h_r/h_m [-]**	**W_t [Nmm]**	**W_e [Nmm]**	**W_d [Nmm]**	**W_t / W_e [-]**	**W_t / W_d [-]**	**d_m [mm]**	**d_r [mm]**	**d_r/d_m [-]**	**DSI d_r^2**	**HB_m [HB]**	**HB_r [HB]**	**Force [N]**	**d [mm]**	**Brinell d^2 [mm^2]**	**h [mm]**	**HB [HB]**
Mild steel	2511	0.209	0.068	0.33	241	163	78	1.48	3.10	2.86	1.64	0.57	2.7	382	1175	2500	1.7	2.82	0.1	1120
	2514	0.204	0.062	0.30	245	166	79	1.48	3.11	2.83	1.57	0.56	2.5	392	1291	5000	2.4	5.60	0.1	1120
	2507	0.207	0.066	0.32	244	162	82	1.50	2.99	2.85	1.62	0.57	2.6	385	1209	7500	2.6	6.85	0.2	1370
	5019	0.374	0.119	0.32	877	574	303	1.53	2.89	3.79	2.17	0.57	4.7	427	1343	10000	3.0	9.24	0.2	1345
	5018	0.374	0.12	0.32	874	571	303	1.53	2.89	3.79	2.18	0.57	4.7	427	1331	12500	3.4	11.45	0.3	1349
	7508	0.539	0.174	0.32	1884	1213	672	1.55	2.81	4.52	2.62	0.58	6.8	443	1374	15000	3.6	13.26	0.3	1391
	7515	0.537	0.175	0.33	1896	1212	684	1.56	2.77	4.51	2.62	0.58	6.9	445	1367	17500	3.9	15.02	0.4	1426
	10013	0.712	0.23	0.32	3393	2087	1306	1.63	2.60	5.14	3.00	0.58	9.0	448	1386	20000	4.2	17.36	0.5	1400
	10015	0.717	0.239	0.33	3440	2059	1381	1.67	2.49	5.16	3.05	0.59	9.3	445	1334	22500	4.4	19.14	0.5	1421
	15012	1.086	0.341	0.31	7828	4625	3204	1.69	2.44	6.22	3.63	0.58	13.2	440	1401	25000	4.7	21.62	0.6	1388
	15015	1.089	0.342	0.31	7950	4632	3318	1.72	2.40	6.23	3.63	0.58	13.2	439	1397	27500	4.8	22.88	0.6	1437
	20009	1.41	0.44	0.31	13305	7954	5351	1.67	2.49	6.96	4.10	0.59	16.8	452	1447	30000	4.9	24.30	0.6	1469
	20008	1.425	0.457	0.32	13428	7910	5518	1.70	2.43	6.99	4.18	0.60	17.4	447	1394					
	20015	1.436	0.47	0.33	13975	7884	6090	1.77	2.29	7.01	4.23	0.60	17.9	444	1356					
	25007	1.738	0.545	0.31	20440	12224	8216	1.67	2.49	7.58	4.54	0.60	20.6	458	1461					
	25009	1.749	0.571	0.33	20646	12122	8524	1.70	2.42	7.60	4.64	0.61	21.5	455	1394					
	30020	2.062	0.632	0.31	28982	17219	11763	1.68	2.46	8.09	4.87	0.60	23.7	463	1512					
	30011	2.077	0.662	0.32	29335	17235	12100	1.70	2.42	8.11	4.97	0.61	24.7	460	1443					
		Average		**0.32**						**Average**		**0.59**	Elasto-Plastic							

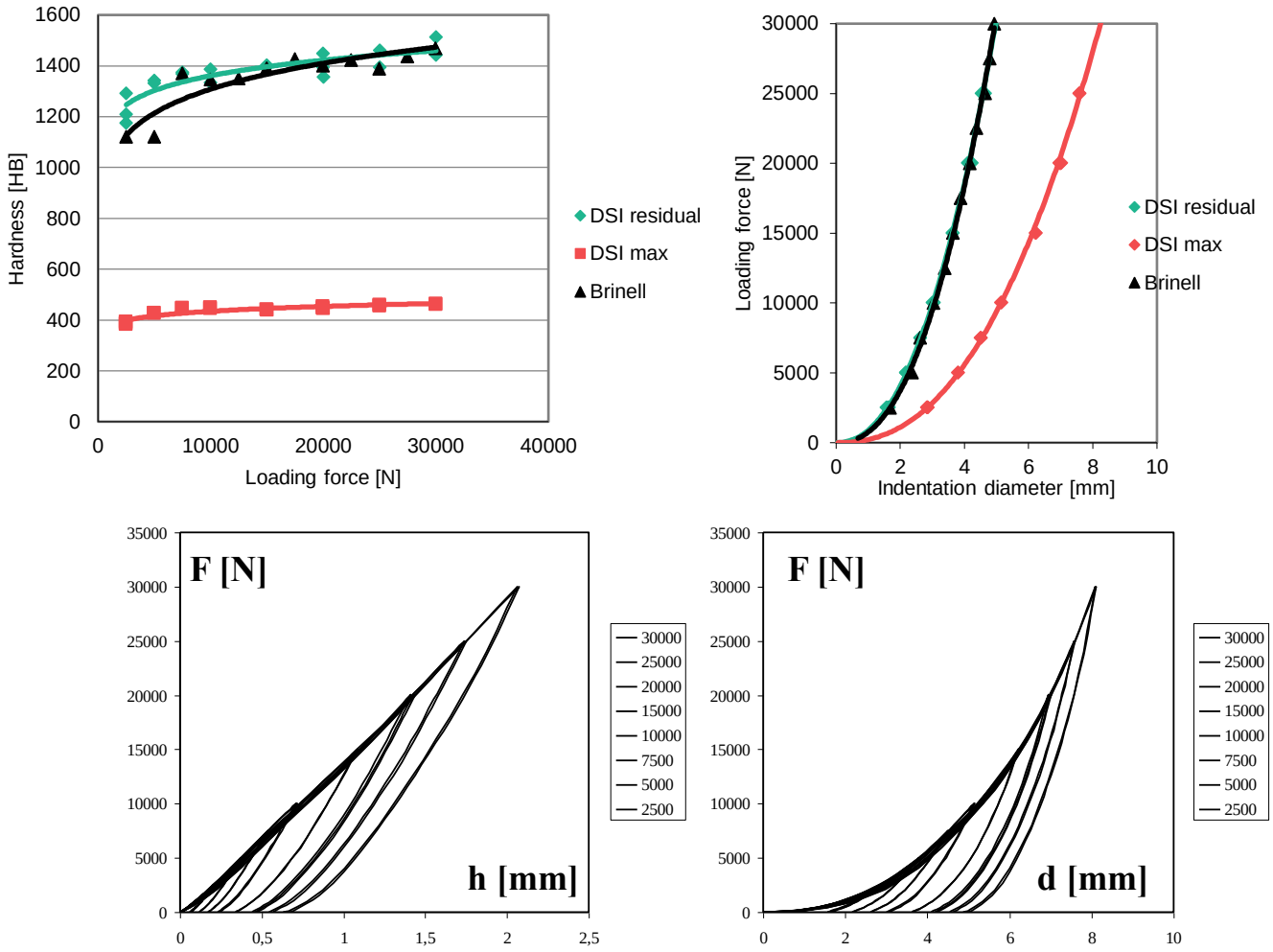

Fig. A-30 *Hardness test results of mild steel*

Table A-27 *Hardness test results of reinforcing steel bar*

	DSI results															Brinell results				
	Force [N]	h_m [mm]	h_r [mm]	h_r/h_m [-]	W_t [Nmm]	W_e [Nmm]	W_d [Nmm]	W_t / W_e [-]	W_t / W_d [-]	d_m [mm]	d_r [mm]	d_r/d_m [-]	DSI d_r^2	HB_m [HB]	HB_r [HB]	Force [N]	d [mm]	Brinell d^2 [mm^2]	h [mm]	HB [HB]
Reinforcing steel bar	2520	0.19	0.04	0.21	220	168	53	1.31	4.19	2.74	1.28	0.47	1.6	418	1957	2500	1.4	1.84	0.0	1722
	2512	0.19	0.05	0.25	209	169	40	1.23	5.28	2.74	1.37	0.50	1.9	419	1701	5000	2.1	4.28	0.1	1473
	2524	0.19	0.05	0.25	212	166	46	1.28	4.58	2.73	1.38	0.51	1.9	423	1673	7500	2.2	4.84	0.1	1950
	5023	0.33	0.07	0.21	779	594	185	1.31	4.21	3.58	1.68	0.47	2.8	483	2252	10000	2.5	6.29	0.2	1992
	5018	0.33	0.07	0.22	790	593	197	1.33	4.01	3.59	1.70	0.47	2.9	478	2188	12500	2.6	6.86	0.2	2278
	7519	0.48	0.11	0.23	1689	1254	435	1.35	3.89	4.26	2.07	0.49	4.3	503	2216	15000	3.0	9.00	0.2	2074
	7516	0.47	0.10	0.22	1691	1255	436	1.35	3.88	4.25	2.02	0.48	4.1	506	2323	17500	3.1	9.82	0.3	2212
	10021	0.61	0.12	0.20	2911	2173	738	1.34	3.95	4.79	2.20	0.46	4.9	523	2593	20000	3.5	12.44	0.3	1982
	10025	0.62	0.14	0.23	2974	2157	817	1.38	3.64	4.84	2.36	0.49	5.6	511	2263	22500	3.6	13.22	0.3	2093
	15522	0.79	0.18	0.23	4704	3324	1380	1.42	3.41	5.39	2.66	0.49	7.1	627	2745	25000	3.8	14.55	0.4	2104
	12520	0.78	0.18	0.23	4675	3301	1374	1.42	3.40	5.38	2.64	0.49	7.0	508	2251	27500	3.9	15.53	0.4	2163
	15525	0.77	0.19	0.25	4619	3297	1322	1.40	3.49	5.32	2.74	0.51	7.5	645	2587	30000	4.2	17.26	0.5	2113
	15029	0.93	0.20	0.22	6684	4701	1983	1.42	3.37	5.80	2.82	0.49	8.0	516	2357					
	15032	0.92	0.19	0.21	6638	4698	1940	1.41	3.42	5.77	2.76	0.48	7.6	522	2466					
	17529	1.07	0.22	0.21	8937	6384	2553	1.40	3.50	6.18	2.95	0.48	8.7	522	2513					
	17518	1.08	0.24	0.22	9038	6352	2686	1.42	3.36	6.20	3.03	0.49	9.2	518	2373					
	20023	1.24	0.28	0.23	11684	8190	3494	1.43	3.34	6.59	3.32	0.50	11.0	514	2252					
	20022	1.22	0.27	0.22	11621	8200	3421	1.42	3.40	6.55	3.23	0.49	10.4	521	2378					
	25016	1.51	0.33	0.22	17869	12635	5234	1.41	3.41	7.16	3.59	0.50	12.9	527	2391					
	25024	1.50	0.32	0.22	17838	12592	5246	1.42	3.40	7.13	3.54	0.50	12.5	533	2458					
	30023	1.79	0.40	0.22	25405	17823	7582	1.43	3.35	7.67	3.91	0.51	15.3	534	2401					
	30015	1.77	0.38	0.22	25125	17763	7362	1.41	3.41	7.63	3.84	0.50	14.8	540	2488					
		Average		**0.22**						**Average**		**0.49**	Elasto-Plastic							

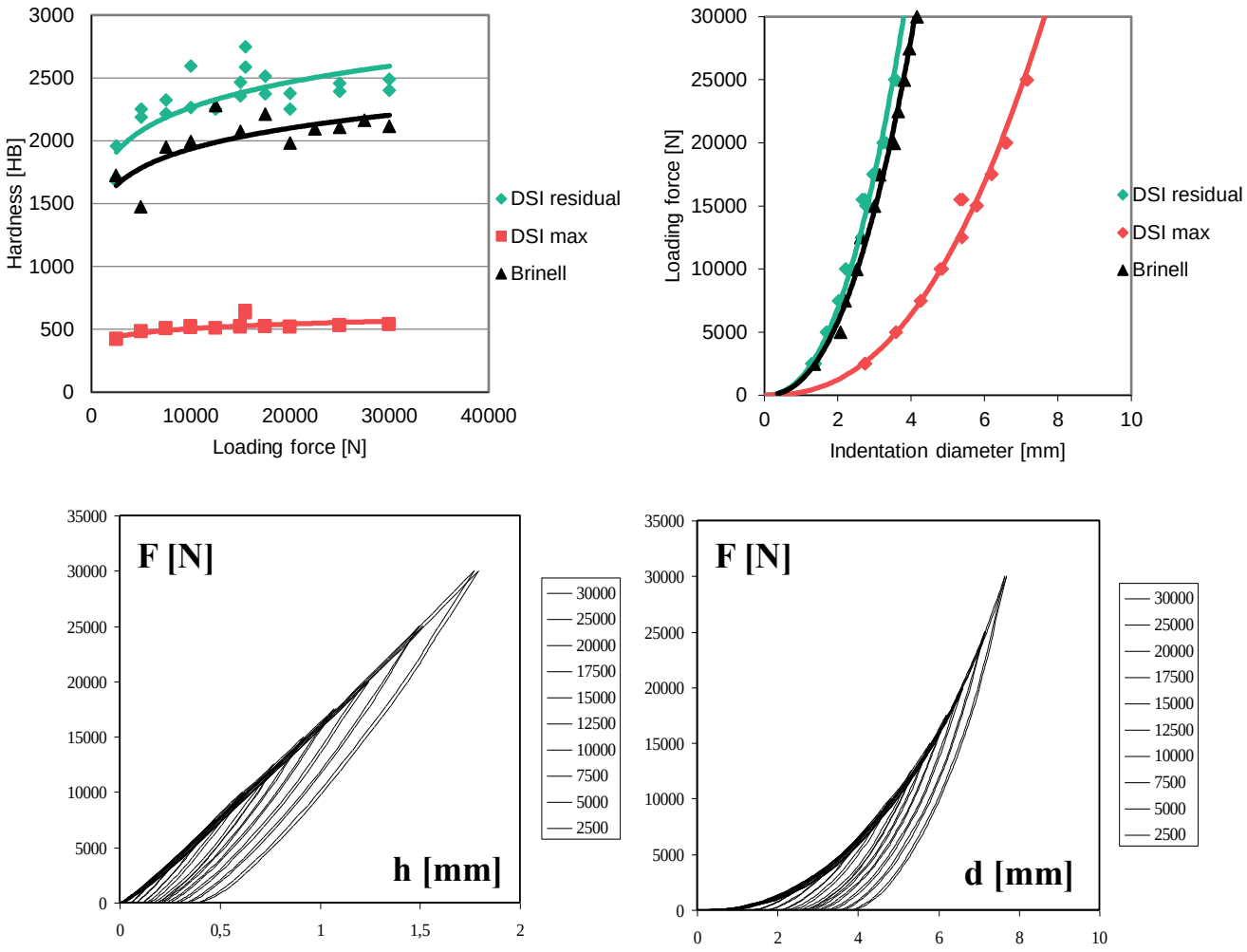

Fig. A-31 *Hardness test results of reinforcing steel*

Table A-28 *Hardness test results of normal strength concrete*

	DSI results															Brinell results				
	Force [N]	**h_m [mm]**	**h_r [mm]**	**h_r/h_m [-]**	**W_t [Nmm]**	**W_e [Nmm]**	**W_d [Nmm]**	**W_t / W_e [-]**	**W_t / W_d [-]**	**d_m [mm]**	**d_r [mm]**	**d_r/d_m [-]**	**DSI d_r^2**	**HB_m [HB]**	**HB_r [HB]**	**Force [N]**	**d [mm]**	**Brinell d^2 [mm^2]**	**h [mm]**	**HB [HB]**
Normal strength concrete	2510	0.413	0.218	0.53	457	196	261	2.33	1.75	3.98	2.92	0.73	8.5	193	367	2500	2.9	8.29	0.2	376
	2509	0.417	0.218	0.52	483	199	284	2.42	1.70	4.00	2.92	0.73	8.5	191	366	5000	3.8	14.42	0.4	425
	5013	0.619	0.262	0.42	1239	713	526	1.74	2.35	4.82	3.19	0.66	10.2	258	609	7500	4.4	19.14	0.5	474
	5007	0.626	0.249	0.40	1284	721	563	1.78	2.28	4.84	3.12	0.64	9.7	255	640	10000	5.0	24.83	0.7	479
	7522	0.869	0.35	0.40	2762	1580	1182	1.75	2.34	5.63	3.68	0.65	13.5	276	684	10625	5.2	27.04	0.7	464
	7519	0.874	0.359	0.41	2805	1591	1214	1.76	2.31	5.65	3.72	0.66	13.8	274	667	12500	5.3	28.49	0.8	516
	10013	1.082	0.489	0.45	4629	2438	2191	1.90	2.11	6.21	4.31	0.69	18.6	295	652	15000	5.8	34.18	0.9	506
	10014	1.095	0.47	0.43	4850	2532	2318	1.92	2.09	6.25	4.23	0.68	17.9	291	678	17500	6.3	39.39	1.1	503
	12513	1.331	0.561	0.42	7532	3746	3786	2.01	1.99	6.79	4.60	0.68	21.2	299	710					
	12517	1.332	0.54	0.41	7513	3855	3659	1.95	2.05	6.80	4.52	0.67	20.4	299	738					
	15009	1.607	0.732	0.46	11341	5156	6185	2.20	1.83	7.35	5.21	0.71	27.1	297	653					
	15011	1.588	0.76	0.48	10966	5173	5793	2.12	1.89	7.31	5.30	0.73	28.1	301	629					
	15015	1.597	0.766	0.48	11083	5274	5809	2.10	1.91	7.33	5.32	0.73	28.3	299	624					
	17507	1.827	0.796	0.44	14584	6903	7681	2.11	1.90	7.73	5.41	0.70	29.3	305	700					
	17517	1.823	0.804	0.44	14606	7047	7560	2.07	1.93	7.72	5.44	0.70	29.6	306	694					
		Average		**0.45**						**Average**		**0.69**	Elasto-Plastic							

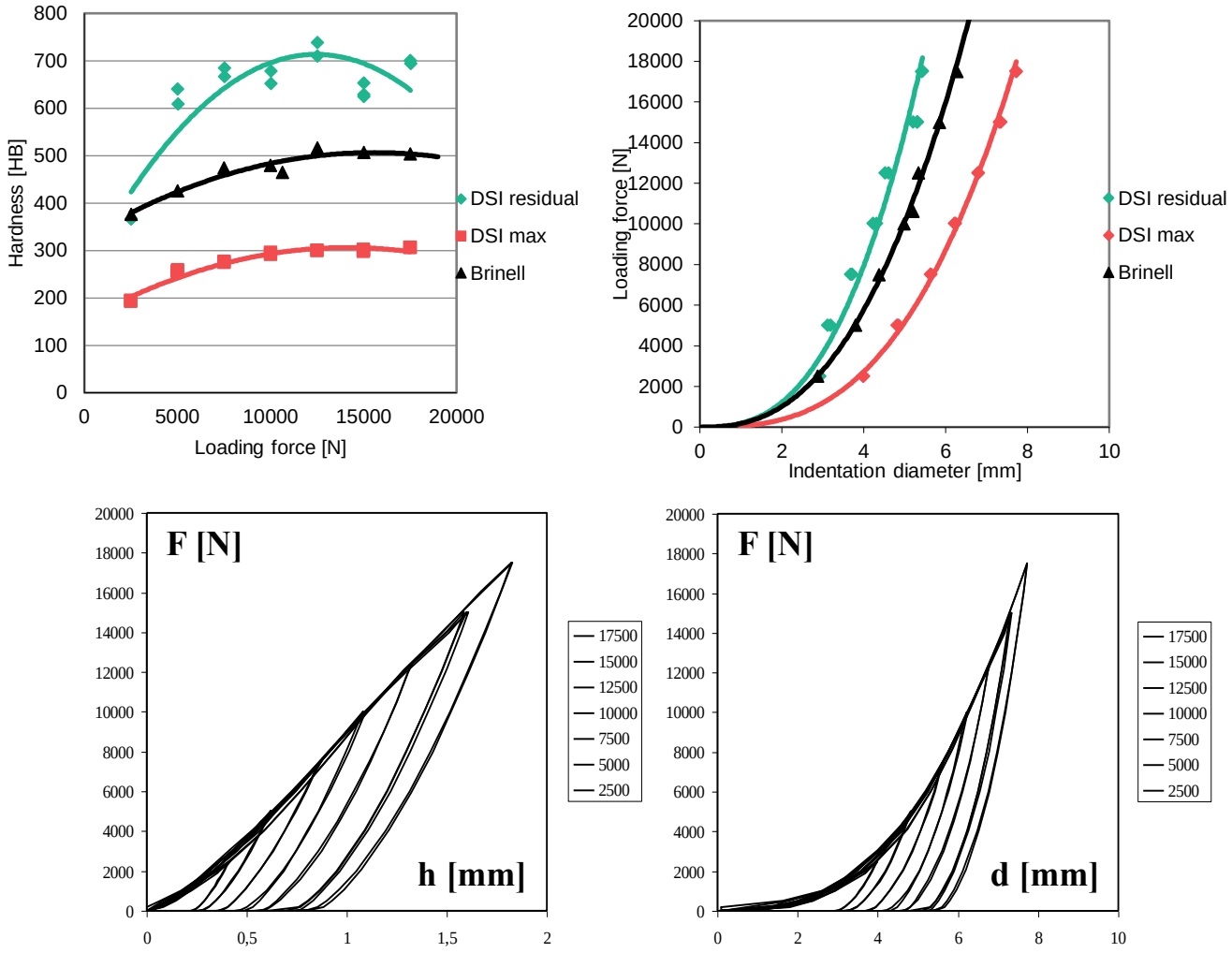

Fig. A-32 *Hardness test results of normal strength concrete*

Table A-29 *Hardness test results of high strength concrete*

	DSI results															Brinell results				
	Force [N]	**h_m [mm]**	**h_r [mm]**	**h_r/h_m [-]**	**W_t [Nmm]**	**W_e [Nmm]**	**W_d [Nmm]**	**W_t / W_e [-]**	**W_t / W_d [-]**	**d_m [mm]**	**d_r [mm]**	**d_r/d_m [-]**	**DSI d_r^2**	**HB_m [HB]**	**HB_r [HB]**	**Force [N]**	**d [mm]**	**Brinell d^2 [mm^2]**	**h [mm]**	**HB [HB]**
High strength concrete	2511	0.501	0.112	0.22	475.1	307.9	167.2	1.54	2.84	4.36	2.10	0.48	4.4	160	714	2500	1.8	3.16	0.1	1000
	2509	0.501	0.103	0.21	485.5	303.5	181.9	1.60	2.67	4.36	2.02	0.46	4.1	159	775	5000	2.4	5.85	0.1	1072
	5011	0.718	0.139	0.19	1407	927.6	479.9	1.52	2.93	5.16	2.34	0.45	5.5	222	1147	7500	2.9	8.53	0.2	1095
	5012	0.722	0.138	0.19	1456	912.2	544.4	1.60	2.68	5.18	2.33	0.45	5.4	221	1156	10000	3.3	10.81	0.3	1145
	7516	0.947	0.214	0.23	2853	1851.1	1001.9	1.54	2.85	5.86	2.89	0.49	8.4	253	1118	12500	3.6	13.24	0.3	1161
	7513	0.955	0.194	0.20	2858	1874.8	983.4	1.52	2.91	5.88	2.76	0.47	7.6	250	1233	15000	4.0	15.94	0.4	1148
	10013	1.126	0.246	0.22	4537	3028.2	1509.1	1.50	3.01	6.32	3.10	0.49	9.6	283	1296	17500	4.4	19.45	0.5	1087
	10013	1.129	0.253	0.22	4698	3006.4	1692.2	1.56	2.78	6.33	3.14	0.50	9.9	282	1260	20000	4.7	22.40	0.6	1069
	12521	1.368	0.316	0.23	6558	4493.2	2065.4	1.46	3.18	6.87	3.50	0.51	12.2	291	1261	22500	5.0	25.31	0.7	1055
	12516	1.373	0.316	0.23	6720	4514.1	2205.9	1.49	3.05	6.88	3.50	0.51	12.2	290	1261					
	12514	1.363	0.288	0.21	6626	4544.2	2082.2	1.46	3.18	6.86	3.34	0.49	11.2	292	1383					
	15015	1.562	0.398	0.25	9735	6105.4	3629.8	1.59	2.68	7.26	3.91	0.54	15.3	306	1201					
	15016	1.563	0.357	0.23	9604	6214.8	3389.4	1.55	2.83	7.26	3.71	0.51	13.8	306	1339					
	17516	1.733	0.395	0.23	12305	8198.2	4107.2	1.50	3.00	7.57	3.90	0.51	15.2	322	1412					
	17514	1.737	0.367	0.21	12945	8149.7	4795.9	1.59	2.70	7.58	3.76	0.50	14.1	321	1519					
	20015	1.976	0.521	0.26	15909	10131	5770.5	1.57	2.76	7.96	4.44	0.56	19.8	322	1223					
	20019	1.984	0.542	0.27	16328	10170	6157.7	1.61	2.65	7.98	4.53	0.57	20.5	321	1176					
	22516	2.18	0.591	0.27	21197	12545	8651.6	1.69	2.45	8.26	4.72	0.57	22.2	329	1213					
	22509	2.178	0.61	0.28	21488	12349	9138.9	1.74	2.35	8.26	4.79	0.58	22.9	329	1175					
		Average		**0.23**						**Average**		**0.51**	Elasto-Plastic							

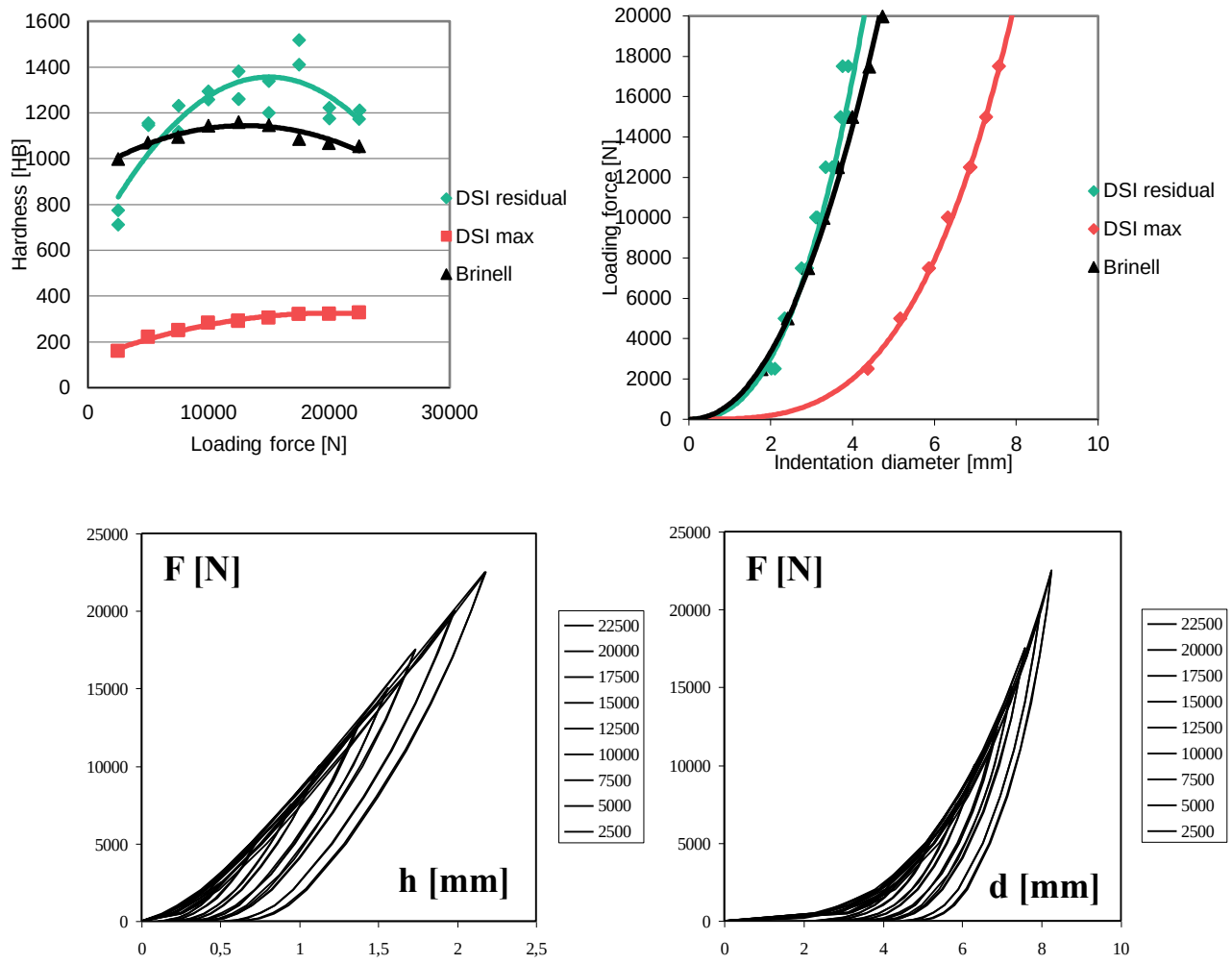

Fig. A-33 *Hardness test results of high strength concrete*

Table A-30 *Hardness test results of polymer concrete*

	DSI results															Brinell results				
	Force [N]	**h_m [mm]**	**h_r [mm]**	**h_r/h_m [-]**	**W_t [Nmm]**	**W_e [Nmm]**	**W_d [Nmm]**	**W_t / W_e [-]**	**W_t / W_d [-]**	**d_m [mm]**	**d_r [mm]**	**d_r/d_m [-]**	**DSI d_r^2**	**HB_m [HB]**	**HB_r [HB]**	**Force [N]**	**d [mm]**	**Brinell d^2 [mm^2]**	**h [mm]**	**HB [HB]**
Polymer concrete	2511	0.351	0.084	0.24	397.8	246.6	151.1	1.61	2.63	3.68	2.23	0.60	5.0	228	638	2500	2.4	5.79	0.1	542
	2512	0.349	0.076	0.22	395.9	248	147.9	1.60	2.68	3.67	2.12	0.58	4.5	229	701	5000	3.4	11.31	0.3	547
	5008	0.58	0.151	0.26	1348.7	788.4	560.3	1.71	2.41	4.67	2.95	0.63	8.7	275	716	7500	4.1	16.49	0.4	554
	5011	0.581	0.16	0.28	1376.1	789.8	586.4	1.74	2.35	4.68	2.88	0.62	8.3	275	753	10000	4.6	21.01	0.6	572
	6043	0.805	0.301	0.37	3115.2	1586.3	1528.9	1.96	2.04	5.44	3.42	0.63	11.7	239	639	12500	5.1	26.14	0.7	566
	7510	0.872	0.313	0.36	3091.6	1572.7	1518.8	1.97	2.04	5.64	3.48	0.62	12.1	274	764	15000	5.7	32.55	0.9	534
	10004	1.21	0.381	0.31	5886	2592.9	3293.1	2.27	1.79	6.52	3.83	0.59	14.7	263	836	17500	6.2	38.20	1.1	521
	10010	1.219	0.511	0.42	5947.5	2544	3403.5	2.34	1.75	6.54	4.40	0.67	19.4	261	624	20000	6.7	44.27	1.3	502
	11891	1.449	0.573	0.40	7957.6	3686.4	4271.2	2.16	1.86	7.04	4.65	0.66	21.6	261	661					
	11889	1.451	0.457	0.31	8029.4	3632.5	4397	2.21	1.83	7.04	4.18	0.59	17.4	261	828					
	12504	1.487	0.621	0.42	8632.3	3942.4	4689.9	2.19	1.84	7.12	4.83	0.68	23.3	268	641					
	12505	1.476	0.619	0.42	8446.6	3997.2	4449.4	2.11	1.90	7.09	4.82	0.68	23.2	270	643					
	12511	1.478	0.539	0.36	8619.1	3867.4	4751.7	2.23	1.81	7.10	4.52	0.64	20.4	269	739					
	12505	1.5	0.658	0.44	8859.9	3942.8	4917.1	2.25	1.80	7.14	4.96	0.69	24.6	265	605					
	15008	1.753	0.736	0.42	12838	5539	7299.6	2.32	1.76	7.60	5.22	0.69	27.3	273	649					
	15010	1.747	0.715	0.41	12775	5534	7241.1	2.31	1.76	7.59	5.15	0.68	26.6	273	668					
	15011	1.73	0.721	0.42	12530	5588.5	6942.5	2.24	1.80	7.56	5.17	0.68	26.8	276	663					
	17509	2.003	0.786	0.39	16860	7388.5	9472.1	2.28	1.78	8.00	5.38	0.67	29.0	278	709					
	17504	2.007	0.865	0.43	17163	7119.7	10044	2.41	1.71	8.01	5.62	0.70	31.6	278	644					
	17512	1.99	0.834	0.42	16920	7441.9	9478.9	2.27	1.79	7.98	5.53	0.69	30.6	280	668					
	20005	2.33	0.979	0.42	22564	9313.4	13251	2.42	1.70	8.45	5.94	0.70	35.3	273	650					
	20009	2.32	0.96	0.41	22593	9321.8	13272	2.42	1.70	8.44	5.89	0.70	34.7	275	663					
		Average		**0.37**						**Average**		**0.65**	Elasto-Plastic							

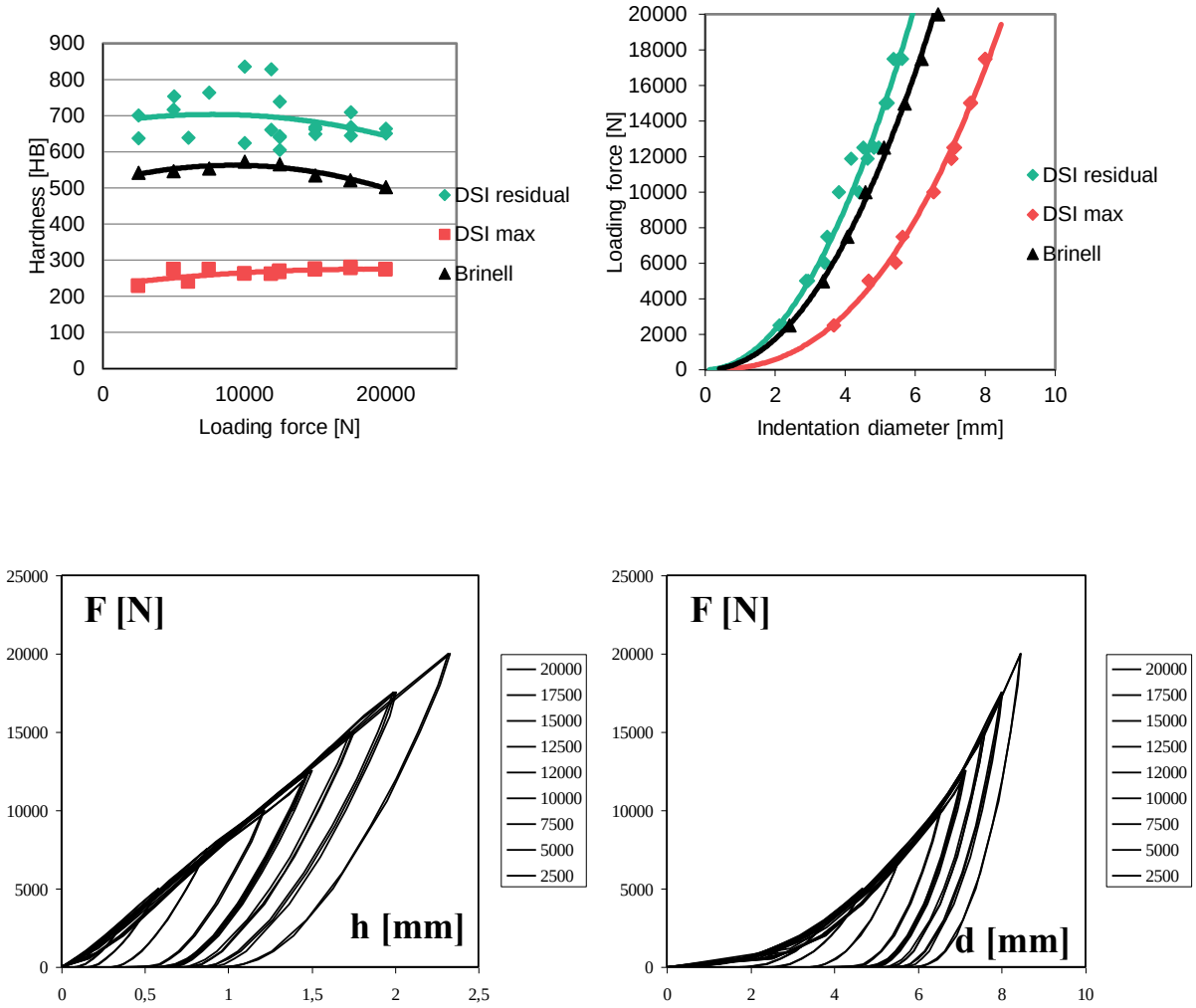

Fig. A-34 *Hardness test results of polymer concrete*

Table A-31 *Hardness test results of cellular concrete*

	DSI results															Brinell results				
	Force [N]	**h_m [mm]**	**h_r [mm]**	**h_r/h_m [-]**	**W_t [Nmm]**	**W_e [Nmm]**	**W_d [Nmm]**	**W_t / W_e [-]**	**W_t / W_d [-]**	**d_m [mm]**	**d_r [mm]**	**d_r/d_m [-]**	**DSI d_r^2**	**HB_m [HB]**	**HB_r [HB]**	**Force [N]**	**d [mm]**	**Brinell d^2 [mm^2]**	**h [mm]**	**HB [HB]**
Cellular concrete block	149	0.703	0.626	0.89	51.8	3.9	48	13.28	1.08	5.31	4.94	0.93	24.5	6.2	7.3					
	150	0.697	0.621	0.89	50.8	3.7	47	13.73	1.08	5.39	4.93	0.91	24.3	6.0	7.4					
	200	0.979	0.883	0.90	100.1	5.6	94.5	17.88	1.06	5.94	5.67	0.95	32.2	6.5	7.2					
	200	0.989	0.892	0.90	101.7	5.5	96.2	18.49	1.06	5.97	5.70	0.95	32.5	6.4	7.1					
	250	1.228	1.109	0.90	159.9	8.7	151.2	18.38	1.06	6.56	6.28	0.96	39.4	6.5	7.2					
	250	1.231	1.094	0.89	159.9	8.7	151.2	18.38	1.06	6.57	6.24	0.95	39.0	6.5	7.3					
	300	1.454	1.303	0.90	211.1	12.9	198.2	16.36	1.07	7.05	6.73	0.95	45.3	6.6	7.3					
	301	1.452	1.294	0.89	215.1	12.7	202.4	16.94	1.06	7.05	6.71	0.95	45.1	6.6	7.4					
	351	1.661	1.506	0.91	291.4	15.6	275.8	18.68	1.06	7.44	7.15	0.96	51.2	6.7	7.4					
	349	1.662	1.495	0.90	299.3	15.5	283.8	19.31	1.05	7.45	7.13	0.96	50.9	6.7	7.4	Brinell test was not possible, because even on the lowest load level the sample broke.				
	350	1.659	1.496	0.90	290.2	15.7	274.6	18.48	1.06	7.44	7.13	0.96	50.9	6.7	7.5					
	401	1.938	1.764	0.91	384.7	18.5	366.2	20.79	1.05	7.91	7.62	0.96	58.1	6.6	7.2					
	400	1.916	1.746	0.91	366.6	18.9	347.7	19.40	1.05	7.87	7.59	0.96	57.6	6.7	7.3					
	400	1.931	1.765	0.91	381.7	19	362.7	20.09	1.05	7.89	7.62	0.97	58.1	6.6	7.2					
	450	2.206	2.033	0.92	498.9	21.9	476.9	22.78	1.05	8.29	8.05	0.97	64.8	6.5	7.0					
	450	2.21	2.044	0.92	501.6	21.8	479.9	23.01	1.05	8.30	8.07	0.97	65.0	6.5	7.0					
	450	2.204	2.041	0.93	496.1	21.1	474.9	23.51	1.04	8.29	8.06	0.97	65.0	6.5	7.0					
	500	2.462	2.288	0.93	614.1	26.1	588.1	23.53	1.04	8.62	8.40	0.98	70.6	6.5	7.0					
	500	2.459	2.289	0.93	616.9	25.6	591.4	24.10	1.04	8.61	8.40	0.98	70.6	6.5	7.0					
		Average		**0.91**						**Average**		**0.96**	Plastic							

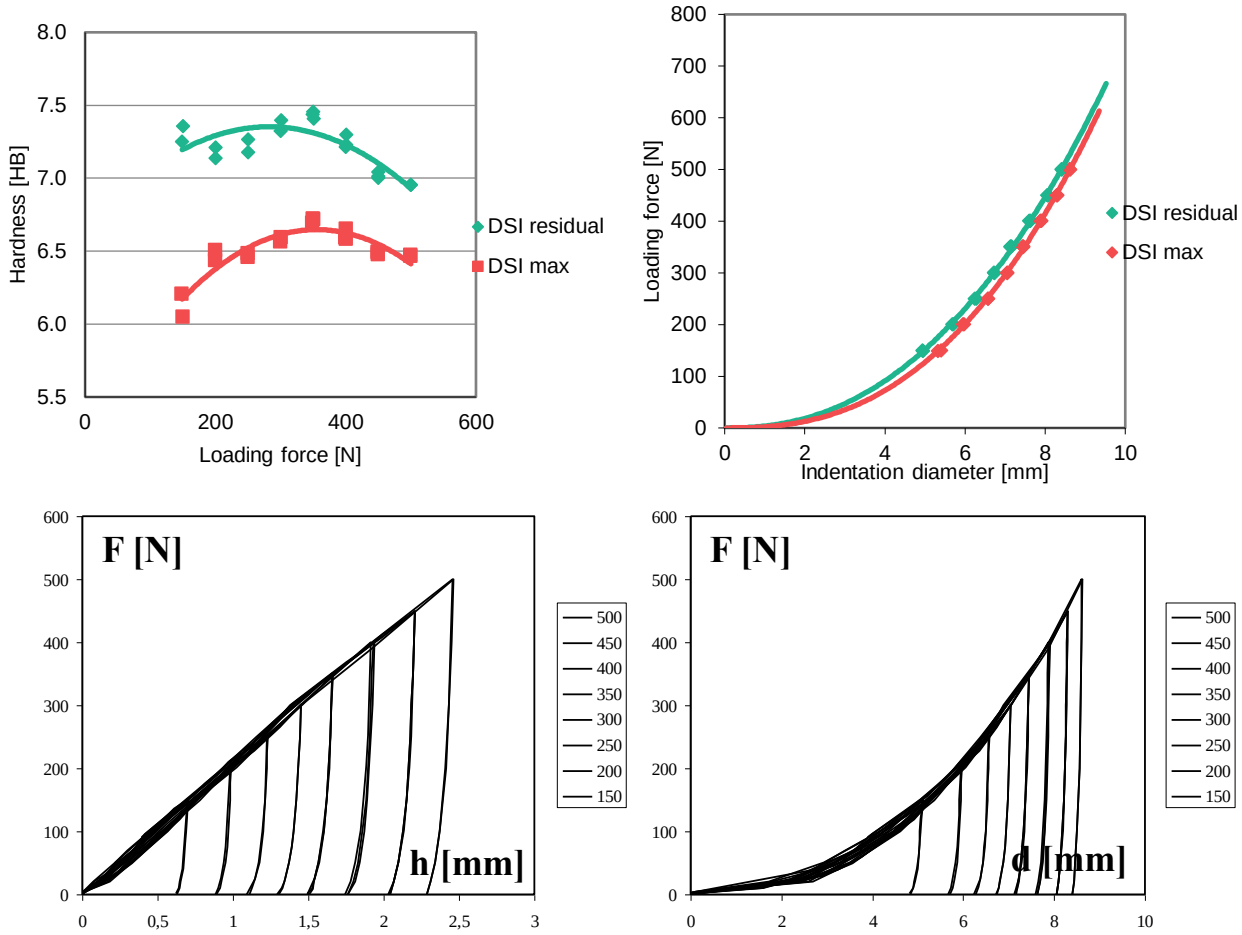

Fig. A-35 *Hardness test results of cellular concrete*

Table A-32 *Hardness test results of sand-lime brick*

	DSI results															Brinell results				
	Force [N]	**h_m [mm]**	**h_r [mm]**	**h_r/h_m [-]**	**W_t [Nmm]**	**W_e [Nmm]**	**W_d [Nmm]**	**W_t / W_e [-]**	**W_t / W_d [-]**	**d_m [mm]**	**d_r [mm]**	**d_r/d_m [-]**	**DSI d_r^2**	**HB_m [HB]**	**HB_r [HB]**	**Force [N]**	**d [mm]**	**Brinell d^2 [mm^2]**	**h [mm]**	**HB [HB]**
Sand-lime brick	1502	0.573	0.377	0.66	391.8	96.4	295.4	4.06	1.33	4.65	3.81	0.82	14.5	83	127	1875	4.5	20.25	0.5	112
	1505	0.564	0.375	0.66	389.1	97.9	291.2	3.97	1.34	4.61	3.80	0.82	14.4	85	128	2500	5.1	25.84	0.7	115
	1502	0.572	0.382	0.67	396.1	95.3	300.8	4.16	1.32	4.64	3.83	0.83	14.7	84	125	3125	5.6	30.80	0.8	118
	1878	0.693	0.446	0.64	567.2	141.3	425.8	4.01	1.33	5.08	4.13	0.81	17.0	86	134	4375	6.4	40.46	1.1	122
	1877	0.704	0.471	0.67	588.4	140.3	448.1	4.19	1.31	5.12	4.24	0.83	18.0	85	127	5000	6.8	46.57	1.3	118
	1878	0.726	0.485	0.67	619.9	142.5	477.5	4.35	1.30	5.19	4.30	0.83	18.5	82	123	5625	7.2	51.12	1.5	119
	2504	0.836	0.547	0.65	960.1	237.4	722.7	4.04	1.33	5.54	4.55	0.82	20.7	95	146	6875	7.8	60.55	1.9	118
	2503	0.835	0.57	0.68	945.5	234.7	710.8	4.03	1.33	5.53	4.64	0.84	21.5	95	140					
	3129	1.043	0.704	0.67	1480.8	362.6	1118.2	4.08	1.32	6.11	5.12	0.84	26.2	95	141					
	3131	1.025	0.695	0.68	1444.2	353.8	1090.4	4.08	1.32	6.07	5.09	0.84	25.9	97	143					
	3804	1.267	0.882	0.70	2239.7	529.3	1710.4	4.23	1.31	6.65	5.67	0.85	32.2	96	137					
	3802	1.241	0.869	0.70	2191.9	516	1675.9	4.25	1.31	6.59	5.63	0.85	31.7	98	139					
	4380	1.433	0.999	0.70	2943.6	698.9	2244.7	4.21	1.31	7.01	6.00	0.86	36.0	97	140					
	4377	1.461	1.022	0.70	3017	679.6	2337.4	4.44	1.29	7.06	6.06	0.86	36.7	95	136					
	5003	1.619	1.147	0.71	3810.9	888.8	2922.1	4.29	1.30	7.37	6.37	0.87	40.6	98	139					
	5002	1.593	1.113	0.70	3753.2	867.2	2886	4.33	1.30	7.32	6.29	0.86	39.6	100	143					
	5630	1.823	1.294	0.71	4861.2	1076.8	3784.4	4.51	1.28	7.72	6.71	0.87	45.1	98	139					
	5610	1.799	1.27	0.71	4752.1	1089	3663.1	4.36	1.30	7.68	6.66	0.87	44.3	99	141					
	6879	2.116	1.554	0.73	6748.9	1454.6	5294.4	4.64	1.27	8.37	7.35	0.88	54.0	97	136					
	6883	2.112	1.517	0.72	6813.6	1478.6	5335	4.61	1.28	8.16	7.37	0.90	54.4	99	135					
	Average			**0.69**						**Average**		**0.85**	Plastic							

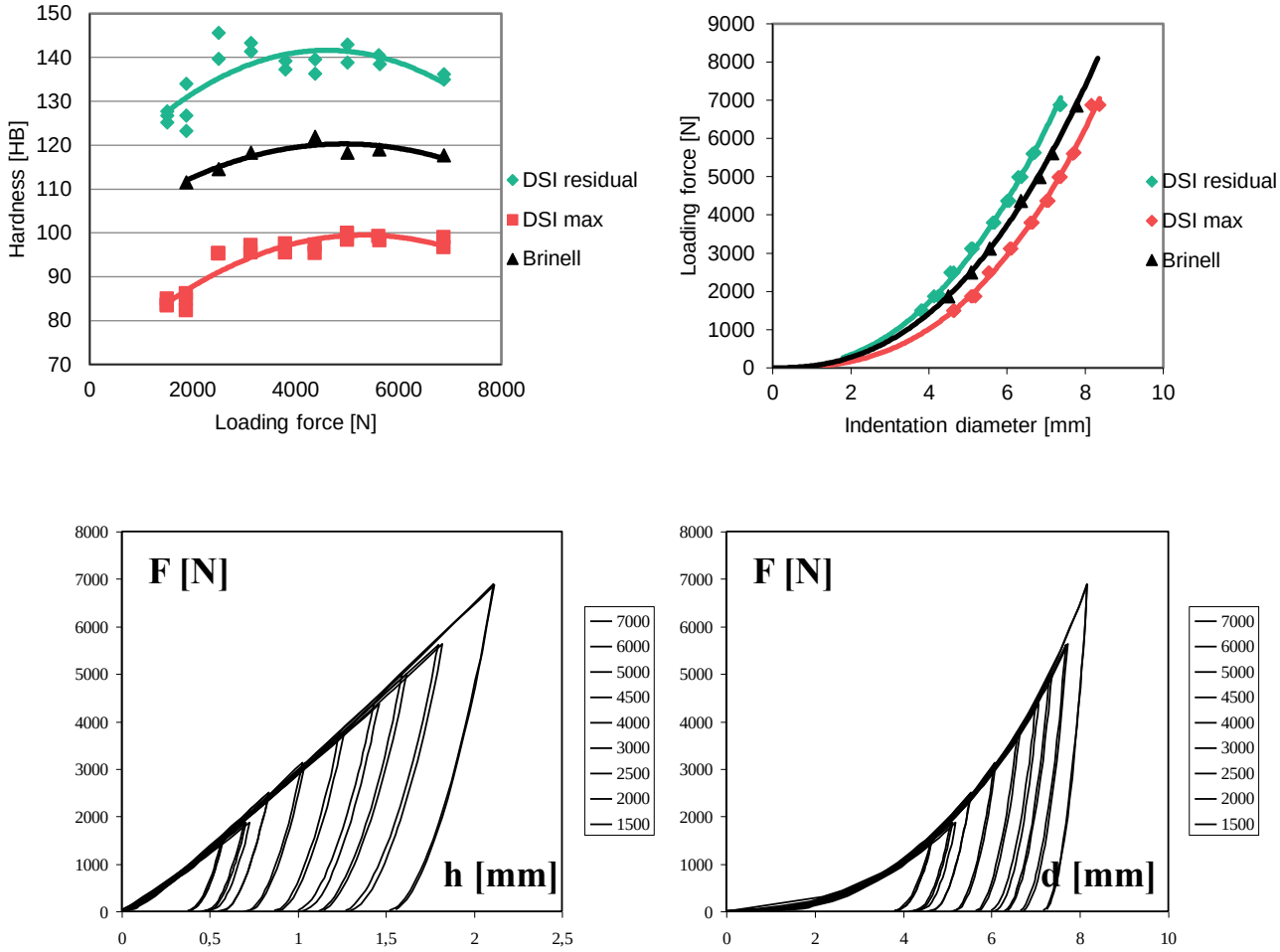

Fig. A-36 *Hardness test results of sand-lime brick*

Table A-33 *Hardness test results of clinker brick*

	DSI results															Brinell results				
	Force [N]	**h_m [mm]**	**h_r [mm]**	**h_r/h_m [-]**	**W_t [Nmm]**	**W_e [Nmm]**	**W_d [Nmm]**	**W_t / W_e [-]**	**W_t / W_d [-]**	**d_m [mm]**	**d_r [mm]**	**d_r/d_m [-]**	**DSI d_r^2**	**HB_m [HB]**	**HB_r [HB]**	**Force [N]**	**d [mm]**	**Brinell d^2 [mm^2]**	**h [mm]**	**HB [HB]**
Clinker brick	2515	0.365	0.034	0.09	389.7	278.1	111.6	1.40	3.49	3.75	1.16	0.31	1.4	219	2354	2500	1.2	1.55	0.0	2047
	2512	0.368	0.035	0.10	402.7	281.8	120.9	1.43	3.33	3.77	1.18	0.31	1.4	217	2285	5000	1.7	2.89	0.1	2187
	5013	0.595	0.074	0.12	1247.4	974.1	273.4	1.28	4.56	4.73	1.71	0.36	2.9	268	2156	7500	2.1	4.43	0.1	2132
	5014	0.595	0.076	0.13	1278	987.3	290.7	1.29	4.40	4.73	1.74	0.37	3.0	268	2100	10000	2.4	5.60	0.1	2242
	5017	0.593	0.077	0.13	1292.5	1002.6	289.9	1.29	4.46	4.72	1.75	0.37	3.1	269	2074	12500	2.6	6.75	0.2	2316
	7519	0.794	0.089	0.11	2553.9	2056.9	496.9	1.24	5.14	5.41	1.88	0.35	3.5	301	2689	15000	2.8	8.12	0.2	2303
	7518	0.796	0.087	0.11	2524.8	2017.1	507.7	1.25	4.97	5.41	1.86	0.34	3.4	301	2751	17500	3.2	10.31	0.3	2104
	10015	1	0.143	0.14	4163.7	3378.2	785.5	1.23	5.30	6.00	2.37	0.40	5.6	319	2229	20000	3.3	11.04	0.3	2242
	10014	1.006	0.127	0.13	4283.4	3451.5	822	1.24	5.21	6.02	2.24	0.37	5.0	317	2510	22500	3.7	13.32	0.3	2076
		Average		**0.12**						**Average**		**0.35**	Elastic			25000	3.9	15.12	0.4	2022
																27500	4.1	16.74	0.4	2000

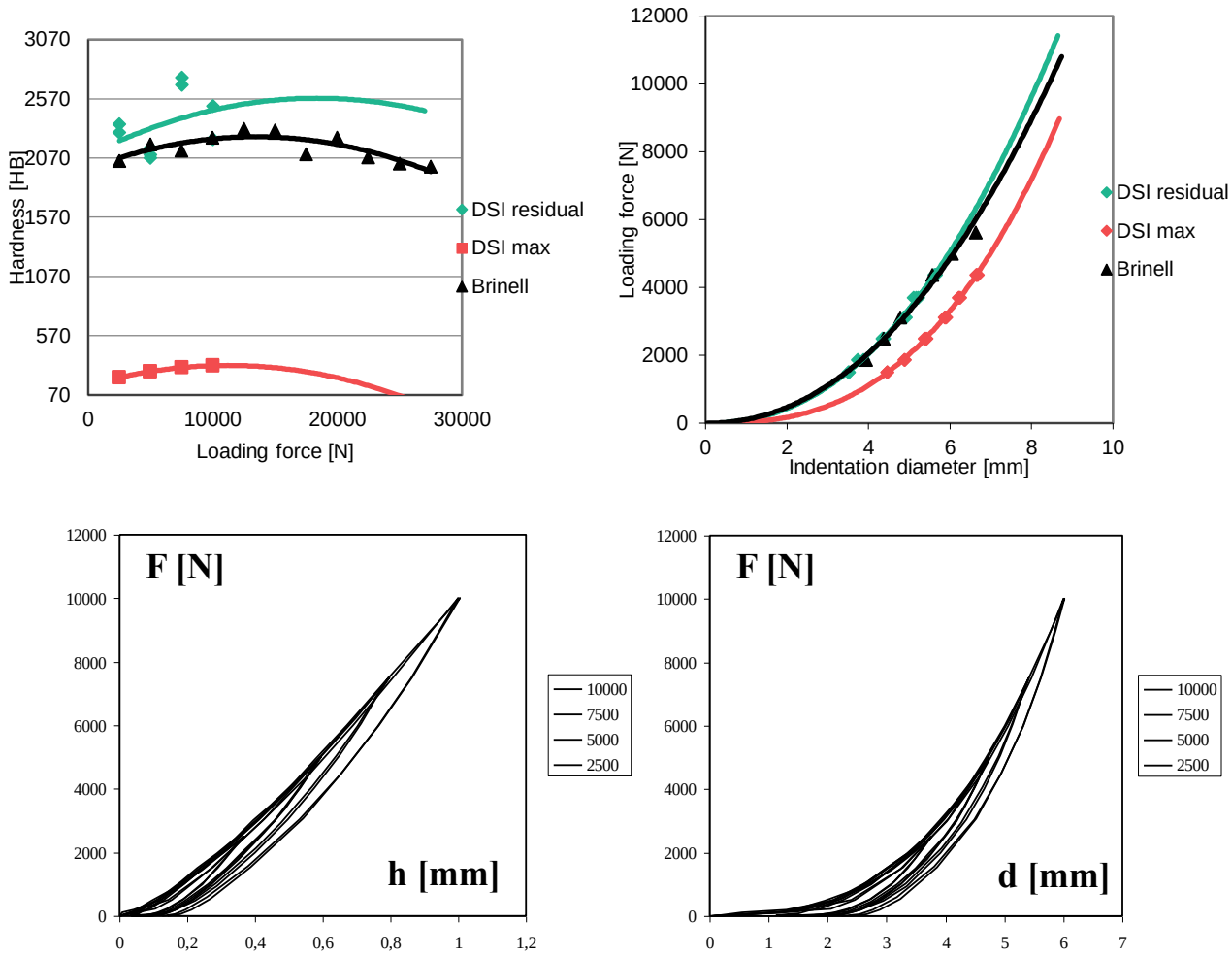

Fig. A-37 *Hardness test results of clinker brick*

Table A-34 *Hardness test results of facebrick*

	DSI results															Brinell results				
	Force [N]	**h_m [mm]**	**h_r [mm]**	**h_r/h_m [-]**	**W_t [Nmm]**	**W_e [Nmm]**	**W_d [Nmm]**	**W_t / W_e [-]**	**W_t / W_d [-]**	**d_m [mm]**	**d_r [mm]**	**d_r/d_m [-]**	**DSI d_r^2**	**HB_m [HB]**	**HB_r [HB]**	**Force [N]**	**d [mm]**	**Brinell d^2 [mm^2]**	**h [mm]**	**HB [HB]**
Facebrick	1504	0.524	0.321	0.61	356.2	100.6	255.5	3.54	1.39	4.46	3.53	0.79	12.4	91	149	1875	3.9	15.48	0.4	148
	1504	0.524	0.318	0.61	347.7	96.6	251.1	3.60	1.38	4.46	3.51	0.79	12.3	91	151	2500	4.4	19.13	0.5	158
	1875	0.637	0.392	0.62	549.7	149.2	400.5	3.68	1.37	4.88	3.88	0.79	15.1	94	152	3125	4.8	22.79	0.6	164
	1878	0.639	0.362	0.57	556.4	149.6	406.8	3.72	1.37	4.89	3.74	0.76	14.0	94	165	4375	5.6	30.91	0.8	165
	2501	0.798	0.497	0.62	912.7	253.7	658.99	3.60	1.38	5.42	4.35	0.80	18.9	100	160	5000	6.0	36.52	1.0	157
	2501	0.785	0.497	0.63	878	247.3	630.7	3.55	1.39	5.38	4.35	0.81	18.9	101	160	5625	6.6	44.00	1.3	142
	2502	0.793	0.505	0.64	915.8	243.9	671.9	3.75	1.36	5.40	4.38	0.81	19.2	100	158					
	3127	0.951	0.632	0.66	1384.6	348.5	1036.1	3.97	1.34	5.87	4.87	0.83	23.7	105	158					
	3126	0.956	0.636	0.67	1384.7	335.4	1049.2	4.13	1.32	5.88	4.88	0.83	23.8	104	156					
	3128	0.966	0.647	0.67	1448.8	339.7	1109.1	4.26	1.31	5.91	4.92	0.83	24.2	103	154					
	3705	1.088	0.737	0.68	1815.9	461.1	1354.8	3.94	1.34	6.23	5.23	0.84	27.3	108	160					
	3706	1.096	0.722	0.66	1867	477.6	1389.5	3.91	1.34	6.25	5.18	0.83	26.8	108	163					
	3701	1.083	0.701	0.65	1806.1	477.8	1328.3	3.78	1.36	6.22	5.11	0.82	26.1	109	168					
	4378	1.262	0.863	0.68	2551.9	614.3	1937.6	4.15	1.32	6.64	5.62	0.85	31.5	110	161					
	4379	1.267	0.87	0.69	2596.4	625.7	1970.7	4.15	1.32	6.65	5.64	0.85	31.8	110	160					
	4377	1.282	0.874	0.68	2699.6	622.8	2076.8	4.33	1.30	6.69	5.65	0.84	31.9	109	159					
		Average		**0.65**						**Average**		**0.82**	Elasto-Plastic							

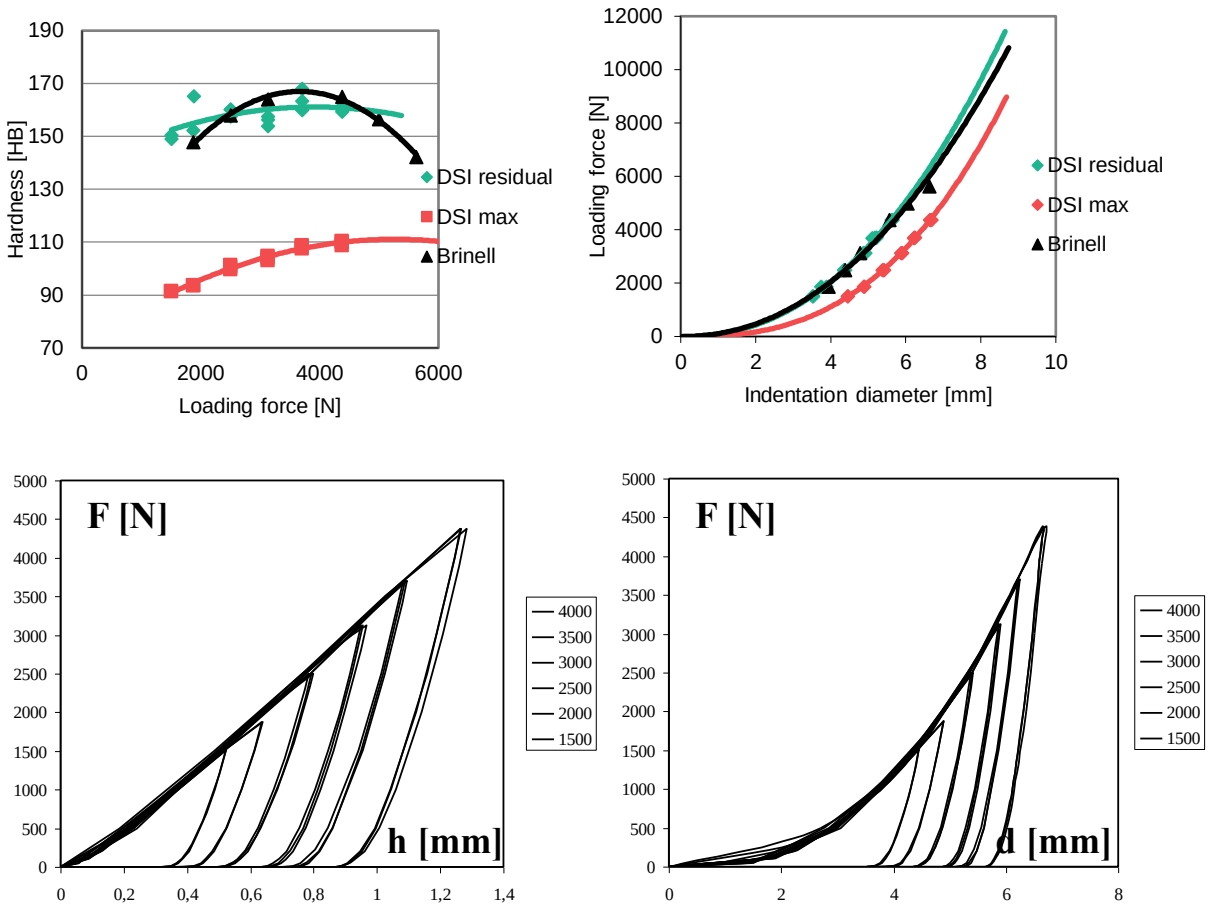

Fig. A-38 *Hardness test results of facebrick*

Table A-35 *Hardness test results of clinker tile*

	DSI results															Brinell results				
	Force [N]	**h_m [mm]**	**h_r [mm]**	**h_r/h_m [-]**	**W_t [Nmm]**	**W_e [Nmm]**	**W_d [Nmm]**	**W_t / W_e [-]**	**W_t / W_d [-]**	**d_m [mm]**	**d_r [mm]**	**d_r/d_m [-]**	**DSI d_r^2**	**HB_m [HB]**	**HB_r [HB]**	**Force [N]**	**d [mm]**	**Brinell d^2 [mm^2]**	**h [mm]**	**HB [HB]**
Clinker tile	1008	0.256	0.006	0.02	100.4	74.8	25.6	1.34	3.92	3.16	0.49	0.16	0.2	125	5348	1875	0.7	0.50	0.01	4782
	2012	0.39	0.009	0.02	286.7	230.7	56	1.24	5.12	3.87	0.60	0.15	0.4	164	7117	2500	0.8	0.66	0.02	4840
	2015	0.389	0.011	0.03	286.6	226.4	60.1	1.27	4.77	3.87	0.66	0.17	0.4	165	5832	3125	0.9	0.78	0.02	5068
	2505	0.463	0.014	0.03	559.5	470.5	89.1	1.19	6.28	4.20	0.75	0.18	0.6	172	5694	4375	1.1	1.18	0.03	4723
	3017	0.497	0.018	0.04	551.4	464.6	86.7	1.19	6.36	4.35	0.85	0.20	0.7	193	5335	5000	1.2	1.36	0.03	4682
	4015	0.589	0.023	0.04	860.1	735.7	124.4	1.17	6.91	4.71	0.96	0.20	0.9	217	5556					
	4019	0.591	0.025	0.04	863.4	741.3	122.1	1.16	7.07	4.72	1.00	0.21	1.0	216	5118					
	5018	0.675	0.029	0.04	1257.8	1090.4	167.4	1.15	7.51	5.02	1.08	0.21	1.2	237	5508					
	5020	0.677	0.032	0.05	1244	1068.8	175.1	1.16	7.10	5.02	1.13	0.22	1.3	236	4994					
		Average		**0.03**						**Average**		**0.19**	Elastic							

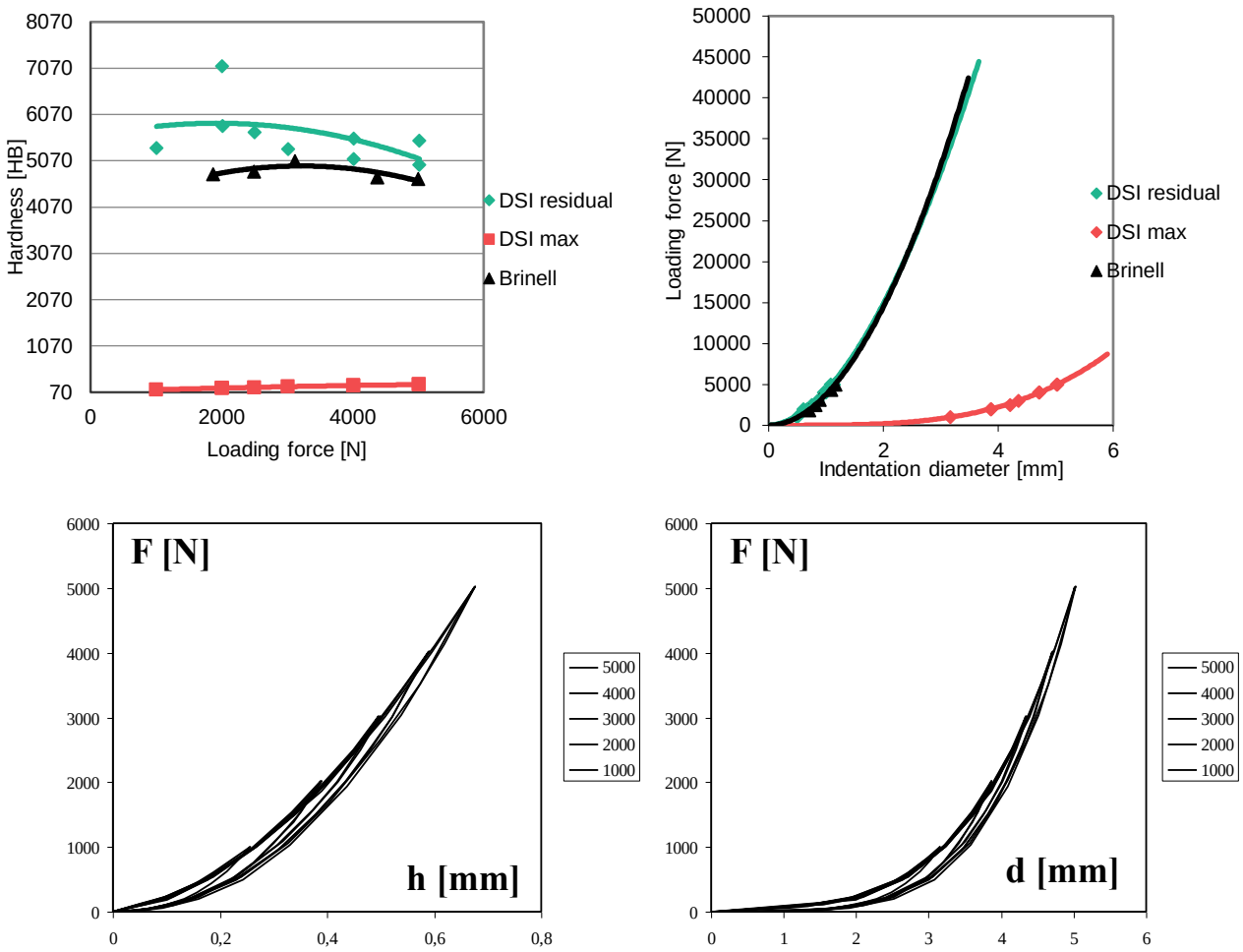

Fig. A-39 *Hardness test results of clinker tile*

Table A-36 *Hardness test results of porous limestone A*

	DSI results															Brinell results				
	Force [N]	**h_m [mm]**	**h_r [mm]**	**h_r/h_m [-]**	**W_t [Nmm]**	**W_e [Nmm]**	**W_d [Nmm]**	**W_t / W_e [-]**	**W_t / W_d [-]**	**d_m [mm]**	**d_r [mm]**	**d_r/d_m [-]**	**DSI d_r^2**	**HB_m [HB]**	**HB_r [HB]**	**Force [N]**	**d [mm]**	**Brinell d^2 [mm^2]**	**h [mm]**	**HB [HB]**
Porous limestone A	1003	0.95	0.84	0.88	381.6	40.4	341.2	9.45	1.12	5.86	5.55	0.95	30.8	34	38	1875	7.09	50.27	1.47	40
	1001	0.955	0.825	0.86	395.5	36.6	358.9	10.81	1.10	5.88	5.50	0.94	30.3	33	39	2500	7.71	59.44	1.82	44
	1001	0.955	0.811	0.85	402.5	36.1	366.4	11.15	1.10	5.88	5.46	0.93	29.8	33	39	3125	8.33	69.39	2.23	45
	1251	1.098	0.946	0.86	594.5	55.9	538.6	10.64	1.10	6.25	5.85	0.94	34.3	36	42	4375	9.36	87.61	3.24	43
	1251	1.097	0.964	0.88	608.2	52.9	555.3	11.50	1.10	6.25	5.90	0.94	34.8	36	41	5000	9.78	95.65	3.96	40
	1516	1.294	1.119	0.86	856.2	88	768.2	9.73	1.11	6.71	6.30	0.94	39.8	37	43					
	1500	1.299	1.095	0.84	887.3	80	807.3	11.09	1.10	6.72	6.25	0.93	39.0	37	44					
	1502	1.307	1.149	0.88	891.9	80.1	811.9	11.13	1.10	6.74	6.38	0.95	40.7	37	42					
	1502	1.287	1.058	0.82	852.4	79	773.4	10.79	1.10	6.70	6.15	0.92	37.8	37	45					
	1886	1.504	1.341	0.89	1231.2	126.6	1104.6	9.73	1.11	7.15	6.82	0.95	46.4	40	45					
	1880	1.498	1.321	0.88	1238.1	125.6	1112.5	9.86	1.11	7.14	6.77	0.95	45.9	40	45					
	2502	1.953	1.715	0.88	2141.3	193.2	1948.1	11.08	1.10	7.93	7.54	0.95	56.8	41	46					
	2501	1.955	1.719	0.88	2254.9	200.9	2054	11.22	1.10	7.93	7.55	0.95	56.9	41	46					
	2471	1.947	1.685	0.87	2153.4	185.6	1967.7	11.60	1.09	7.92	7.49	0.95	56.0	40	47					
	3128	2.354	2.039	0.87	3368.5	292.2	3076.3	11.53	1.09	8.48	8.06	0.95	64.9	42	49					
	3127	2.388	2.094	0.88	3443.7	308.4	3135.2	11.17	1.10	8.53	8.14	0.95	66.2	42	48					
	3128	2.387	2.134	0.89	3553.7	294.3	3259.4	12.08	1.09	8.53	8.19	0.96	67.1	42	47					
	3700	2.882	2.557	0.89	5016.7	397.3	4619.4	12.63	1.09	9.06	8.73	0.96	76.1	41	46					
	3702	2.843	2.541	0.89	4911.1	397.3	4513.8	12.36	1.09	9.02	8.71	0.97	75.8	41	46					
	3700	2.886	2.549	0.88	4988.1	406.1	4581.9	12.28	1.09	9.06	8.72	0.96	76.0	41	46					
	4376	3.47	3.08	0.89	7315.7	552	6763.7	13.25	1.08	9.52	9.23	0.97	85.3	40	45					
	4375	3.417	3.029	0.89	7220.3	539.4	6680.8	13.39	1.08	9.49	9.19	0.97	84.5	41	46					
		Average		**0.87**						**Average**		**0.95**	Plastic							

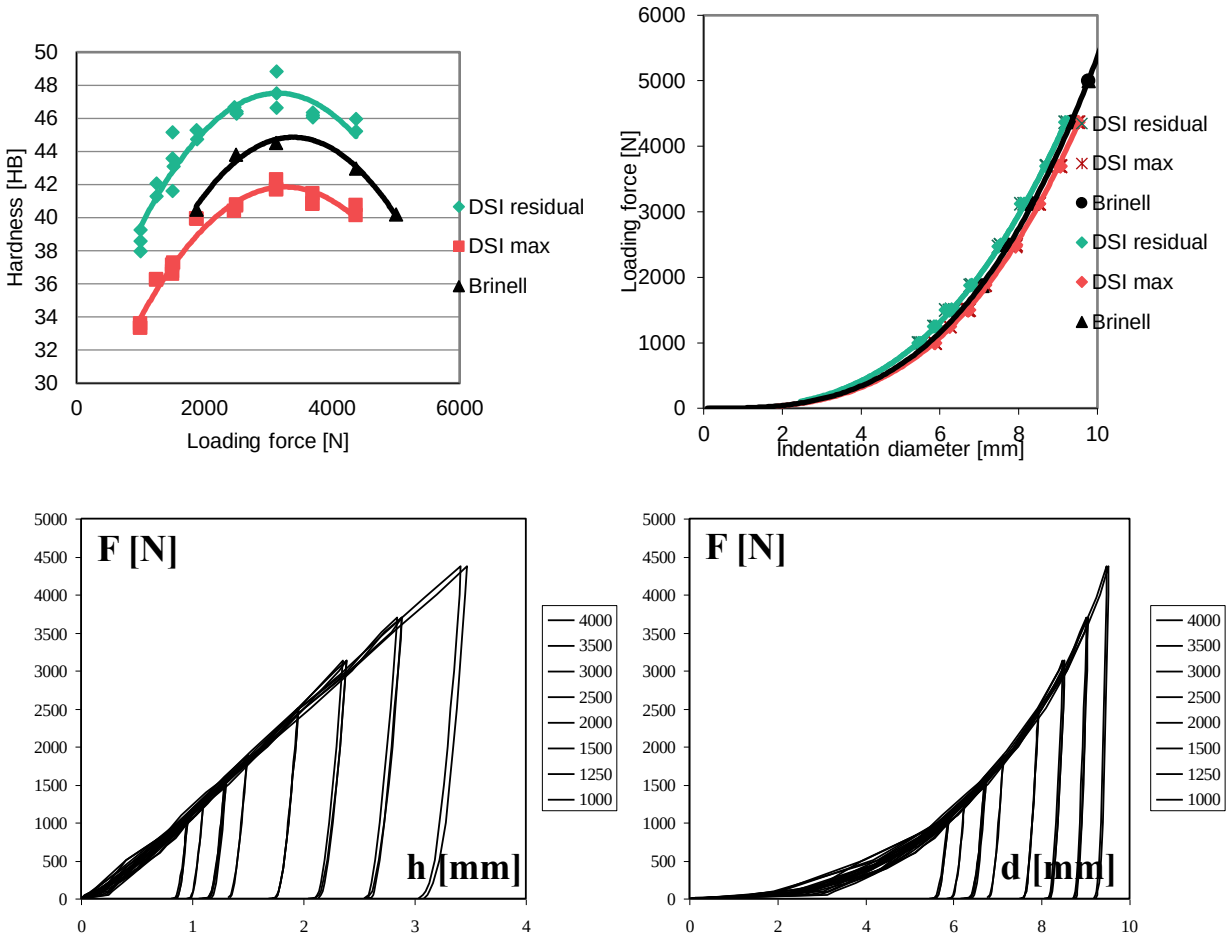

Fig. A-40 *Hardness test results of porous limestone A*

Table A-37 *Hardness test results of porous limestone B*

	DSI results															Brinell results				
	Force [N]	**h_m [mm]**	**h_r [mm]**	**h_r/h_m [-]**	**W_t [Nmm]**	**W_e [Nmm]**	**W_d [Nmm]**	**W_t / W_e [-]**	**W_t / W_d [-]**	**d_m [mm]**	**d_r [mm]**	**d_r/d_m [-]**	**DSI d_r^2**	**HB_m [HB]**	**HB_r [HB]**	**Force [N]**	**d [mm]**	**Brinell d^2 [mm^2]**	**h [mm]**	**HB [HB]**
Porous limestone B	500	0.51	0.431	0.85	121	17.1	103.9	7.08	1.16	4.40	4.06	0.92	16.5	31	37	1875	6.9	47.86	1.39	43
	501	0.513	0.391	0.76	120.6	15.05	105.5	8.01	1.14	4.41	3.88	0.88	15.0	31	41	2500	7.6	57.86	1.75	45
	751	0.7	0.554	0.79	236.9	30.4	106.4	7.79	2.23	5.10	4.58	0.90	20.9	34	43	3125	8.4	70.80	2.30	43
	755	0.698	0.543	0.78	240	32.3	207.8	7.43	1.15	5.10	4.53	0.89	20.5	34	44					
	1001	0.877	0.73	0.83	405.7	46.3	359.4	8.76	1.13	5.66	5.20	0.92	27.1	36	44					
	1001	0.889	0.728	0.82	417.7	47.1	370.7	8.87	1.13	5.69	5.20	0.91	27.0	36	44					
	1251	1.048	0.877	0.84	621.3	70.4	550.9	8.83	1.13	6.13	5.66	0.92	32.0	38	45					
	1252	1.049	0.894	0.85	606.9	65.7	541.3	9.24	1.12	6.13	5.71	0.93	32.6	38	45					
	1501	1.222	1.018	0.83	876.8	92.6	784.2	9.47	1.12	6.55	6.05	0.92	36.6	39	47					
	1505	1.23	1.04	0.85	862.1	93.4	768.7	9.23	1.12	6.57	6.11	0.93	37.3	39	46					
	1750	1.355	1.132	0.84	1056.2	126.1	930.1	8.38	1.14	6.85	6.34	0.93	40.2	41	49					
	1751	1.348	1.142	0.85	1075.1	122.6	952.5	8.77	1.13	6.83	6.36	0.93	40.5	41	49					
	1755	1.351	1.14	0.84	1049.6	128.7	920.9	8.16	1.14	6.84	6.36	0.93	40.4	41	49					
	2001	1.519	1.295	0.85	1337.8	156.2	1181.6	8.56	1.13	7.18	6.72	0.94	45.1	42	49					
	2002	1.532	1.296	0.85	1384.3	160.7	1223.6	8.61	1.13	7.20	6.72	0.93	45.1	42	49					
	2251	1.692	1.431	0.85	1760.2	199.4	1560.8	8.83	1.13	7.50	7.00	0.93	49.0	42	50					
	2253	1.688	1.391	0.82	1756.5	211.9	1544.6	8.29	1.14	7.49	6.92	0.92	47.9	42	52					
		Average		**0.83**						**Average**		**0.92**	Plastic							

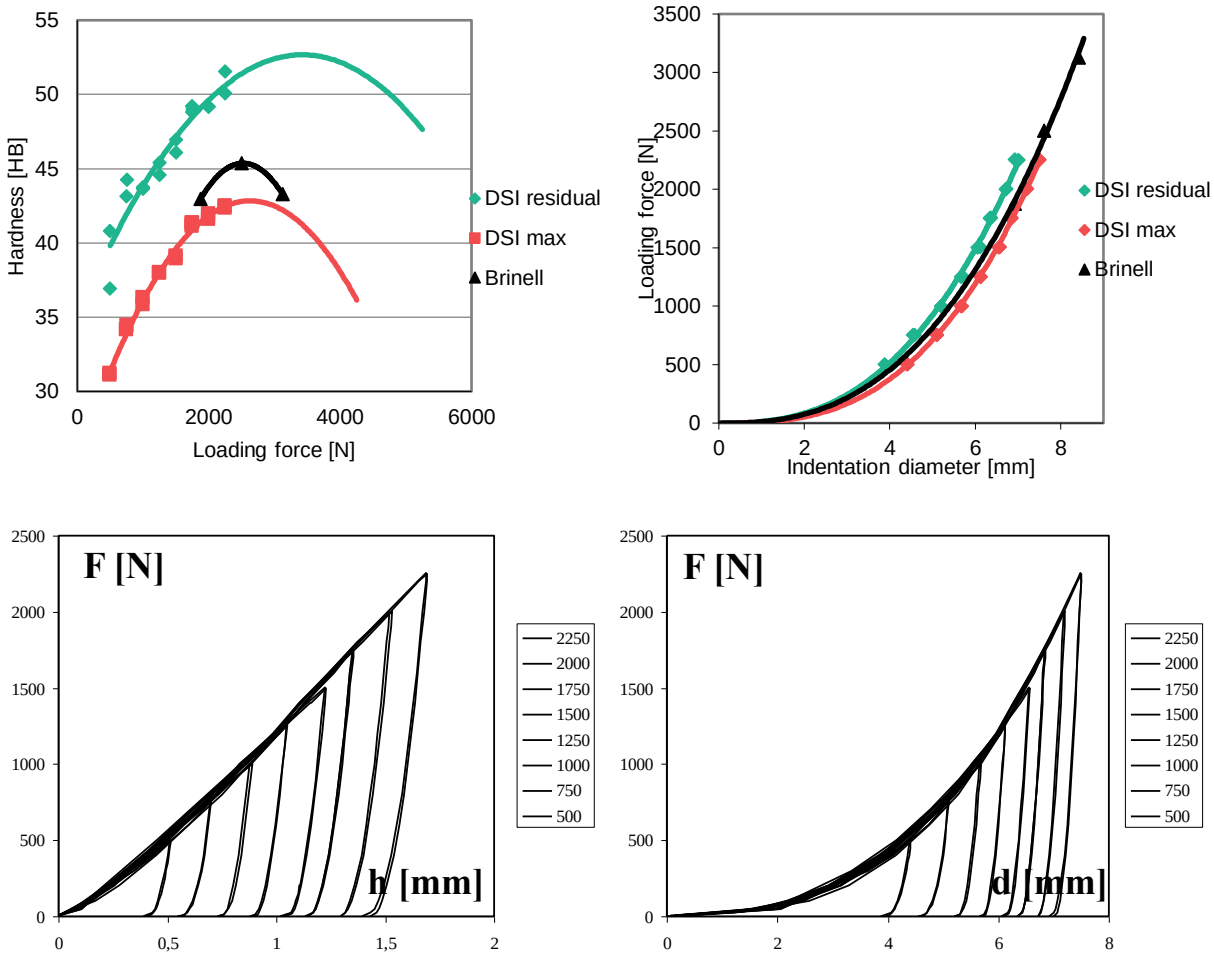

Fig. A-41 *Hardness test results of porous limestone B*

Table A-38 *Hardness test results of compact limestone*

	DSI results															Brinell results				
	Force [N]	**h_m [mm]**	**h_r [mm]**	**h_r/h_m [-]**	**W_t [Nmm]**	**W_e [Nmm]**	**W_d [Nmm]**	**W_t / W_e [-]**	**W_t / W_d [-]**	**d_m [mm]**	**d_r [mm]**	**d_r/d_m [-]**	**DSI d_r^2**	**HB_m [HB]**	**HB_r [HB]**	**Force [N]**	**d [mm]**	**Brinell d^2 [mm^2]**	**h [mm]**	**HB [HB]**
Compact limestone	2008	0.455	0.06	0.15	385.1	221.9	163.2	1.74	2.36	4.17	1.63	0.39	2.7	140	954.1	2500	2.1	4.55	0.11	692
	2010	0.448	0.06	0.15	383.3	225.3	158	1.70	2.43	4.14	1.62	0.39	2.6	143	969.4	4375	2.8	7.56	0.19	722
	2008	0.448	0.07	0.16	386	218.9	167.1	1.76	2.31	4.14	1.69	0.41	2.9	143	887.8	5000	2.9	8.56	0.22	728
	2507	0.453	0.06	0.15	470.5	313.6	156.9	1.50	3.00	4.16	1.62	0.39	2.6	176	1209	6875	3.3	10.73	0.28	794
	2507	0.457	0.07	0.16	479.6	307.2	172.4	1.56	2.78	4.18	1.73	0.41	3.0	175	1063	7500	3.5	12.43	0.32	744
	5013	0.75	0.15	0.21	1434.8	981	453.8	1.46	3.16	5.27	2.46	0.47	6.1	213	1036	9375	4.0	15.73	0.41	728
	5014	0.742	0.15	0.21	1371.4	936.8	434.6	1.46	3.16	5.24	2.49	0.47	6.2	215	1017	10000	4.0	15.97	0.42	764
	5004	0.745	0.11	0.15	1405.9	888	518	1.58	2.71	5.25	2.43	0.46	5.9	214	1061	12500	4.4	18.92	0.50	799
	7513	0.995	0.23	0.23	3047.9	1922.5	1125.4	1.59	2.71	5.99	3.01	0.50	9.1	240	1031	15000	5.0	24.91	0.67	715
	7510	0.996	0.22	0.23	3100.4	1903.7	1196.6	1.63	2.59	5.99	2.98	0.50	8.9	240	1053	17500	5.6	30.97	0.85	659
	10004	1.245	0.29	0.23	5387.7	2976.7	2411	1.81	2.23	6.60	3.36	0.51	11.3	256	1094					
	10012	1.259	0.32	0.26	5615.8	3023.6	2592.2	1.86	2.17	6.63	3.55	0.53	12.6	253	981					
	12514	1.469	0.30	0.21	7553	4628.6	2924.4	1.63	2.58	7.08	3.44	0.49	11.8	271	1306					
	12510	1.473	0.34	0.23	7404	4484.2	2919.9	1.65	2.54	7.09	3.65	0.51	13.3	270	1158					
	15017	1.694	0.44	0.26	10684	6202.7	4481.9	1.72	2.38	7.50	4.12	0.55	17.0	282	1074					
	15019	1.699	0.47	0.28	10848	6203.2	4645.6	1.75	2.34	7.51	4.24	0.56	18.0	281	1013					
	17508	1.921	0.43	0.22	14445	8133.9	6311.1	1.78	2.29	7.88	4.39	0.56	19.2	290	1100					
	17516	1.941	0.51	0.27	14718	8076.3	6641.8	1.82	2.22	7.91	4.44	0.56	19.7	287	1074					
		Average		**0.21**						**Average**		**0.48**	Elasto-Plastic							

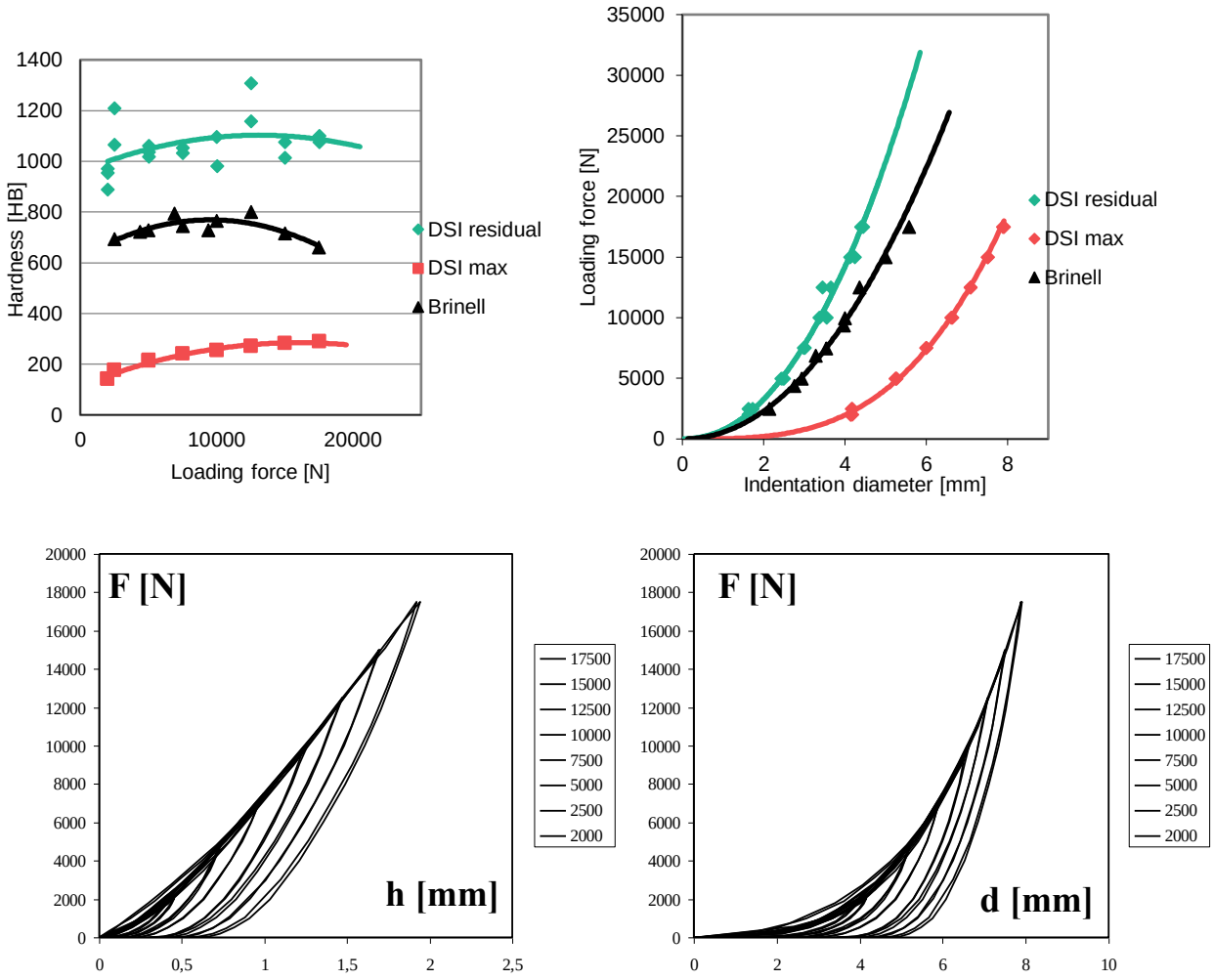

Fig. A-42 *Hardness test results of compact limestone*

Table A-39 *Hardness test results of rhyolite tuff*

	DSI results															Brinell results				
	Force [N]	**h_m [mm]**	**h_r [mm]**	**h_r/h_m [-]**	**W_t [Nmm]**	**W_e [Nmm]**	**W_d [Nmm]**	**W_t / W_e [-]**	**W_t / W_d [-]**	**d_m [mm]**	**d_r [mm]**	**d_r/d_m [-]**	**DSI d_r^2**	**HB_m [HB]**	**HB_r [HB]**	**Force [N]**	**d [mm]**	**Brinell d^2 [mm^2]**	**h [mm]**	**HB [HB]**
Rhyolite tuff	1254	0.415	0.23	0.57	224	73.8	150.2	3.04	1.49	3.99	3.03	0.76	9.2	96	170	1875	4.2	17.94	0.47	127
	1249	0.418	0.24	0.58	225.8	65.1	160.7	3.47	1.41	4.00	3.08	0.77	9.5	95	164	2500	4.9	23.55	0.63	127
	1879	0.618	0.33	0.54	567.1	151	416.1	3.76	1.36	4.82	3.60	0.75	13.0	97	179	3125	5.3	28.38	0.77	129
	1876	0.613	0.32	0.52	575.2	156.8	418.4	3.67	1.37	4.80	3.53	0.73	12.4	97	186	4375	6.1	37.21	1.04	134
	2501	0.764	0.48	0.63	855	240.5	614.6	3.56	1.39	5.31	4.30	0.81	18.5	104	164	5000	6.6	43.23	1.23	129
	2503	0.763	0.47	0.62	871.4	241.2	630.2	3.61	1.38	5.31	4.26	0.80	18.1	104	167	5625	6.8	46.13	1.33	135
	3131	0.897	0.57	0.64	1328.4	359.7	968.7	3.69	1.37	5.72	4.64	0.81	21.6	111	174	6875	7.5	55.50	1.66	131
	3128	0.891	0.55	0.63	1336.5	359.5	976.9	3.72	1.37	5.70	4.59	0.81	21.1	112	178	7500	7.8	60.84	1.87	128
	4377	1.164	0.73	0.63	2580.9	674	1906.9	3.83	1.35	6.41	5.20	0.81	27.1	120	191					
	4380	1.171	0.74	0.63	2547.3	663.7	1883.6	3.84	1.35	6.43	5.25	0.82	27.5	119	188					
	5004	1.344	0.85	0.64	3366.4	871.4	2495	3.86	1.35	6.82	5.59	0.82	31.2	119	187					
	5001	1.337	0.87	0.65	3388.6	840.1	2548.5	4.03	1.33	6.81	5.65	0.83	31.9	119	182					
	5631	1.458	0.94	0.65	3689.5	1046.7	2642.8	3.52	1.40	7.06	5.86	0.83	34.4	123	189					
	5628	1.46	0.94	0.65	3569.1	1054.3	2514.7	3.39	1.42	7.06	5.85	0.83	34.3	123	189					
	6879	1.811	1.18	0.66	6001.6	1445.3	4556.3	4.15	1.32	7.70	6.47	0.84	41.8	121	184					
	6882	1.806	1.16	0.64	6118.7	1436.5	4682.2	4.26	1.31	7.69	6.41	0.83	41.0	121	189					
	7505	2.019	1.20	0.60	7632.5	1684.7	5947.8	4.53	1.28	8.03	6.81	0.85	46.4	118	178					
	7503	2.018	1.33	0.66	7611.3	1678.5	5932.8	4.53	1.28	8.03	6.79	0.85	46.2	118	179					
	Average			**0.62**						**Average**		**0.81**	Elasto-Plastic							

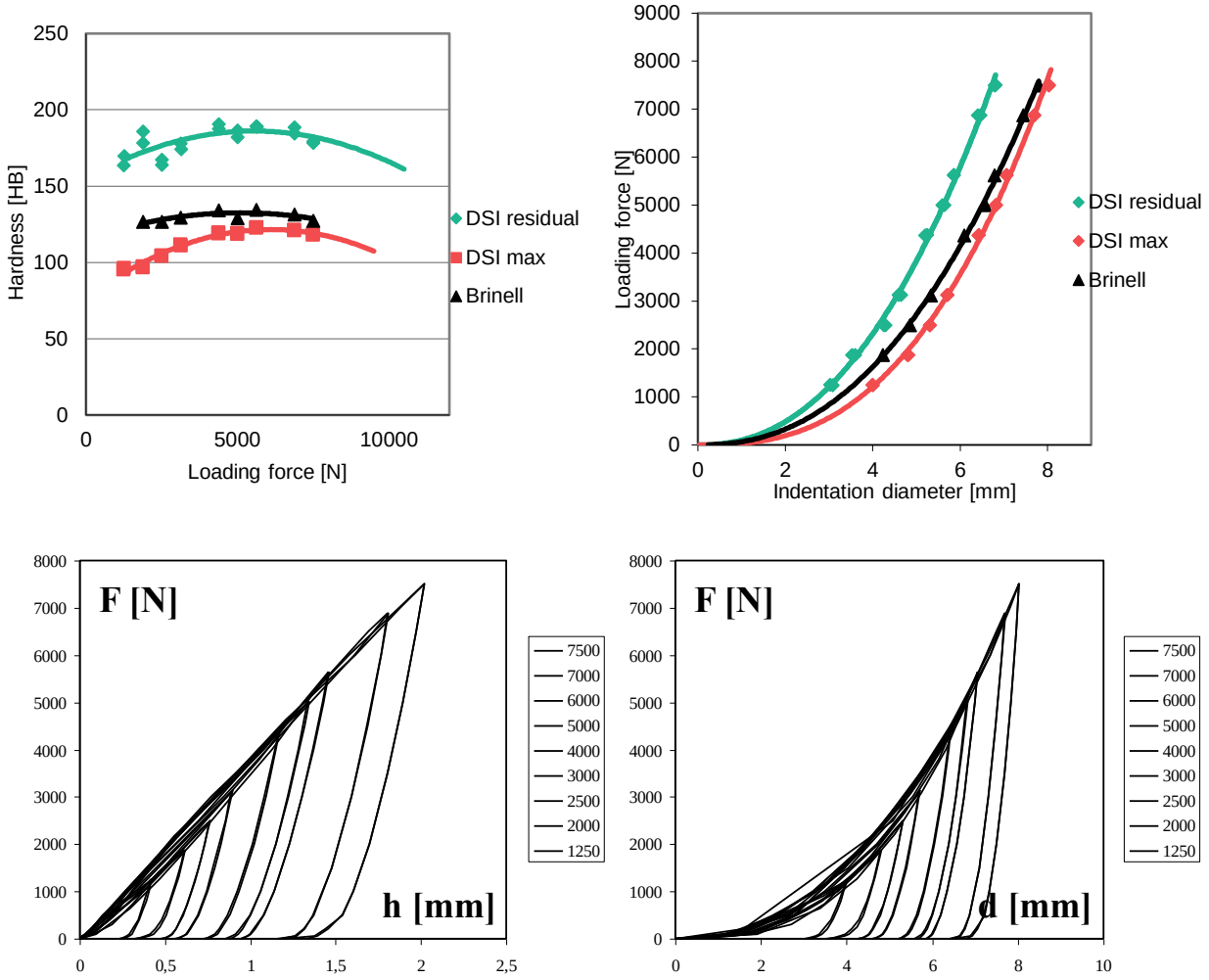

Fig. A-43 *Hardness test results of rhyolite tuff*

XXV. Test data used to evaluate the estimation method considering different aggregate types

Table A-40 *Laboratory test and model evaluation results used to test the algorithm developed for the consideration of different aggregate types in DEM*

								Parameters:			m_R	m_C	c_N		c_L		c_{Dens}	
											0.845	1.04	2022.9		2438.1		2153.9	
#	Aggerate size distribution [%]			Density [kg/m^3]	Compressive strength [N/mm^2]	Aggregate type	Pb strength [N/mm^2]	Crushed	No fines	Light weight	m_R	m_C	m_L	m_N	m_{Dens}	Estimated Pb strength [N/mm^2]	Error [-]	Error [%]
	0/4	4/8	8/16															
Gra	70	15	15	2257.56	26.69	Gravel	20.8	0	0	0	0.845	1	1	1	0.95	21.52	-0.72	-3.4
Gra	40	30	30	2343.9	33.73	Gravel	25.9	0	0	0	0.845	1	1	1	0.92	26.19	-0.29	-1.1
Gra	0	50	50	2095.5	22.45	Gravel	21.23	0	1	0	0.845	1	1	1.07	1.03	20.92	0.31	1.4
Liap	0	100	0	1200.5	12.66	Light	13.12	0	1	1	0.845	1	2.03	0.35	1.79	13.73	-0.61	-4.6
Crus	70	15	15	2364.06	53.29	Crushed	42.3	1	0	0	0.845	1.04	1	1	0.91	42.67	-0.37	-0.9
Crus	40	30	30	2430.17	40.58	Crushed	32.35	1	0	0	0.845	1.04	1	1	0.89	31.61	0.74	2.3
Crus	0	50	50	1854.3	9.44	Crushed	7.85	1	1	0	0.845	1.04	1	0.84	1.16	8.10	-0.25	-3.1
R_1	100	0	0	2240	69.2	Gravel	55.81	0	0	0	0.845	1	1	1	0.96	56.23	-0.42	-0.7
R_6	38	31	31	2142.5	49.6	Crushed	39.52	1	0	0	0.845	1.04	1	1	1.01	43.82	-4.30	-10.9
R_1	42	58	0	2119	49.5	Crushed	40.01	1	0	0	0.845	1.04	1	1	1.02	44.22	-4.21	-10.5
R_R	42	18	40	2318	49.3	Crushed	40.51	1	0	0	0.845	1.04	1	1	0.93	40.26	0.25	0.6
Size	36	25	39	2381	57.8	Gravel	45.95	0	0	0	0.845	1	1	1	0.90	44.18	1.77	3.8
Size	56	20	24	2293	55.054	Gravel	43.3	0	0	0	0.845	1	1	1	0.94	43.70	-0.40	-0.9
Size	47	28	25	2327	40.17	Gravel	31.5	0	0	0	0.845	1	1	1	0.93	31.42	0.08	0.3
Size	36	25	39	2338	67.56	Gravel	53.87	0	0	0	0.845	1	1	1	0.92	52.59	1.28	2.4
Size	46	27	27	2336	73.62	Gravel	58.5	0	0	0	0.845	1	1	1	0.92	57.36	1.14	2.0
Har	40	22	38	2300	54.2	Gravel	42.51	0	0	0	0.845	1	1	1	0.94	42.89	-0.38	-0.9
S_3	42	29	29	2355	38.7	Gravel	30.03	0	0	0	0.845	1	1	1	0.91	29.91	0.12	0.4

								Parameters:			m_R	m_C	c_N		c_L		c_{Dens}	
											0.845	1.04	2022.9		2438.1		2153.9	
#	Aggerate size distribution [%]			Density [kg/m^3]	Compressive strength [N/mm^2]	Aggregate type	Pb strength [N/mm^2]	Crushed	No fines	Light weight	m_R	m_C	m_L	m_N	m_{Dens}	Estimated Pb strength [N/mm^2]	Error [-]	Error [%]
	0/4	4/8	8/16															
S_2	45	20	35	2311	35.33	Gravel	27.93	0	0	0	0.845	1	1	1	0.93	27.82	0.11	0.4
S_2	45	20	35	2356	66.1	Gravel	53.61	0	0	0	0.845	1	1	1	0.91	51.06	2.55	4.8
S_1	55	45	0	2282	85.9	Gravel	69.94	0	0	0	0.845	1	1	1	0.94	68.51	1.43	2.0
S_1	55	45	0	2350	96.37	Gravel	79.58	0	0	0	0.845	1	1	1	0.92	74.64	4.94	6.2
S_1	55	45	0	2315	85.19	Gravel	67.54	0	0	0	0.845	1	1	1	0.93	66.98	0.56	0.8
S_1	100	0	0	2305	93.23	Gravel	77.2	0	0	0	0.845	1	1	1	0.93	73.62	3.58	4.6
P_1	42	20	38	2346	69.3	Gravel	55.63	0	0	0	0.845	1	1	1	0.92	53.76	1.87	3.4
P_1	42	20	38	2365	68.6	Gravel	57.62	0	0	0	0.845	1	1	1	0.91	52.79	4.83	8.4
P_2	45	25	30	2318	47.7	Gravel	39.19	0	0	0	0.845	1	1	1	0.93	37.45	1.74	4.4
P_4	46	26	28	2411	82.88	Crushed	67.55	1	0	0	0.845	1.04	1	1	0.89	65.07	2.48	3.7
P_4	47	25	28	2384	75.69	Crushed	61.18	1	0	0	0.845	1.04	1	1	0.90	60.10	1.08	1.8
V_	45	25	30	2256.86	57.06	Gravel	47.27	0	0	0	0.845	1	1	1	0.95	46.02	1.25	2.7
V_	45	25	30	2339.22	65.25	Gravel	51.47	0	0	0	0.845	1	1	1	0.92	50.77	0.70	1.4
V_I	42	25	33	2344	51.22	Gravel	40.84	0	0	0	0.845	1	1	1	0.92	39.77	1.07	2.6
V_	43	22	35	2810	60.87	Gravel	48.8	0	0	0	0.845	1	1	1	0.77	39.43	9.37	19.2
V_I	43	22	35	2347	65.92	Gravel	49.8	0	0	0	0.845	1	1	1	0.92	51.12	-1.32	-2.6
C_I	50	25	25	2415	47.14	Crushed	35.12	1	0	0	0.845	1.04	1	1	0.89	36.95	-1.83	-5.2
C_I	30	30	40	2451	37.21	Crushed	26.98	1	0	0	0.845	1.04	1	1	0.88	28.74	-1.76	-6.5
C_I	48	30	22	2378	45.78	Crushed	37.91	1	0	0	0.845	1.04	1	1	0.91	36.44	1.47	3.9
C_I	65	20	15	2371	48.91	Crushed	41.03	1	0	0	0.845	1.04	1	1	0.91	39.05	1.98	4.8
LW	0	100	0	1272	14.23	Light	14.12	0	1	1	0.845	1	1.92	0.40	1.69	15.43	-1.31	-9.3

										Parameters:		m_R	m_C	c_N		c_L		c_{Dens}	
												0.845	1.04	2022.9		2438.1		2153.9	
#	Aggerate size distribution [%]			Density [kg/m^3]	Compressive strength [N/mm^2]	Aggregate type	Pb strength [N/mm^2]	Crushed	No fines	Light weight	m_R	m_C	m_L	m_N	m_{Dens}	Estimated Pb strength [N/mm^2]	Error [-]	Error [%]
	0/4	4/8	8/16																
LW	0	100	0	1145	11.32	Light	11.87	0	1	1	0.845	1	2.13	0.32	1.88	12.28	-0.41	-3.4
LW	0	100	0	1331	16.11	Light	16.54	0	1	1	0.845	1	1.83	0.43	1.62	17.47	-0.93	-5.6
NF_	0	50	50	2125	22.45	Gravel	22.11	0	1	0	0.845	1	1	1.10	1.01	21.22	0.89	4.0
NF_	0	70	30	2210	27.12	Gravel	26.61	0	1	0	0.845	1	1	1.19	0.97	26.66	-0.05	-0.2
NF_	0	50	50	2062	22.02	Gravel	19.55	0	1	0	0.845	1	1	1.04	1.04	20.19	-0.64	-3.3

XXVI. Durability measurements and their discussion

XXVI.I Durability properties

Durability is defined as the resistance against weather actions, abrasion, chemical attack and any other condition coming from the usage of a given material *(ACI CT-13, 2013)*. Durability performance of a material shows us how the material will endure the vicissitudes of its environment on a long run. Nowadays in structural design we are aiming to achieve a long structural service life (*fib, 2009*). In case of concrete, its durability properties are mainly dependent on the properties of its ingredients, their method of mixing and their proportions. In Europe the major cause of durability problems of concrete structures are freezing and thawing cycles during the winter period. Thus in this study this feature was highlighted and investigated as most important durability property.

XXVI.I.I Frost resistance

There are two major methods, how the resistance against freezing is measured. One of them is frost resistance, while the other is freeze-thaw resistance. Frost resistance is the property that a material can withstand several freeze-thaw cycles without being destroyed and its strength does not decrease seriously when the material absorbs water to saturation (*Zhang, 2011*). The reason of this damage is a volume expansion that is caused by the freezing of water within the pores of the material. If a material's pores are full of water, then this expansion (when the water is frozen into ice) can reach 9% volume increase, causing tensile stress to pore walls. This stress can exceed the tensile strength of a porous material, that are mostly more resistant against compression. This can lead to microcracks that will cause in long term the decrease of the strength of the material.

The main influencing factors of frost resistance of a material are: composition, porosity, the characteristics of pores, strength, water resistance, and so on. In case of concrete those factors affecting the frost resistance are the type of cement, water-cement ratio and the strength of the aggregates. The best measures to improve frost resistance are to enhance its density, reduce water-cement ratio and/or add air-entraining agent into the concrete mix.

XXVI.I.II Freeze/thaw resistance

Freezing and thawing is one of the most common physical deterioration of porous materials in cold environment. Freezing and thawing cycles of real structures are leading to their surface scaling, especially in case of concrete. Surface scaling is caused by freezing of the concrete surface when it is in contact with weak saline solutions. This type of damage can be described as the removal of small chips from the surface of the material (*fib, 2009*). Similarly to frost

resistance one of the best solutions for enhancing the freeze/thaw resistance is the he adoption of air-entraining admixtures. It will introduce a specific amount of appropriately sized air voids in the cement matrix, creating space for increase in water volume during freezing. The other option is also the increase of material density, when not new pores are created, but the existing ones are filled with appropriate sized materials.

XXVI.II Description of the applied durability tests

XXVI.II.I Testing for frost resistance

With this test, it was aimed to investigate the effect of frost on the compressive strength of concrete. The test was done based on the *MSZ 4715-3* standard. 100×100×100 mm cube specimens were put into water until they did not become saturated. After that, the specimens were put into a laboratory freezer, and there 50/100/150 freezing cycles were applied to them. One cycle contains 2 hours of cooling, 2 hours on -20 °C, 2 hours melting and 2 hours on +20 °C. In the freezing phase, the specimens are surrounded by air, while during the melting phase, the freezer compartment is filled with water. After the given number of freezing cycles were applied on the specimen, they were rested in water for three days to avoid any residual freezing inside the material. Finally, uniaxial compressive strength test was performed on the samples. This type of test can be applied if one would like to assure or determine the frost resistance of a vertical structure (XF1 and XF2; e.g. wall, pillar, etc.).

XXVI.II.II Freeze-thaw resistance test

During the freeze-thaw test, the samples were subjected to alternating freezing and thawing cycles based on the recommendations of the standard *CEN/TS 12390-9*. First, the originally 100×100×100 mm specimen was cut in half. The tests were done on three different sides of the specimens: sawn surface, top surface and the surface cast against formwork. The standard recommends the evaluation based on the results of the sawn surface. Then the sides, which were not subjected to test liquid, were isolated. After that, the test liquid (3 m% NaCl solution) was placed on the tested surface in 5 mm thickness. The prepared specimens were placed into the freezer and were subjected to 56 freeze-thaw cycles (6 hours cooling, 6 hours on -20 °C, 6 hours melting, 6 hours on +20 °C). After 7, 14, 28 and 56 cycles, the specimens were taken out from the freezer, and the scaled material from the tested surface was removed and weighed. The more weight is measured, the higher the scaling is and the worse the freeze-thaw resistance is.

XXVI.III Comparison of CCP against other recycled powders

XXVI.III.I Frost resistance test results

150 freeze cycles were applied to all concrete mixes, and the change of the compressive strength was monitored. In case of the reference mix, only a minor change in compressive strength was observable until 100 cycles. However, after 150 cycles of freezing, a significant drop of the compressive strength was measured as it can be seen in *Fig. A-44*. In case of the mix with air-entraining agent, the strength decrease was around 7%.

In case of both mixes with additional waste materials, the decrease of the compressive strength after 150 cycles of freezing was less than 10%. The effect of freezing was particularly small in case of the mix with cellular concrete powder where the difference in compressive strength between the 0 and 150 cycles was less than 3.5%, see *Fig. A-44* and *A-45*. This indicates that additional waste materials can have a positive effect on the durability of concrete.

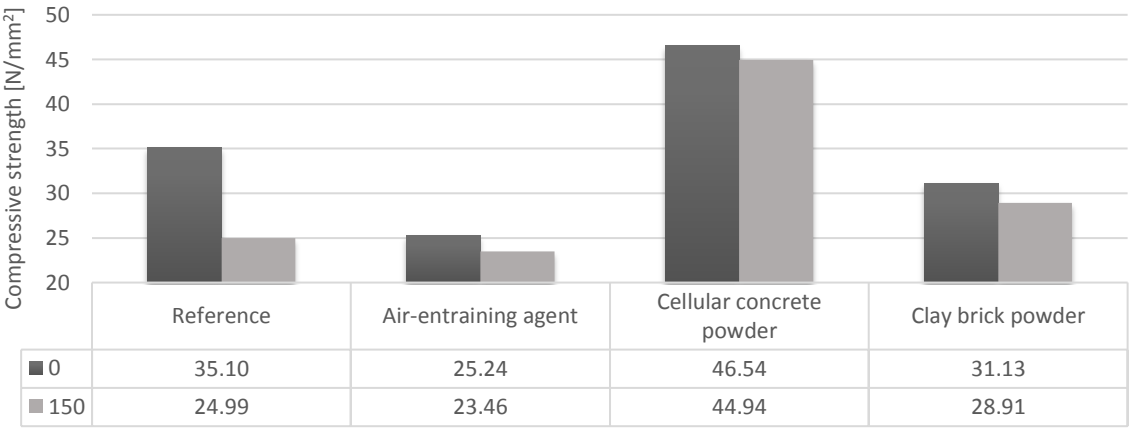

Fig. A-44 *Compressive strength before freezing and after 150 freeze cycles*

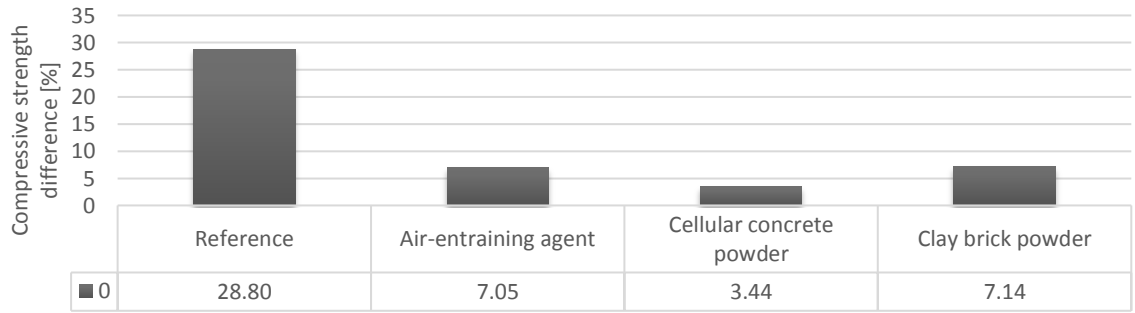

Fig. A-45 *Decrease of compressive strength after 150 freeze cycles*

The effect of frost on the mass of the concrete samples was measured as well, but no significant differences were found.

XXVI.III.II Freeze-thaw test results

The deterioration of the concrete surface was determined by freeze-thaw test, and the weight loss of the material was measured. The results of the sawn surfaces were used for the evaluation. The results of the sawn surfaces showed that, compared to the reference, the mix with air-entraining agent has the best performance, as it can be seen in *Fig. A-46*. In that case, the amount of material loss is lower with an order of magnitude than in case of the reference mix. The clay brick powder has not improved the durability of the material; the values of material loss are slightly higher than in case of the reference mix. The cellular concrete powder significantly decreased the value of material loss compared to the reference mix; the values of the mix with cellular concrete powder are less than the half of the values got from the reference mix. As it was aimed during the mix design, the reference mix has low resistance against freeze-thaw.

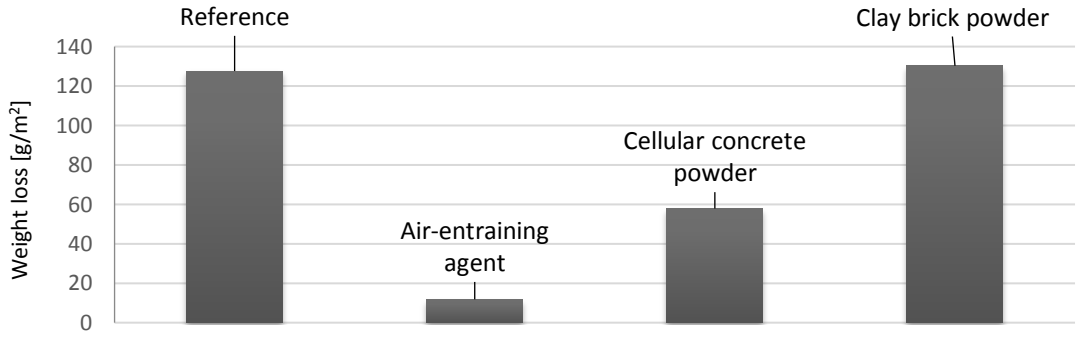

Fig. A-46 *Weight loss of the samples after 56 freeze-thaw cycles mix)*

Based on the results of the tests it can be drawn that the air-entraining agent highly improved the freeze resistance of concrete as it was expected, although it significantly decreases the compressive strength (30%) of the material and its cost is high compared to the other solutions investigated in this study. The clay brick powder has no significant effect on the strength of concrete or on its durability. The cellular concrete powder is able to increase the compressive strength significantly (37%), and it has a positive effect on the durability performance of the concrete as well. Based on the freeze test, the concrete with cellular concrete powder lost less than 5% of its compressive strength after 150 cycles of freezing. On top of that, the cellular concrete powder is a waste material, which is the result of the cutting of cellular concrete bricks; thus, it has a minimal cost. It does not require any preparation before mixing, while clay brick powder has to be pulverized first.

XXVI.IV Detailed investigation of CCP in powder form

XXVI.IV.I Frost resistance test results

XXVI.IV.I.I Normal strength concrete with CCP and MK substituting cement

The results of the frost resistance measurements are presented in a similar order, as it was in case of the compressive strength results. In *Fig. A-47* the results of the compressive strength tests are presented after 0 and 150 freezing cycles (described in *Chapter XVI.II.I*) as well as the ratio of the two measurements (indicated by black stripes on the figures). The left axis of the figure belongs to the bars showing the compressive test results, while the secondary axis on the right side of the figure belongs to the ratio of the compressive strengths (after 150 and 0 cycles). A concrete can be considered as frost resistant if the 150 to 0 ratio is above 85%. Thus with these additional materials, a frost-resistant concrete could be mixed. 150 freezing cycles were applied based on the recommendation of the standard (*MSZ 4715-3*), and because in case of the reference mix, only a minor change in compressive strength was observable until 100 cycles.

When the cement was partly substituted by CCP, the values presented in *Fig. A-47* were measured. The results show a clear tendency for both cases (after 0 and 150 freezing cycles):

- With the increase in the amount of CCP, the compressive strength is increasing as well, until a given point, around 10%.
- After that point, a strong reduction in strength is observed.

The most advantageous of the investigated mixes is the Y10 mix, which significantly increases the strength before and after the freezing cycles as well. It is important to mention that the proportional strength increase is even higher after the freezing cycles compared to the reference mix, meaning that the CCP not only increases the compressive strength itself but the frost resistance as well. This statement is true below a given amount (around 10%) of CCP in the mix. When the ratio of the two measured values is considered, the most outstanding is the Y3 mix (81%). The Y10 (76%) mix was also able to increase the ratio of compressive strengths.

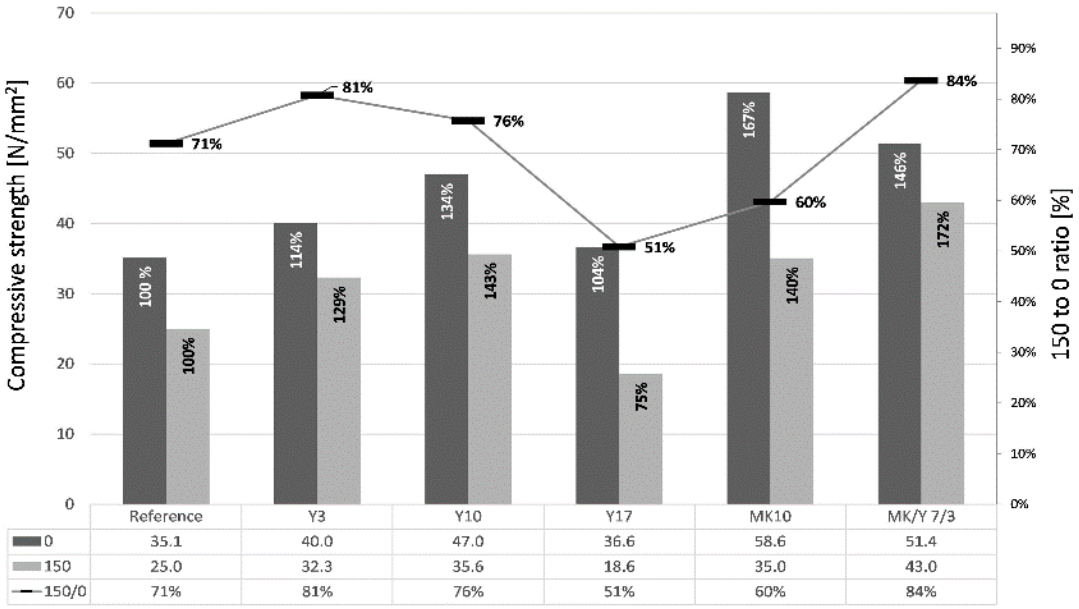

	Reference	Y3	Y10	Y17	MK10	MK/Y 7/3
0	35.1	40.0	47.0	36.6	58.6	51.4
150	25.0	32.3	35.6	18.6	35.0	43.0
150/0	71%	81%	76%	51%	60%	84%

Fig. A-47 *Frost resistance of the normal strength concretes containing different amount of CCP or MK after 0 and 150 freezing cycles*

The MK10 mix is still advantageous compared to the reference mix after 150 freezing cycles (*Fig. A-47*). However, its proportional strength increase (40%) is significantly lower than it was before the freezing cycles (67%). After the freezing cycles, the Y10 mix had better performance than the MK10 mix. The MK/Y mix showed an outstanding performance in this test. After the freezing cycles, it increased the compressive strength by 72%, which is the second-best performance among the investigated mixes. This means that the interaction of the CCP and MK can even lead to better performance than separately. From a frost resistance viewpoint, the MK10 mix was found to be the weakest (60% 150/0 ratio), while the MK/Y mix had a good performance (84%). However, quantitatively the compressive strength of the MK10 mix (35 N/mm^2) is still higher, than the reference mix's (25 N/mm^2). This means that the substitution of cement by MK is still advantageous in a normal strength concrete, but for durability design purposes, it has to be considered, that its frost resistance is lower than the mix containing only cement.

The reason behind the outstanding performance of CCP can be seen on the SEM results (*Fig. 58*). The small CCP particles work as a filling material, while the larger ones introduce ideal size pores in the concrete. The chemical structure of concrete and CCP are very similar, and CCP has high internal porosity. Thus, the new CSH crystals, developing during the hydration of concrete, are able to grow amid the already existing CSH crystals of CCP. There is no proof of a chemical connection between the newly developed CSH crystals and the already existing ones; however, based on the test results, the physical connection could be strongly assumed. In case of clay brick, this effect is not present.

XXVI.IV.I.II High strength concrete with CCP and MK substituting cement

Similar trends can be observed in the frost resistance results of the high strength concrete (containing different amounts of CCP), as it was seen on the compressive strength results (*Fig. A-48*). CCP reduces the compressive strength, and above 10% dosage, the decrease becomes significant. The results of the Y3 and Y10 mixes are close to each other (within 5% in both cases). The 150/0 ratio is almost identical for all CCP dosages. The outcome of this test shows that the CCP used as an SCM is not advantageous in case of high strength concrete unless the 10-20% of strength loss is acceptable for lower material cost (-10% cement). Thus, it is not compared in that case to MK.

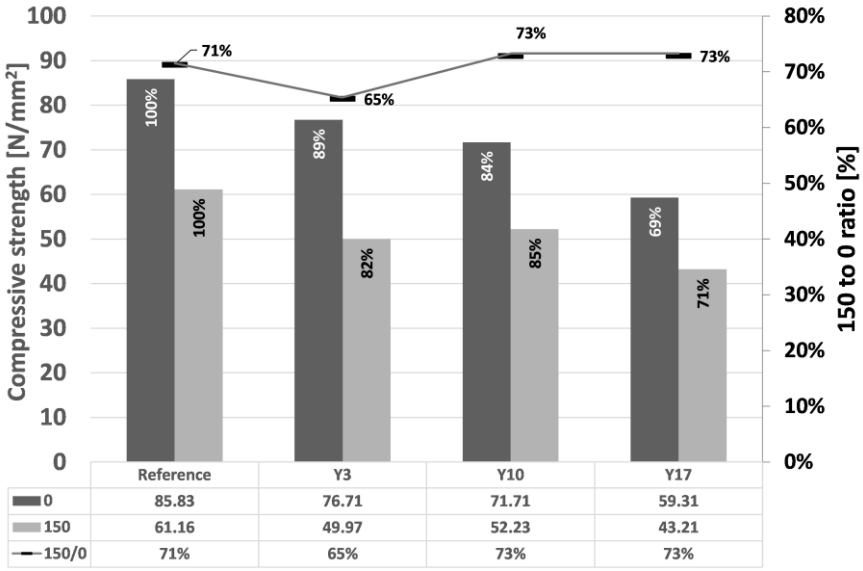

	Reference	Y3	Y10	Y17
0	85.83	76.71	71.71	59.31
150	61.16	49.97	52.23	43.21
150/0	71%	65%	73%	73%

Fig. A-48 *Frost resistance of the high strength concretes containing different amount of CCP after 0 and 150 freezing cycles*

XXVI.IV.II Freeze-thaw resistance test results

XXVI.IV.II.I Normal strength concrete with CCP and MK substituting cement

Freeze-thaw test was used to determine the deterioration of the concrete surface, and the weight loss of the material was measured. The results of the sawn surfaces were used for the evaluation. The higher amount of weight loss means more deterioration of the surface. The freeze-thaw test with different amount of CCP applied had an interesting result (*Fig. A-49*). CCP addition has resulted in superior resistance compared to the reference mix at the tested relatively low cement substitution ratios. The loss of mass was influenced by the amount of CCP applied in the mix. The higher the cement substitution ratio was, the higher the loss of mass caused by the internal damage due to the freeze-thaw cycles. Similar behaviour was observed in (*Borosnyói, 2016*) for MK.

The Y3 mix only lost 18% of its mass compared to the reference mix, the Y10 lost 36%, but the Y17 already lost 78% that is close to the mass lost by the reference mix. Based on these

results, the lower the CCP dosage is, the better, however, if cost reduction is significant as well, then the Y10 mix can be advantageous as well. In case of the frost resistance, the optimum of the amount of CCP was found to be around 10%. However, in case of the freeze-thaw resistance, this optimum is around 3% (or below). Later more detailed investigation would be necessary to determine this optimum.

Metakaolin addition has resulted in superior resistance compared to the reference mix as well. MK10 has 52% less weight loss than the reference mix, which is somewhat higher than the weight loss of the Y10 mix. The most superior performance was done by the MK/Y mix, as it showed in *Fig. A-49*. It can be concluded based on these results and the results presented in the previous chapters that the combined use of MK and CCP could be advantageous for increasing durability of normal strength concrete. However, the combined MK/Y mix produced still higher loss of mass, than the Y3 mix. Thus, the combination of the two materials is not favourable against the Y3 mix. In *Fig. A-50*, it can be seen that over the freeze-thaw cycles at every cycle the Y3 mix is the most favourable. All applied additives decreased the initial slope of the figures (thus delaying the damage of a structure) and had favourable values in long term (after 56 cycles) as well.

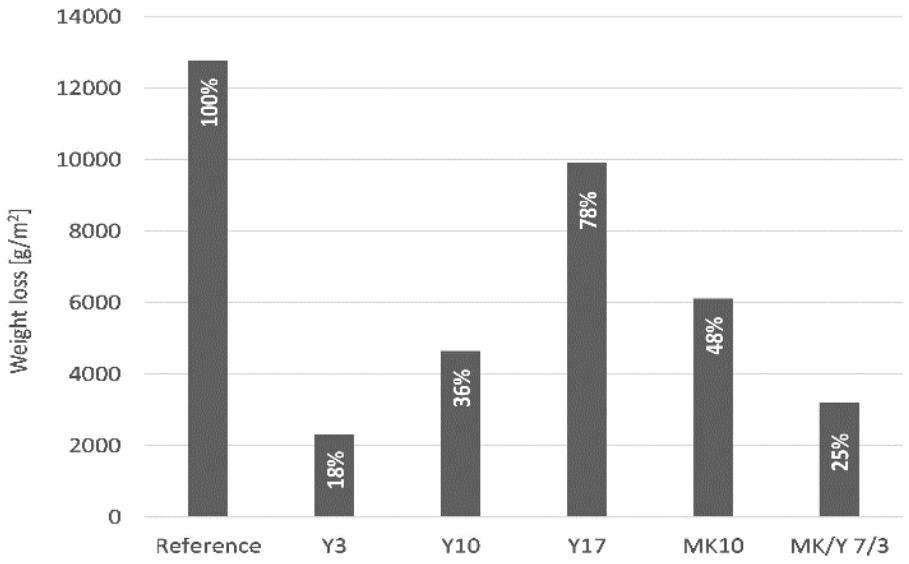

Fig. A-49 *Weight loss of the normal strength concretes with 10% dosage of CCP or MK after 56 freeze-thaw cycles*

The superior performance of the mixes containing CCP can be explained by the presence of tobermorite crystals ($C_5S_6H_5$ - special type of CSH, which can be found in cellular concrete). Tobermorite is well known for its resistance against salty water (Roman concrete) (*Jackson et al, 2017*). In the present case, the tobermorite crystals in the concrete could increase its resistance against the salty water applied during the freeze-thaw resistance test.

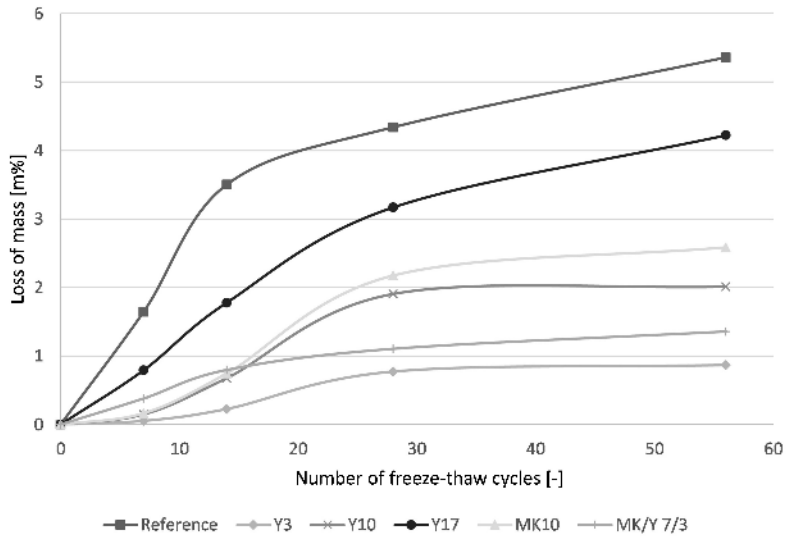

Fig. A-50 *Change of mass loss during the freeze-thaw cycles for normal strength concretes*

XXVI.IV.II.II High strength concrete with CCP and MK substituting cement

On high strength concrete, CCP has very strong effect from the viewpoint of freeze-thaw resistance. *Fig. A-51* shows that smaller amount (Y3 and Y10) of CCP highly decreased (12% and 1%) the loss of mass caused by deterioration. However, higher amount of CCP caused higher weight loss, than it was in case of the reference mix. MK has advantageous effect as well in correspondence with (*Borosnyói, 2016*), as it can be seen in *Fig. A-51*. In case of the high strength concrete, the combination of CCP and MK was not so well performing as it was in case of the normal concrete. In this case, the MK10 mix had much lower weight loss (7%) compared to the MK/Y mix (22%). The Y10 mix performed better than any other mix in this comparison. It is important to highlight that both the Y10 and MK10 mixes had weight loss of less than 200 g/m^2, which is the limit value in the standards (*CEN/TS 12390-9*). These values measured are so small that it is not appropriate to differentiate them (due to the uncertainty of the measurement process); thus, as conclusion, the following remarks can be declared:

- In case of high strength concrete, the Y3, Y10 and MK10 mixes all performed exceptionally.
- The Y17 mix had an unfavourable effect.
- The MK/Y mix performed quite well; however, compared to the mixes, where only CCP or MK was applied, it is unfavourable. Thus, based on the freeze-thaw resistance test results, the combination of the two materials is not advantageous, similarly to literature data, where two SCMs were combined (*Borosnyói, 2016*).

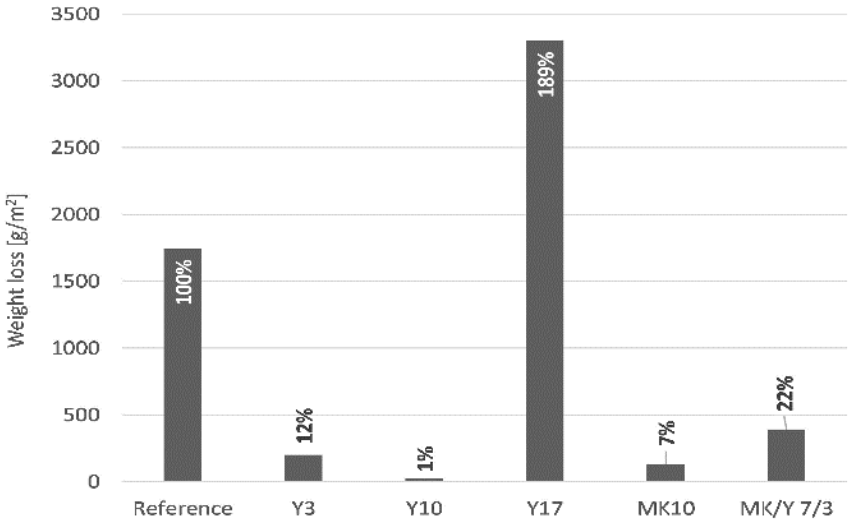

Fig. A-51 *Weight loss of the high strength concretes with different amount of CCP or MK after 56 freeze-thaw cycles*

XXVII. TG analysis of Y10 and MK10 mortars

Table A-41 *Mass loss and amount of portlandite in the samples from 0 to 180 days of age*

	Thermal decomposition range [°C]	**Mass loss [%]**					
		After mixing	**2 days**	**7 days**	**28 days**	**90 days**	**180 days**
Reference	20-240	23.68	15.74	15.61	14.89	15.85	15.52
	430-540	0.14	2.5	2.85	2.87	2.75	3.05
	600-800	1.38	1.54	1.79	1.29	1.51	2.59
	20-800	26.02	23.92	24.76	23.46	23.71	25.17
Y10	20-240	24.9	17.32	17.88	15.53	14.91	16.07
	430-540	0.29	2.13	2.63	2.61	2.8	3.14
	600-800	1.07	2.13	1.91	1.83	2.03	1.73
	20-800	27.67	24.55	26.19	24.17	23.99	25.74
MK10	20-240	22.63	10.12	16.41	16.07	15.57	16.18
	430-540	0.16	1.99	2.65	2.36	2.45	2.43
	600-800	1.14	1.2	1.32	1.39	1.54	2.09
	20-800	24.72	24.2	24.23	24.4	24.13	24.73

REFERENCES

In this section the references are listed that are used only in the appendices.

André, D., Jebahi, M., Iordanoff, I., Charles, J., Neauport, J. "Using the discrete element method to simulate brittle fracture in the indentation of a silica glass with a blunt indenter", Computational Methods in Applied Mechanical Engineering, 265:136–147, 2013. https://doi.org/10.1002/9781119103042.ch3

Bagi, K. "An algorithm to generate random dense arrangements for discrete element simulations of granular assemblies", Granual matter, Vol. 7. 31-43, 2005. https://doi.org/10.1007/s10035-004-0187-5

Chung, Y. C., Lin, C. K., Chou, P. H., Hsiau, S. S. "Mechanical behavior of a granular solid and its contacting deformable structure under uni-axial compression – Part I: Joint DEM–FEM modelling and experimental validation", Chemical Engineering Science, 144: 404–420, 2016. https://doi.org/10.1016/j.ces.2015.11.024

Cundall, P. A. "Formulation of a three-dimensional distinct element model – Part I: A scheme to detect and represent contacts in a system composed of many polyhedral blocks" International Journal of Rock Mechanics and Mining Sciences & Geomechanics Abstracts, Vol. 25, pp. 107-116, 1988. https://doi.org/10.1016/0148-9062(88)92293-0

Jackson, M. D., Mulcahy, S.R., Chen, H., Li, Y., Li, Q., Cappelletti, P., Wenk, H.R. "Phillipsite and Al-tobermorite mineral cements produced through low-temperature water-rock reactions in Roman marine concrete", American Mineralogist, 102(7): 1435–1450, 2017. https://doi.org/10.2138/am-2017-5993CCBY. ISSN 0003-004X

Rousseau, J. "Modélisation numérique du comportement dyna-mique de structures sous impact sévère avec un couplage élémentsdiscrets / éléments finis [Numerical modeling of dynamic behavior ofreinforced concrete structures under severe impact using DEM/FEMcoupling]."Ph.D. thesis, Université de Grenoble, Saint-Martin-d'Hères, France (in French), 2009.

Shui, Z., Lu, J., Tian, S., Shen, P., S., Ding, S., "Preparation of New Cementitious System using Fly Ash and Dehydrated Autoclaved Aerated Concrete", Journal of Wuhan University of Technology-Mater. Sci. Ed. 29(4), 726-732, 2014. https://doi.org/10.1007/s11595-014-0987-3

Sobolev, K., Amirjanov, A. „The development of a simulation model of the dense packing of large particulate assemblies", Powder Technology,141, 155–160, 2004

Szilágyi, K. “DEM modelling of the Brinell-testing of concrete”, Micromechanics of granular media – Manuscript, BME Faculty of Civil Engineering, Budapest, 2009

Vadluga, V., Kacaianauskas, R. “Investigation of the single-spring lattice model in simulation of 2D solid problems by DEM”, Mechanika, 67:5-13, 2007.

Zhang, H. “Building Materials in Civil Engineering”, 1st Edtition, Woodhead Publishing, p. 440, ISBN: 9781845699567, 2011.